PHYSICAL AND NUMERICAL MODELING OF OFFSHORE ANCHOR PILES UNDER MOORING FORCES

MOHAMED I.H. RAMADAN

PHYSICAL AND NUMERICAL MODELING OF OFFSHORE ANCHOR PILES UNDER MOORING FORCES

by

© Mohamed I. H. Ramadan, B.Sc., M.Sc.

A Thesis submitted to the

School of Graduate Studies

in partial fulfillment of the requirements for the degree of

Doctor of Philosophy

Faculty of Engineering and Applied Science

Memorial University of Newfoundland

November 2011

St. John's Newfoundland

ABSTRACT

Floating Production Storage Offloading vessels (FPSOs) are widely used in offshore oil and gas industry in harsh environments reach at the Grand Banks. Vessels working at an offshore site must be held in position despite the effects of wind, waves, and current. Many FPSOs are keeping position using seafloor anchors which are commonly secured using anchor piles. Anchor piles are very effective in many soils. The pile can either be drilled in and grouted, using an offshore mobile drilling rig, or driven in with an underwater hammer or a follower. The anchor pile resists pullout by a combination of bending plus passive resistance and skin friction shear.

Correctly designed pile anchors should transfer the environmental loads on the floating platforms to the seabed safely. In-service, these anchor piles are subjected to a wide range of monotonic and cyclic lateral to oblique pull forces. The large cyclic forces applied during extreme storm will tend to govern the design.

The presented work aims at identifying the behavior and capacity of anchor piles used for anchoring offshore floating structures in dense sand. As full-scale experimental verification is not always possible, this raises up the need to design a physical model which can simulate the behavior of the full-scale case. To simulate the important gravitational component, the physical model tests were conducted using the geotechnical centrifuge to investigate the anchor piles response to mooring forces in saturated dense sand. Two centrifuge tests setup were carried out. In each test setup four model pipe piles were jacked in flight in homogeneous saturated sand and subjected to monotonic and

cyclic pull-out forces with inclination angle 0° (pure lateral loading), 16°, 30°, and 90° (pure tension loading) with the horizontal. The soil pile interaction behavior was monitored through the strain gauges attached on the pile. While the undisturbed soil stiffness distribution with depth will be measured using a shear wave measurement system of bender elements which can provide soil shear modulus distribution with depth.

To study many factors that are affecting the model, a 3-D finite element model (FEM) was validated from the experimental centrifuge results. The validated FEM was used to do a parametric study to get design procedures and provide better understanding of the response of anchor piles to a variety of loading conditions. The parameters that will affect the pile behavior as suggested from the previous researchers and will be studied here are pile diameter, pile flexibility, load inclination angle, and padeye depth on the pile.

From the present study, it was found that there is a significant interaction between lateral and tension loading. A design method was proposed to predict the ultimate capacity of offshore anchor pile depending on pile flexibility, loading angle and padeye depth. Also, a design method was proposed to predict the maximum bending moment.

ACKNOWLEDGEMENTS

The author would like express his deep appreciation to his supervisor, Prof. Stephen D. Butt, for his valuable guidance, advice and financial support during my program of study. I would like also to express my sincere appreciation to my co-supervisor, Prof. Radu Popescu, for his academic guidance and valuable technical comments during my program of study. I am also grateful to Dr. Hesham Dief, a supervisory committee member, for his experimental research advice.

The experimental work in this research has been conducted in C-Core, Memorial University of Newfoundland. I wish to express my appreciation to Dr. Ryan Phillips for his guidance during all my centrifuge tests. I also would like to express my deep appreciation to the staff members at C-Core who helped me in the tests; Gerry Piercey, Brad Elliote, Karl Tuff, Don Cameron, and Derry Nicholl. My appreciation should be extended to Shawn Organ, a technician at Faculty of Engineering, Ted Lee, Bill Maloney, at the electronic technical service and all staff members at the technical services.

My deep and sincere thanks and appreciations are expressed to my mother, Seham, and my father who is my teacher, Prof. Ibraheem Ramadan, for their prayers, love, and continuous support. They spent long nights suffering and praying to see me happy and in the best position in this life. I wish I can be always a good son for them. My deep and sincere thanks and appreciations are expressed to my wife, Hanaa, for her love, prayers, patience, great support and encouragement. She suffered a lot with me during my study program. I wish I can give her all love and best wishes. It would have been impossible to complete this work without understanding, and sacrifices of my family. I would also like to express my deep love to my daughter, Haneen, who I would to see her in the best position and be her friend forever. My deep thanks should be expressed to my sister, Heba, and my brother, Ahmed, and all my aunts, uncles and friends for their support.

TABLE OF CONTENTS

List of Tables

List of Figures

LIST OF SYMBOLS AND ABBREVIATIONS

Roman Letters

A	factor to account for cyclic or static loading condition
A_s	embedded pile surface area
a	fitting parametr
b	fitting parametr
c'	effective cohesion
C_1	coefficient determined using API
C_2	coefficient determined using API
C_3	coefficient determined using API
D	the foundation depth
DF	the load amplitude
Dr	sand relative density
d	width or diameter of the pile
d_{eq}	the diameter of a solid pile of equivalent section area to the open-ended pile
d_i	the pile internal diameter
d_{10}	sand grain size at passing percentage 10%
d_{50}	sand grain size at passing percentage 50%
E_p	pile modulus of elasticity
E_s	soil Young's modulus
E_{max}	maximum soil Young's modulus
e	loading eccentricity
e_{max}	maximum void ratios
e_{min}	minimum void ratios
F_o	ultimate pile capacity
F_{max}	the maximum applied load
f	average unit skin friction
f	cyclic frequency
f_L	a reduction factor
f_r	resonant frequency
G	the soil shear modulus
G_{max}	the maximum soil shear modulus
G_s	specific gravity
g	earth gravity
g_{31}	piezoelectric voltage constant
H	horizontal load at pile head
H_f	lateral load at failure
H_n	normalized horizontal load component
H_{Nn}	lateral load at n cycle
H_{N1}	lateral load at the first cycle
h	distance from pile tip
h_m	model height in centrifuge
h_p	prototype height
I_p	moment of inertia of the pile section

I_R relative dilatancy index
K global stiffness
K_o lateral earth pressure coefficient at rest
K_a active lateral earth pressure coefficient
K_p passive lateral earth pressure coefficient
K_h soil stiffness
$K_{h\ Nn}$ soil stiffness at n cycle
$K_{h\ N1}$ soil stiffness at the first cycle
K_{max} maximum lateral earth pressure coefficient
K_{min} minimum lateral earth pressure coefficient
K_u uplift coefficient
k initial modulus of subgrade reaction (kN/m^3)
k_h subgrade.reaction modulus, in units of force/ length square
k_L value of k_h at the pile tip (z = L)
k_{py} gradient of initial p-y stiffness with depth (FL^{-3} dimensions).
L pile length
L_{tt} distance tip to tip between the source and the receiver bender element
l_b cantilever length of the bender element
M pile bending moment at depth z
M_{max} maximum bending moment
$M_{n\text{-}max}$ normalized maximum bending moment
$M_{max\ Nn}$ maximum bending moment at n cycle
$M_{max\ N1}$ maximum bending moment at the first cycle
m mass
N cycles number
N centrifuge scaling factor
N_L number of applied load cycles
n an empirical index equal to or greater than zero
n_h constant of horizontal subgrade reaction (FL^{-3} dimensions)
P soil pressure (kN/m^2)
P_z axial load on pile at depth z
P_u ultimate uplift pile capacity
P_L ultimate lateral pile resistance
P_θ ultimate inclined pullout load at pile head
P_{mean} mean cyclic load
P_{cyc} cyclic load component
P_o mean effective stress
P_a atmospheric pressure
p soil reaction per unit-length of pile
p_u ultimate soil pressure at depth z, (kN/m)
q_c cone resistance
q_b pile end bearing resistance
Q_{uv} gross ultimate vertical pile resistance
Q_{ov} net vertical ultimate uplift capacity
Q_{uH} gross ultimate lateral load at pile head
R pile installation effect factor
R pile radius

R_n pile normalized roughness
T thickness of the bender element
T pile elastic length
t degradation factor
t travel time
t pile wall thickness
t_s thickness of the center shim
V vertical load at pile head
V_f failure tension load
V_{Nn} axial load at n cycle
V_{N1} axial load at the first cycle
Vs shear wave velocity
V_u ultimate tension capacity under pure tension loading
$V(z)$ shear force at depth z
W bender element width
x depth to the point of rotation of the pile
x' padeye depth ratio
y pile horizontal deflection
y_n pile head displacement measured at the peak load value of cycle n
y_o deflection at the pile head
y_1 initial displacement measured at the end of initial loading
z *depth*

Greek Letters

δ the interface friction angle between soil and pile
τ soil shear stress
τ_s soil limiting shear stress
$\Delta\sigma'_{rd}$ stress change due to dilation effects
σ'_{vo} initial vertical soil stress
σ'_{rc} soil radial stress around the pile
σ_m stresses in centrifuge model
σ_p stresses in prototype scale
σ_h normal stress on the contact surface
σ_b average axial stress in pile section
ν_p Poisson's ratio for pile
β pile inclination angle
θ loading angle at pile head
α P_u/P_L
ω swept angular velocity
ρ material of density
ζ dimensionless depth factor
λ dimensionless deflection factor
λ wave length

π_3 flexibility ratio
Φ_1 dimensionless ratio
γ soil unit weight
γ' effective unit weight of soil
ε_1 value of the strain on the extrados points of pile section
ε_2 value of the strain on the extrados points of pile section
ε_b pile bending strain
ε_a pile axial strain
φ' effective soil internal friction angle
φ'_c critical state friction angle
ψ soil dilation angle
μ friction coefficient
α_H fitting parameter
β_H fitting parameter

Abbreviations

API American Petroleum Institute
CHT Cross-Hole Test
CLR Cyclic Loading Ratio
CPT Cone Penetration Test
DHT Down-Hole Test
FEM Finite Element Model
ICP Imperial College Pile
MTD Marine Technology Directorate
OCR Over Consolidation Ratio
SR Surface Refraction

Chapter 1

Introduction

1.1 Background:

It has only been in the latter half of the 20th century that full recognition has been given to the oceans and their sediments as a major source of mineral wealth, both hard minerals and petroleum. Offshore oil and gas now supply almost one third of the world's energy needs: in fact, it has been stated by the U.S. Geological Survey that the offshore sedimentary basins within the U.S. Economic Zone hold forth the greatest potential for major new discoveries. Because of the tremendous economic importance of offshore oil and gas and the concentrated development of technology for their exploitation, much of the recent marine construction practice has been devoted to the installation of facilities to serve the needs of the petroleum industry, Gerwick (2000)

In deep water, fixed offshore platforms are not economical due to the large amount of steel needed in constructing the supporting frame. Therefore, floating offshore structures became the economic alternative in deep waters. Floating structures are structures which are intended to remain floating throughout their service life. They include floating production, storage, and offloading (FPSO) vessels, the hulls of tension leg platforms and semisubmersible platforms, floating terminals, spars, floating bridges, industrial plants, floating dry docks, guide walls, and even the proposed floating heliports and airports, some of them shown in Figure 1.1. In service, they must endure the cyclic dynamic loading from waves and swells, so fatigue endurance is a significant consideration.

Floating Production Storage Offloading vessels (FPSOs) are widely used in offshore oil and gas industry in harsh environments reach at the Grand Banks. Vessels working at an offshore site must be held in position despite the effects of wind, waves, and current. The

current forces are relatively constant in direction in the offshore zones; in closer-in areas and opposite the mouths of great estuaries they may vary with the tidal cycle. The wave forces can be considered as comprising an oscillatory motion plus a steady, slow drift force. Both the mean forces of a quasi-static nature and dynamic forces must be resisted.

Mooring systems for deep water have considerations which differ significantly from shallower water. These include the weight of the mooring lines, the increased influence of low-frequency motion of the vessel, and line dynamics. Since there are significant increases in total current force in the deep sea, both the chain and the anchor need to be well designed. Anchors used to hold offshore floating structures include piles, drag anchors, and suction caissons. The focus of this research is on piles.

1.2. Anchor Piles:

At the Grand Bank, Off Newfoundland, many FPSOs are keeping position using seafloor anchors which are commonly secured using anchor piles. Anchor piles are very effective in many soils. The pile can either be drilled in and grouted, using an offshore mobile drilling rig, or driven in with an underwater hammer or a follower. The anchor line, usually a shot of chain at this location, can lead from the top or from a point a few meters down the pile. The anchor pile resists pullout by a combination of bending plus passive resistance and skin friction shear.

Correctly designed pile anchors should transfer the environmental loads on the floating platforms to the seabed safely. In-service, these anchor piles are subjected to a wide range of monotonic and cyclic lateral to oblique pull forces. The large cyclic forces applied during extreme storm will tend to govern the design. The design of these anchor piles has not been codified as jacket piles which are widely used for fixed offshore platforms, Bhattacharya et. al.(2006). Also, both piles are different in geometry and applied loads. While jacket piles are fixed-head and axially loaded piles (compression/tension), anchor piles are free-head and incline loaded (close to lateral) piles. It is important to remember that the parameters for the lateral design of jacket piles are derived from lateral pile load tests on small diameter piles. The controlling design loads for jacket piles are usually the

axial compressive and tensile loads, rather than the cyclic lateral loads. In contrast, the axial loads on FPSO piles are always tensile, and the lateral loads are much larger in comparison to the axial load. Therefore, the design of these anchor piles should not be the same as the jacket piles and extensive need to develop an accepted design method for this type of piles.

1.3. Research Scope:

There is relatively limited experimental information on anchor piles or piles subjected to oblique pull loads. Some of the existing theoretical models are semi-empirical based on 1g experimental tests. As indicated by Altaee & Fellenius (1994), the dilation of the sand occurring at low confining stress –shallow depth- increases the lateral soil stress against the pile. So, doing a test even in field using a small scale pile will only eliminate the boundary conditions problem in the laboratory test, but the physical modeling issue will not be controlled because of the small size of the pile at low confining stress – shallow depth- and therefore their results cannot correctly reproduce the real behavior of piles under mooring forces for sandy soil. Other models are based on the net uplift and the ultimate lateral capacity of the pile, whichever is smaller, as reported by Poulos and Davis (1980) and so neglected the interaction between horizontal and vertical pull forces on the pile.

The presented work aims at identifying the behavior and capacity of anchor piles used for anchoring offshore floating structures in dense sand. Offshore structures anchored in dense sand are typical in the Grand Bank, Off Newfoundland, and in other parts of the world, Gerwick (2000). Sand deposits in off Newfoundland have been subjected to continuous pounding by the storm waves above. What does happen is that the internal pore pressure in the upper layers of the sand is alternatively raised then drained, only to be raised again. After millions of cycles, the sand becomes extremely dense, often with consolidation higher than can be reconstituted in the laboratory. Friction angles in excess of 40° may be found.

As full-scale experimental verification is not always possible, this raises up the need to design a physical model which can simulate the behavior of the full-scale case. To simulate the important gravitational component, the physical model tests were conducted using the geotechnical centrifuge to investigate the anchor piles response to mooring forces in saturated dense sand. Not only to observe the load-displacement behavior at the pile head, but also to monitor the soil-pile interaction through a well instrumented pile to measure pile friction and bending moment of the pile that can be derivate twice to get the soil pressure on the pile. A shear wave velocity system of 6 bender elements (3 transmitters and 3 receivers) was designed to get the shear modulus distribution with depth of an undisturbed zone of the soil model. To study many factors that are affecting the model, a 3-D finite element model (FEM) will be calibrated from the experimental centrifuge results. The calibrated FEM will be used to do a parametric study to get design procedures and provide better understanding of the response of anchor piles to a variety of loading conditions. Based on this discussion, the main objectives of the current research can be summarized as:

1. Investigate and understand the behavior of anchor piles in dense sand based on the physical modeling results.
2. Calibrate and validate a numerical tool for analysis based on the physical modeling results.
3. Provide a well documented design methodology in a form of design equations based on the parametric study using the numerical model.

1.4. Thesis Organization:

The thesis includes nine chapters. The first chapter is the current introduction. The second chapter presents the literature review. The literature review is divided to three parts. The first part presents the behavior of piles under pure lateral loading. The different methods used before by other researchers to predict the behavior of piles under lateral loading. The second part presents the behavior of piles under tension loading especially of pipe sections that are used in offshore environment. The last part is related to the

previous research conducted for the study of the behavior of piles under inclined pullout loading.

Chapter three presents the centrifuge modeling technique. It shows the scaling principles and laws, and scaling effects and errors relevant for centrifuge modeling. It describes also a detailed discussion on the design of centrifuge tests, dense sand model preparation, centrifuge facility and test equipment, and centrifuge test procedure. The in-flight cone penetration tests (CPTs) were conducted to check sand homogeneity and were used to obtain sand properties. Shear wave velocity measurements using bender elements are presented in chapter four. Soil shear modulus was obtained as a function with depth. The measurement of shear wave velocity was used to predict the lateral earth pressure coefficient at rest using the results of CPT. Shear wave measurements were carried out also during pile installation in-flight.

Chapter five presents the centrifuge test results. It includes the results of pure lateral, pure tension, and inclined pullout loading cases at 70g and 50g centrifuge acceleration. The load-displacement relationships at the pile head are presented. Also the soil-pile interaction was studied using strain gages attached to pile surface. Bending moment of the pile was obtained and it was derivate twice to get the soil pressure on the pile and integrated twice to obtain pile lateral deflection profile. P-y curves were obtained and compared by other available methods in the literature.

Finite Element Model (FEM) was established and presented in chapter six. The FEM was in three dimensions. A detailed description on the development of the FEM is presented, including FEM mesh and element type, boundary conditions and soil model. The FEM was calibrated using the centrifuge tests results. The calibrated model was used to carry out a parametric study in chapter seven. Pile diameter, pile flexibility, loading angle, and padeye depth were the parameters used in the study. A design method to predict the ultimate pile capacity under inclined pullout loading was presented. Another method was given to predict the maximum bending moment of the pile under such loading conditions.

Chapter eight presents the cyclic loading analysis. The centrifuge test results for cases under cyclic loading were discussed. FEM were calibrated to predict the change of load at pile head and maximum bending moment with cycle number.

Finally, the conclusions were drawn from the present research are presented in chapter nine. Also, recommendations for the future work are given.

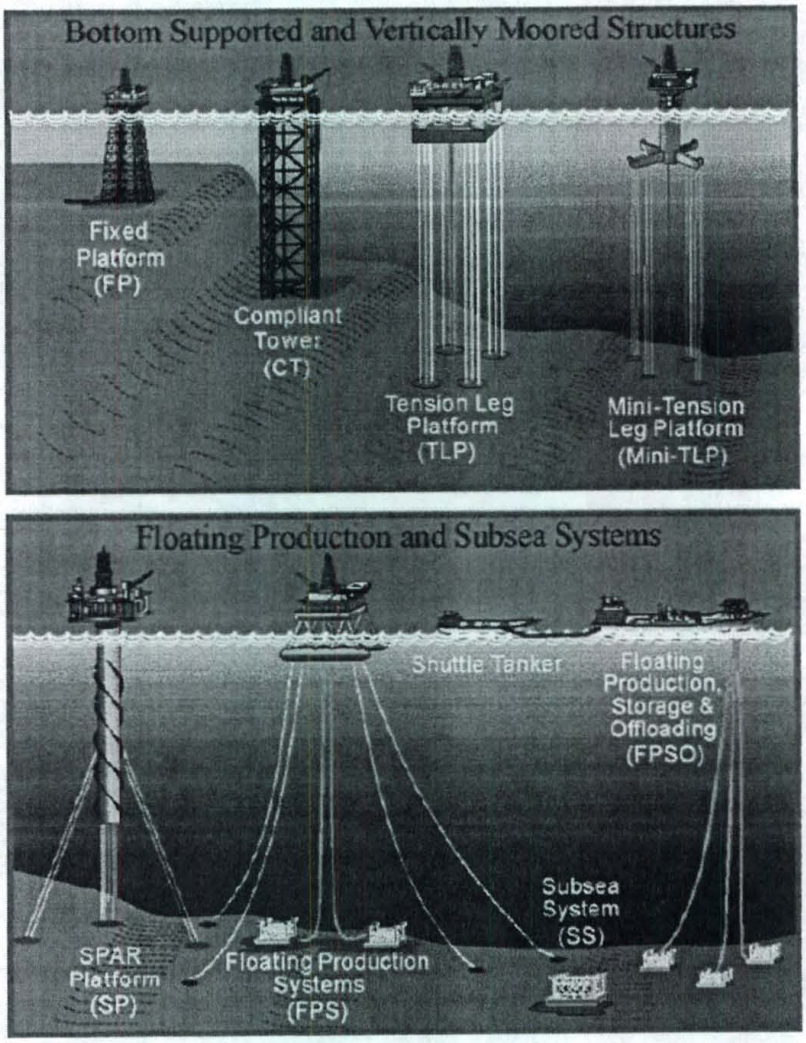

Figure (1.1) Deep-water development systems, (After El-Sherbiny, 2005)

1.5. Original Contributions:

The original contributions of the current thesis are:

1. It was found that under inclined pullout loading, offshore piles should not be analyzed using *p-y* curves alone. The shear stresses at the soil-pile interface (called t-z curves) should be considered in the analysis. Neglecting these shear stresses will overestimate the design of these anchor piles in terms of maximum bending moment and the expected total carried load at the pile head.
2. There is a significant interaction between the lateral and vertical pullout (tension) loading. The tension load component causes pile elongation. This elongation increases pile bending stiffness and decreases soil pressure around the pile except at depths close to the pile tip due to pile driving effects.
3. Design methods were proposed to predict the pile ultimate total capacity. The total capacity of the pile can be obtained by determining both the tension pile capacity and the corresponding lateral capacity of the pile at failure in tension as a function in pile flexibility (*L/T*) and the ultimate lateral capacity of rigid pile.
4. Another method is to predict the maximum positive bending moment of a pile subjected to inclined pullout loading.
5. For cyclic loading, a degradation model was suggested based on the soil stiffness degradation. The model was implemented in the FEM. The proposed model is limited to medium load and deflection levels and up to 50 cycles.

Chapter 2

Literature Review

2.1 Introduction:

In this chapter, the review of the behavior of piles in sand under oblique pull monotonic and cyclic loads is presented. Some comments on the previous research work will be discussed. Before going through this review, a brief discussion will be given for the behavior of piles in sand under lateral and tension loads which should be considered to understand the behavior of piles under the oblique pull loading case.

2.2 Behavior of Laterally Loaded Piles:

Vertical piles resist lateral loads or moments by deflecting until the necessary reaction in the surrounding soil is mobilized. The behavior of the foundation under such loading conditions depends essentially on the stiffness of the pile and the strength of the soil.

As reported by the Canadian Foundation Engineering Manual, 2007, the horizontal load capacity of vertical piles may be limited in three different ways:

- The capacity of the soil may be exceed, resulting in large horizontal movements of the piles and failure of the foundation;
- The bending moments and/ or shear may generate excessive bending or shear stresses in the pile material, resulting in structural failure of the piles; or
- The deflections of the pile heads may be too large to be compatible with the superstructure.

All the three methods of failure must be considered in design. The best design method is still the one based on well-planned and well-executed lateral test loading.

These different design methods depend on the relative stiffness of the pile and the soil. This will take us first to distinguish between "short" (rigid) and "long" (flexible) piles. The definition of pile rigidity depends on what is called subgrade reaction of the soil, as will be discussed later in this section. The relative stiffness can be assessed with parameter T in cohesionless soils, considering the horizontal subgrade modulus increasing with depth as follows:

$$T = \sqrt[5]{\frac{E_p I_p}{n_h}} \tag{2.1}$$

where;

n_h = constant of horizontal subgrade reaction (FL^{-3} dimensions), given

$k_h = n_h z$ (FL^{-2} dimensions), where z = depth.

When the relation between the installation depth of the pile; L, and parameter; T, i.e. relation of stiffness; L/T, is at most two, the pile is treated as a "short" (rigid), which rotates rigidly in the soil, and the deformations of the pile can be ignored. Soil failure occurs then before the pile fails. The location of the rotation center is calculated assuming that the bending moments are in equilibrium. In homogeneous soil it can be assumed, that the rotation center is situated at a depth approximately equal to 70% of the installation depth. If this ratio (L/T) is at least four, the pile is considered as a "long" (flexible) pile, which bends as the lateral load exceed. The pile failure may then be occurred before the soil fails. The influence of the stiffness relation on the failure mechanism of the pile is shown in Figure (2.1).

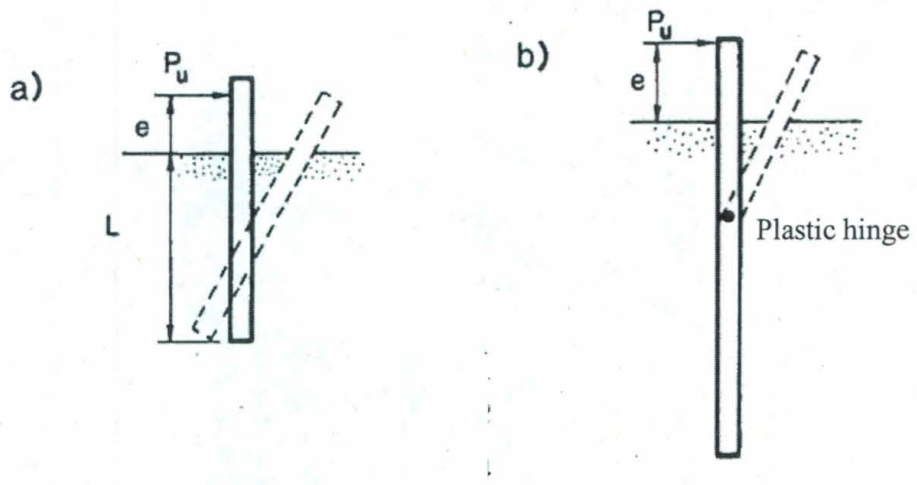

Figure (2.1) The influence of the stiffness relation on the failure mechanism of the pile

The existing methods for the analysis of laterally loaded single piles can be classified into the following categories:

2.2.1 The limit state method:

Broms (1964) presented a simple limit state method for the design of laterally loaded piles in uniform cohesionless soil profile. Failure modes involving either the pile (plastic hinge formation) or the soil (ultimate lateral resistance mobilization) were proposed for long and short piles, respectively. He considered the general behavior of the pile and the deformation in the soil at ultimate conditions to be dependent on the depth, as shown in Figure (2.2). Soil towards the surface exhibits upwards movement, while in depth only moves horizontally around the pile. He also suggested a deformed separation of the soil from the back of the deflected pile with downwards movement of soil to fill the gap created at the back of the deflected pile. He produced design charts at working loads based on the linear subgrade reaction theory for dimensionless ground line lateral deflection versus dimensionless pile length, as shown in Figure (2.3).

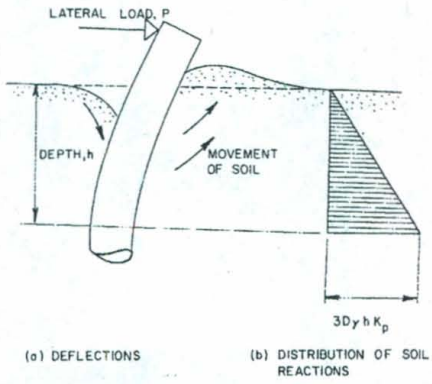

Figure (2.2) General Behavior under Ultimate Conditions (after Broms, 1964)

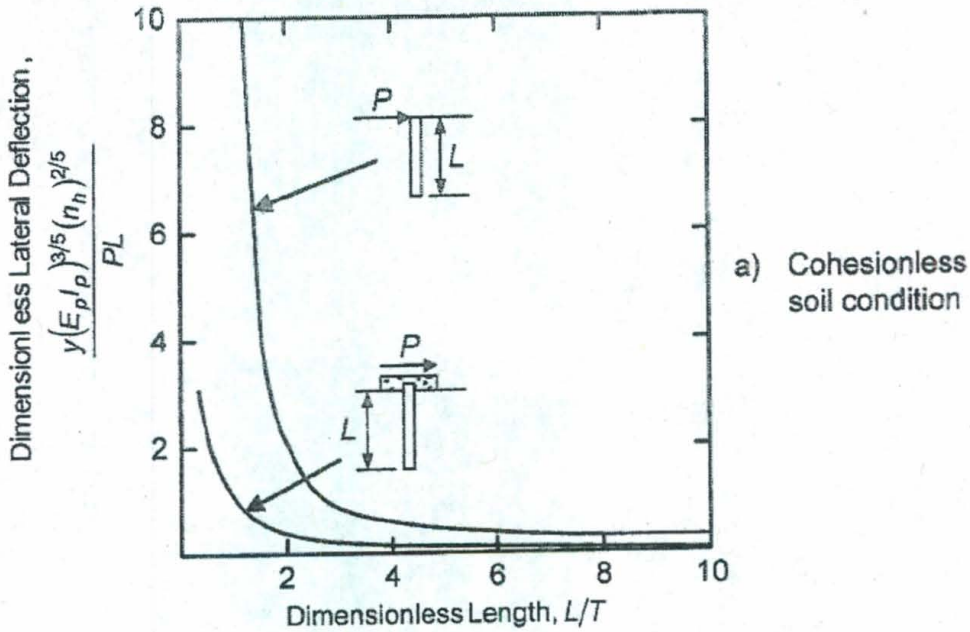

Figure (2.3) Broms Lateral Deflection Design Charts (after Broms 1964)

2.2.2 The discrete load-transfer method:

a) The subgrade reaction method:

The subgrade reaction theory is based on the classical beam-on-elastic-foundation model. In this method the soil foundation is idealized as a Winkler foundation, consisting of a series of infinity closely spaced, independent linearly-elastic springs.

The obvious disadvantage of this soil model is the lack of continuity; real soil is at least to some extent continuous, since the displacements at a point are influenced by stresses and forces at other points within the soil. A further disadvantage is that the spring modulus of the model (the modulus of subgrade reaction) is dependent on the size of the foundation. Also, pile geometry can be considered only indirectly.

As discussed by Polous and Davis (1980), in the Winkler soil model, the pressure p and deflection w at a point are assumed to be related through a modulus of subgrade reaction, which for horizontal loading, is denoted as k_h. Thus:

$$p = k_h y \tag{2.2}$$

where
p = soil reaction per unit-length of pile
k_h = subgrade.reaction modulus, in units of force/ length square
y = pile horizontal deflection

The pile is usually assumed to act as a thin strip whose behavior is governed by the beam equation:

$$E_p I_p \frac{d^4 y}{dz^4} = -p \tag{2.3}$$

where;
E_p= modulus of elasticity of the pile
I_p = moment of inertia of the pile section
z = depth in soil
d =width or diameter of the pile

From Eqs. (2.2) and (2.3), the governing equation for the deflection of a laterally loaded pile is

$$E_p I_p \frac{d^4 y}{dz^4} + k_h y d = 0 \tag{2.4}$$

By using the finite-difference method to solve the above equation, any variations of k_h with depth may be considered. Several distributions of k_h have been employed; the most widely used being that developed by Palmer and Thompson (1948), which is of the form

$$k_h = k_L\left(\frac{z}{L}\right)^n \tag{2.5}$$

where;

k_L = value of k_h at the pile tip (z = L)

n = an empirical index equal to or greater than zero

The most common assumptions are that n = 0 for clay - as the modulus is constant with depth- and that n = 1 for granular soils -as the modulus increases linearly with depth.

Cases involving a general distribution of k_h with depth, of the form:

$$k_{\mathrm{h}} = n_{\mathrm{h}} z_{\mathrm{n}} \tag{2.6}$$

For piles in sand, assuming that the modulus of elasticity depends only on the overburden pressure and the density of the sand, Terzaghi (1955) showed that

$$n_h = \frac{A\gamma}{1.35}\left(\text{tons/ft}^3\right) \tag{2.7}$$

Typical values of the factor A and n_h are given by Poulos and Davis (1980). For comparison, Rowe (1956) and Davisson and Prakash (1963) reported values of n_h of 2.5 tons/ft^3 and 1.5 tons/ft^3 (cyclic loading) for loose, dry sand, and 79 tons/ft^3 and 86 tons/ft^3 for dense, dry sand.

However, determinations of the modulus of subgrade reaction is generally carried out by using pile-loading tests and instrument the pile so that the soil pressures and pile deflections along the pile can be measured directly. A more convenient procedure is to measure the ground-line deflection and/or rotation and to backfigure the value of k_h, assuming an appropriate distribution with depth.

For cyclic loads effect, Long & Vanneste (1994) proposed a subgrade reaction method with linear increasing subgrade modulus with depth, in which the moduli decrease with the number of load cycles as follows:

$$k_{hN}(z) = N^{-t} n_{h1} z \tag{2.8}$$

where t is a factor dependent on the pile installation method, the load characteristic (one- or two-way loading) and on the relative density of the sand. For a driven pile with one-way loading in medium dense sand t = 0.17 is recommended.

b) The *p-y* method:

The relationship between soil pressure and pile deflection at any point along a pile is nonlinear. Several approaches have been developed to account for this non- linearity. Madhav et al. (1971) (Poulos and Davis, 1980) have employed an elasto-plastic Winkler model, while Kubo (1965) (Poulos and Davis, 1980) has employed the following nonlinear relationships between pressure p, deflection y, and depth z;

$$p = kz^m y^n \tag{2.9}$$

where;
k, m, n = experimentally determined coefficients.

However, the most widely-employed approach appears to be the so-called "*p-y*" approach (p = pressure, y = deflection). In this method, a finite-difference solution is obtained to the following equation:

$$\frac{d^2M}{dz^2} + (P_z)\frac{d^2y}{dz^2} - p = 0 \tag{2.10}$$

where;

M= moment at depth z in pile

P_z= axial load on pile at depth z

The solution of equation (2.10) requires input of a series of "*p-y*" curves for various points along the pile. McClelland and Focht (1958) formalized the procedure for obtaining p and y by strain-gauge measurements on a full-scale test pile. By determining moment diagrams at successive stages of their lateral load test, and obtaining corresponding p and y values at various depths, they derived p versus y relationships appropriate to their pile-soil system. In doing so, they introduced the so-called *p-y* curves as shown in Figure (2.4).

For establishing *p-y* curve, three portions of the curve should be studied. The three portions are the initial stiffness of the curve, the ultimate capacity of the soil, and the transition portion between the previous mentioned portions, as shown in Figure (2.4).

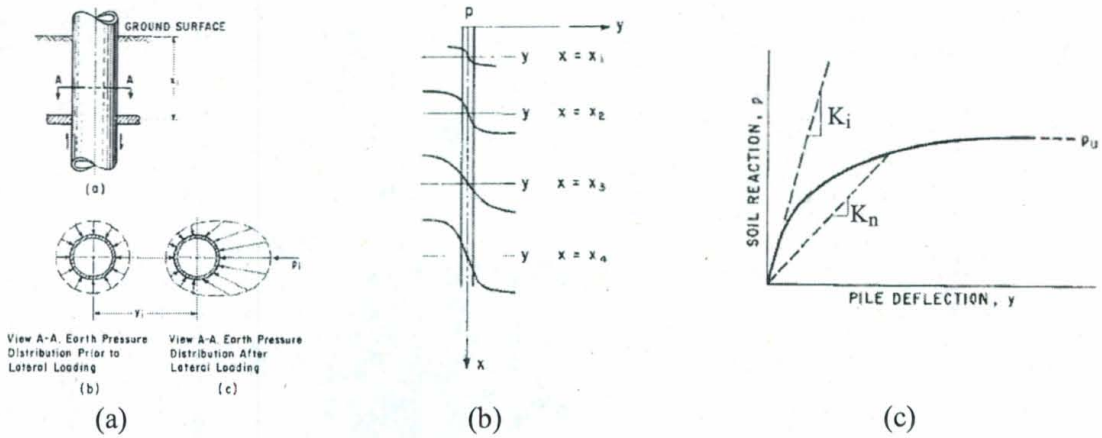

(a) (b) (c)

Figure (2.4) "*p-y*" Curve, (a) Graphical definition of p and y, (b) Set of "*p-y*" curves, (c) Typical "*p-y*" curve, (After Reese, 1974)

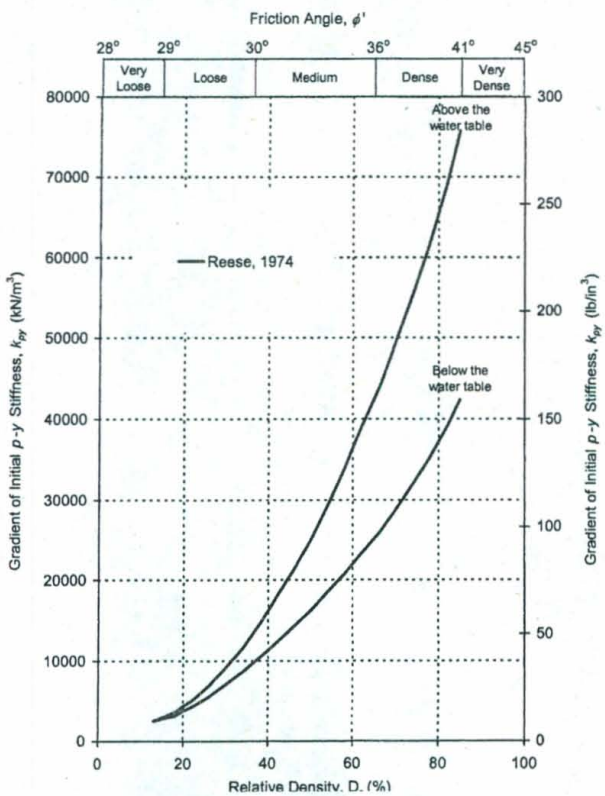

Figure (2.5) Typical k_{py} values for sand (after API, 2000)

The initial stiffness of a *p-y* curve is a matter of small strain where behavior is essentially linear. Thus $K_{p\text{-}y}$ can be considered as a horizontal subgrade modulus (k_h), as used in linear subgrade reaction theory. In terms of appointing an initial stiffness to *p-y* curves in practice, it has been common to simply adopt a $K_{p\text{-}y}$, value that increases linearly with depth and with the gradient a function of density for sands. The usual form of the equation is given by Eq. (2.11), and typical values for k_{py} are indicated in Figure (2.5) for sand.

$$K_{p-y} = k_{py} z \tag{2.11}$$

where;

k_{py} = gradient of initial *p-y* stiffness with depth (FL^{-3} dimensions).

z = depth below ground surface.

Many *p-y* curves have been established based on field or laboratory tests. One of the well known and widely used *p-y* curves that for sand, the hyperbolic tangent function has also been recommended in the form as indicated by API (2000). This formulation is non-linear and in the absence of more definitive information may be approximated at any specific depth z, by the following expression:

$$p = Ap_u \tanh\left[\frac{kz}{Ap_u} y\right] \tag{2.12}$$

where;

A= factor to account for cyclic or static loading condition. Evaluated by:

$$A = 0.9 \qquad \text{for cyclic loading.} \tag{2.13}$$

$$A = \left(3.0 - 0.8\frac{z}{d}\right) \geq 0.9 \qquad \text{for static loading,} \tag{2.14}$$

k = initial modulus of subgrade reaction (kN/m^3). Determine from Figure (2.5) as a function of angle of internal friction, ϕ',

p_u= ultimate bearing capacity at depth z, (kN/m). The ultimate lateral bearing capacity for sand has been found to vary from a value at shallow depths determined by Eq. (2.15) to a value at deep depths determined by Eq. (2.16). At a given depth the

equation giving the smallest value of p_u should be used as the ultimate bearing capacity.

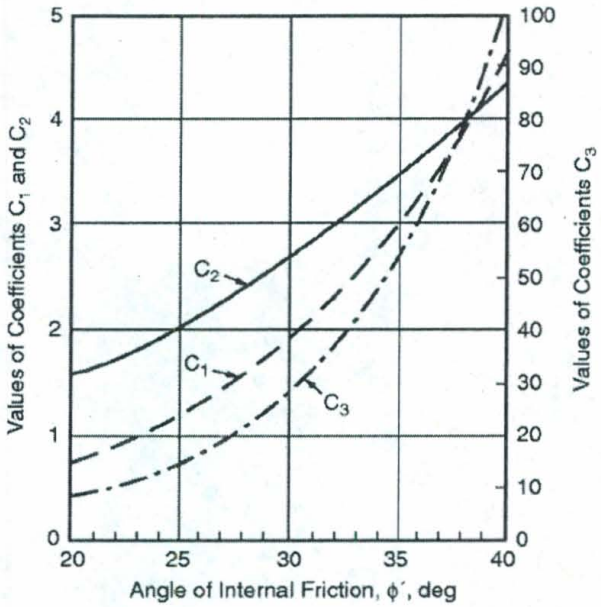

Figure (2.6) C_1, C_2, C_3 coefficients values (after API, 2000)

$$p_{us} = (C_1 z + C_2 d)\gamma z \tag{2.15}$$

$$p_{ud} = C_3 d \gamma z \tag{2.16}$$

where; C_1, C_2, C_3 = Coefficients determined from Figure (2.6) as a function of φ'.

Yan and Byrne (1992) carried out a series of model tests of vertical piles subjected to lateral monotonic pile head loading. In their model tests, they simulated field stress conditions using the hydraulic gradient similitude technique (HGS). They found that p-y curves below one pile diameter can be normalized by the maximum soil young's modulus E_{max} and the pile diameter as follows:

$$\frac{P}{E_{\max} d}\% = a\left(\frac{y}{d}\%\right)^b \tag{2.17}$$

Where a is a function of soil relative density and b has a value of about 0.5.

Dyson and Randolph (2001) conducted centrifuge tests to study the response of piles embedded in calcareous sand under monotonic lateral loading. They recommended p-y curves with a magnitude of lateral resistance linked to the soil strength through the cone resistance as follows:

$$\frac{p}{\gamma' d} = R\left(\frac{q_c}{\gamma' d}\right)^n \left(\frac{y}{d}\right)^m \tag{2.18}$$

Where the force per unit length has been replaced by the net pressure $p=P/d$ and then normalized by the effective vertical stress at a depth of 1 diameter. Linear regression was used to obtain best-fit values of the soil parameters R, n, and m. They found that the cone resistance exponent n averaged 0.72 for all the tests. The parameter R is related to the pile installation effect and a value of 2.84 was recommended. A value of 0.64 was recommended for parameter m for free head piles.

For laterally cyclic loaded piles in sand, Long & Vanneste (1994) proposed the Deterioration of Static p-y Curve method. In which, the resistance provided by a given static p-y curve is deteriorated to account for the effects of cyclic lateral load using the following equations:

$$p_N = p_1 N^{-0.4t} \tag{2.19}$$

$$y_N = y_1 N^{0.6t} \tag{2.20}$$

where t is a factor dependent on the pile installation method, the load characteristic (one- or two-way loading) and on the relative density of the sand. For a driven pile with one-way loading in medium dense sand $t = 0.17$ is recommended.

Rosquoët et al. (2007) examined the effects of lateral cyclic loading on pile head displacements, maximum bending moments M, and p-y curves using a series of centrifuge tests in dry sand. The maximum applied load was one third of the ultimate lateral capacity of the pile. They gave two equations that can predict the pile head displacement according to number of cycles, n:

$$y_n = y_1\left(1+0.08\left(\frac{DF}{F_{\max}}\right)^{0.35}\ln(n)\right) \tag{2.21}$$

where y_n is the pile head displacement measured at the peak load value of cycle n, y_1 is the initial displacement measured at the end of initial loading, and DF and $F_{\max}$ are the load amplitude and the maximum applied load, respectively. For effect of cyclic loads on the maximum bending moment, they concluded that since the change in the maximum bending moments under cyclic loads is small (less than 8%), this aspect, at least in the conditions of their tests, may be not very relevant as regards pile design in practice.

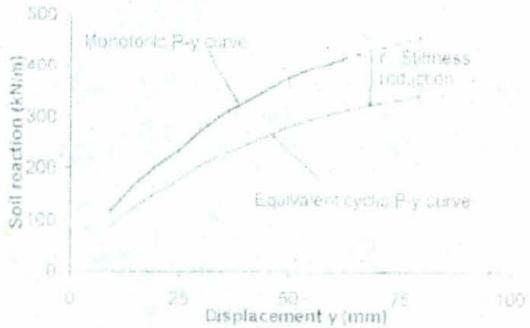

Fig. 20. Cycle effect modelling

Figure (2.7) Cyclic effect modeling (After Rosquoët et al., 2007)

For the effect of the cyclic loads on *p-y* curves, they suggested a proportional transformation applied to the initial monotonic *p-y* curve according to a coefficient, *r*, see Figure (2.7). This reduction coefficient, as for flexible piles, is concentrated in the upper layers (of depth less than 5 times pile diameter).

2.2.3 The continuum methods:

Real soil is inherently a particulate material and thus derives its resistance through innumerable load paths that can generally be considered in a continuous, interactive sense. The replacement of soil with a continuous elastic or elastic-plastic model therefore stands to reason, providing a more fundamental approach to modeling the actual interaction between the pile and soil entities. These include three-dimensional

analyses and simplifications using two-dimensional analyses (plane strain). Three-dimensional analyses offer the most realistic approach to assessing pile-soil interaction, and are divided into integral equation (or boundary element) method and differential method analysis categories.

2.2.3.1 Elasticity Method:

This method deals with the soil as an isotropic, homogeneous, and semi-infinite elastic material, having a Young's modulus E_s, Poisson's ratio v_s which are unaffected by the presence of the pile. The solution by this method is carried out by numerical integration of lateral displacement induced by a horizontal point load over a discretized pile surface, equating lateral displacements from the elastic soil (Mindlin's solution) and elastic pile (Bernoulli-Euler beam theory), and imposing equilibrium conditions, a simultaneous equation solution ensues to solve for unknown forces that then allows determination of pile actions.

Poulos (1971) proposed a solution assuming the pile as a thin rectangular strip of width equal to the pile diameter (d), possessing a length (L) and flexibility (E_pI_p) corresponding to that of the pile. A linear elastic continuum with Young's modulus (E_s) constant with depth was used to represent the surrounding soil, and no separation between the pile and the soil allowed. Any shear stresses at the pile edges were neglected, pile-soil interaction derived solely from uniform distribution of normal stress assumed across each pile-segment width.

The work of Banerjee and Davies (1978) provided a more rigorous boundary element technique whereby both normal and shear stresses around a cylindrical pile-soil interface were incorporated into the solution scheme using an a priori numerical procedure. Budhu and Davies (1987) advanced on Banerjee and Davies (1978). They assigned limited soil stresses at the front, sides and back of the pile. These were based on conventional bearing capacity values for the normal stresses acting against the front face of the pile, empirical adhesion values for shear stresses acting along the sides of the pile, and limiting the decrease in normal stresses at the back of the pile to be no greater than in situ horizontal stresses to prevent tensile stresses and thus

convey a pile-soil separation effect. While only an approximate account of soil non-linearity, this approach emphasized the significant increase in pile displacements, rotations and bending moments as a result of soil yielding. This effect was shown to increase as the level of loading increased, and was most apparent with flexible piles.

2.2.3.2 The finite element method:

The finite element method has the advantage of using non-linear soil models and allowing separation between the soil and the pile. Finite element studies on piles subjected to lateral loads have been conducted by some investigators. Desai and Appel (1976) performed a three-dimensional finite element analysis with both linear and non-linear soil behavior (hyperbolic stress-strain relationship). Pile/soil interface elements were considered in the finite element study. The results showed that the relative movement at the pile/soil interface can have significant influence on pile behavior. Brown and Shie (1990) performed a three dimensional finite element analysis on laterally loaded piles using Von Mises and extended Drucker-Prager constitutive law as soil stress-strain behavior. *P-y* curves were derived from the finite element analyses. Dodds (2005) reported that Trochanis et. al. (1988, 1991a, 1991b) examined the nonlinearity of the soil and allowing separation or slippage between the pile and the soil, investigating the case of a free-head flexible pile subject to a lateral load at the pile head. A series of three axisymmetric analyses were undertaken: The first adopted an elastic soil bonded to the pile, the second an elastic soil but allowing pile-soil separation when tensile normal stresses developed at the pile-soil interface, and the third allowing such separation as well as modeling soil nonlinearity using an elastic-plastic (i.e. Drucker Prager) soil model. Comparison of the analysis runs indicated a 60 percent increase in pile head deflection due to separation alone, and a 30 percent increase at peak load due solely to nonlinear soil behavior. Furthermore, in both the second and third analysis runs, the depth to which separation occurred was observed to be about three meters, or six pile widths. This extent of separation is noteworthy in light of the fact that the theoretical critical length for such a pile model, obtained using the constant elastic modulus.

In addition they observed a more concentrated pattern of horizontal displacements of the soil surface closer to the pile, compared with a more evenly spread distribution around the pile without separation (both assuming elastic soil behavior). Furthermore, when separation was allowed the rate of decay of the displacement with distance away from the pile was greater in the direction normal to loading compared with the direction in line with loading. Such displacement trends reflect the transferal of lateral load resistance to the soil region around the front of the pile once separation occurs. The differing rates of displacement decay also suggest that the region of soil affected by lateral loading is greater in the direction of loading.

Given the complexity of nonlinear pile-soil interaction, it would appear that modeling lateral behavior in any way other than with three-dimensional models using nonlinear soil models and contact elements must constitute a compromise. The advantages of the finite element method over other methods on the problems of laterally loaded piles can be summarized, as reported by Fan (1996), as:

1) It can take into account various boundary conditions and pile geometry.
2) Various types of material constitutive model can be included in the system.
3) The continuity of soil mass and pile/soil interface behavior can be taken into account.
4) Effects of various pile or soil properties on the pile responses can be studied systematically.

2.3. Behavior of Axially Pullout Loaded Piles:

The most important factor that controls the axial pullout behavior of driven piles is the shaft friction or the interaction of soil and pile wall in the transmission of forces from one to the other through the contact surface or interface. Many attempts had been done to predict the shaft friction along the pile experimentally and theoretically. Based on the shaft friction studies simplified theoretical models had been derived to predict the load-displacement curve as a discrete transfer method along the pile length or what is called *t-z* curve.

2.3.1 Shaft friction:

The current API and (draft) ISO (2004) design guidelines adopt a conventional design approach for shaft friction is expressed as:

$$\tau_s = K\sigma_{vo} \tan\delta \qquad \leq \tau_{s-\max} \tag{2.22}$$

with the interface friction angle, δ, and limiting values of τ_s varying with soil type and density. The lateral earth pressure coefficient, *K*, is recommended as 0.7 to 0.8 for open-ended piles loaded in compression and 0.5 to 0.7 for piles loaded in tension, with the lower end applying to loose deposits and the upper end for dense conditions (ISO, 2004), Randolph et. al. (2005).

A more fundamental issue concerns the distribution of limiting shaft friction with depth. Adoption of a constant *K* value with depth in Equation (2.22), together with a limiting value for τ_s is not consistent with data from field tests; even the original work of Vesic (1970) shows evidence of what is often referred to as friction fatigue, Randolph et. al. (2005). Lehane et al. (1993) illustrated the phenomenon of 'friction degradation' with profiles of shaft friction measured in the three instrument clusters at different distances (*h*) from the tip of a pile 6 m long and 0.1 m in diameter, as it is jacked into the ground. Comparison of the profiles from the instrument clusters at *h/d* = 4 and *h/d* = 25 shows that the friction measured at the latter position is generally

less than 50% of that measured close to the pile tip, as shown in Figure (2.8). The leading instrument cluster (4 diameters from the pile tip) shows a shaft friction profile that follows the cone profile closely. The implication is that a maximum value of K occurs close to the pile tip, where the shaft friction is 0.5 to 1 % of the cone resistance (similar to that measured on a cone friction sleeve). The value of K then reduces with distance, h, from the pile tip.

The MTD method (later called ICP' 2005), derived from the Imperial College field studies and database of high-quality pile tests, expresses the shaft friction for driven piles in sand as:

$$\tau_s = \left(\frac{q_c}{45} \left(\frac{\sigma'_{vo}}{p_a} \right)^{0.13} \left(\frac{d_{eq}}{h} \right)^{0.38} + \Delta\sigma'_{rd} \right) \tan\delta_{cv} \qquad (2.23)$$

where d_{eq} is the diameter of a solid pile of equivalent steel area to the open-ended pile (so that $d_{eq} = \rho 0.5d$), $\Delta\sigma'_{rd}$ is a stress change due to dilation effects, generally negligible for prototype pile sizes and δ_{cv} is the interface friction angle corresponding to constant volume or steady state shearing. Friction fatigue is accounted for in the above expression by the power law expression in d_{eq}/h, and the expression is to be applied only for $h \geq 4d$ (below which τ_s is taken as constant).

The physical basis for friction degradation is the gradual densification of soil adjacent to the pile shaft under the cyclic shearing action of installation, as discussed by Randolph (2003). This process is enhanced by the presence of crushed particles from the passage of the pile tip, which gradually migrate through the matrix of uncrushed material, White & Bolton (2002). The far-field soil acts as a spring, with stiffness proportional to G/d (where G is the soil shear modulus), so that any densification close to the pile results in reduced radial effective stress. The operative value of G will be high, as the soil is heavily overconsolidated having moved through the zone of high stress close to the pile tip during installation and is being unloaded.

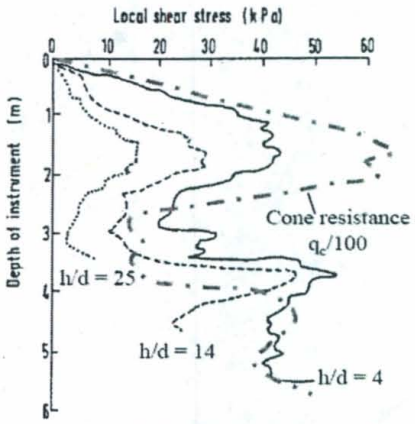

Figure (2.8) Measured profiles of shaft friction on a pile jacked into sand, (After Lehane et al., 1993)

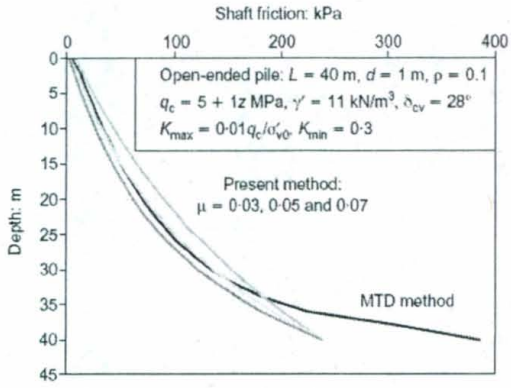

Figure (2.9) Example profiles of shaft friction for driven pile in sand, (After Randolph et. al., 2005)

The incremental volume change, and hence reduction in radial effective stress, is likely to depend on the current stress level, with greater changes at higher stress levels. This suggests an exponential variation of radial stress along the pile shaft of the form, Randolph et al. (1994):

$$K = \frac{\sigma'_r}{\sigma'_{vo}} = \frac{\tau_s}{\sigma'_{vo}\tan\delta_{cv}} = K_{\min} + (K_{\max} - K_{\min})e^{-\mu h/d} \tag{2.24}$$

where K_{max} may be taken as a proportion of the normalized cone resistance, typically 1–2% of q_c/σ_{vo}, and K_{min} lies in the range 0.2–0.4, giving a minimum friction ratio, τ_s/σ_{vo}, of 0.1–0.25, Toolan et al. (1990). The coefficient μ may be taken in the region of 0.05 for typical pile diameters, although there are some indications that the value decreases as the pile diameter increases and vice versa.

A comparison between the MTD and Randolph's method, using equation (2.24) with $K_{max} = 0.01q_c/\sigma_{vo}$, is provided in Figure (2.9), for a 1 m diameter open-ended pile driven 40 m into sand. The main difference is close to the pile tip, where the MTD method yields identical values of shaft friction for open- and closed-ended piles (for

$h/d_{eq} < 4$). The method suggested by Randolph (2003) gives different maximum values of shaft friction, dictated by K_{max}, and it is suggested that K_{max} is increased to 0.015 q_c/σ_{vo} for closed-ended piles in view of the higher normalized end-bearing resistance. The shaft friction ratio between open and closed-ended piles implied by the two methods is quite similar, with an average ratio of around 0.7. The average ratio of 0.7 may be compared with the API (2001) design recommendation of 0.8, but also with recent experimental studies that show a much lower ratio of just under 0.5, Paik et al. (2003).

However, Gavin and Lehane (2003) suggested a proposed design approach to predict the shaft resistance of open ended piles in sand. This method considered an important factor which is the mode of pile penetration during installation which is described by the incremental filling ratio (IFR). IFR is defined as the rate of change in height of the soil plug with respect to the depth advancement during installation and it is zero when no soil plug movement occurs and is unity when the pile is operating in a full coring mode.

$$q_s = f_L \sigma'_{rc} \tan\delta \tag{2.25}$$

where f_L is a reduction factor which is unity for compression and 0.8 for tension loading and;

$$\sigma'_{rc} = 0.029 q_b \left(\frac{h}{R}\right)^{-0.38} \left(\frac{\sigma'_v}{p_a}\right)^{0.12} \tag{2.26a}$$

and;

$$q_b = \frac{q_{plug} R_i^2 + q_{ann} 2Rt}{R^2} \tag{2.26b}$$

and;

$$
\begin{aligned}
q_{plug} &= q_c(1-\text{IFR}) + \text{IFR}\; q_{plugmin} && \text{IFR} \le 1 \\
q_{plug} &= q_{plugmin} && \text{IFR} \ge 1 \\
q_{ann} &= q_c \\
q_{plugmin} &= 0.1 q_c
\end{aligned}
\qquad (2.26c)
$$

Schneider and Lehane (2005) suggested a correlated formula for shaft capacity of offshore piles in sand. Some factors including the (i) level of soil displacement imposed during installation, (ii) nature and method of pile installation (jacking/driving) (iii) dilation at the sand-pile interface, (iv) interface friction angle, (v) direction of loading (compression/tension), and (vi) elapsed time between installation and load testing are examined in the light of recently published data from high quality instrumented load tests. This examination leads to the proposal of a new formulation relating shaft friction with the CPT end resistance. The following equation is proposed as a suitable formulation for evaluating the equalized radial effective stress on a displacement pile:

$$\sigma'_{rc} = q_c \left(d^*/d\right)^d \left[a_1 (h/d)^{-c1}\right] \cdot \left[a_2 (h/d)^{-c2}\right] \qquad (2.27a)$$

where;

$$d^* = d_{eq} = \sqrt{d^2 - IFR \cdot d_i^2} \qquad (2.27b)$$

where d is the pile external diameter and d_i is the pile internal diameter. Equation (2.27b) is to account for the effects of partial plugging. White et al. (2005) propose a d value of 0.7 ± 0.1 based on considerations of cylindrical expansion. The value of $[(d^*/d)^d\, q_c\, a_1\, (h/d)^{-c1}]$ should be limited to a minimum value of $K_o\sigma'_v$ with $[a_1 \cdot (h/d^*)^{-c1}]$ being related to length of the equalization period and the CPT friction ratio (F_r). d^* is used in the $(h/d^*)^{-c1}$ term to account for the possibility of a more rapid decrease in radial stress behind the tip of a coring or partially plugging pile as compared to a closed ended pile. Evidence from multi friction sleeve cones (De-Jong, 2001, as reported by Schneider and Lehane, 2005) suggests that the value of c1 is likely

insignificant and between about 0.05 and 0.15. In general, the value of c2 should increase with the number of hammer blows, although c2 will also be influenced by characteristics of installation cycles and normal stiffness conditions, among other factors. Although a minimum value of σ'_{rc} exists (which will be related primarily to the sand's friction angle), imposition of this limit would have virtually no effect on the shaft capacity evaluated using equation (2.27) for typical offshore pile sizes. Taking the above considerations into account and the need to reduce the number of empirical parameters because of the shortage of experimental data, the following simplified form of equation (2.27) was suggested for open and closed ended piles:

$$\sigma'_{rc} = 0.03 q_c \left(f/f_c\right)\left(d^*/d\right)^{0.6} \cdot \max\left[\left(h/d\right),2\right]^{-0.5} \qquad (2.28)$$

A (f/f_c) ratio of 1.0 and 0.75 was assumed for compression and tension loading respectively, and $\Delta\sigma'_{rd}$ was evaluated using the recommendations of the Imperial College Proposed method (ICP'05). Comparison to a database of pile load tests showed that Equation (2.28) led to mean ratios of calculated to measured capacities (Q_c/Q_m) of 0.91 and 1.02 for open and closed ended piles, respectively. It is noteworthy that Equation (2.28) predicts significantly lower friction capacities when extrapolating to larger diameter piles (which typically install in a coring manner).

2.3.2 Shaft friction in tension and compression

The tensile capacity of piles in sand has been found to be less than the shaft capacity measured in compression, and most design guidelines include a reduction of 10–30% to allow for this (API, 2001). Two factors were identified by De Nicola & Randolph (1993) that contributed to lower tensile shaft friction: the first was a reduction in effective stress levels adjacent to the pile compared with loading in compression (even for a rigid pile), and the second was the Poisson's ratio reduction in diameter (and consequential reduction in radial effective stress). These two effects were quantified for piles fully embedded in sand, by the expression

$$\frac{(Q_s)_{tens}}{(Q_s)_{comp}} \approx \left[1 - 0.2\log_{10}\left(\tfrac{100}{L/d}\right)\right] \cdot \left(1 - 8\eta + 25\eta^2\right) \qquad (2.29)$$

where Q_s is the shaft capacity and $\eta = \nu_p(L/d)(G_{ave}/E_p)\tan\delta$, with G_{ave}, E_p and ν_p being respectively the average soil shear modulus, Young's modulus of an equivalent solid pile and Poisson's ratio for the pile.

The two factors that contribute to reduced tensile capacity tend to compensate as the pile aspect ratio increases, with the average change in effective stress level decreasing and the effect of Poisson's ratio contraction increasing. This is shown in Figure (2.10) where, for a typical modulus ratio of $E_p/G_{ave} = 400$, the shaft capacity ratio is ~0.8 for a range of L/d. Even for quite wide extremes of E_p/G_{ave}, the shaft capacity ratio remains within 0.7–0.85.

Although other effects, such as local stress changes due to dilation as reported from the centrifuge tests by De Nicola & Randolph (1999), will influence the shaft capacity ratio, the expression in equation (2.29) provides a reasonable design basis for assessing the reduced shaft capacity for loading in tension, compared with that for loading in compression.

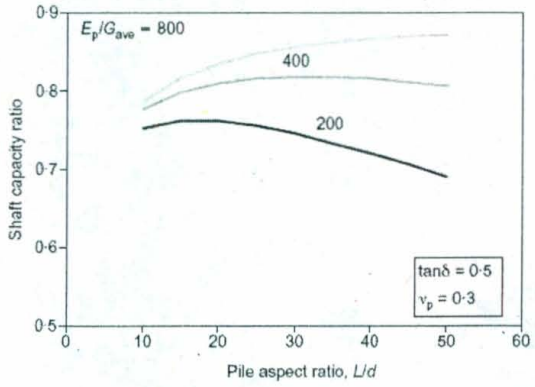

Figure (2.10) Ratio of shaft capacity in tension and compression (De Nicola & Randolph, 1993), (After Randolph, 2003)

2.4. Oblique Pull-out Loading:

2.4.1 Monotonic loading:

Yoshiaki Yoshimi (1964) presented a study of the behavior of a rigid pile (vertical or batter) in a cohesionless soil subjected to oblique pull.

Laboratory tests on three different model piles of steel pipes with closed ends had been carried out in a rectangular steel box 23-in wide and 39.5-in long. Two (rough and smooth) model piles of 1.05-in outside diameter and 10.0-in embedded length were fully driven in Ottawa sand, which had been compacted to a density with angle of internal friction 35.6°. The third model pile was 1.89-in outside diameter and 18.0-in embedded length with smooth surface and fully embedded in fine gravel, compacted to a relative density of 54% with angle of internal friction 42°. All tests were carried out with two major variables, α and β. The angle of pull, α, is 60° for oblique pull tests and 0° for horizontal pull tests The initial pile inclination, β, varies from + 30° to - 30° in increments of 15°. Based on his analysis for the non-linear load displacement curves of a rigid pile (for nonnegative β), he derived formulas for the lateral and pullout resistances.

In reference to Figure (2.11), consider a rigid pile, OB, subjected to oblique pull, P. Let y denote the normal component of the pile displacement and q denote the net transverse soil reaction per unit length of pile. Point A, at x = a, locates the point at which y = 0. Because the pile is assumed rigid, the displacement, y, is a linear function of x. From the analysis of the lateral resistance (perpendicular to the pile), he derived the following equation:

$$P = \left[C_n K_s \gamma d L^2 \frac{\cos\beta}{\cos(\alpha-\beta)} \right] \left(\frac{y_o}{d} \right)^n \quad \text{, but } P \le P_u \tag{2.30}$$

where, C_n is a parameter given in a relation with a, b (see Figure 2.11), and n, K_s is a dimensionless parameter, called the soil reaction coefficient, γ is the initial unit

weight of the soil, d is the pile diameter, L is the pile embedded length, and y_o is the pile head displacement in Y-direction (see Figure 2.11). If C_n and K_s are independent of P and y_o, Eq. (2.30) implies that a logarithmic plot of P versus y_o is a straight line having a slope, n. The values of K_s are computed from the data by using Eq.(2.31) as follows:

$$K_s = \frac{P_1 \cos(\alpha - \beta)}{C_n \gamma d L^2 \cos\beta} \tag{2.31}$$

in which P_1 is the load at $y_o/d = 1$ (extrapolated if less than 1).

In the preceding analysis, a power function is used to approximate the non-linear relationship between the applied load and the normal displacement of a rigid pile. He suggested that the method may be used to analyze laboratory and field test data, and may be helpful in setting a limiting load on the basis of the pile displacement. The power function cannot, however, give a finite ultimate load unless the exponent n equals zero.

The ultimate or pull-out resistance had been studied on the basis of the frictional resistance against the axial load component. Assuming that the normal soil pressure on the pile is proportional to γz and that the friction angle between the pile and soil is constant along the pile length, the following expression is obtained:

$$P_u \sin(\alpha - \beta) = \frac{1}{2} K_n \tan\varphi_w \cos\beta \gamma C L^2 \tag{2.32}$$

in which K_n is a constant of proportionality defined as the ratio of the normal soil pressure on the pile to γz. The obliquity of the pile and the presence of normal load preclude a clear-cut physical significance of K_n.

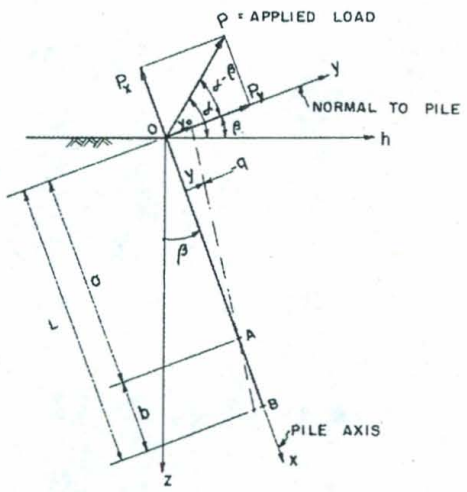

Figure (2.11) Coordinate Axes and Pile Displacement, (After Yoshimi, 1964)

It should be noted that some factors affected his experiments and consequently his analysis for the results should be considered. Using cohesionless soil of medium and coarse grain size with small size model pile (1.05-in and 1.89-in) will give a very small ratio of the pile diameter to the grain size than which in field. Of course this will affect the soil pile interaction behavior. The other factor is using soil with different grain size with the two model piles and different method of pile placement which will not allow studying the effect of the pile diameter. Also, different load inclination angles should be tested before giving lateral and pull out resistance formulas based on a 60° load inclination angle.

Broms (1965), in a discussion for Yoshimi (1964) experiments, attempted to analyze Yoshimi's test data. Based on previous experiments for piles in cohesionless soil subjected to pull out and lateral loads, done by Broms and others, he suggested the following equation for the pull out resistance:

$$Q_v = \frac{1}{2}\pi K_o L^2 d \tan\delta \qquad (2.33)$$

where δ is the interface friction angle of the pile material with respect to the surrounding soil. The coefficient of lateral pressure, K_o, (equal to 3.0) is a function of the roughness of the pile surface, the relative density of the surrounding soil, and the method of loading. He used the angle δ equal to approximately 23.5° (2/3 of the internal friction angle measured from drained triaxial compression tests) for a smooth steel surface and a medium to fine sand. Conversely, for a rough steel surface the friction angle δ is approximately equal to the angle of internal friction of the surrounding soil depending on the relative density of the surrounding soil. The computed pull out resistance compares well with the measured value by Yoshimi (1964) for the pile with inclination angle (β = -30°).

For the laterally loaded pile shown in Figure (2.12), He computed its ultimate capacity as suggested by Broms (1964):

$$Q_h = \frac{5}{6} K_p \gamma L^2 d \qquad (2.34)$$

in which $K_p = (1 + \sin\varphi)/(1 - \sin\varphi)$, is the coefficient of passive earth pressure. In the derivation of Eq. (2.34), it has been assumed that the lateral force is applied at the ground surface. A good agreement was found in the comparison with the computed resistance from Eq. (2.34) with the measured one by Yoshimi (1964) in the case where $\beta = +30°$.

In his derivation for the oblique pull resistance of the pile, he suggested that the change in pressure distribution will be as illustrated in Figure (2.13). When the inclination is small (when the applied load only deviates slightly from the pile axis) the increase in lateral pressure will be small. The largest increase will occur near the top and bottom of the pile. The ultimate capacity of a pile subjected to an oblique load can be calculated from the earth pressure distribution shown in Figure (2.14). It has been assumed that the lateral earth pressure is equal to five times the Rankine passive earth pressure to the depth g below the ground surface and that the high

lateral earth pressure at pile tip can be replaced by a concentrated load. The total pull-out resistance V can be calculated from the relationship:

$$V = Q_v + \Delta Q_v \tag{2.35}$$

in which Q_v is the pull-out resistance when the applied load acts along the pile axis and ΔQ_v is the increase in pull-out resistance caused by the two lateral forces T and R (Figure 2.14). The increase in pull-out resistance ΔQ_v depends on T and R and on the friction angle φ_a expressed by:

$$\Delta Q_v = (T + R)\tan\varphi_a \tag{2.35.a}$$

The lateral force T (see Figure 2.14) can be calculated from equilibrium requirements as:

$$T = \frac{5}{2} K_p \gamma g^2 d \tag{2.35.b}$$

and the force R (see Figure 2.14) from:

$$R = \frac{T\left(\frac{2}{3}g + e\right)}{L + e} \tag{2.35.c}$$

The resulting horizontal component H of the applied load can then be calculated as:

$$H = \frac{T\left(L - \frac{2}{3}g\right)}{L + e} \tag{2.36}$$

The failure load Q can finally be calculated (Figure 2.14) as:

$$Q = \sqrt{V^2 + H^2} \tag{2.37}$$

This analytical solution was the first one for the piles subjected to oblique pull in cohesionless soil and supported by experimental results. Some considerations should be taken in Broms analysis. The lateral pressure distribution suggested by Broms is passive along the pile length and replaced the active pressure with a concentrated force at the pile tip. Also, he considered a constant pressure distribution along the pile width. Both of these assumptions will over estimate the expected lateral resistance and consequently the oblique pull resistance.

Meyerhof (1973) gave a general solution of a rough rigid vertical anchor wall under oblique pull. At the ultimate load Q_u applied to the wall at ground level and inclined at an angle α from the vertical, the net lateral passive earth pressures P_1 and P_2 are inclined at angles δ_1 and δ_2, to the horizontal, respectively (Figure 2.15). The pressures P_1 and P_2 which represent the difference between the corresponding passive and active earth pressures, act together with the adhesion forces C_1 and C_2 on the upper and lower part of the wall, respectively. For a small load inclination, α, both P_1 and P_2 act downwards; as α increases, the point of application of P_1 rises and the angle decreases so that P_1 acts upwards as a approaches 90°, while the point of application of P_2 approaches the base level at roughly unchanged δ_2.

The ultimate load per unit length of the anchor wall can be estimated from the force polygon shown in (Figure 2.19) and may be expressed by the semi-empirical equation:

$$Q_u = cK_cL + \gamma L^2 K_b/2 + W\cos\alpha \qquad (2.38)$$

where L is the depth of the wall base, K_b and K_c are uplift coefficients, W is the weight of the wall, c is the soil cohesion and γ is the unit weight of the soil. For vertical uplift $K_b = 2K_u \tan\varphi$, where K_u = the earth pressure coefficient on the wall, δ_1 and $\delta_2 = 2\varphi/3$, approximately, while for horizontal pull $\delta_1 = -\varphi/2$ and $\delta_2 = \varphi$, approximately, to satisfy vertical equilibrium. For intermediate values of α, the uplift coefficients, K_b, for a rigid vertical rough wall can be determined using a linear variation of δ_1 and δ_2 between these limits.

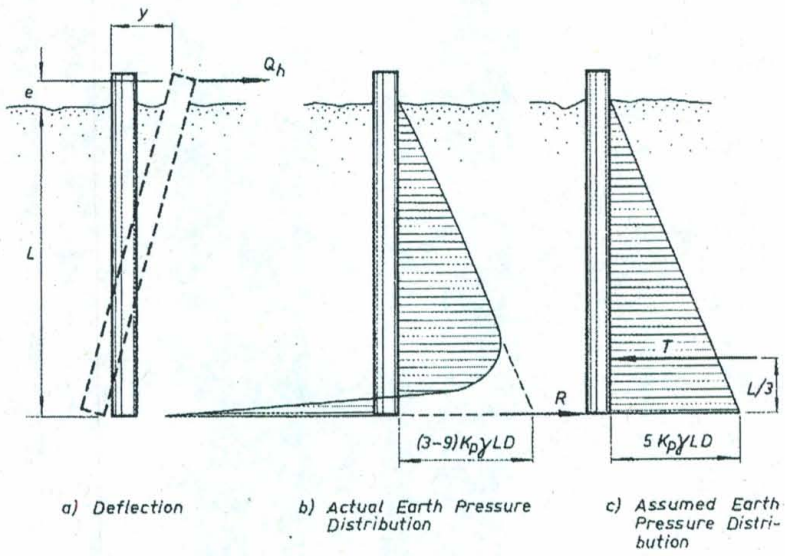

Figure (2.12) Lateral Resistance, (After Broms, 1965)

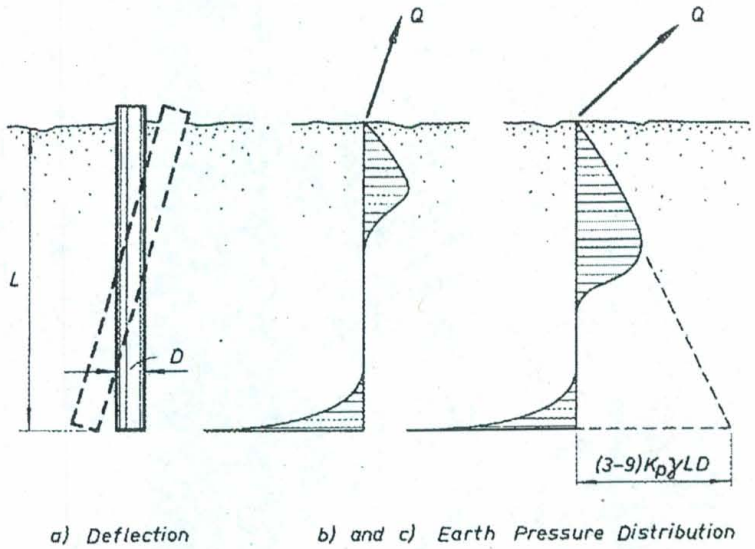

Figure (2.13) Earth Pressure Distribution at Oblique Pull, (After Broms, 1965)

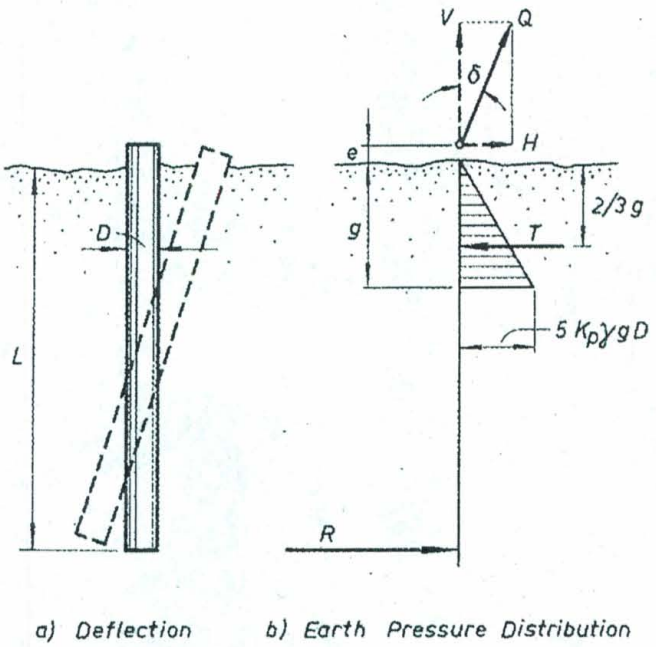

Figure (2.14) Assumed Earth Pressure Distribution, (After Broms, 1965)

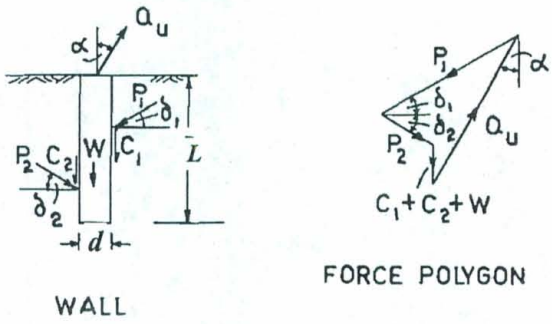

Figure (2.15) Forces at failure of anchor wall under oblique pull, (After Meyerhof, 1973)

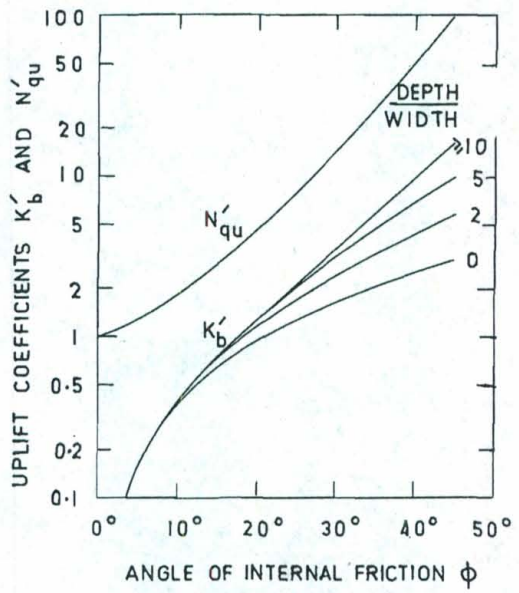

Figure (2.16.a) Vertical Uplift coefficients for rough piles, (After Meyerhof, 1973)

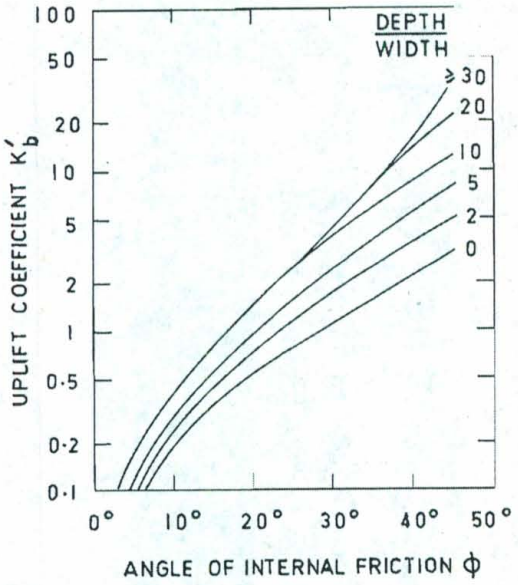

Figure (2.16.b) Horizontal uplift coefficients for rigid rough piles, (After Meyerhof, 1973)

Meyerhof modified the analysis of anchor walls under oblique pull to be adapted for rigid piles of width d by multiplying the above uplift coefficients by shape factors to obtain the corresponding coefficients for piles. The shape factors for vertical uplift and for horizontally loaded rigid piles increase roughly linearly with the ratio of L/d up to a critical depth beyond which the shape factors remain constant. The ultimate load on rigid piles may then be expressed by

$$Q_u = \left(cK_c L + \gamma L^2 K_b / 2\right)d + W\cos\alpha \qquad (2.39)$$

with symbols as before. The resulting uplift coefficients, K'_b, for vertical rough circular piles are shown in Figs. (2.16.a & b) for vertical uplift and horizontal pull, respectively, and values of K'_b for intermediate load inclinations can readily be interpolated, as for vertical walls.

To determine the relation between the angle of application of the load and bearing capacity of a pile, Leshukov (1975) carried out experimental field investigations on large-scale instrumented models of two types: rigid and flexible. The length of the rigid models was 800 mm, section 80 x 80 mm, and the length of the flexible model was 1200 mm, section 50 x 50 mm. The soil of the plot from the surface to a depth of 4 m was fine-grained silty sand with angle of friction 34°, cohesion 35 kPa, degree of saturation 0.53.

From his results, he found that the ultimate capacity of the model depends on the angle of load inclination (see Figure 2.17), increasing within 15-45° and then gradually decreasing. The maximum increase of the bearing capacity is observed at load application angles of 23-25° and in comparison with the model under a vertical load (taken as 100%) amounts to about 45% in the given case.

Although he did not define how he selected the ultimate capacity from the load displacement curves, his results agree with the results from tests on batter piles presented by Awad et. al. (1968). In their tests, the maximum ultimate capacity of the

model was determined at a load inclination angle of 22.5°. In this case the ultimate capacity is about 35% greater than in the case of a vertical load.

He concluded that when calculating the effect of oblique extracting forces on a pile the ultimate capacity of a single pile can be determined at load inclination angles from 0 to 10° (from the vertical) for pure extraction without consideration of horizontal forces and from 10 to 40° with consideration of the simultaneous effect of vertical and horizontal forces.

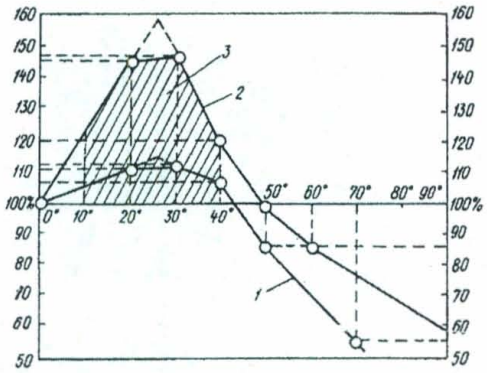

Figure (2.17) Graph of the bearing capacity of the pile models vs. angle of application of the load, (After Leshukov, 1975)

1- For a rigid model; 2- For flexible model; 3- Zone for which the joint action of vertical and horizontal forces should be taken into account.

Das, et. al. (1976) conducted model tests for 305-mm and 200-mm long, L and with diameter, *d*, of 25-mm of wooden rough piles embedded in sand with angle of friction 31°. Thus, the length-to-diameter ratios were 12 and 8, respectively. Pullout tests were conducted in a sand box measuring 0.61 m x 0.45 m x 0.61 m for load inclinations varying from 0° to 90° with the vertical. The gross ultimate loads were determined from the load displacement diagrams by investigating the region where sudden failure occurred or a large displacement was derived for a small increment of applied load. They pointed out that the former type (sudden failure) occurred in the case where the inclination of the applied load with respect to the vertical was less than about 30° and the latter type failure occurred for 0° greater than 30°.

To predict the oblique uplift capacity of rigid piles, they used the analysis suggested by Meyerhof (1973) for rigid vertical anchors with enlarged base:

$$\frac{Q_{u\theta}\cos\theta}{Q_{uv}}+\left(\frac{Q_{u\theta}\sin\theta}{Q_{uH}}\right)^2=1 \qquad (2.40)$$

in which Q_{uv} = gross ultimate resistance for $\theta = 0^\circ$ which can be given from:

$$Q_{uv}=Q_{ov}+W \qquad (2.40.a)$$

in which Q_{ov} = net vertical ultimate uplift capacity and can be calculated as follow:

$$Q_{ov}=f\,A_s=\left(\frac{1}{2}K_u\,\gamma\,L\tan\delta\right)A_s \qquad (2.40.b)$$

in which f = average unit skin friction; K_u = uplift coefficient (K_b in Figure 2.16.a); A_s = embedded pile surface area; and δ = skin friction parameter of the soil to the pile.

; and Q_{uH} = gross ultimate load for $\theta = 90^\circ$ and it can be calculated as suggested by Broms (1964) in Eq. (2.34).
By comparing the measured resistances from the experiments with the computed resistances from Eq. (2.40), he found a good agreement.

Poulos and Davis (1980), based on the experiments of Yoshimi (1964) and the analysis of Broms (1965), proposed a theoretical method to predict the ultimate resistance of vertical pile to oblique pull, in a simplified manner. Depending on the value of ultimate uplift capacity P_u and ultimate lateral resistance P_L of the vertical pile, the ultimate resistance P_θ is assumed to be the minimum of the two values:

$$P_u\sec\theta \quad \text{or} \quad P_L\operatorname{cosec}\theta \qquad (2.41)$$

It is assumed to be unaffected by the presence of the lateral component of the inclined pull. To remove tie shortcomings in the Poulos and Davis (1980), Chattopadhyay and Pise (1986) found that it is necessary to propose an analysis which will reasonably estimate the ultimate resistance of piles under oblique pull. They proposed a semi-empirical theoretical expression to evaluate the ultimate resistance of a pile embedded in sand, under oblique pull based on the experimental results. It takes into account the effects of the angle of inclination of the pull, the ultimate vertical uplift capacity and ultimate lateral resistance of the pile.

Results on 19 mm diameter model piles embedded in dense dry sand of three pile surface characteristics and length to diameter ratios varying from 11.44 to 39.10 are reported. The piles were tested under oblique pull with inclination $\theta = 0°$, 30°, 60°, and 90° with the vertical axis of the pile. The ultimate resistance P_θ of the pile has been related to the ultimate vertical net uplift capacity P_u of the pile, and presented through polar diagrams for different values of $\alpha = P_u/P_L$ ratio. P_L is the ultimate lateral resistance of the pile corresponding to $\theta = 90°$.

Under increasing oblique load, failure occurred either by excessive axial movement when piles were pulled out or by excessive normal deflection of the pile top. When axial failure occurred, ultimate resistance of the pile was taken as the load when the pile was pulled out. In case of failure due to excessive normal deflections, it was taken from the log load versus log normal deflection diagrams as the load corresponding to normal deflection equal to the diameter of the pile.

A semi-empirical method has been proposed to predict the net ultimate resistance P_θ in terms of $\alpha = P_u/P_L$ and θ as follows:

$$\frac{P_\theta}{P_u} = \cos^2\theta \exp\left[-\left(\frac{1-\theta/90}{1+\theta/90}\right)\right] + \frac{\sin\theta}{\alpha}\exp\left[-\left(\frac{1-((90-\theta)/45)}{1+((90-\theta)/45)}\right)\right] \qquad (2.42)$$

The experimental results of the authors as well as those of Das et al (1976) have been analyzed using the proposed theory. Values of net ultimate resistance to oblique pull under different conditions as obtained from the experimental results have been compared with the theoretical estimations made by using Eq. (2.42). For $\alpha < 1$ and $\alpha > 1$, the comparison is shown in polar diagram in Figs (2.18.a & 2.18.b), respectively. Reasonably close agreement is observed between the estimated and observed values for all cases. For a pile having $\alpha > 1$, it is observed that the maximum resistance to oblique pull is attained when the inclination of the pull is 30°. For α lying between 0.18 - 0.72, it is attained when the inclination is 60°. For α less than 0.18, it is mobilized when the inclination is 90°.

Ismael (1989) examined the ultimate oblique pull of vertical bored piles in sand by a field testing program. The Piles used were 101 mm in diameter by 1.5 m long and were installed in fine, medium-dense sand with angle of internal friction 35°. The piles had been subjected to lateral loads, axial uplift loads and oblique pull loads at an angle of 30° with the vertical. All tests were continued until failure had occurred and a displacement of 25 mm was recorded. The failure loads were determined by the slope-tangent method. Examination of the test results indicates that the failure under oblique loading caused by lateral failure since at this load the horizontal component was 8.3 kN, which is close to the 8.8 kN designated as the failure load from the lateral load tests. He concluded that the lateral capacity was little affected by the axial component of the load during the oblique test, while the lateral component of the load appears to have some influence on the axial capacity in cohesionless soils.

Based on the analysis of Broms (1965), he tried to determine the critical inclination load angle at which failure changes from axial to lateral. He found that axial failure will occur if $Q_L > Q_u \tan \delta$ and lateral failure will occur if $Q_L < Q_u \tan \delta$, where Q_L is the ultimate lateral resistance, Q_u is the ultimate uplift resistance, and δ is the load inclination angle with the vertical. So, the occurrence of axial or lateral failure will depend on whether the ratio Q_L / Q_u is larger than or less than $\tan \delta$. From his test results, he found that:

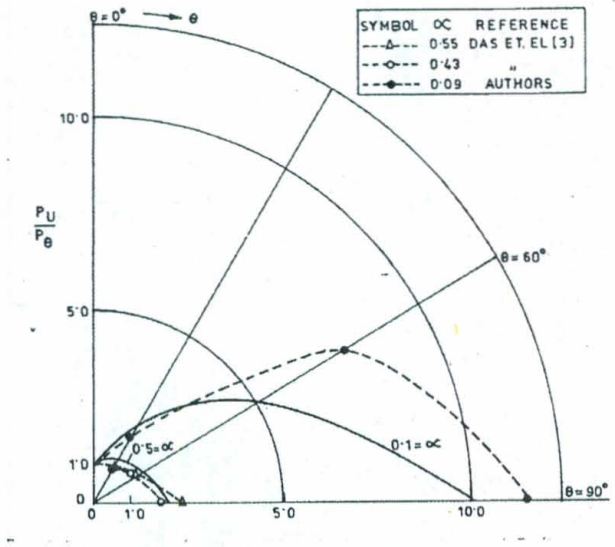

Figure (2.18.a) Comparison of estimated and observed values of P_θ/P_u ($\alpha < 1$), (After Chattopadhyay and Pise, 1986)

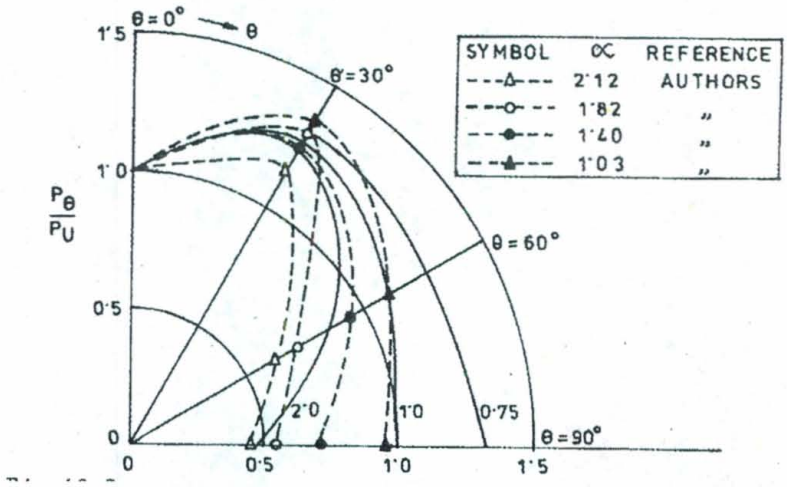

Figure (2.18.b) Comparison of estimated and observed values of P_θ/P_u ($\alpha > 1$), (After Chattopadhyay and Pise, 1986)

$$\frac{Q_L}{Q_u} = \frac{K_p}{\pi K_u \tan\varphi'} \qquad (2.43)$$

From the test conditions, he found that axial failure will occur if the load inclination is less than 18.75°. However he found that more tests should be carried out at a small inclination from vertical to induce axial failure and check the calculated critical inclination load angle.

It should be noted that the test had been carried out at shallow depth in field. As indicated by Altaee and Fellenius (1994), the dilation of the sand occurring at low confining stress –shallow depth- increases the lateral soil stress against the pile. So, doing a test in field using a small scale pile will only eliminate the boundary conditions problem in the laboratory test, but the physical modeling issue will not be controlled.

Jamnejad and Hesar (1995) did experimental and theoretical studies of the response of single pile anchors vertically installed in saturated cohesionless soil and subjected to either monotonic or cyclic loading applied at different angles of inclination. The experiments were conducted in a cylindrical steel tank of 2.4m diameter and 1.3m depth containing saturated uniform medium sand. The tank was welded onto a steel vibratory table in order to achieve different densities of sand by fluidizing, and by vibratory compaction.

The model pile anchors were fabricated from seamless steel pipe sections. The diameters of the tested model pile anchors were between 50 mm and 100 mm and the embedded length ranged from 700 mm to 1150 mm. Pile anchors with 100 mm diameter, when installed to the full effective depth available, would have *L/d* ratio of approximately 11. This value corresponds to the transition stage from a short to a long pile anchor. Larger diameters would, therefore, have little potential for experimental investigation other than for a short pile anchor response. The pile anchors were instrumented with strain gauges to measure bending and shear forces.

Both the monotonic lateral and axial loading have been carried out first. In the lateral loading *p-y* curves have been obtained from the experiments and gave a good agreement with the API (1980) design code. The radial soil stress distribution in front of the pile anchor is concentrated towards the plane of loading, even at a distance of more than three diameters.

In the axial loading tests, the radial stresses had been observed and showed how rapidly these stresses decay away from the shaft. Stresses approach a constant value at a distance of approximately 1.4 of the diameter from the shaft. The pore pressures adjacent to the pile anchor shaft reduce due to the suction resulting from dilation of the dense sand.

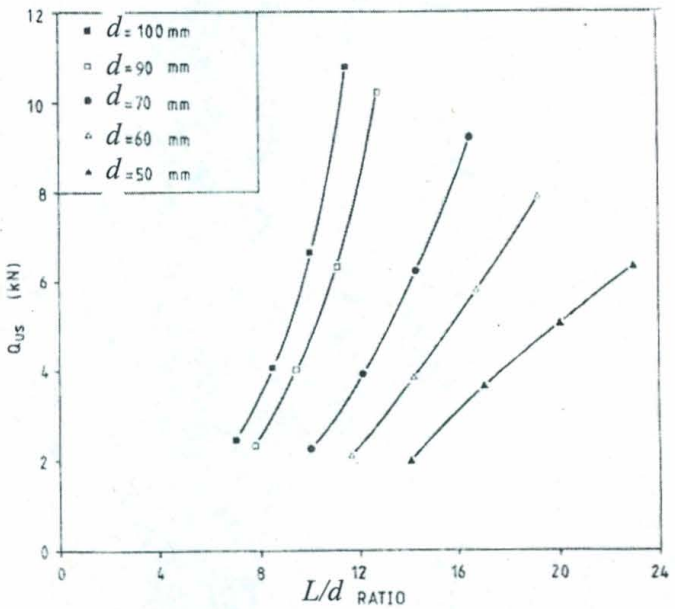

Figure (2.19) Influence of *L/d* ratio on the ultimate static capacity of pile anchors (constant *d*, variable *L*, θ= 30°), (After Jamnejad and Hesar, 1995)

The ultimate static capacity of obliquely loaded pile anchors increases in a parabolic manner with *L/d* ratio, up to a limit beyond which the relative benefit of increasing embedment depth diminishes and further increases in embedded length only

contribute to an increase in the vertical component of resistance and have little influence on the horizontal component of resistance, which is the dominant component in the case of $\theta = 30^{\circ}$, as shown in Figure (2.19). The flexural rigidity of cross section and, therefore, the relative stiffness factor have an important role to play, particularly when the load inclination is closer to the horizontal than to the vertical.

Achmus et al (2007) investigated and quantified, by means of numerical modeling, the effect of interaction of axial and lateral forces for driven steel pipe piles. They presented the behavior of these piles under loading conditions for offshore wind energy foundation structures in the German offshore regions. Figure (2.20.a) shows the horizontal load-displacement behavior with variable axial tensile loads for the pile with a diameter of 3 m and 20 m long. At first there is no significant influence of the vertical load on the H-w-curve, where H is the horizontal load at the pile head and w is the corresponding horizontal displacement at the pile head. But, from a certain load level which is dependent on the load inclination, the curves for inclined loads deviate from the curve for pure horizontal loading. Larger horizontal displacements then apply, i.e. the horizontal pile stiffness is decreased. The respective vertical load-displacement curves for the case with $d = 3$ m are shown in Figure (2.20.b). A significant influence of the horizontal load is found. The vertical pile stiffness is distinctly reduced when compared to the case with pure axial tension. But, on the other hand, a horizontal load increases the ultimate vertical pile capacity. Thus, the unfavorable effect of decreased stiffness is joined by the favorable effect of increased capacity. They concluded that the reason for the deviation in the H-w-curves is obviously that the pile capacity for tension load is smaller than the horizontal pile capacity in the cases considered. If the vertical load approaches the ultimate load, this ultimate load becomes decisive for the combined ultimate load. Their results show that in sand soil the interaction between horizontal and vertical load must only be considered in the determination of axial displacements due to tension loads. However, they reported that cyclic loads will affect the interaction behavior and it should be studied.

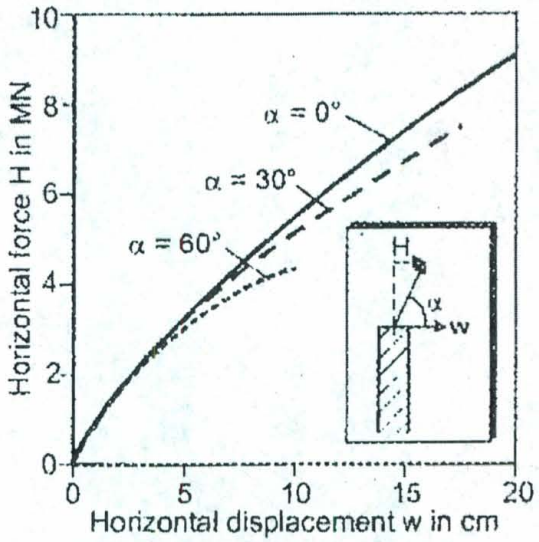

Figure (2.20.a) Horizontal displacement at the pile head dependent on horizontal load (inclined tension, $d = 3.0$ m, $L = 20.0$ m), (After Achmus et. al., 2007)

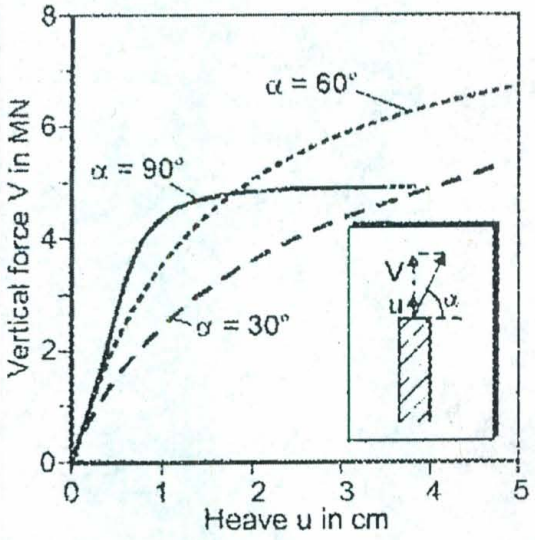

Figure (2.20.b) Pile heave dependent on vertical load (inclined tension, $d = 3.0$ m, $L = 20.0$ m), (After Achmus et. al., 2007)

Ramadan et al. (2009a) carried out a numerical study using 3D FEM to study the behavior of offshore anchor piles in dense sand under mooring forces. Steel pipe pile of 2 m diameter, 0.05 m wall thickness, and length to diameter ratio of 15 has been used in the analysis. The dimensions of this pile have been selected based on the in-service mooring piles at the Grand bank (personal communication with Husky Energy). The material behavior of the pile was assumed to be linear elastic with the parameters; Young's modulus (E) = 2.1×10^8 kN/m2 and Poisson's ratio (ν) = 0.2 for steel. The sand has been modeled as an elasto-plastic material with Mohr-Coulomb failure criterion. Constant values of soil Young's modulus (E_s) and lateral earth pressure coefficient (K_o) were assumed. The increase in lateral soil stress around the pile due to pile driving effect was not considered in the analysis. All piles were loaded under displacement control condition. Figures (2.21) and (2.22) show the load-displacement curves of the horizontal and vertical components for the different inclination load angles. In Fig. (2.21), the horizontal load component versus the horizontal displacement component is plotted. It can be seen that all curves have the same initial stiffness up to a certain load level after which the curves deviate from the curve of pure horizontal load; $\theta = 0^\circ$. As the load inclination angle increases, the stiffness of the curve decreases at a smaller horizontal displacement. This can be expected, as the ultimate lateral capacity of this pile is larger than the ultimate uplift capacity. By increasing the load inclination angle to horizontal, the vertical load component will gradually decrease the horizontal pile stiffness.

However, to better understand this behavior, we can see Fig. (2.22). The vertical load component versus the vertical displacement component is plotted. It can be seen that the initial stiffness of the load-displacement curves decreases slightly by increasing the load inclination angle to horizontal. Also, the stiffness for all curves start to decrease at certain level of load which is close to the ultimate uplift capacity of the pile as shown from the pure vertical loading curve. It can be concluded that the ultimate lateral capacity of this pile controls the initial loading stiffness of the pile, however, as much pull (10-15 mm) progresses the uplift capacity control the loading stiffness of the pile. However, more load inclination angles with small increments

need to be studied to find the critical inclination angle of the load at which the failure changes from axial failure to lateral failure.

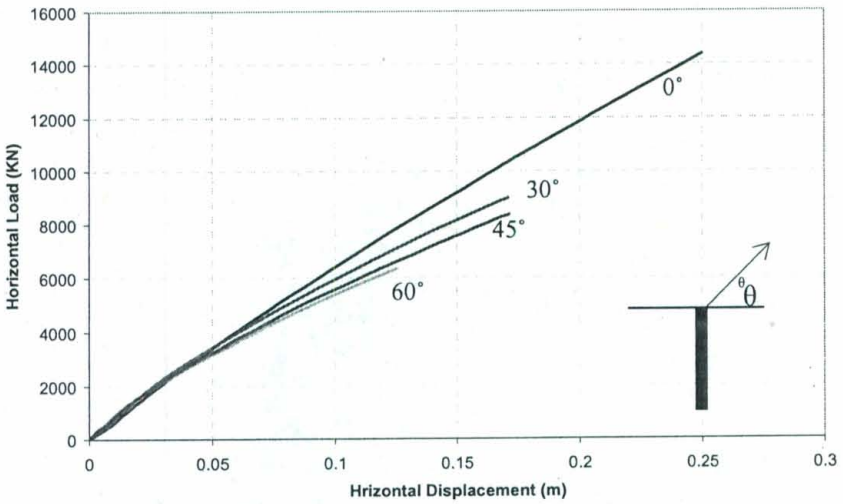

Fig. (2.21) Horizontal load versus horizontal displacement curves at the pile head for different inclination load angles, (after Ramadan et. al, 2009a)

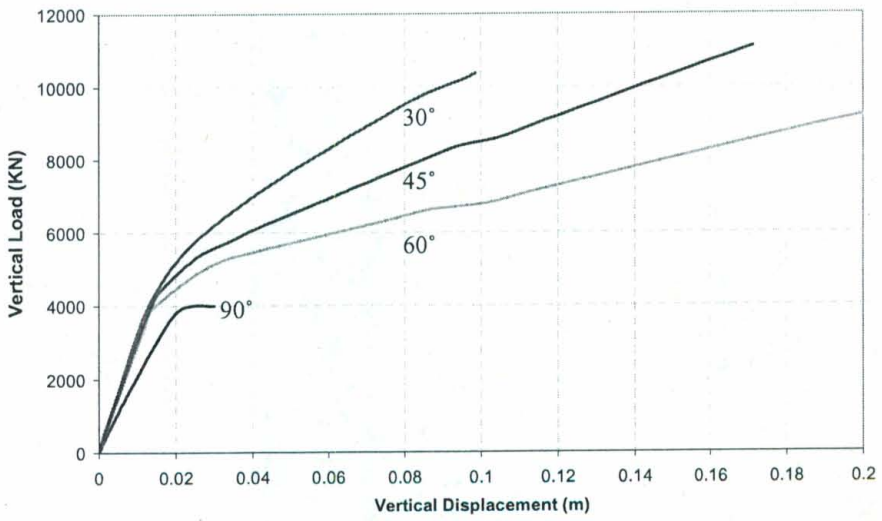

Fig. (2.22) Vertical load versus vertical displacement curves at pile head for different inclination load angles, (after Ramadan et. al, 2009a)

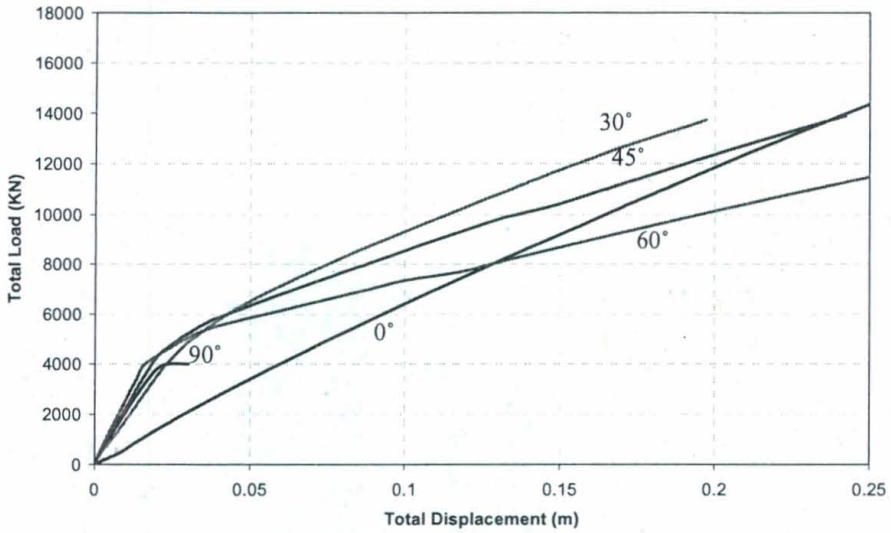

Fig. (2.23) Total load versus total displacement curves at pile head for different inclination load angles, (after Ramadan et. al, 2009a)

Figure (2.23) shows the total load-displacement curves for the different load inclination angles. For the curves of $\theta = 30°, 45°, 60°$, and $90°$, the failure load can be easily picked by drawing the tangent to the initial and end portion of the curve. The intersecting point of the two tangents will give the failure load. However, the curve of $\theta = 0°$ (horizontal load) is flat curve and the ultimate capacity has been selected at 10% of the pile diameter, as described by Hesar (1991).

The ultimate uplift and lateral capacity obtained by the finite element model of the pile have been used in the recommended Eqs. (2.40) and (2.42) to calculate the capacity of the pile under mooring force of angles $\theta = 30°, 45°$, and $60°$. It was found that the calculated ultimate capacities by Eq. (2.40) are much closer to the predicted one by the finite element than those by Eq. (2.42).

The reason of that much difference between the two equations in the estimated ultimate capacity is that what mentioned by Altaee & Fellenius (1994). Both equations are based on 1g test results. Because of the nonlinear stress-strain behavior

and the dependence of behavior on initial level of confining stress, small-scale physical modeling under lg conditions has little relevance to the behavior of a full-scale prototype. However, if we reanalyze the 1g results based on the steady state line of the soil as described by Altaee & Fellenius (1994), the 1g model that prepared in a loose state will simulate a prototype model of dense state. So, if the 1g model is prepared in a dense state, this will simulate a prototype of very hard soil which may not be exist in reality. If we considered this physical modeling view, Eq. (2.40), which had been derived from a 1g loose sand model of $\varphi = 31^{\circ}$, will simulate the behavior of a pile in dense sand. However, Eq. (2.42), which had been derived from a 1g dense sand model of $\varphi = 41^{\circ}$, will simulate the behavior of a pile in a stiffer soil than that can be found in field. Based on their results, the following conclusions were made:

1. The ultimate resistance of a pile under oblique pull is a continuous function of the inclination of the pull and depends also on the net uplift and the ultimate lateral capacity of the pile.
2. Considering soil-pile interaction behavior of piles plays a main role in defining the critical inclination angle of the load at which the failure changes from axial failure to lateral failure.
3. Comparing the present results with the previous theoretical models shows that most of the available models did not consider the prototype scale. So, they should be modified to be practically useful.
4. More scaled experimental work should be done to get the prototype scale behavior. Using these experimental results some numerical parameters can be well estimated and a good numerical model can be designed to simulate the behavior of pipe piles under mooring forces.

However, in their study, the effect of pile installation was not considered. Ramadan et al. (2009b) carried out the same study as before considering the effect of pile installation. ICP' (2005) has been used to calculate the lateral stress profile along the pile length. The soil model has been divided into layers. The lateral earth pressure

coefficient (K) value calculated based on ICP' (2005) has been assigned to each layer. Although the increase in the lateral stress should be limited to a limited zone around the pile, it has been found, to simplify the model and due to convergence problems, that increasing the lateral stress along the full width of the soil model has little effect on the results as the main increase in the lateral stresses is concentrated to the pile tip vicinity which will have a negligible movement for a flexible pile. Also, soil Young's modulus was implemented in the FEM to increase by depth. The model was calibrated to ultimate pile tension capacity, lateral flexible pile capacity, and lateral rigid pile capacity using available methods in literature.

It was observed that the oblique ultimate capacity is highly influenced by the tension load component. Even for a small inclination angle of 15°, the ultimate capacity is much higher than that for pure lateral loading. This is an important result which is different from the previous studies that suggest that the tension loading component can be neglected. This effect results from the pile installation effect which allows for much higher tension capacity than if the installation effect is neglected. This tension capacity can be compared to that obtained by Ramadan et al. (2009a). The pile tension capacity from Ramadan et al. (2009a) study was 5 times lower than that obtained by Ramadan et al. (2009b) study.

2.4.2 Cyclic loading:

Jamnejad and Hesar (1995) did an experimental and theoretical study of the response of single pile anchors vertically installed in saturated cohesionless soil and subjected to cyclic loading applied at different angles of inclination. In these tests loads were to be applied over long periods of time, eg. 7–10 days, at frequencies of 0.05–0.2 Hz. Even the fastest rate of cyclic loading was not sufficient to cause a significant build up of excess pore pressure. In Figure (2.24), the movement per cycle reduces rapidly during the early stages of cycling, as a progressively stable condition seems to develop with the flattening of the curves. However, as the cyclic loading continues further, the movement per cycle becomes gradually larger and the curves climb back

up again. The development of this minimum condition signifies the critical stage and system instability begins to set in.

A series of cyclic loading tests was carried out in order to establish the influence of a pile anchor's physical dimensions, including flexural stiffness, on its cyclic loading life. It was found that the cyclic life of a pile anchor is a function of several factors including diameter, flexural stiffness and, most dominantly, load amplitude. The influence of flexural stiffness was investigated in isolation by comparing the response of two pile anchors of identical length (L = 700 mm) and diameter (d = 90 mm) but one having half the EI-value, by selecting a section with a smaller wall thickness. The thin walled model exhibited a more resilient response. The life of the system in terms of the number of cycles increased from about 1000 to around 7000 cycles. They interpreted this that a rigid pile anchor transmits the shearing stresses to greater depths in the soil, causing a more extensive degradation effect there. This increased degree of shearing stresses results in an accelerated migration of soil particles from stressed regions to the opposite side of the pile anchor shaft (i.e. from the passive to the active side). From their study of pore pressure changes around the pile anchors they observed that as failure approaches the pore pressures increase, resulting in a net reduction in effective stresses and, hence, a corresponding net reduction in the instantaneous value of the internal friction angle. It can be argued that with each cycle of load the whole of the soil domain in the stressed regions is subjected to shearing stresses. The magnitude of these shear stresses obviously depends on the actual position of the soil element concerned. However, apart from a relatively small zone immediately adjacent to the pile anchor shaft, the strain levels are small and cause mainly elastic deformations. Only a small amount of permanent deformation results from each load cycle. Therefore, it is possible that a reduction in the internal friction angle could accelerate this process, which results in a permanent volume increase and hence loosening of the soil structure. At well past the failure stage pore pressure gauges registered a mean value of zero excess pore pressure. This would seem to confirm that the soil structure is sufficiently loosened down at those zones, where soil resistance against applied loads is generally mobilized.

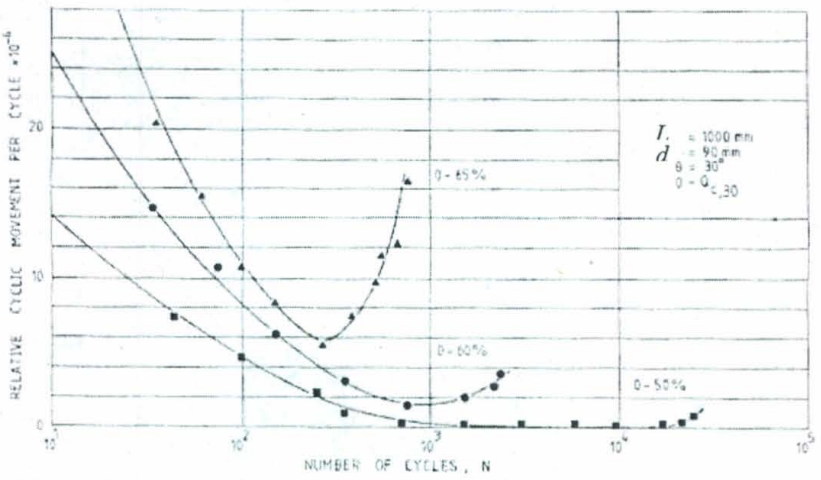

Figure (2.24) Influence of load amplitude on the cyclic life of a pile anchor: relative displacement per cycle versus number of cycles, (After Jamnejad and Hesar, 1995)

Vidich et al (1998) conducted load tests on laboratory models of rough shafts in sand under static and one way cyclic inclined loading. The shaft models were with a 52 mm diameter and depth to diameter ratios of 3, 6, and 9. Testing was done in uniform deposits of loose and medium dense normally consolidated sand and dense overconsolidated sand. As a part of their testing program, they loaded the shafts at load inclinations: 0° (axial uplift), 15°, 45° (inclined uplift), 90° (lateral) all measured from the upward vertical pile axis.

The main variables in the cyclic testing program included the mean cyclic load (P_{mean}), cyclic load component (P_{cyc}), cyclic frequency (f), and number of applied load cycles (N_L). They defined the cyclic load ratio (CLR) as (P_{cyc} / P_{mean}). A schematic of a single level cyclic test showing load versus displacement is shown in Figure (2.25). In their study, a frequency of 0.02 Hz was selected as the loading frequency and 100 cycles at each given load level were applied for three levels of loading for four hours of loading to simulate a typical storm. Given that the cyclic displacement accumulation rate tends to be very small for a CLR less than 20%, even for high mean cyclic loads, the CLR range in this study was extended from 12% to 80%. The mean cyclic load level (P_{mean}) for each loading level was selected so that the maximum applied peak load remained less than 70% of the shaft failure load.

In their analysis of the test results, they presented the load-displacement curves by plotting the horizontal and vertical load components versus the corresponding displacement components. They reported that the concept of inclined displacement is inappropriate for unrestrained shafts, because they don't necessarily move in the applied load direction and the loading angle might change slightly during the test, although this small deviation from the initial value was not considered significant for the overall test results.

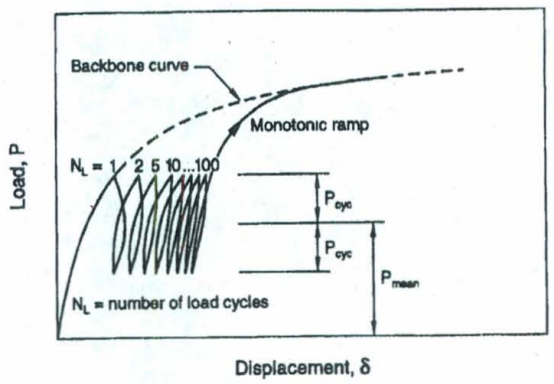

Figure (2.25) Components of cyclic load testing, (After Vidich et. al., 1998)

From the typical inclined uplift test results shown in Figure (2.26), cyclic loading leads to displacement accumulation at a decreasing rate, but otherwise it does not affect significantly the shaft capacity or stiffness. This response was observed for the range of shaft geometries, initial soil stresses, and loading conditions investigated in their study. They also presented an empirical method for quantifying the accumulated cyclic displacements that requires two parameters: the static displacement at the initiation of cyclic loading and the cyclic displacement accumulation parameter (t). The parameter (t) relates the accumulated peak to peak displacement after N_L cycles (δ_N) to the static displacement ($\delta_{N=1}$) at the initiation of cyclic loading, as given below:

$$\delta_N = \delta_{N=1} N_L^t \tag{2.44}$$

Parameter t can be obtained as the slope of the log δ_N versus log N_L curve. As with the load-displacement response, they established the cyclic displacement accumulation parameters for both the horizontal and vertical load-displacement components. The results for the inclined uplift tests at 45° are shown in Figure (2.26) for the same conditions shown in Figure (2.25). They concluded that conducting cyclic tests at low load levels and low cyclic load ratios results in negligible cyclic displacement accumulation, especially for the vertical displacement component. Although a good linear approximation of the data had been obtained for inclination angle 45°, they reported that cyclic loading at 15° is more complex and can be modeled using either a constant or bilinear slope for the displacement accumulation curve, depending on the cyclic load ratio and peak applied load. A constant t seems appropriate if the CLR is less than 20% or if the ratio of the applied to failure load is maintained under 40%, in which case a CLR up to 55% can be sustained.

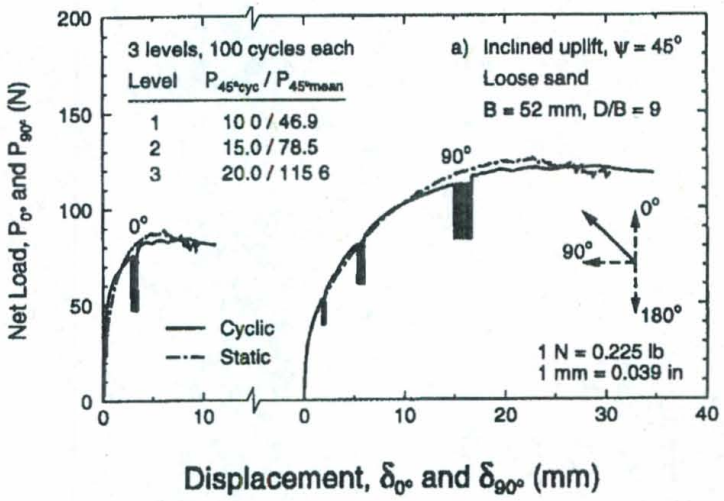

Figure (2.26.a) Comparison of static and cyclic inclined uplift (45°) tests in loose sand, (After Vidich et. al., 1998)

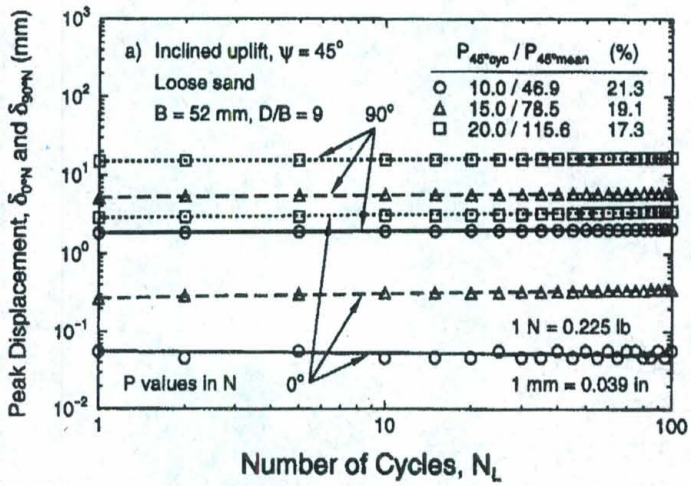

Figure (2.26.b) Cyclic displacement accumulation for inclined uplift (45°) tests in loose sand, (After Vidich et. al., 1998)

Chapter 3

Centrifuge Model Tests

3.1. Introduction:

In this chapter, the experimental work will be discussed. A series of centrifuge tests was conducted at C-CORE, Memorial University of Newfoundland. The model piles had been jacked in-flight into saturated dense sand. After installing the piles, they were monotonically loaded at different loading angles. Also, the piles were tested at different g-levels to simulate different pile diameters.

3.2. Centrifuge Modeling

Centrifuge modeling is now widely used to solve many geotechnical engineering problems. It has the capability to achieve stress similarity between the model and the prototype. This is accomplished by accelerating the model of scale $1{:}N$ to an acceleration of N gravities (Ng).

The Geotechnical centrifuge test benefits from the additional centripetal force acting on a model while the centrifuge is rotating. The mechanical principle that underpins centrifuge modeling is simple: if a body of mass m is rotating at constant radius r about an axis with steady speed v Fig (3.1) then in order to keep it in that circular orbit it must be subjected to a constant radial centripetal acceleration v^2/r or $r\omega^2$ where ω is the swept angular velocity. In order to produce this acceleration the body must experience a radial force $mr\omega^2$ directed towards the axis. We can normalize the centripetal acceleration with earth's gravity g and state that the body is being subjected to an acceleration of Ng where $N = r\omega^2 = g$, Wood (2004). So, by spinning the soil package and testing the model at a high speed, an artificial gravity is induced. The increase in gravity allows the stress, strain, and strength to be modeled in a scaled soil model.

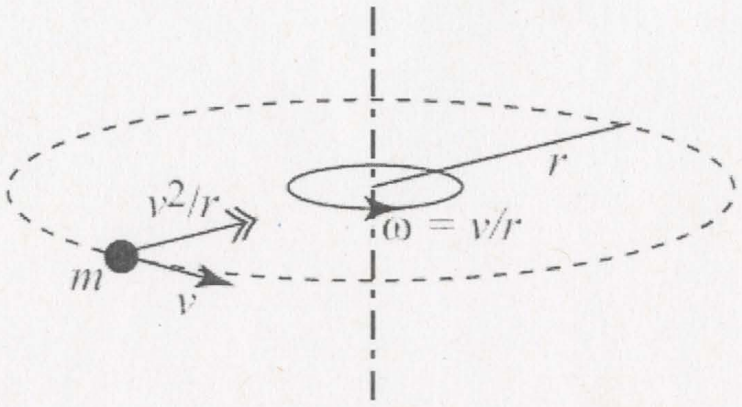

Figure (3.1) Object moving in steady circular orbit, (After Wood, 2004)

Two key issues in centrifuge tests are scaling laws and scaling errors. Scaling laws can be used by dimensional analysis. Centrifuge modeling is often criticized as having some scaling errors due to the non-uniform acceleration field and also the difficulty of representing sufficient detail of the prototype in a small-scale model and the difficulty of representing sufficient detail of the prototype in a small-scale model, Taylor (1995).

3.2.1 *Scaling laws:*

The basic scaling law derives from the need to ensure stress similarity between the model and the corresponding prototype. As discussed by Taylor (1995), if an acceleration of N times earth's gravity (g) is applied to a material of density ρ, then the vertical stress, σ_v at depth h_m in the model (using subscript m to indicate the model) is given by:

$$\sigma_{vm} = \rho N g h_m \qquad (3.1)$$

In the prototype, indicated by subscript p, then:

$$\sigma_{vp} = \rho g h_p \qquad (3.2)$$

Thus for $\sigma_{vm} = \sigma_{vp}$, then $h_m = h_p N^{-1}$ and the scale factor (model: prototype) for linear dimensions is 1: N. Since the model is a linear scale representation of the prototype,

then displacements will also have a scale factor of 1: N. It follows therefore that the strain has a scaling factor of 1:1, and the stress-strain curve mobilized in the model will be identical to the prototype, as shown in Figure (3.2). The scaling factors of parameters are shown in Table (3.1).

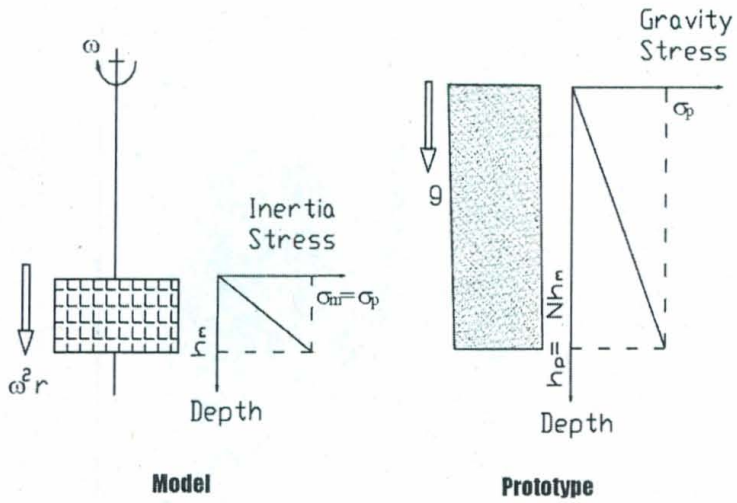

Figure (3.2) Stresses in Model and Prototype, (After Fu, 2004)

Table (3.1) Scaling Factors for Centrifuge Tests

Parameter	Model
Acceleration, N	*N:1*
Density, N_ρ	*1:1*
Stress, N_σ	*1:1*
Strain, N_ε	*1:1*
Velocity, N_v	*1:1*
Length, N_l	*1:N*
Area, N_A	*1: N^2*
Volume, N_V	*1: N^3*
Force, N_F	*1: N^2*
Time (static), N_t	*1:1*

The current study is related to piles subjected to inclined pullout loads. So when discuss the centrifuge laws both the lateral and tension loading cases should be considered.

a- Pile under lateral loading:

Wood (2004) explained in details the physical modeling law that is guiding the piles under lateral loading. He assumed that the pile is not being so heavily loaded that it is stressed by axial load or in bending beyond its elastic range. He assumed also that we are not concerned with the ultimate lateral load capacity of the pile moving relative to the soil. Let us consider initially simply the response of the pile to lateral loading which will be governed primarily by the flexural rigidity of the pile *EI*. The pile can be considered as a beam with certain loads applied both by loading at the ground surface or at the head of the pile and by the resistance of the ground to relative movement of pile and soil. If the soil responds elastically to this relative movement then the resisting force will be proportional to relative displacement according to some coefficient of subgrade reaction k and the equation governing the deformation of the pile will be of the form:

$$EI\frac{d^4y}{dz^4} = -ky \tag{3.3}$$

where z is the distance measured down the pile and y is the horizontal deflection of the pile. The coefficient k will be expected to be proportional to the shear modulus G of the soil $k = \beta G$ (although the pile-soil interaction is not strictly a process of pure shear).

By assuming a dimensionless depth factor ζ:

$$\zeta = \frac{z}{l} \tag{3.4}$$

where l is the pile length, and a dimensionless deflection factor λ:

$$\lambda = \frac{y}{y_o} \tag{3.5}$$

where y_o is the deflection at the pile head. The equation then becomes:

$$\frac{EI}{l^4}\frac{d^4\lambda}{d\zeta^4} = -\beta G\lambda \tag{3.6}$$

This means that a natural dimensionless group to characterize the problem is Gl^4/EI which describes pile-soil stiffness. The soil quantity Gl^4 somehow has equivalence to the flexural rigidity EI of the pile. Then we might suppose that correct physical modeling will be obtained if we maintain the dimensionless ratio Φ_1 identical in the model and the prototype:

$$\Phi_1 = \frac{Gl^4}{EI} \tag{3.7}$$

If we have scale factors N_G , N_E and N_I for soil shear modulus, pile material Young's modulus E and second moment of area I of the pile, respectively, then we deduce that:

$$N_E N_I = N_G N_l^4 \tag{3.8}$$

For centrifuge modeling of acceleration Ng, N_G=1 and $N_l = N$.

b- Pile under tension loading:

Nunez and Randolph (1985) discussed the similarity requirements for tension piles. They used the flexibility ratio π_3 as the relative stiffness between the pile and soil:

$$\pi_3 \approx 2\left(\frac{l}{d}\right)^2 \frac{G}{E_p} \tag{3.9}$$

where E_p is the young's modulus of an equivalent solid pile.

So for piles under inclined pullout loading, both Φ_1 and π_3 should be identical in the model and the prototype.

3.2.2 *Limitation of Centrifuge Modeling:*

In physical modeling studies, it is seldom possible to replicate precisely all of the details of the prototype, and some approximations have to be made. Some of these limitations that may be encountered in the present study are:

1) *Acceleration Field Scaling Errors:*

a- Variation in Vertical Direction:

The Earth's gravity is uniform for the practical range of soil deposits in prototypes. When using a centrifuge to generate the high acceleration field, there is a slight variation in acceleration through the model, Taylor (1995). This is because the inertial acceleration field is given by $r\omega^2$ as discussed before with r is the radius to any element in the soil model. This apparent problem turns out to be minor if care is taken to select the radius at which the gravity scale factor N is determined. Figure (3.2) shows the distributions of vertical stress in the model and corresponding prototype. When both are plotted against corresponding depth, as shown in Figure (3.3), there is exact correspondence in stress between model and prototype two-thirds of the model depth, and the maximum under-stress and the maximum over-stress exist at one third of the height of the model and at the bottom of the model, respectively (the nonlinear variation of stress in the model is shown exaggerated for clarity). For the current centrifuge models, h_m / R_e is 0.1 which is less than 0.2, and therefore the maximum error in the stress profile is generally less than 3% of the prototype stress, Taylor (1995).

b- Lateral Acceleration Component:

As discussed before, the inertial radial acceleration is proportional to the radius which leads to a variation with depth in the model. Also, this acceleration is directed towards the center of rotation and hence in the horizontal plane, there is a change in its direction relative to vertical across the width of the model. There is therefore a

lateral component of acceleration, the effect of which should be considered. To minimize this effect, it is good practice to ensure that the major events occur in the central region of the model where the error due to the radial nature of the acceleration field is small or use a centrifuge with a large radius. For the current study the centrifuge effective radius is 5 m which is a large radius to minimize such effect.

2) *Particle size effect:*

In the centrifuge test, the dimensions of a prototype is scaled down by a factor of *N*, but generally, the soil particles can not be scaled down at the same scale. This will produce grain size effects. In case of piles in sand, the size of soil particles relative to pile diameter may have a significant effect. Ovesen (1979) showed that the scale effects are negligible on the shallow foundation bearing capacity studies if the ratio D/d_{50} is larger than 30, where D is the foundation depth. Remaud (1999) performed a series of "modeling of models" tests on the same pile under lateral loads. No scale effects had been observed for $d/d_{50} > 60$, where d is pile diameter. Also, Firavante (2002) confirmed through a series of centrifuge tests the as $d/d_{50} > 30$-50 the scale effects produced by small scale models on the ultimate shaft friction can be neglected. In the present study d/d_{50} ratio is about 77, which is within the acceptable ratio.

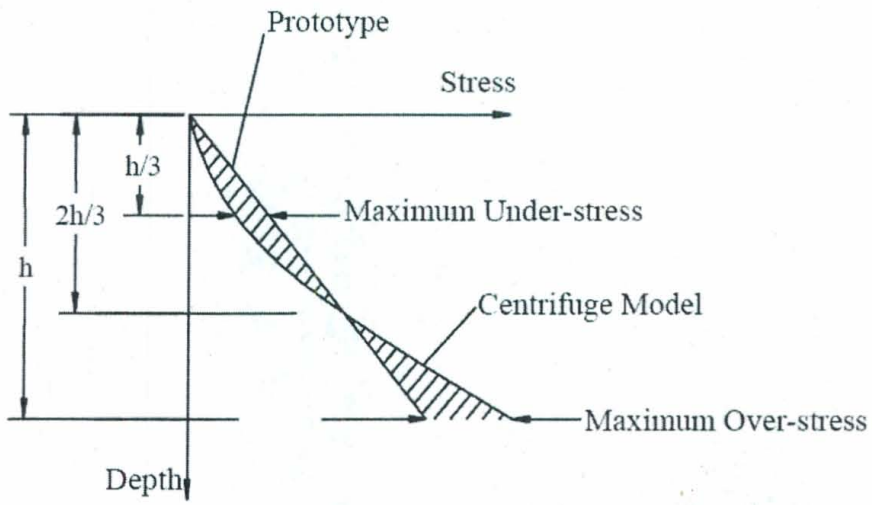

Figure (3.3) Stress Variation with Depth in a Centrifuge Model, (After Taylor, 1995)

3) *Boundary effects:*

The centrifuge model test is normally a simulation of the behavior of an infinite half space with a localized perturbation. The container boundaries should replicate the behavior of the far field half-space. To cope with the high stresses within the centrifuge the test containers or strongboxes must be rigid and strong. To maintain similitude to the prototype, the non-compliance of the test container base and side walls must be considered. High lateral stiffness is required to prevent lateral soil movement and therefore requires a rigid boundary. Some modelers considered the effect of wall friction by placing a glass sheet between the model material and the container wall or using a lubricated latex membrane at the soil boundary that will stretch and accommodate any vertical soil displacements, Phillips (1995). As the later technique has been found by other modelers to have a little to no effect, it has been shown that the model soil width to depth ratio should be greater than four to eliminate general boundary influence. Proper design of the test set-up with respect to test and instrumentation locations can assist in limiting the influence from container boundaries. Testing involving any soil displacement should be positioned as far away from any rigid frictional boundary as possible, Hanke, 2001.

In case of pile models or Cone Penetration Tests (CPT) during centrifuge flight, beside the particle size effect there are two more boundary conditions should be considered. The first condition is the distance to the rigid horizontal boundary in terms of pile or cone diameters. Bolton et al. (1999) stated that a CPT must not be performed at a distance less than 10 cone diameters from any rigid boundary in order for cone data to be meaningful. The CPT tests in the present study were at the center of the sand bed. The distance to the strong box wall is about 45 times the cone diameter. The distance to the pile tests locations is 20 times the cone diameters. All CPT tests were conducted after conducting all the pile tests in the same sand bed. Also, other modelers (as Di Nicola and Randolph, 1997) performed axial model pile tests recommended horizontal boundary conditions of 7 to 8 pile diameters. In the current tests, the distance between the pile and the strong box wall is 12 times the pile diameter. The second boundary condition is the test container bottom or the model

depth limitation. The general rule followed by centrifuge modelers is to keep the model at least 6 to 10 model diameters or widths away from the rigid bottom surface. In the current tests, this distance was 10 times the pile diameter.

3.3.Centrifuge Tests Setup

The present study has been conducted using C-Core centrifuge. The C-Core Centrifuge Centre at Memorial University of Newfoundland houses the Acutronic 680-2 centrifuge as shown in Fig. (3.4). The centrifuge can carry masses up to 650 kg at 200 gravities. The maximum centrifugal rotational speed is 189 r.p.m. and the maximum acceleration at an effective radius of 5.0 m is 200 gravities. The data acquisition system can provide 78 channels for data sampling the electrical signal from transducers during tests.

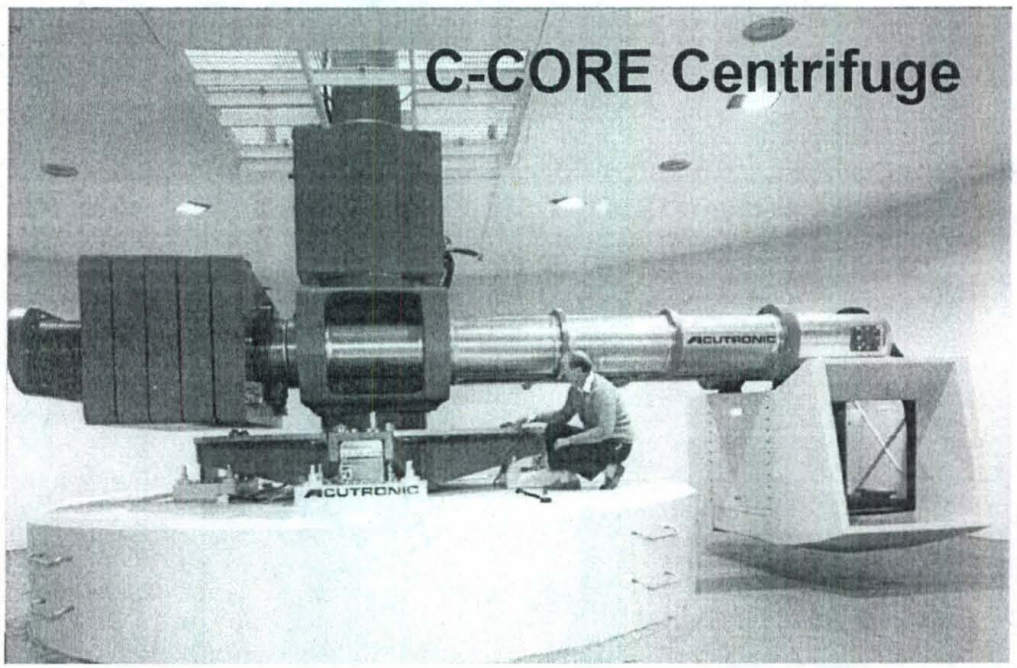

Figure (3.4) C-Core Acutronic 680-2 Centrifuge

Eight centrifuge tests were undertaken to investigate the behavior of offshore anchor piles under mooring forces. Four tests were loaded monotonically and the other tests were initially monotonically loaded then sustained under cyclic loading. All tests were carried out under drained conditions. Five piles were tested at 70g. The other three piles were tested at 50g.

3.3.1 *Soil Properties:*

Fraser River sand was used in the experiment. It has been selected because of its availability at C-Core, it has been extensively used in centrifuge testing and its properties are well known. As reported by Wijewickreme et al. (2005), the Fraser River sand, that had been used in the present tests, has an average particle size d_{50} = 0.26 mm, d_{10} = 0.17 mm, specific gravity G_s = 2.71, and uniformity coefficient C_u = 1.6. The maximum and minimum void ratios (e_{max} and e_{min}) for the sand are 0.94 and 0.62, respectively. Fraser river sand is composed of 40% quartz, quartzite, and chert; 11% feldspar; 45% unstable rock fragments; and 4% miscellaneous detritus. The sand grains are generally angular to subrounded.

3.3.2 *Soil container and sample preparation:*

All tests were carried out in a round steel tub of 914 mm diameter and 500 mm height, as shown in Figs. (3.5) and (3.6). The sand was prepared by dry air pluviation into the model container using a hopper. The characteristic variation of relative density with average fall height determined by Chakrabortty (2008) was used in the tests preparation. First, a 20 mm drainage layer of coarse sand was placed at the bottom of the tub. This drainage layer was used to uniformly distribute the water throughout the sample during the saturation process. Then the sand was rained from a constant height of 1.2 m to the bottom of the soil container as shown in Fig. (3.7). During model preparation the hopper speed was kept constant at about 10cm/sec. Three density cups were used to check the relative density of the rained sand at the bottom, the middle and the top of the soil model. The average relative density was 86 %. After raining the sand into the tub up to 470 mm height, the tub was sealed at the

top and the saturation process was started using de-aired water as described by Dief (2000). Two in-flight Cone Penetration Tests (CPTs) were performed at 50g and 70g to check the repeatability of the sand models as shown in Fig. (3.8). The results of the CPT were used to calculate the angle of internal friction as recommended by Mayne (2001). The angle of internal friction was found to be 43°. Also, the shear wave velocity of the sand (*Vs*) was measured in-flight using bender elements at three depths as will be discussed in the next chapter.

3.3.3 *Sample Saturation:*

The saturation process was conducted as sketched in Fig. (3.9) and as shown in Fig. (3.10). First, after raining the sand into the model container, the model container was sealed with a tight led. Then, the sample was de-aired by the application of vacuum to the prepared sand for a period of approximately 24 hours at about 80 kPa. After this, the vacuum pump to the sealed model container was shut off and carbon dioxide is then used to displace the less soluble air that may be present in the voids of the sand model. Carbon dioxide gas is introduced into the bottom of the model at virtually atmospheric pressure from a depressurization chamber that serves to regulate the high-pressure carbon dioxide gas from the compressed gas supply bottle. Following this process, the sample container is again placed under vacuum to bring it back to the 80 kPa vacuum level. The process of introducing carbon dioxide followed by vacuum is repeated again to be sure that the majority of gas inside the container is carbon dioxide which is much more soluble than air and allows for more complete saturation. The next step of the process was to close all valves and allow the de-aired water to pass slowly in the soil from the bottom to the top. The water passed in the soil under the effect of gravity through a 10 mm layer of permeable drain material. This layer is a mix of fine gravel and coarse sand and was installed at the base of the model container to aid in the saturation of the model under vacuum conditions as the water is introduced from the bottom of the model. The saturation process continued over a period of approximately 2 days. The saturation process was stopped after supplying an amount of water equals to the soil voids volumes which was calculated based on

the measured average relative density of the dry sand. The final water level was almost 20 mm above the sand surface.

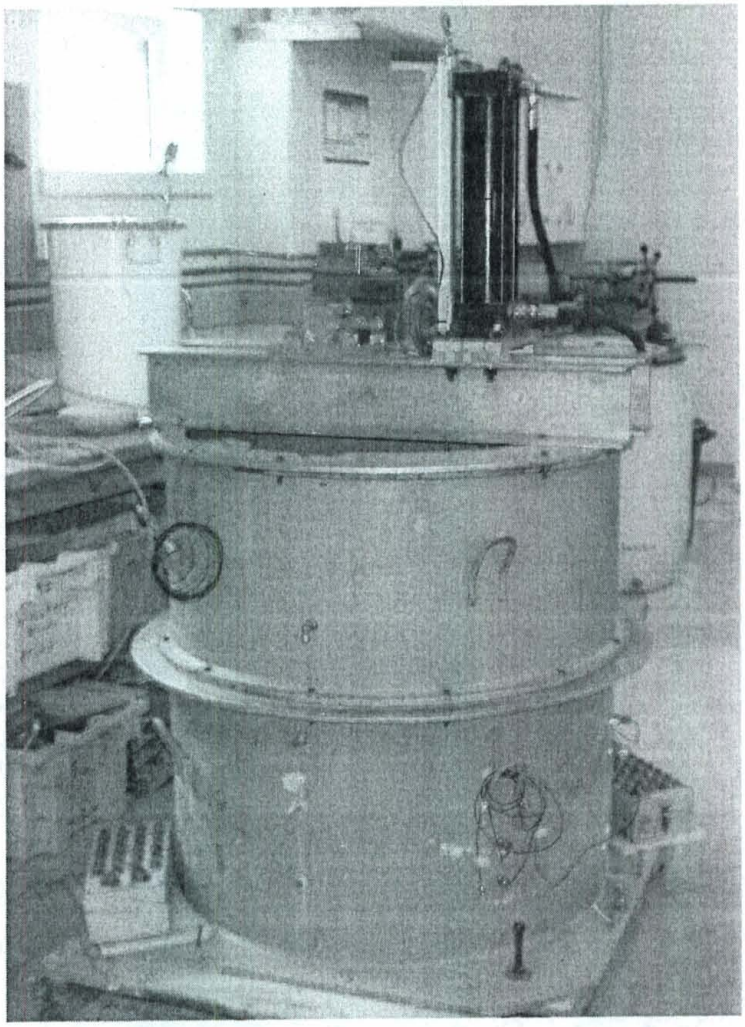

Figure (3.5) Test Package before Loading on the Centrifuge

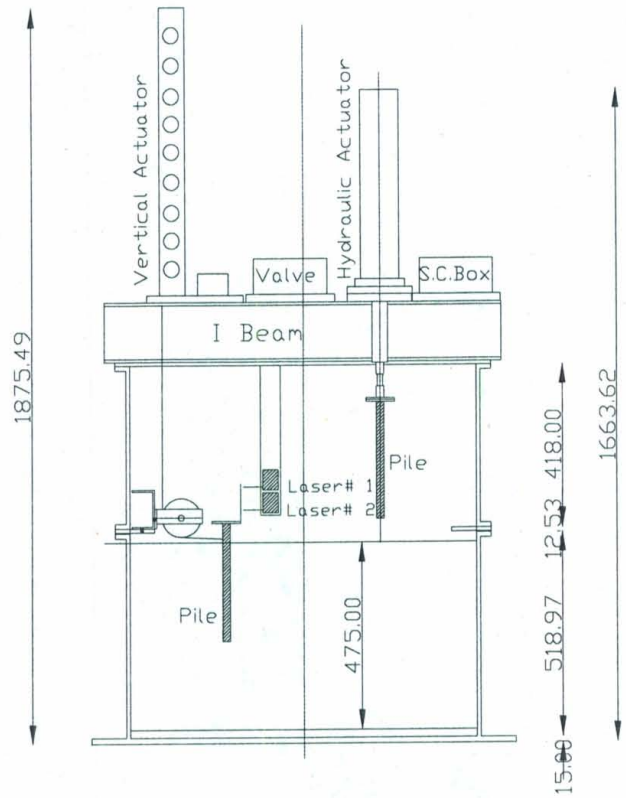

Section Elevation

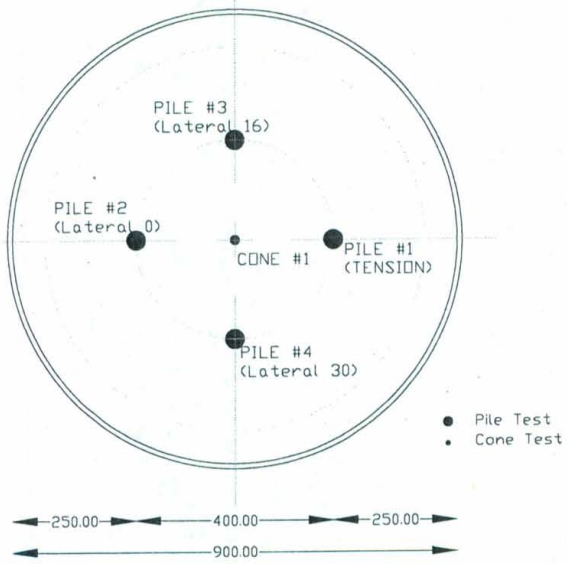

Plan View

Figure (3.6) Centrifuge Test Setup

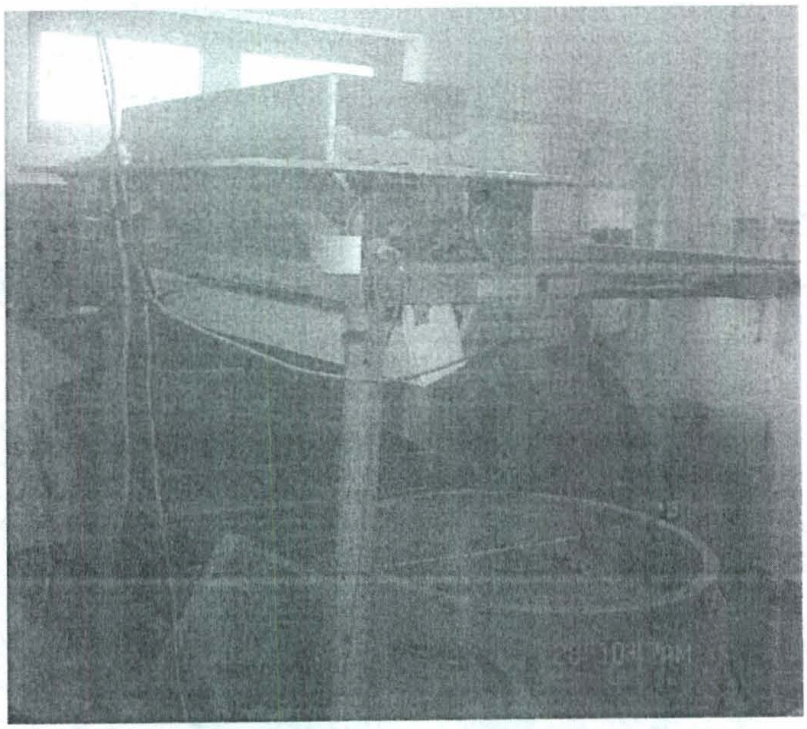

Figure (3.7) Setup for Sand Raining Process

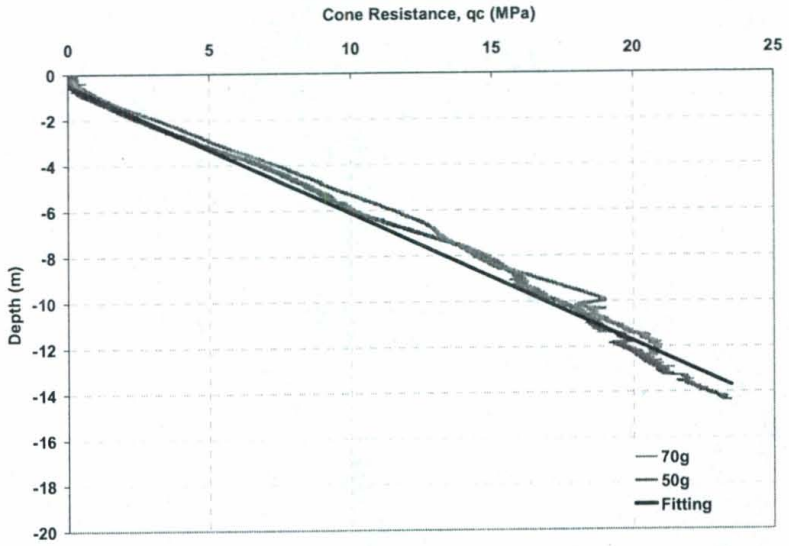

Figure (3.8) Cone Penetration Tests

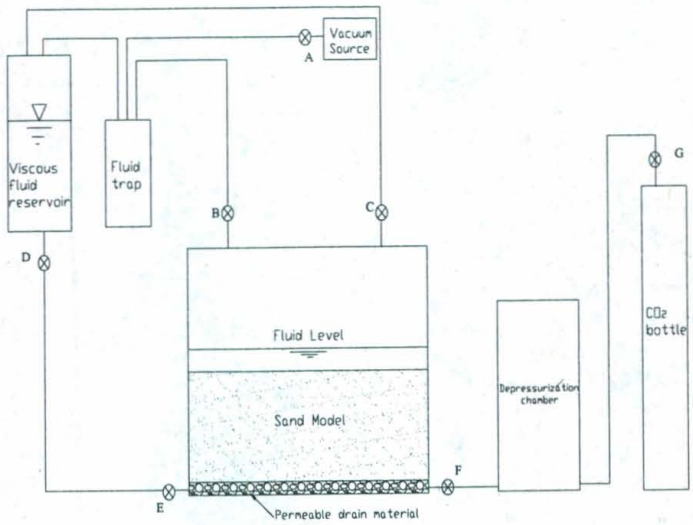

Figure (3.9) Schematic Diagram for Saturation Setup

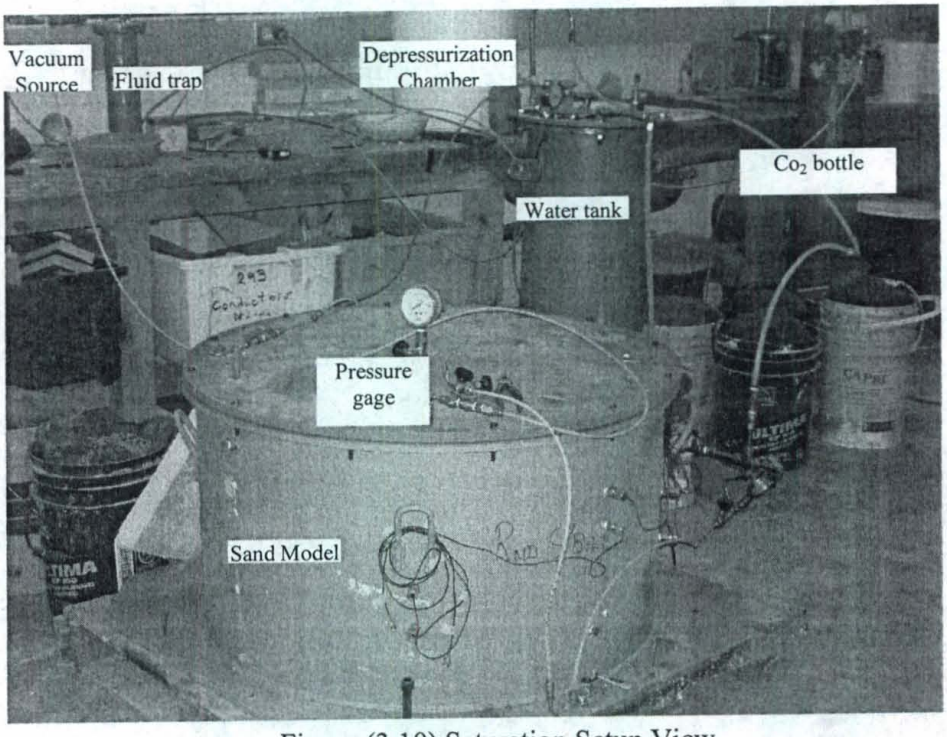

Figure (3.10) Saturation Setup View

3.3.4 *Model Pile:*

Four instrumented open ended model piles were made of aluminum. The dimensions of the model piles were 18 mm by 1.5 mm by 300 mm in outside diameter, wall thickness, and pile length, respectively, as shown in Fig. (3.11) and (3.12). The embedment depth of the pile was 250 mm that gives length to diameter ratio (*L/d*) of 12.5. For FPSO piles, Bhattacharya [1] reported that pile length usually ranges between 15m to 25m. He also reported that pile diameter ranges between 1m to 2m. FPSO piles at offshore Newfoundland have pile diameter of 2m and pile length of 30m which will give *L/d* of 15. Based on these dimensions and the test boundary effects, *L/d* ratio of 12.5 was selected.

All model piles were instrumented with 10 pairs of strain gages. Twenty quarter bridge strain gages (CEA-06-240UZ-120) have been attached to the external surface of the pile model. The spacing between the strain gages is shown in Fig. (3.11). The quarter bridge configuration allows strains to be measured both while the pile was in axial loading and while in bending occurring during lateral loading. It should be noted that full bridge configuration was used on another pile. This pile was instrumented of bending and axial strain gages at ten levels. However, this pile was damaged during in-flight installation as shown in Fig. (3.13). The reason for trying to use full bridge configuration was to measure both axial and bending strain at the same time during the inclined pullout loading. The model pile had been coated with a thin layer of 1 mm of epoxy resin. This layer protected the strain gages on the pile surface from damaging during jacking the pile into the sand and from water. This protecting layer increased the diameter of the pile without modifying the pile stiffness as found from the calibration tests. *The pile diameter after coating with epoxy is 20 mm.* All pile models were calibrated as a cantilever beam. The pile model was horizontally fixed at the pile cap and perpendicular loads were hanged at the other end (pile tip). The calibration tests were conducted before and after coating the pile models with the epoxy resin layer to check the change in the flexural stiffness of the pile model. After calibrating these strain gages the bending moment profile at ten levels versus depth

during the centrifuge tests is achieved. The prototype pile properties are shown in Table (3.2).

Table (3.2) Prototype Pile Characteristic at 70g and 50g tests

Characteristic	Prototype (70g)	Prototype (50g)
Length up to loading point (m)	18.2	13
Embedded length (m)	17.5	12.5
External diameter (m)	1.4	1.0
Young's Modulus, E (MPa)	$2.1x10^5$	$2.1x10^5$
Flexural Stiffness (MPa)	4484.0	1167.23
Axial Stiffness (MPa)	26670	13607

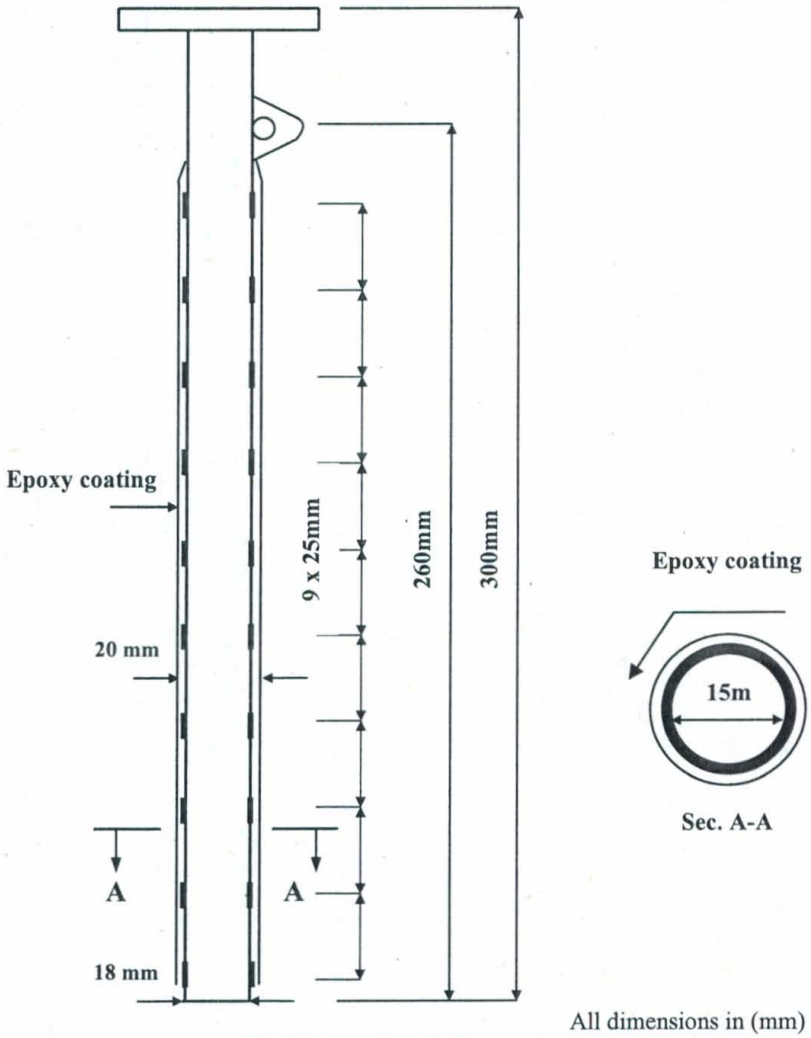

Figure (3.11) Pile Model

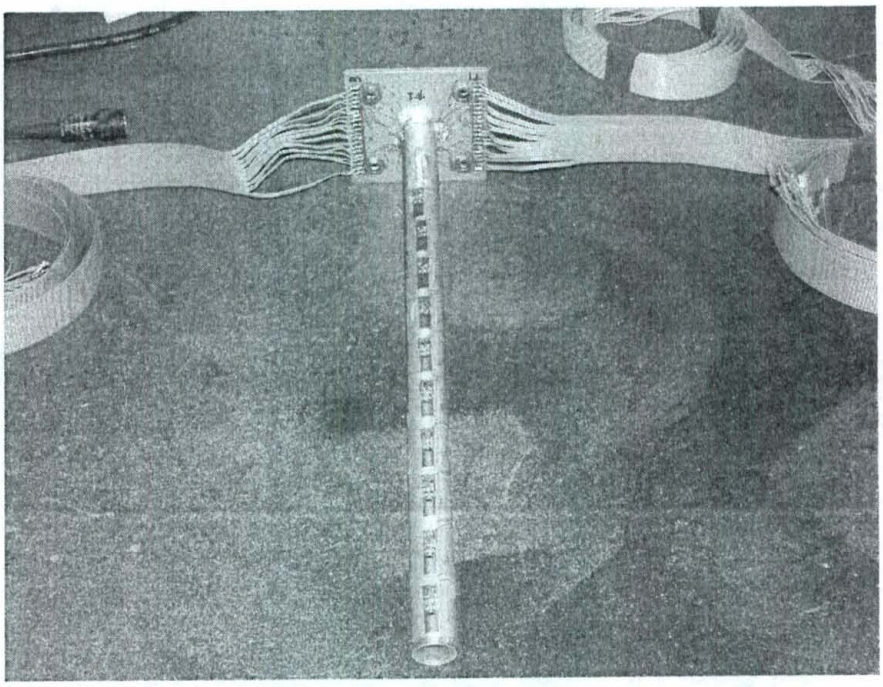

Figure (3.12) Pile Model View

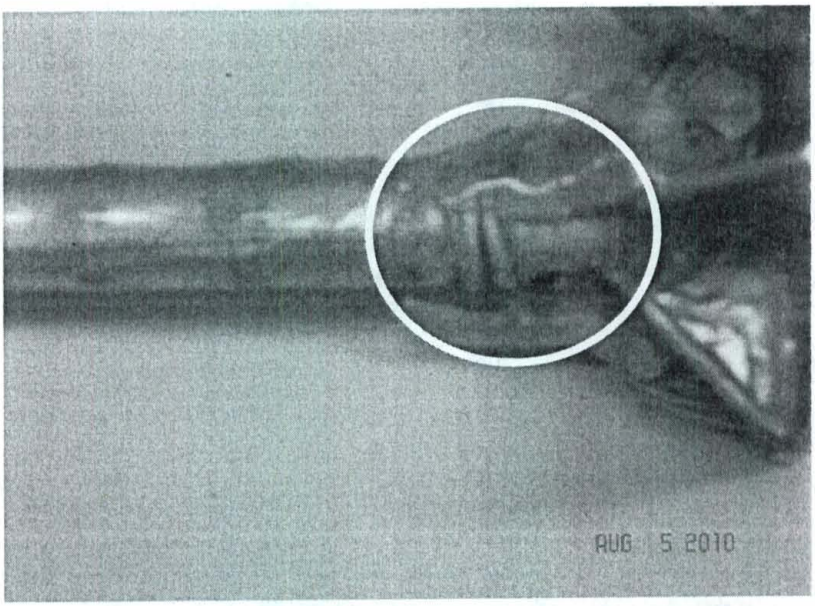

Figure (3.13) Damaged Pile Model View

3.3.5 *Pile Installation:*

The model piles were kept hanged attached to the hydraulic actuator in air before spinning up the centrifuge as shown in Figs. (3.14). After spinning up the centrifuge the pile was jacked into the sand bed at the same g-level of the loading tests. All piles were installed into the sand bed at a rate of 0.1 mm/sec to ensure the drained conditions. To check the drained conditions during pile installation, miniature Pore Pressure Transducer (PPT) was located at a depth of 10 times the pile diameter and at a distance of one pile diameter away from the pile surface in horizontal direction. The PPT reading did not change during pile installation. Due to the large reaction loads during pile installation, a hydraulic actuator was used. During the pile installation the total compression load from jacking was measured through a load cell attached between the pile head and the hydraulic actuator, as shown in Fig. (3.14). Also, the axial load along the pile was measured from the strain gages on the pile. These measurements have been used to estimate the shaft friction and lateral earth pressure coefficient profiles along the pile length, as will be discussed in another chapter. Once the pile was penetrated 250 mm (17.5 m and 12.5 m at 70g and 50g in prototype dimensions, respectively) in the sand bed, the hydraulic actuator movement was stopped then the centrifuge was stopped to disconnect the hydraulic actuator from the pile. The test package was unloaded from the centrifuge and the bottom tub was rotated to hook up the pile to the loading device. All axial load measurements during in-flight pile installation from the load cell at pile head and from the strain gages along the pile as well are given in Appendix-A.

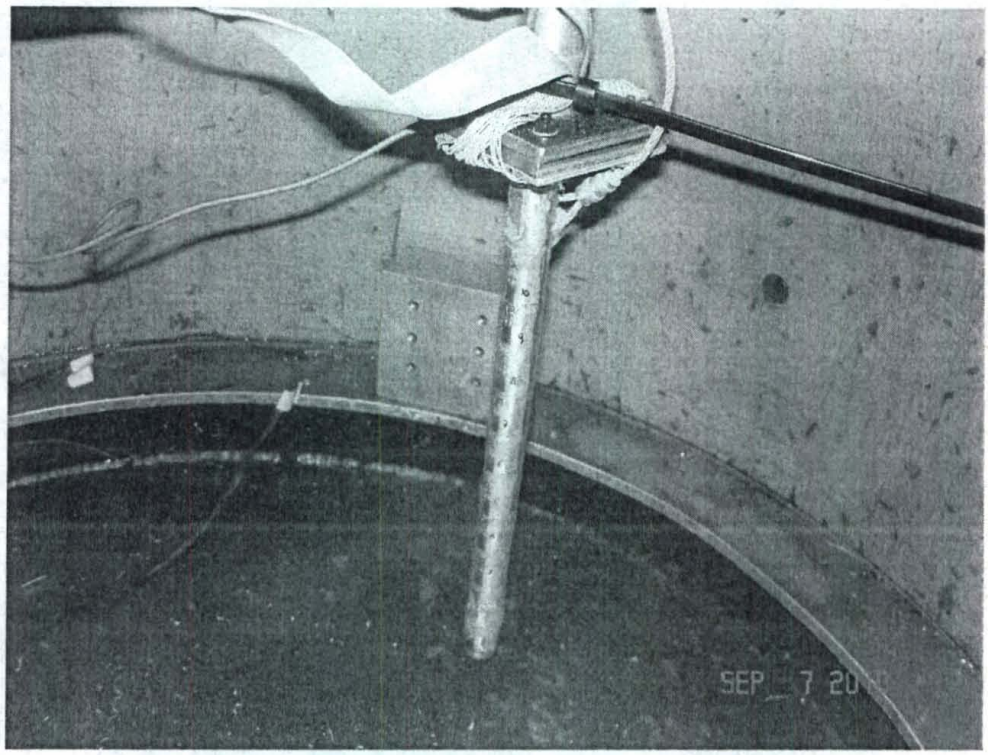

Figure (3.14) Pile Model Ready for Installation

3.3.6 *Loading Device:*

The load was applied using a vertical actuator of 10 kN maximum capacity supported on two I-Beams on a round extension above the round tub. The load was transferred to the pile through a stainless steel aircraft flexible cable. The cable was connected to the pile through a pad eye 10 mm above the sand surface. The loading angle was controlled by passing the loading cable on a ball bearings pulley. The pulley level can be changed at three different levels to get 0°, 3°, 16°, and 30° loading angles to horizontal at the pad eye. This load was measured with an in-line load cell of a capacity of 2.5 kN. The loading rate was constant throughout the tests, at a displacement controlled rate of 0.10 mm/sec to satisfy drained conditions as suggested by Nunez et. al. (1988). The drained conditions was checked at one test by placing PPT at a depth of three pile diameter and at a distance two pile diameter from

the pile surface in horizontal direction. The PPT readings did not change during the loading process. The loading device details are shown in Figs. (3.15) and (3.16).

All tests were displacement controlled using the vertical actuator displacement transducer. However, due to the cable stretch during loading, other transducers were used to measure the actual pile head displacements. Two laser displacement transducers were mounted at different levels above the pile, as shown in Figs. (3.16). The measured displacements allowed estimation of pile head rotation and displacement.

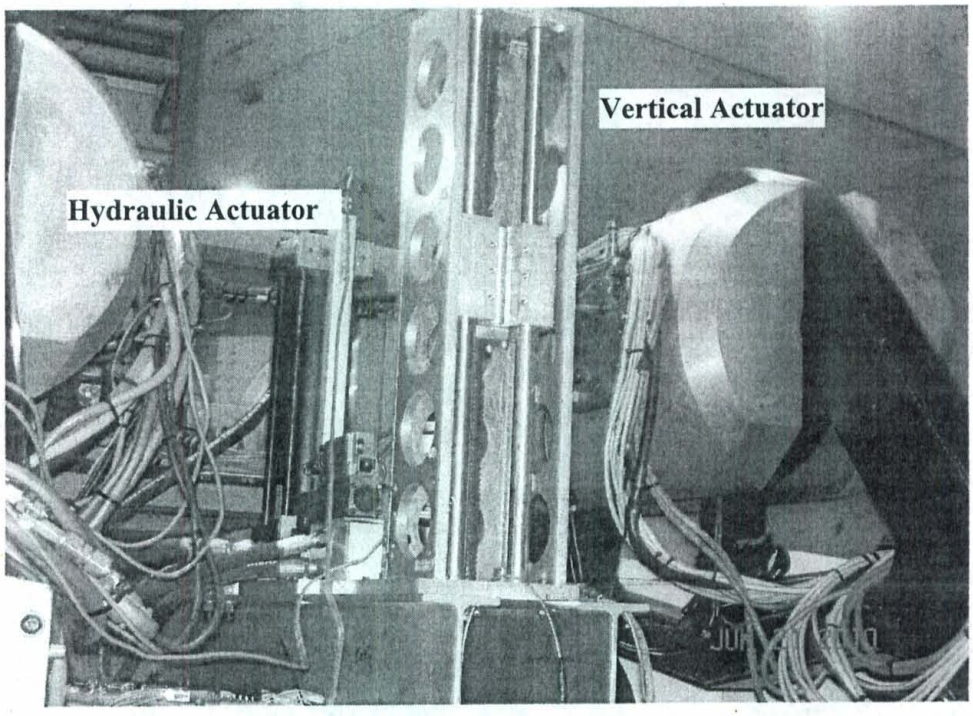

Figure (3.15) Vertical Actuator Loaded on the Centrifuge

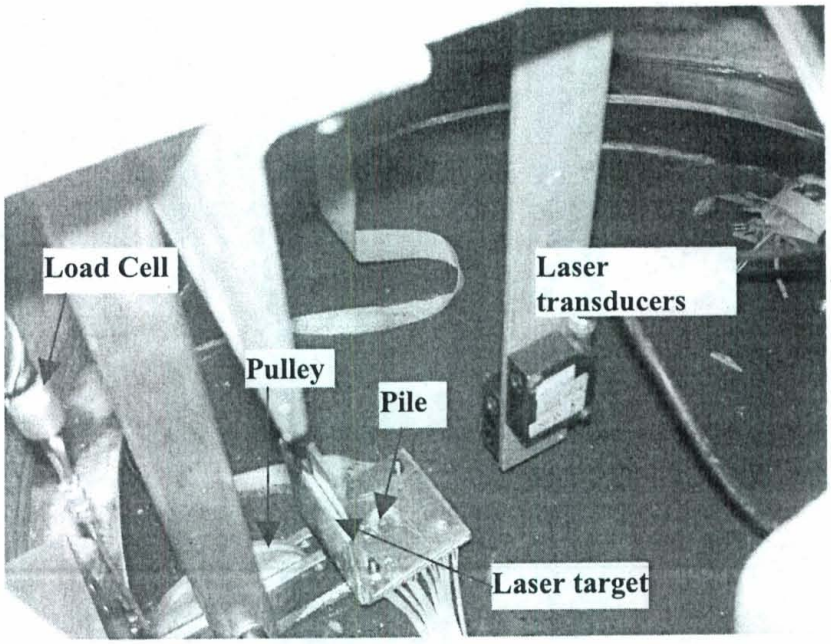

Figure (3.16) Loading System Setup

Chapter 4

In-Flight Soil Properties

4.1. Introduction:

In this chapter, Soil properties have been measured in-flight during the centrifuge test. Shear wave velocity was measured using piezoelectric transducers at three depths. The measurements were carried out in two flights to check the effect of loading-unloading of the stiffness of soil model in centrifuge. In the second flight, the measurements were carried out before and during pile installation in-flight. The results support the friction fatigue phenomenon.

4.2. Shear wave velocity measurement

Shear wave velocity (V_s) measurement has received high attention over the last few decades. It has a direct relationship to the maximum shear modulus (G_{max}) as:

$$V_s = \sqrt{\frac{G_{max}}{\rho}} \tag{4.1}$$

where $\rho = \gamma/g$ = total mass density, γ = soil unit weight, and g = 9.8 m/s^2 =gravitational constant. The modulus G_{max} is a fundamental stiffness of all solids in civil engineering and can be measured in all soil types. Interestingly, G_{max} applies to drained and undrained soil behavior, because at small strains (less than 10^{-5} %), porewater pressures have not yet been generated. The measurement of G_{max} profile has an important effect in geotechnical engineering design. In addition to the maximum shear modulus, the knowledge of Vs provides a crucial information about the the engineering properties of geomaterials in terms of stress state, layering and other digenesis such as inclusions and cementation (Stokoe and Santamarina 2000).

The use of geophysical techniques to measure in-situ soil properties has been widely used. The shear wave velocity can be measured in conventional cased boreholes using the crosshole test (CHT), downhole test (DHT), and surface refraction (SR) and reflection methods are some of the geophysical methods being used in in-situ geotechnical investigation. In these methods, in general, an impulse source generates shear or compression wave that propagates in the soil media and being received by other receivers. By knowing the distance between the source and the receiver and calculating the travel time of the propagated wave in the soil media the shear or compression wave can be obtained.

$$V_s = L/t \tag{4.2}$$

where L is the distance between the source and the receiver and t is the travel time. Doing these tests at multiple locations or using multiple receivers the shear or compression wave profile can be obtained.

To simulate in-situ geophysical techniques methods in laboratory and small scale model tests, Shirley et al. (1978) specifically developed the bender elements, as will be discussed latter, to measure V_s and shear attenuation in sediments. In centrifuge tests, Gohl and Finn (1987) were the first to use bender elements to generate and receive shear waves. The transmitter bender element was pushed tip into the soil surface. The receiver bender elements were arranged vertically pointing upward towards the transmitter bender element. Despite the success of this test, two issues were reported by Ismail and Hourani (2003). The first issue was that the layout of the bender elements implies isotropic material, as the shear wave velocity will only be measured in the vertical plane. Secondly, the vertical layout of the bender elements results in the measured shear wave velocity being an average over the depth between the source and the receiver. This has significant effect, as the velocity may vary significantly, according to the stress state, density and other geological features. Another study has been conducted by Kita et al. (1992). They used a piezoelectric

oscillator to generate a seismic shear wave in a sand model in the centrifuge. The propagated shear wave was detected by an accelerometer of a piezoelectric type. Another method to generate and detect shear wave in centrifuge was carried out by Arulnathan et al. (2000) and Zhao et. al. (2006). They used a mini air-hammer to generate shear waves which were received by accelerometers. Ismail and Hourani (2003) developed an innovative system to enable multi-directional measurement of shear waves in a dry dense sand model in the centrifuge. The system allowed the shear waves to propagate in a horizontal direction, with polarization in either a horizontal and vertical direction for each test setup. Fu et al. (2004) measured the shear wave velocity using a series of three pairs (transmitter and receiver) of bender elements in a sand sample during centrifuge experiments, as shown in Fig. (4.1). They showed a good agreement between the measured shear wave velocity in the centrifuge and the results of resonant column tests carried out on the same sand with the same density. Rammah et al. (2006) developed a high resolution seismic tomography (ST) technique of bender elements that can be used to image the variation of soil stiffness for different soil models in centrifuge. The system consisted of 26 transmitters in the left-hand vertical array, and 51 receivers, 26 in the right-hand vertical array and 25 in the base array as shown in Fig. 4.2.

Although the bender element transducer is an intelligent tool to measure soil properties, it has some difficulties in using at noisy environment as centrifuge tests as will be discussed latter.

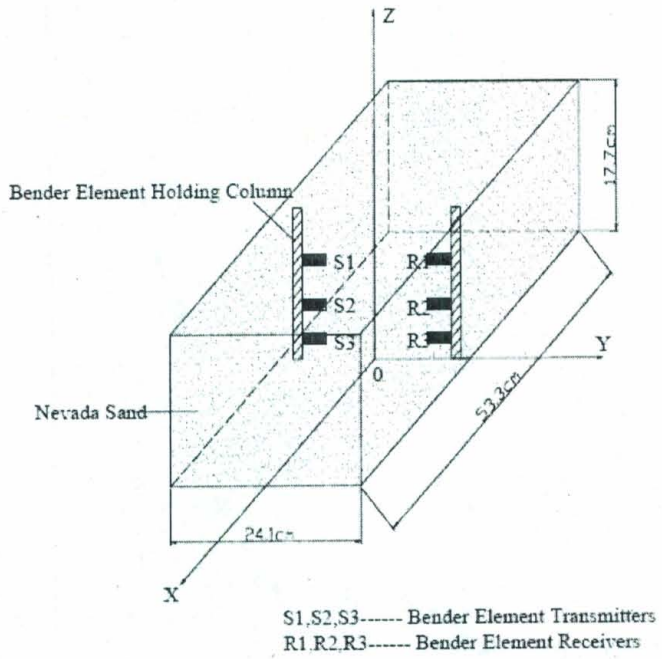

Fig. (4.1) Bender Elements in Soil Model After Fu (2004)

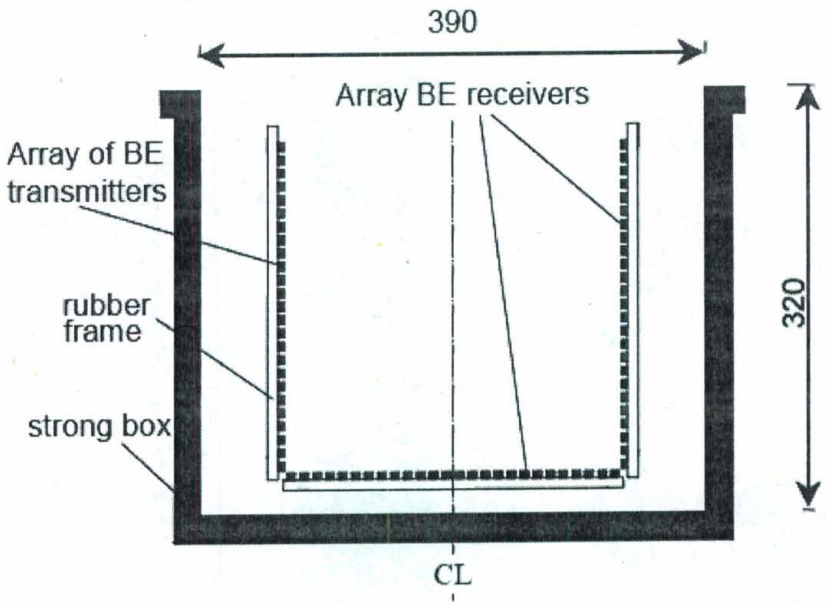

Fig. (4.2) Bender Elements Arrangement in Soil Model After Rammah et al. (2006)

4.3. Bender Elements

A bender element takes the form of a thin plate. It is made from piezoelectric materials which are capable of converting mechanical vibration into electrical energy and vice versa. The element itself consists of two thin piezoelectric plates that are rigidly bonded together with conducting surfaces between them and on the outside, as shown in the detail of Fig. (4.3). One end of the bender element is usually fixed and the other end is free so the bender element protrudes as a cantilever of a certain length. When a voltage change is applied to the transmitting element one plate elongates and the other one shortens which causes the element to bend. This mechanism is used in the bender element transmitter which in turn propagates a shear wave through the sample. When this wave reaches a receiving element, at the opposite end of the sample, it causes the element to bend and thus generates a change in voltage, which can be measured to determine the wave arrival time.

There are two types of bender elements connections; series and parallel connections. The element arranged in series as shown in Fig. (4.4b) can generate a total output voltage two times the voltage generated by an element arranged in parallel. For this reason, series connection is recommended for receiver bender elements. On the other hand, for the same motion, an element arranged for parallel operation, Fig. (4.4c), needs only half the voltage required for series operation. An applied electrical field causes maximum deformation, making this arrangement suitable for a transmitter.

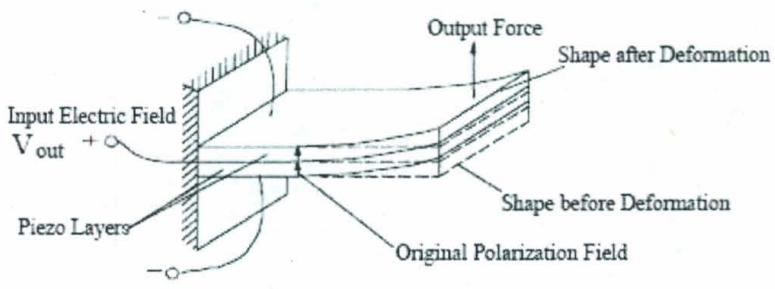

Fig. (4.3) 2-Layer Bender Element Poled for Parallel Operation

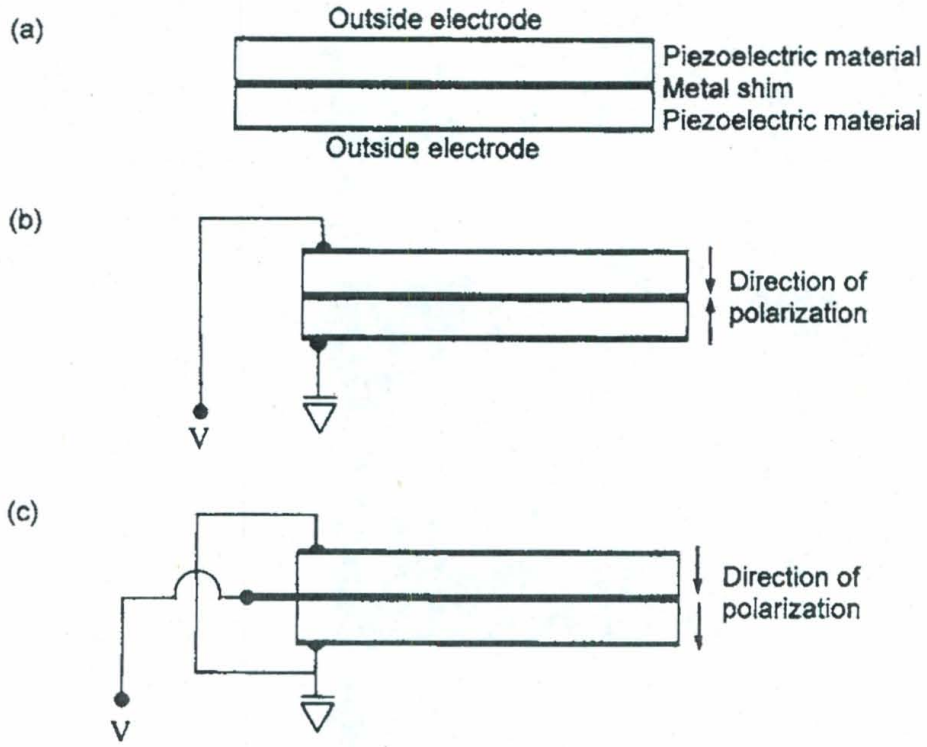

Figure (4.4) Bender Elements: (a) schematic representation of bender element, (b) series type, and (c) parallel type, (After Lee and Santamarina 2005)

4.4. Experiment Setup

In previous studies, bender elements have been mounted to rigid frames embedded in the soil as Fu et al. 2004, Lee and Santamarina (2005), and Rammah et. al. (2006). Use of free benders will minimize boundary effects and avoided disturbance of the model that may be caused by an embedded mounting frame or relatively heavy mounting blocks. In the following sections, the details of the system components and bender elements preparation will be discussed.

4.4.1 *System Components:*

Three bender element transmitters and three bender element receivers were used as shown in Fig. (4.5). They are located at three different depths; 110 mm, 160 mm, and 220 mm. The distance, L_{tt}, (tip to tip) between the transmitting and receiving elements at each depth level is 70 mm as shown in Fig. (4.6). A one cycle sine wave was used as triggering signals in the test using an Agilent E1434 signal generator card located on the slip ring. The input power was amplified ± 90 volts using a designed amplification unit located in the centrifuge basket. Maximizing the amplitude of the elastic waves was desired to maximize the signal to noise ratio and to improve the ability to record the waves over large distances, S. Brandenberg et. al. (2008). A multiple switch was used to switch between the three transmitter bender elements from the control room. The traveled signals in the soil were received on the other three receiver bender elements. The received signals were amplified 100 times using a signal conditioning box. The amplified received signals were recorded on 8 channel CompuScope high speed data acquisition system (125 MS/s per channel). The data acquisition software (GageScope Professional) allowed doing several features. The recorded signals were averaged with a factor of 256. Figures (4.7) and (4.8) shows the recorded signal before and after averaging. Signal averaging is an effective method to obtain clear signals in the presence of noise. The process of signal averaging consists of measuring the output signal multiple times and averaging the signal voltage at the corresponding time record. The assumption in this process is that the noise has zero mean. Therefore, adding the values of the multiple arrays of averaged signals at a discrete time would cancel the random noise component and improve the amplitude of the correlated component. Figure (4.6) shows the location of the components of the system on the centrifuge.

4.4.2 *Bender Elements Preparation:*

In the current study, bender element types Q220-A4-203YB are supplied by Piezo System Inc. with dimensions (28.6 L x 6.3 W x 0.66 T mm). The bender elements

were supplied with tinny wires connected to the bender layers in a parallel connection. The tiny wires had been connected to a well shielded coaxial cable. The connection between the bender element and the coaxial cable was covered by a heat shrink tube. After wiring, the bender elements were coated to be protected against water. The following procedures were used to produce water-proof bender elements as suggested by Fu (2004):

1) Prepare the sensors' surface by making them clean and dry;
2) Apply epoxy evenly on the surfaces of the sensors;
3) After about 8 hours, add another layer of the epoxy onto the sensors;
4) Coat the sensors with a layer of plastic dip. It was found that using this layer is very important. Without this layer the epoxy layer was removed if left for a long time in saturated soil.

The sensors treated by the above procedures worked well in the saturated sand model tests.

To have the bender element as a cantilever, a good fixed condition to one end should be provided. This has been achieved by using a mould of steel greased from inside. The bender element was hanged in the mould with a specified cantilever length. The mould was filled with epoxy. After 8 hours when the epoxy reached its full strength, the mould was removed. After this another layer of plastic dip was applied. The final shape of the bender element is shown in Fig. (4.6).

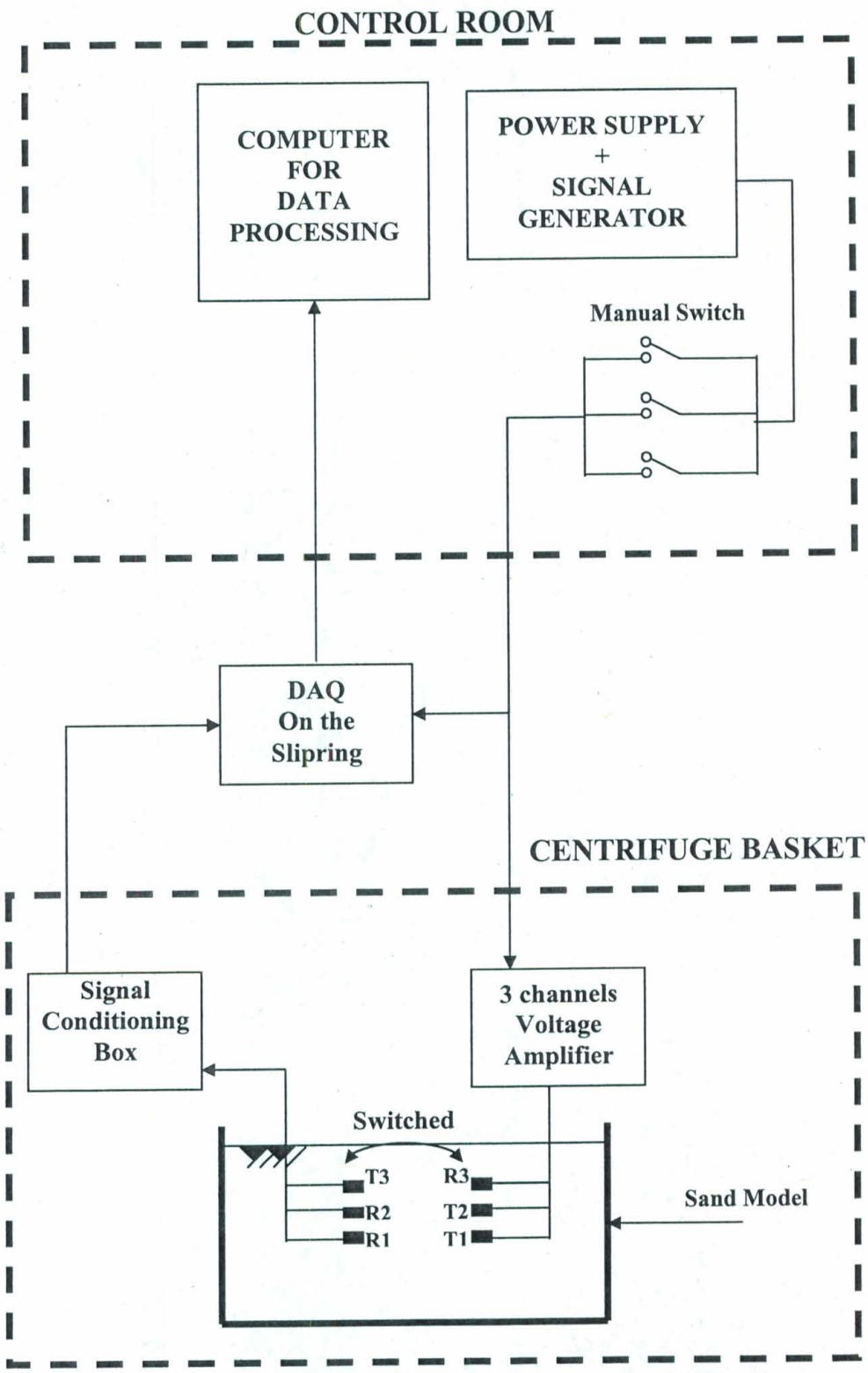

Figure (4.5) Shear wave measurement system components on the centrifuge

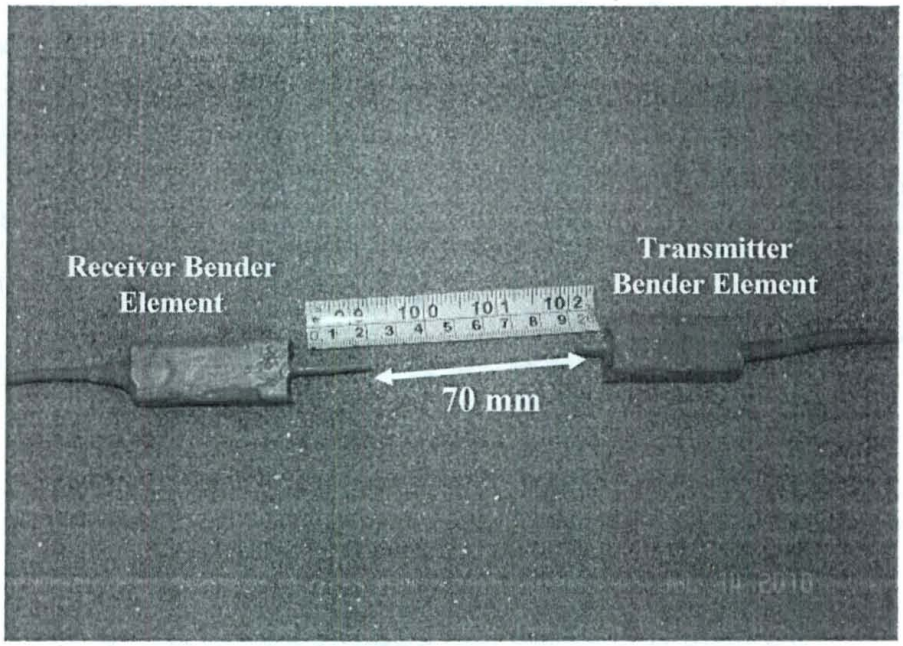

Figure (4.6) Bender Elements Prepared for the Tests

4.4.3 *Bender Elements Length Selection:*

As mentioned before, a bender element in series connection generates a total output voltage two times the voltage generated by an element arranged in parallel. To use the bender element in parallel connection as a receiver, it was decided to have the receiver bender element cantilever length twice the transmitter one based on the following equation to calculate the output voltage:

$$V_0 = \frac{3}{4} g_{31} \left(\frac{F l_b}{WT} \right) \left(1 - \frac{t_s^2}{T^2} \right) K \qquad (4.3)$$

where g_{31} is the piezoelectric voltage constant, F is the applied force, l_b is the cantilever length of the bender element, W is the width of the bender element, T is the thickness of the bender element, t_s is the thickness of the center shim ($t<<T$), and K is an empirical weighting factor (>>1).

The transmitter bender element cantilever length was selected based on the analytical solution given by Lee and Santamarina (2005). They gave a solution to calculate the

resonant frequency, f_r, of a bender element in air and soil. Based on this solution and the current soil properties it was found the 10 mm cantilever length is long enough to provide good coupling with the soil. Also, it provides a wave length, λ, of around 20 mm ($\lambda = V_s / f_r$) which eliminate the near field effect. It is recommended by that near field effect can be eliminated if the ratio (L_{tt}/ λ) is greater than 2. In the current tests this ratio is about 3.5 which is enough to eliminate this effect as will be seen later.

4.4.4 *Test Procedures:*

Many trials had been carried out to have the bender elements working in saturated sand. After that, two tests were carried out on the same sand package. The first test was to check that all the system components are working. In the second test, shear wave velocity was measured again before and during in-flight pile installation. Unfortunately, we could not record all the signals from all the bender elements during pile installation. During pile jacking, soil stresses at pile tip increased to high level that caused the amplitude of the received signal to increase. As the received signal was amplified, the signal saturated. However, the recorded signals from the successful bender elements were useful to give an idea about the change in soil stiffness during pile installation.

In the tests carried out before the pile installation, shear wave velocity was measured at 10g increments during centrifuge spinning up (i.e. 1g, 10g, 20g, 30g, 40g, 50g). In the first test the frequency of the input sine wave was changed to check the received signal resolution. In the other tests, frequency of 5 kHz was used.

In the test carried out during pile installation, the pile was installed at 50 mm increments. At each increment, shear wave velocity was measured.

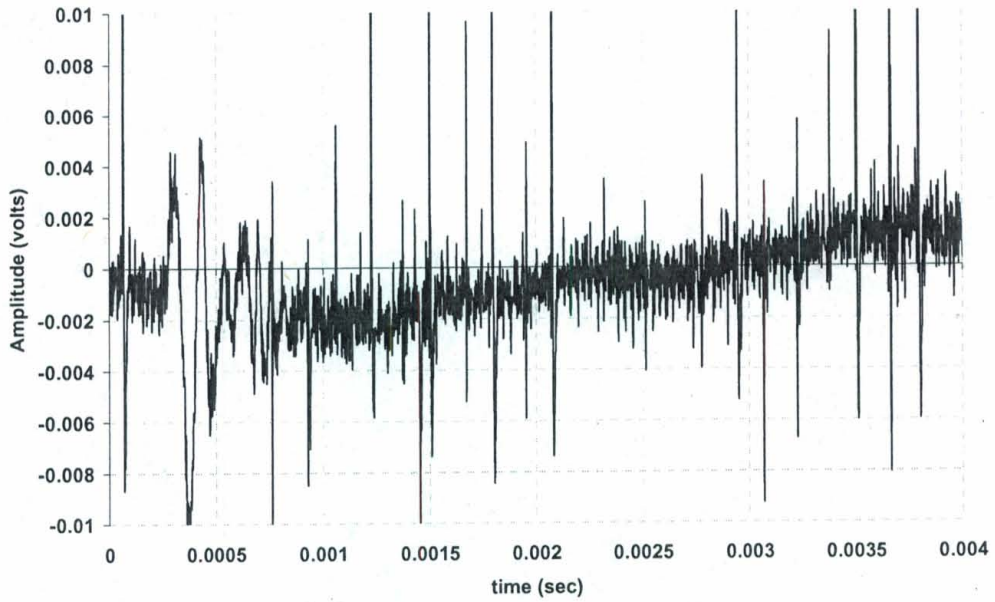

Figure (4.7) Received Signal without Averaging

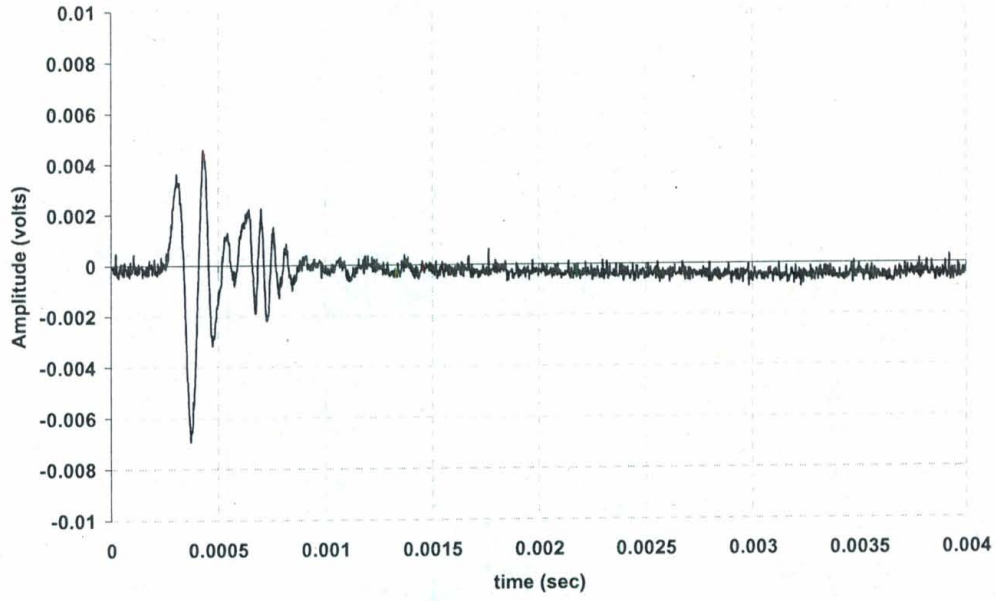

Figure (4.8) Received Signal after Averaging

4.5. Experiment Results

In the following sections we will first discuss the shear wave velocity (V_S) measurements in both tests. Then the results of the shear wave measurements during pile installation will be discussed. It should be noted that the amplitude of the input signal is 100 times the one shown in all figures for presentation needs only.

4.5.1 *Tests before Pile Installation:*

The input signal frequency effect was examined in the first test. Figure (4.9) shows the received signals after averaging at the receiver bender element (R1) from the transmitter bender element (T1) at 50g. It can be seen that only the input signal of frequency 10 kHz gives a less clean received signal. In all cases the first arrival can easily be picked as shown in Fig. (4.9).

Figure (4.10) shows the received signals at the receiver bender element (R1) from the transmitter bender element (T1) at 10g increments during centrifuge spinning up. As the g-level increases the arrival time decreases and the signal amplitude increases. The first arrivals are indicated by the arrows. Table (4.1) shows the measured shear wave velocity (V_S) in both tests.

Figures (4.11) and (4.12) show the relationship between the measured V_S and vertical effective stresses at the bender elements levels in the first and second tests, respectively. The measured shear wave velocities increase with increasing the vertical effective stresses. However, the measured values in the first test are lower than those in the second test. Figures (4.13) to (4.15) show the difference between both tests. It can be seen also that shear wave velocity (V_S) and maximum shear modulus (G_{max}) increases with depth as shown in Figs. (4.16) and (4.17). The same trend can be observed in both tests. In the first test, as the centrifuge acceleration increases the soil consolidates. The effect of this change is clear at shallow depths and decreases at deep depths.

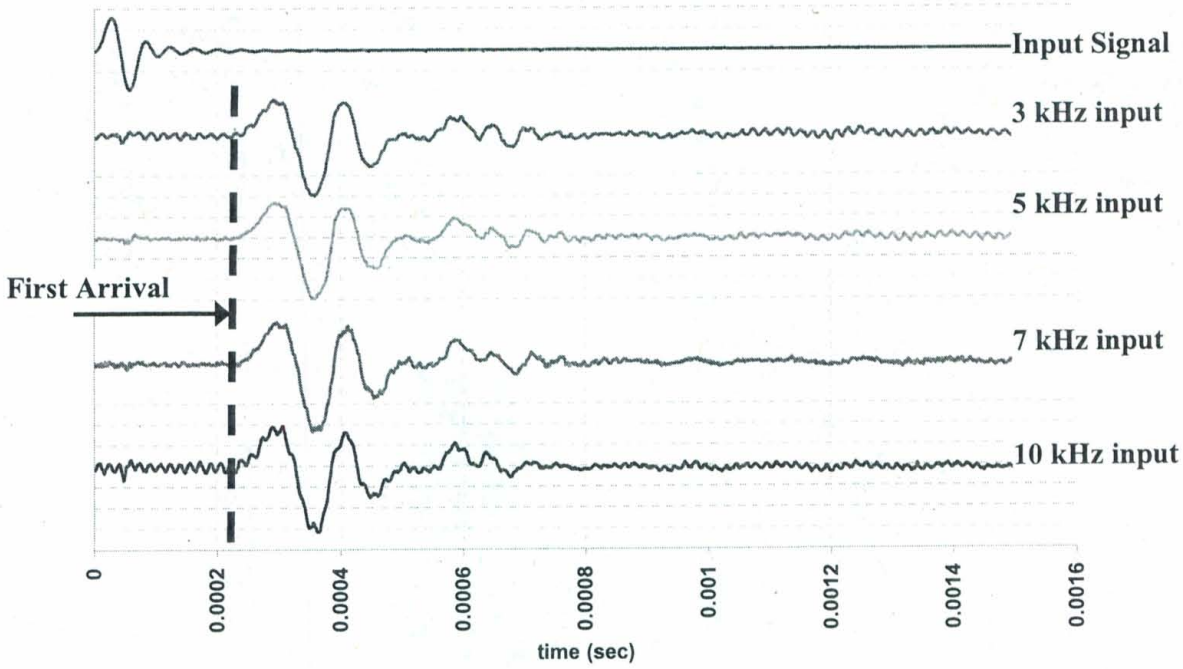

Figure (4.9) Received Signal (T1-R1) at different input signal frequencies- 50g test

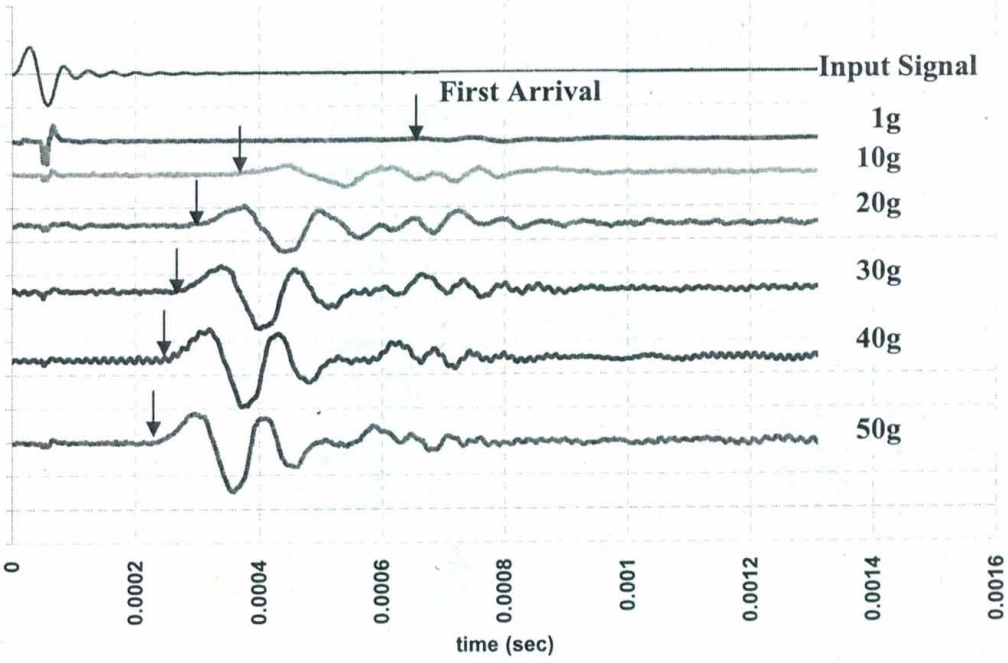

Figure (4.10) Received Signals (T1-R1) at different centrifuge accelerations- 5 kHz

This can be observed in Figs. (4.11), where shear wave velocity (V_S) increases with increasing the depth. However, as shown in Fig. (4.12), all the three curves are very close and can be joined as one curve. A reason for the difference between both tests could be the sample preparation method. The sand model was prepared by dry pluviation method by raining the sand from constant height. Although the density cubs used to check the density in the model showed a difference of only 4% in the relative density between the bottom of the model and the sand surface, this difference could be a reason for this increase in the shear wave velocities. Another reason also could be a little disturbance in the sand during saturation process although this process was conducted very slowly. Fu (2004) observed similar behavior with loose and medium sand models during centrifuge spin-up and spin-down. He observed an increase in soil stiffness after experiencing a high stress at 50g. He concluded that this likely due to the lock up of horizontal effective stresses as a result of the plastic deformation of the soil, a commonly encountered soil behavior during a loading and unloading cycle.

Figure (4.18) shows the relationship between maximum shear modulus (G_{max}) and vertical effective stresses for both tests. The plotted data are for all measurements during centrifuge spin-up from 1g to 50g. It can be seen that the values of the first test are scattered. In the first test, the measurements at each depth follow one function different from other depths. The maximum shear modulus (G_{max}) is getting higher by increasing depth and g-level. However, in the second test, all data follow a unique relationship. The data of the second test were fitted as:

$$G_{max} = 18591 \cdot \sigma_v'^{0.477} \qquad (4.4)$$

where σ_v' is the vertical effective stresses. To have Eq. (4.4) as a function of mean stresses, the lateral earth pressure coefficient (K_o) should be calculated. Cone Penetration Test (CPT) was carried out in the same test package. The cone resistance (q_c) was correlated with available correlation method by Mayne (2001) to calculate peak friction angle of sand (φ'). The calculated φ' was used to calculate the Over

Table (4.1) The Measured Shear Wave Velocity Values in (m/sec.)

Bender Element #	G-Level	Test #1	Test #2
T1 – R1	1g	114.75	113.64
	10g	210.84	203.49
	20g	233.33	236.49
	30g	253.62	259.26
	40g	271.32	284.55
	50g	289.26	291.67
T2 – R2	1g	105.92	105.91
	10g	174.06	183.74
	20g	203.18	218.04
	30g	220.78	239
	40g	235.91	257.16
	50g	247.52	271.17
T3 – R3	1g	95.08	99.15
	10g	148.70	177.67
	20g	170.86	209.58
	30g	184.08	222.93
	40g	195.35	237.29
	50g	203.94	246.48

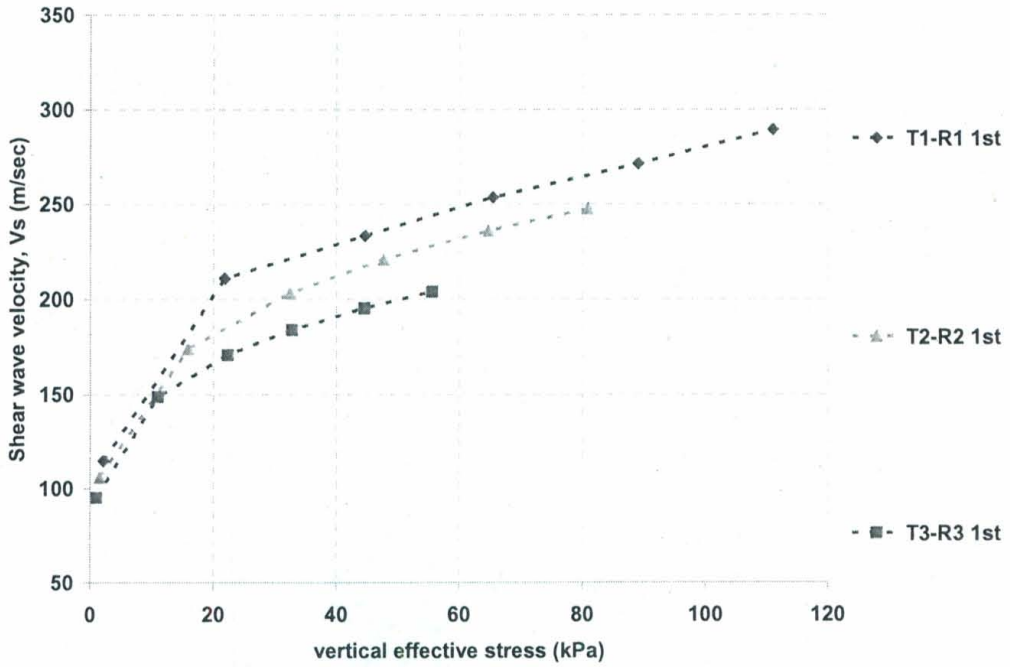

Figure (4.11) Relationship between V_S and vertical effective stress in the first test

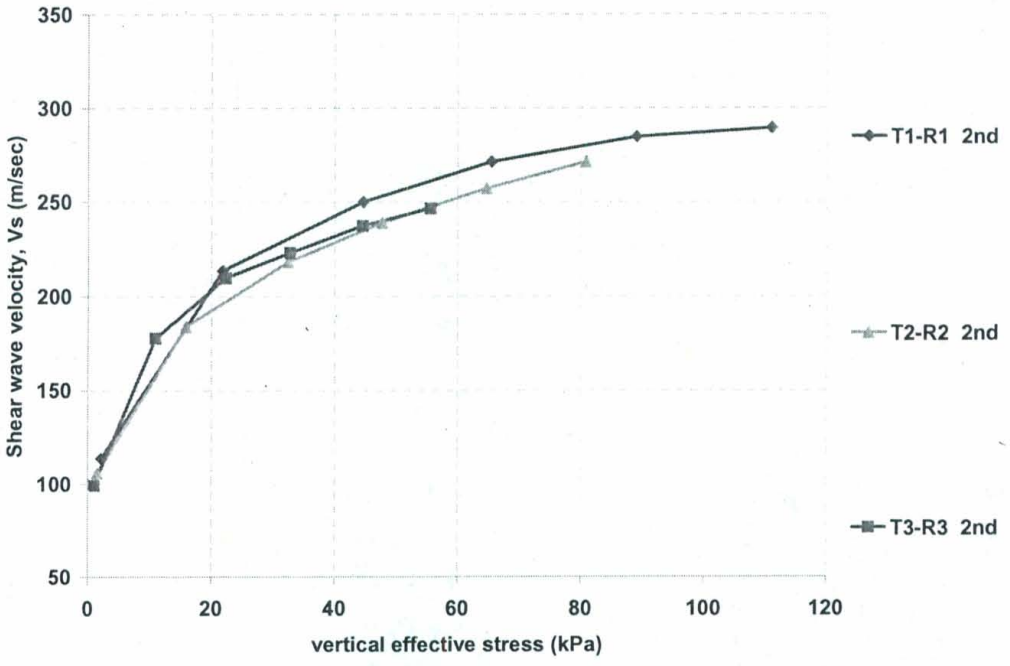

Figure (4.12) Relationship between V_S and vertical effective stress in the second test

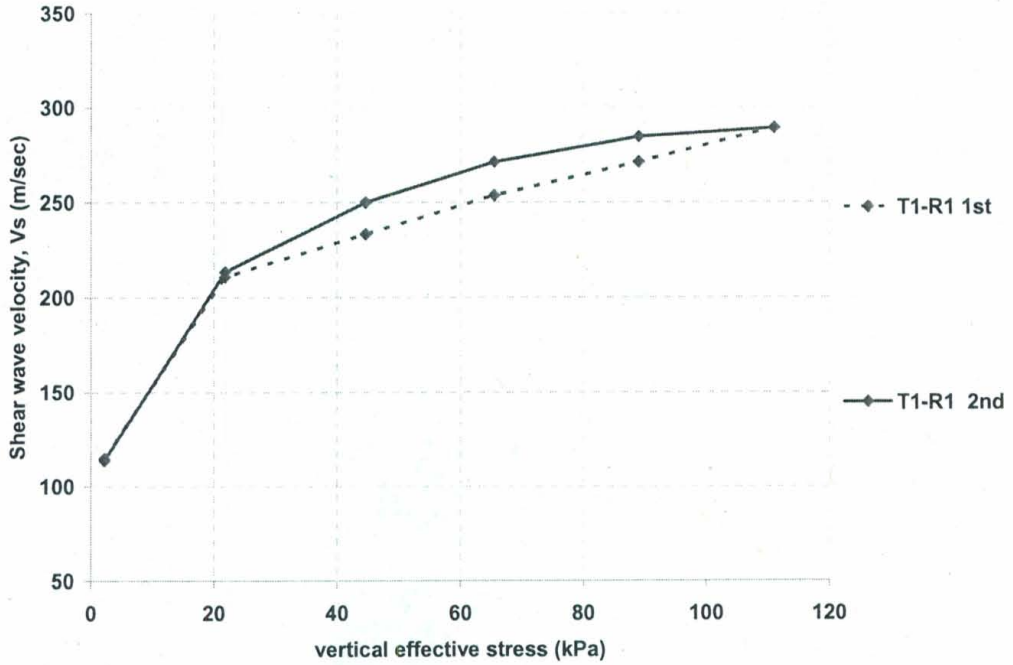

Figure (4.13) Relationship between V_S and vertical effective stress between T1 – R1 in both tests

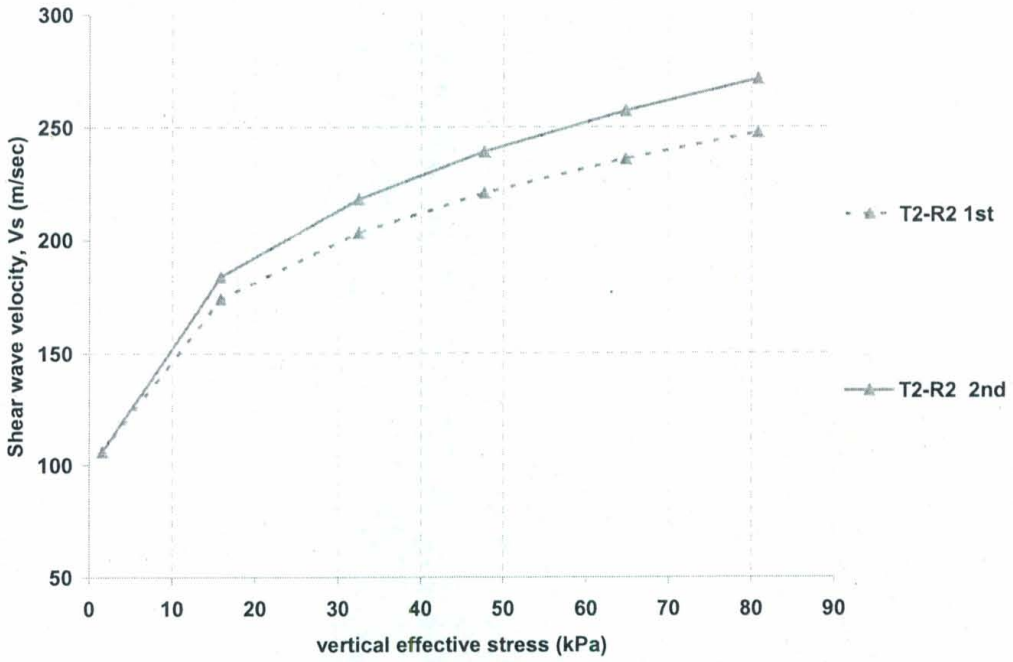

Figure (4.14) Relationship between V_S and vertical effective stress between T2 – R2 in both tests

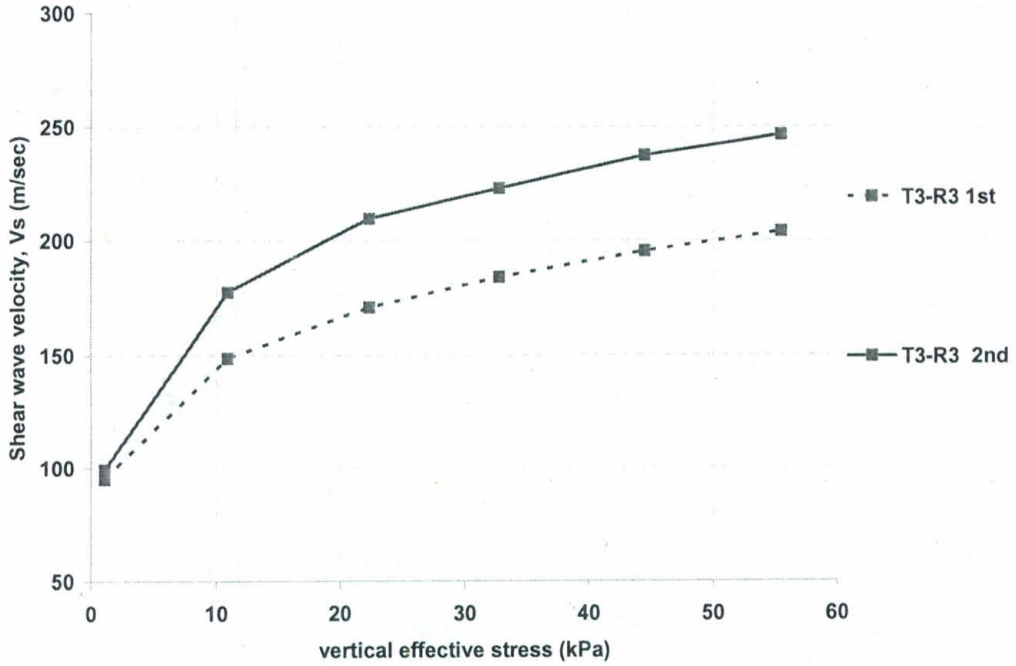

Figure (4.15) Relationship between V_S and vertical effective stress between T3 – R3 in both tests

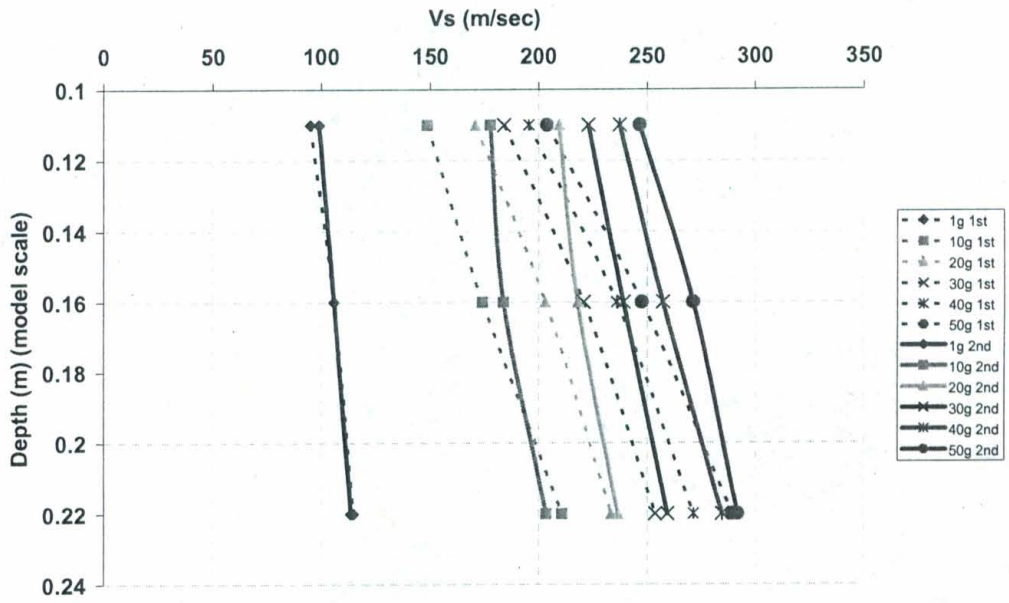

Figure (4.16) Shear wave velocity (V_S) profile at different g-level in both tests

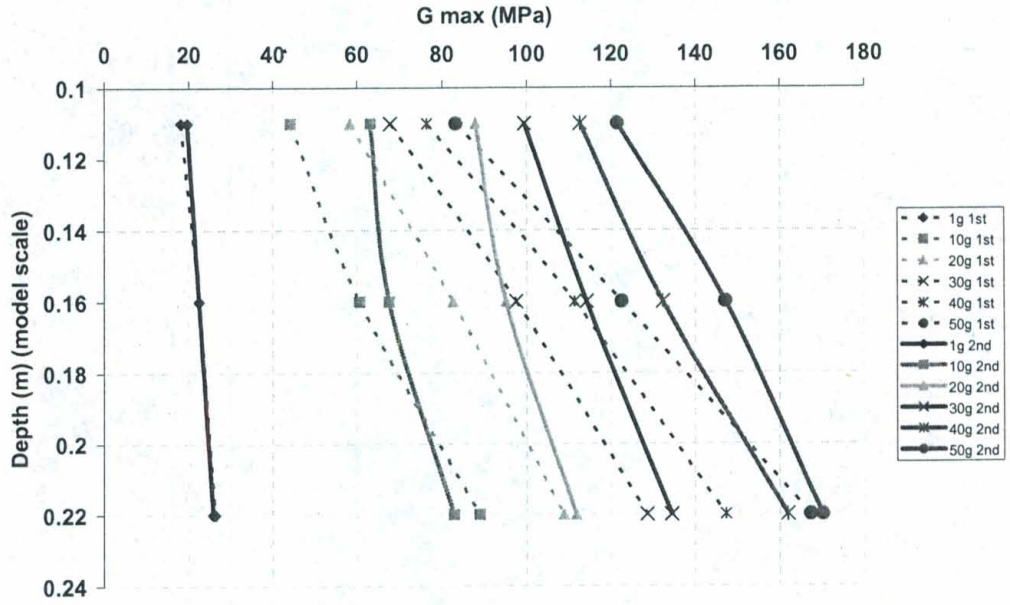

Figure (4.17) Maximum shear modulus (G_{max}) profile at different g-level in both tests

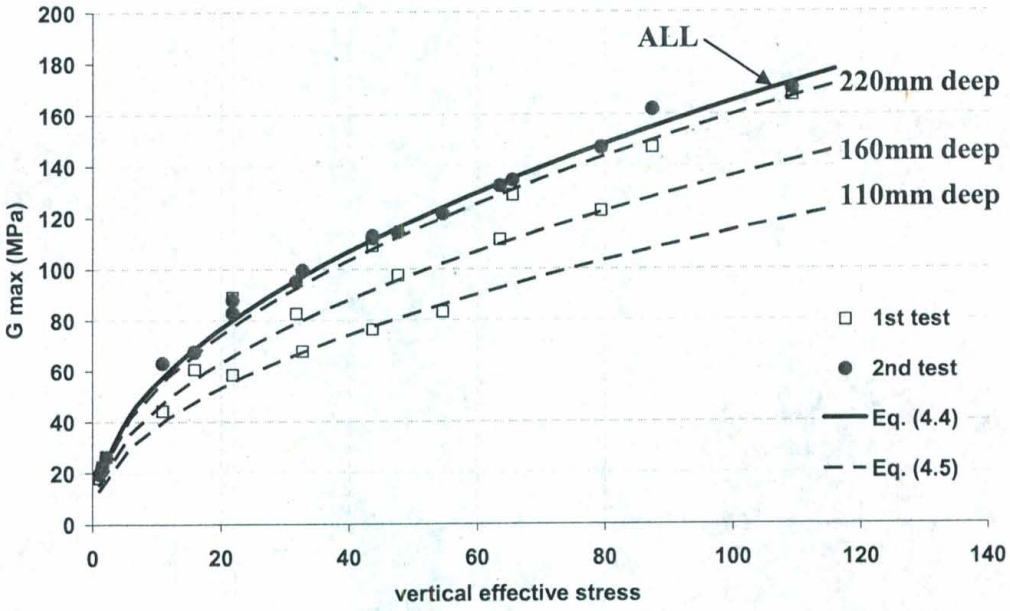

Figure (4.18) Change of maximum shear modulus (G_{max}) with vertical effective stress in both tests

Consolidation Ratio (OCR) and K_o. It was found that the sand has an average K_o value of 1. Using this value of K_o Eq. (4.4) can be rewritten as:

$$G_{\max} = 1670 \cdot P_a \cdot \left(\frac{P_o'}{P_a} \right)^{0.477} \tag{4.5}$$

where P_a is the atmospheric pressure (100 kPa), and P_o is the mean effective stress ($P_o = \sigma_v'(1+2K_o)/3$).

Equation (4.5) is used to calculate $G_{\max}$ at different values of K_o as shown in Fig. (4.18). It was found that K_o values of 0.2, 0.5 and 0.9 fit the experimental data of the first test at depths of 110mm, 160mm, and 220mm, respectively. Also K_o value of 1 fits well with the experimental data of the second test. Figures (4.19) and (4.20) show a comparison between Eq. (4.5) and the experimental data of the first and second tests, respectively. It can be seen that the equation results fit well for both tests. For the first test, K_o values of 0.2, 0.5, and 0.9 are used at top, middle, and bottom levels, respectively. However, for the second test a constant value of 1 is used. This means that K_o changes from 0.2 at shallow depth to 0.9 deeper depth in the first test. As the soil consolidates, the horizontal effective stresses increase as a result of the loading un-loading process. The soil becomes more uniform in the second flight and K_o value becomes almost constant along depth. It should be noted that this overconsolidation happened after the first flight. However, as the sand is very dense of about 86% relative density, the subsequent flights will not have much effect on the sand properties.

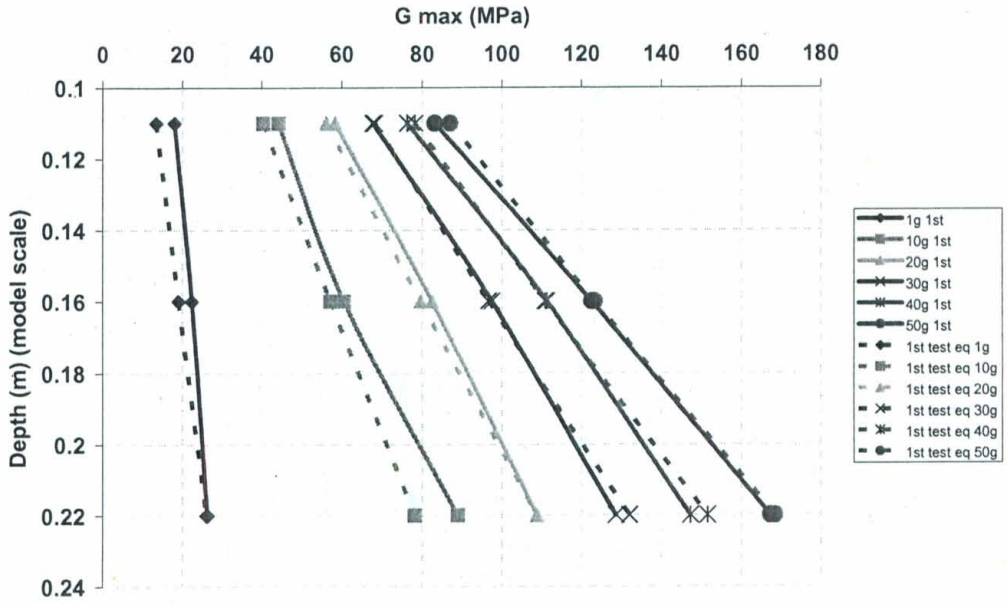

Figure (4.19) Maximum shear modulus (G_{max}) profile from experimental results and predicted by Eq. (4.5) - The first test

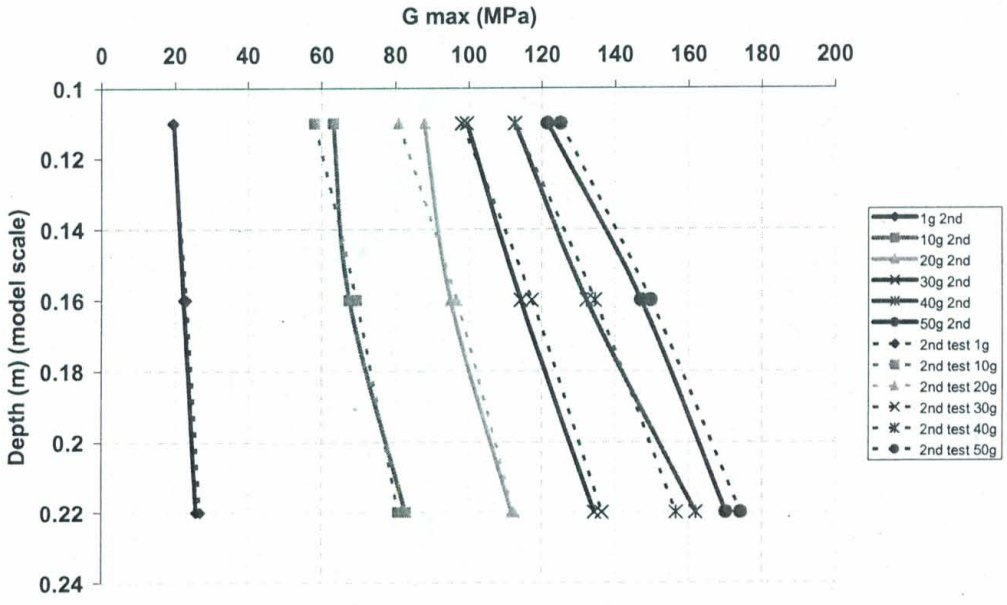

Figure (4.20) Maximum shear modulus (G_{max}) profile from experimental results and predicted by Eq. (4.5) - The second test

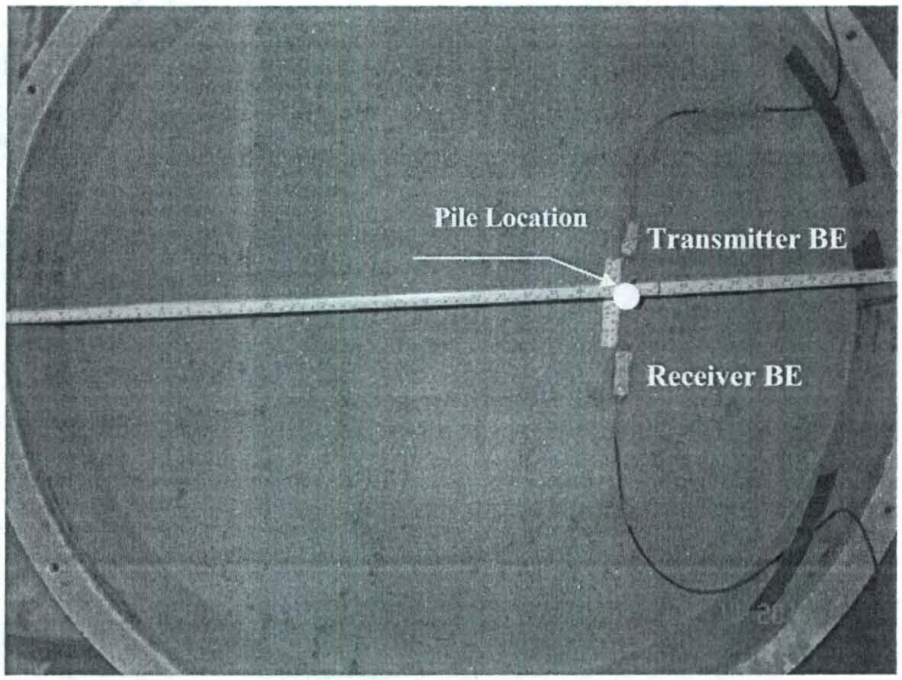

Figure (4.21) Bender Element Location in the test package

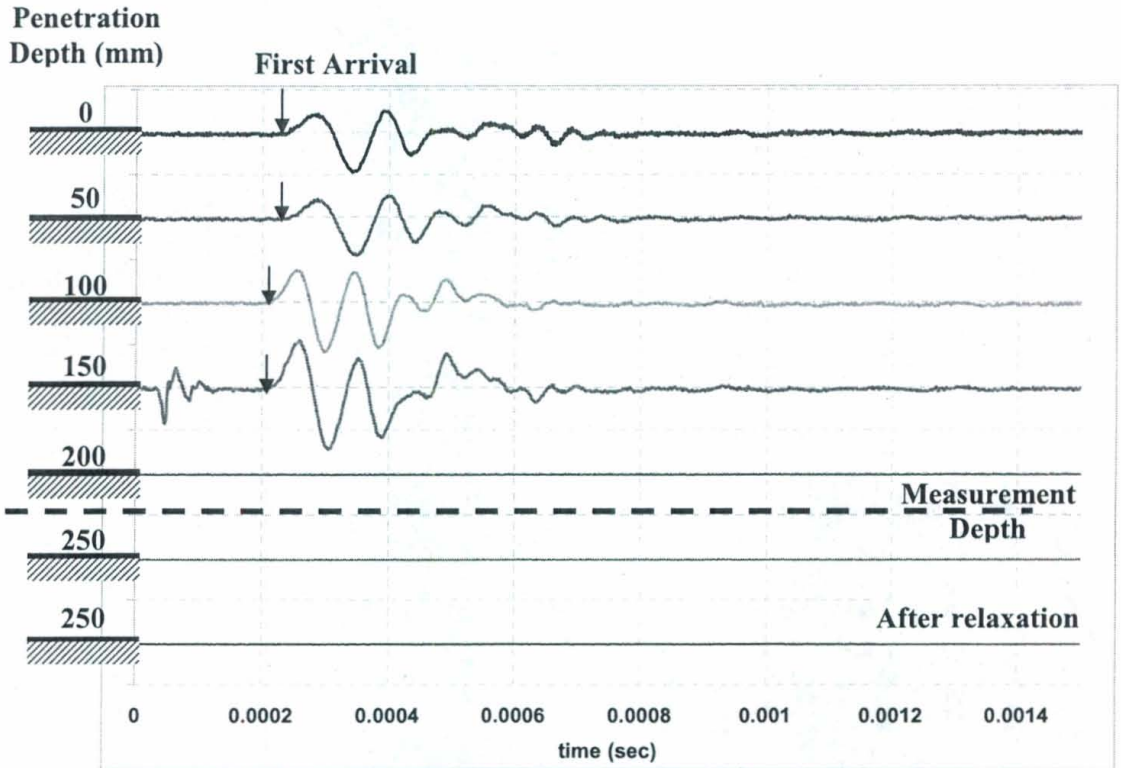

Figure (4.22) Received Signal (T1-R1) during pile installation at 50g

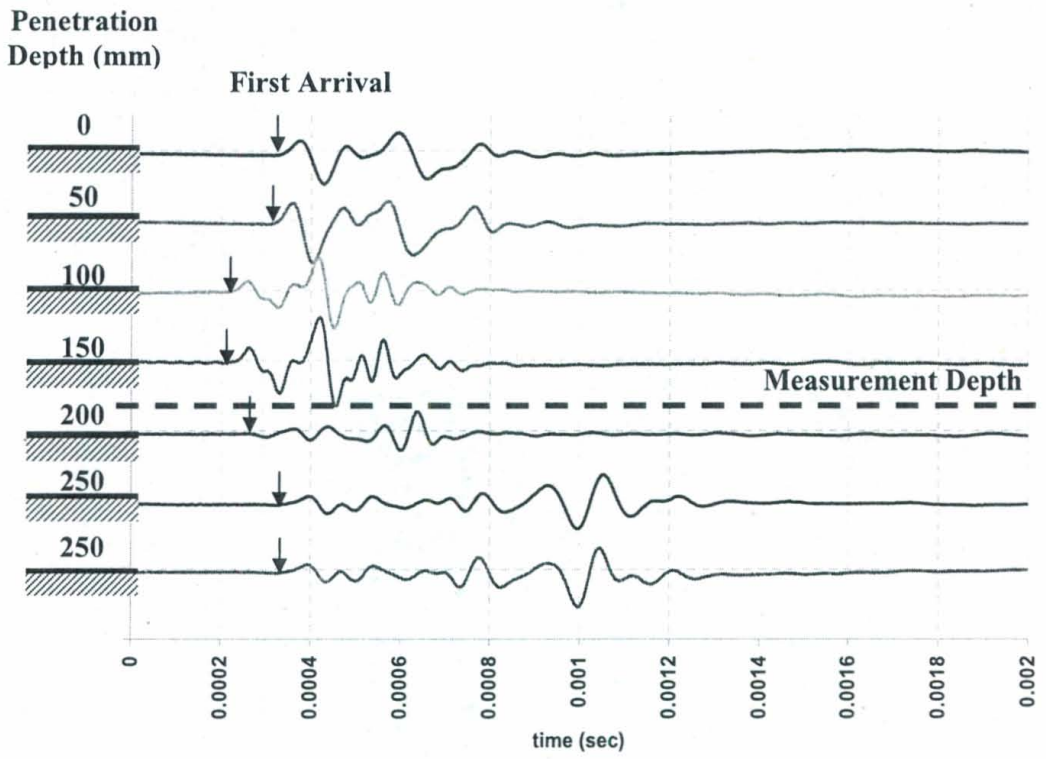

Figure (4.23) Received Signal (T1-R2) during pile installation at 50g

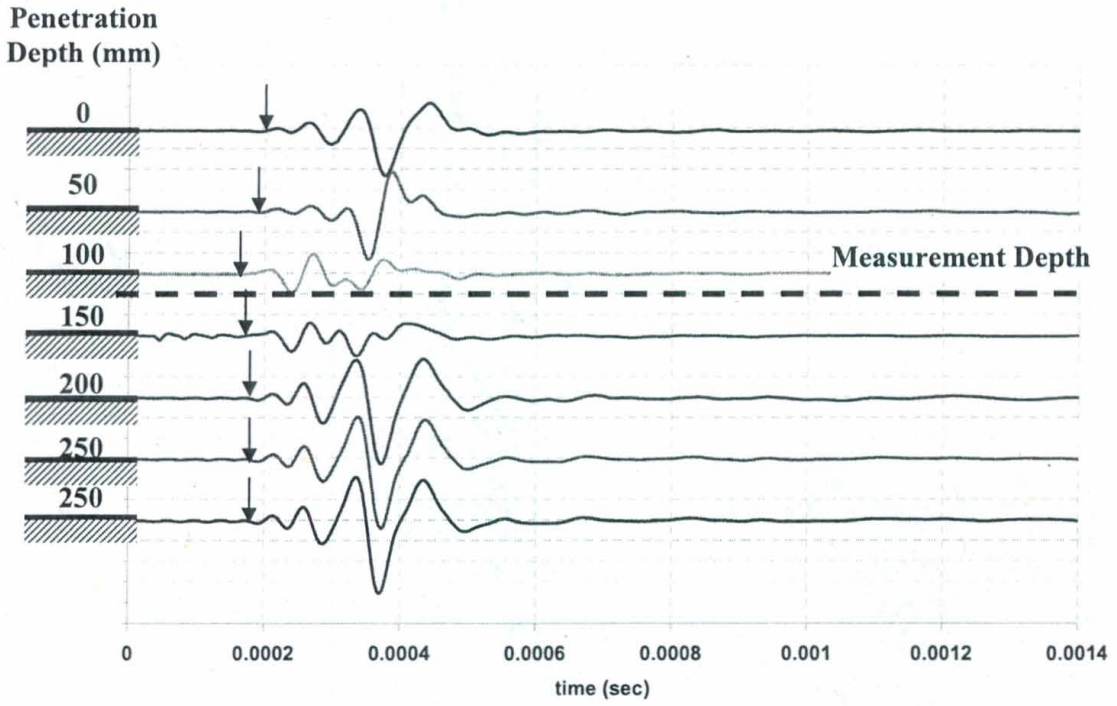

Figure (4.24) Received Signal (T3-R2) during pile installation at 50g

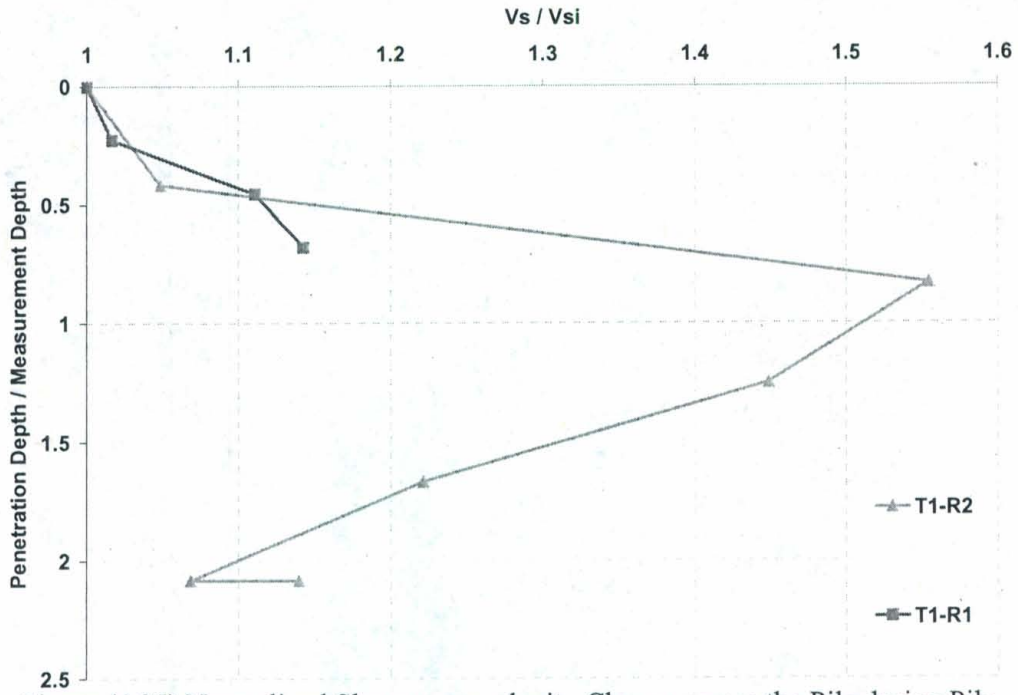

Figure (4.25) Normalized Shear wave velocity Change across the Pile during Pile Installation at 50g

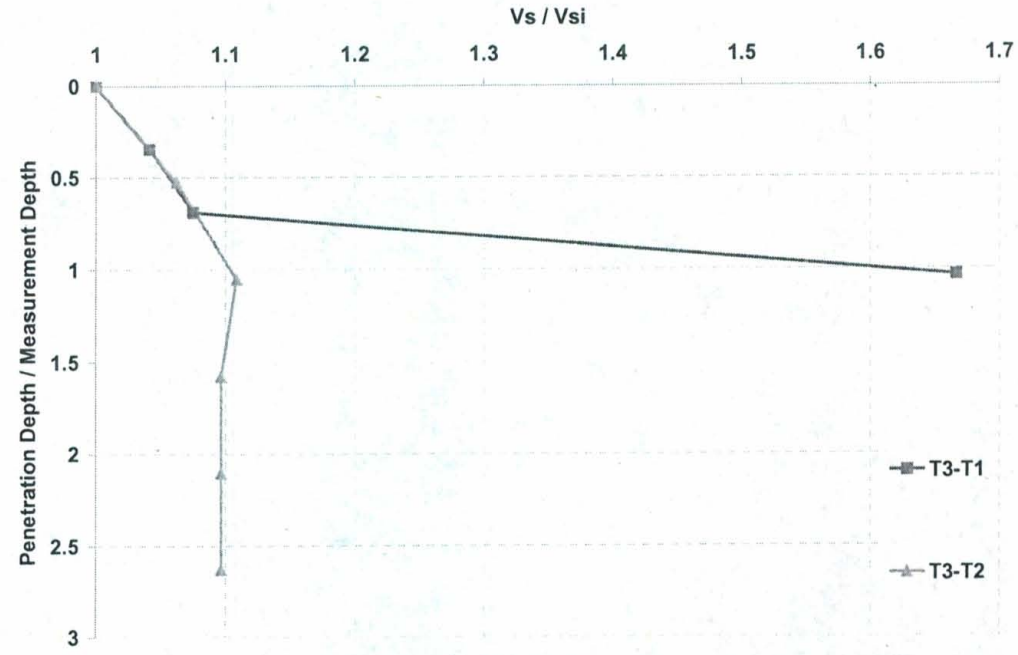

Figure (4.26) Normalized Shear wave velocity Change adjacent to the Pile during Pile Installation at 50g

4.5.2 *Tests during Pile Installation:*

In this test, we faced some problems due to the high stresses developed during pile jacking. We could not record any signal from both the receiver bender elements (R3 and R1) when the pile tip reached a level close to these bender elements. Only receiver bender element R2 worked well along the test. The presented results will only be for T1 – R1 and T3 – R1 (up to penetration depth of 150 mm), and T1 – R2 and T3 – R2 (full penetration depth of 250 mm). The bender elements were excited every 50 mm pile penetration depth up to 250 mm. Both the transmitter and receiver bender elements are away from pile surface about 1.25 times the pile diameter. Figure (4.21) shows a plan view of the bender elements location in the test package. For the traveled signals on skew (T1 – R2) or vertical planes (T3 – R2 and T3 – R1), the measured shear wave velocity is considered at a middle depth between the transmitter and receiver bender elements.

Figures (4.22) to (4.24) show the recorded signals during pile installation. It can be seen that the travel time decreases as the pile reaches the measurement depth as indicated in these figures. The measured shear wave velocities during pile installation were normalized to that one before installing the pile and plotted in Figs. (4.25) and (4.26). The measured shear wave velocities (V_S) across the pile (T1 – R1) and (T1 – R2) in Fig. (4.25) show that V_S increases gradually as the pile tip reaches the measurement depth with an increase of 55 % at the measurement depth. However, the normalized V_S decreases as the pile tip advances beyond the measurement depth. The same trend is shown in Fig. (4.26) where the measurements are on vertical planes 1.25 times pile diameter (*d*) away from the pile. It can also be observed from Fig. (4.26) that soil stiffness along the pile shaft increases at the pile tip with higher rate at deeper depth. The reduction in V_S beside the pile is less than that across the pile. However, in both cases there is an increase of 10 % by the end of pile installation. Figure (4.27) shows the normalized soil stiffness degradation. This reduction in soil stiffness along pile shaft is indicative of a degradation of the radial stress acting on the pile shaft. This degradation in soil stiffness or stress is a phenomenon called the

friction fatigue (Lehane et al. 1993, Jardine and Chow 1998, and Schneider and Lehane 2005). Jardine and Chow (1998) suggested a factor of $(h/d)^{-0.38}$; where h is the distance between the pile tip and the measurement depth, to attenuate the radial stresses acting on the pile shaft from a maximum value close to the pile tip (at $h/d = 2$) due to pile installation. In the current case a factor of $(h/d)^{-0.275}$ was observed for the soil stiffness measurement across the pile. Also a factor of $(h/d)^{-0.037}$ was found at $1.25d$ away from the pile shaft. This means that the change in soil stiffness decreases as we go far from the pile.

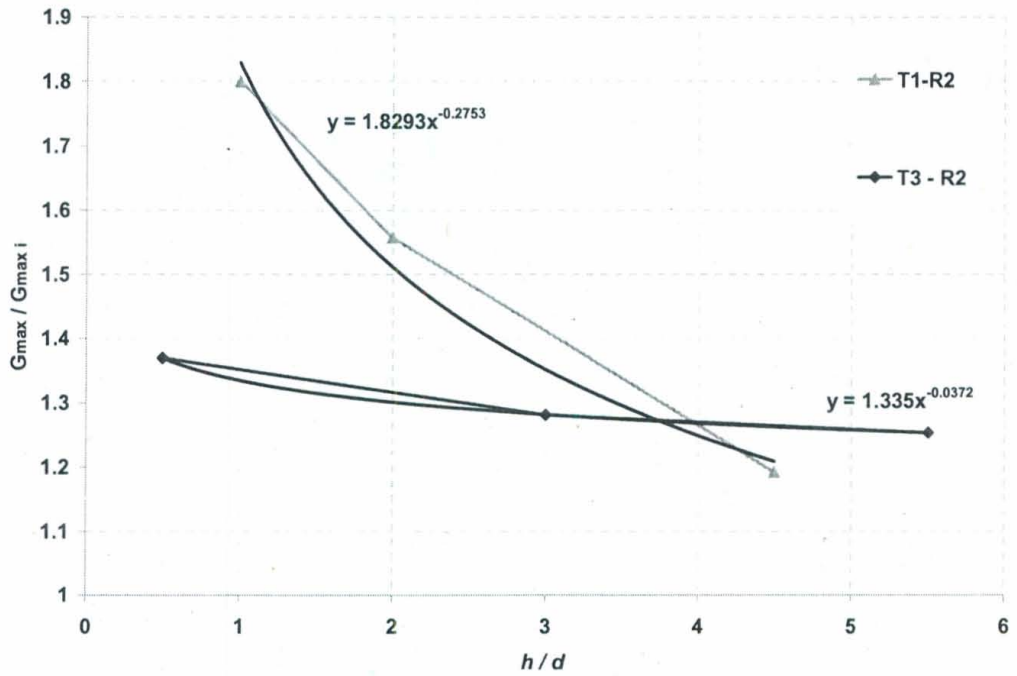

Figure (4.27) Normalized Maximum Shear Modulus Change during pile installation at 50g

4.6.Conclusion

In the current tests, shear wave velocity (V_S) was measured using piezoelectric transducers called bender elements. The measurements were carried out at three different depths in two tests. In both tests, V_S was measured during centrifuge spinning-up at increments of 10g up to 50g. It was observed that V_S values are higher

in the second test than that in the first test. It was concluded that as the soil consolidates, the horizontal effective stresses increase as a result of the plastic deformation of the soil. The lateral earth pressure coefficient was calculated from the CPT results. An equation was given to predict the maximum shear modulus with depth.

In the second part, V_S was measured during pile installation at centrifuge acceleration of 50g. The measurements were taken at pile penetration increments of 50 mm (model scale). It was found that soil stiffness increases gradually as the pile tip reaches the measurement depth. However, as the pile tip advances beyond the measurement depth, soil stiffness decreases. This degradation in soil stiffness was recommended by other authors as a phenomenon called friction fatigue. A degradation factor was obtained from the current test to account for soil stiffness degradation along the pile shaft. Also, it was found that this degradation in soil stiffness decreases as we go far from the pile shaft.

Chapter 5

Experimental Results – Monotonic Loading

5.1. Introduction:

In this chapter, the centrifuge tests monotonic loading results will be discussed. The pile head load displacement relationship and the soil-pile interaction p-y curves are presented. The main objectives of these tests are to understand the interaction between the lateral and vertical pullout response of the piles under combined loads. The tests were conducted at 70g and 50g.

Eight centrifuge tests were carried out at different loading angles and different g-levels. Five piles were tested at 70g. These piles were loaded at 0°, 3°, 16°, 30°, and 90° angles to horizontal. The other three piles were tested at 50g and loaded at 0°, 16°, and 90° angles to horizontal. For piles tests loaded at 50g, they were initially loaded monotonically then sustained cyclic loading. In the following sections the analysis of the results will be discussed.

5.2. Test Results and Analysis:

From all tests, load-displacement curves were obtained. For piles that had been tested under lateral loading, bending moment profiles were obtained. The measured bending moment was fitted by quintic spline function and then differentiated twice to get the soil pressure (p) and integrated twice to get the pile deflection (y). At some load increments the load transfer curves or p-y curves can be derived at different depths. It was found that the horizontal load component is almost same as the total load as will be discussed in the following section. All results will be presented at prototype scale.

5.2.1 Tension Loading:

Figures (5.1) and (5.2) show the vertical load- vertical displacement curves for tension tests at 70g and 50g, respectively. In the case of the 70g test, the pile was installed in-flight and then pulled out with the same hydraulic actuator without stopping the centrifuge in between the two processes. In the case of the 50g test, the centrifuge was stopped after installing the pile and then the pile was pulled out in another flight. The effect of stopping the centrifuge is clear from the shear stress distribution along pile shaft before pulling out the pile as shown in Fig. (5.3). What happened at sand-pile interface due to centrifuge stopping and re-spinning up is similar to what called "Negative Skin Friction" phenomenon for piles driven in clay. Negative skin friction produces (accumulates to) a dragload which can be very large for long piles (Fellenius, 1984). Fellenius and Broms (1969) and Fellenius (1969) presented measurement showing that a dragload can develop alone from the reconsolidation following the disturbance caused by the pile driving. This is exactly what happened when stopping and re-spinning up the centrifuge. The stresses around the pile highly increased after pile driving. By stopping the centrifuge these stresses reduced to a very low level which is 70 and 50 times based on the g-level. When re-spinning the centrifuge, the sand reconsolidated and this will be accompanied by small settlement of soil. Although this settlement could be very small (few millimeters), as reported by Fellenius (1984), Bjerin (1977) found that negative skin friction was fully mobilized to a depth of about 25 m after a relative displacement of about 5 mm as measured at a short distance away from the pile (about 0.12 m). Although this phenomenon may not happen in dense sand deposits in field, it can happen in centrifuge due to the high gravity force applied on the sand model as can be seen in Fig. (5.3).

When the centrifuge was not stopped, the residual stresses, built up around the pile after driving the pile, increased the pile tension capacity. It can be seen the very high shear stress close to pile tip that caused high tension capacity. Figure (5.4) shows the axial load distribution along pile shaft at different load increments up to failure. The total tension capacity of the pile is 32 MN. The residual load is about 29 MN of the

total capacity as can be seen in the figure. It can be seen in Fig. (5.4) the high residual load at pile tip locked in the pile. This residual load is very high due to the restriction from the free movement at the pile head after pile jacking. Before pulling out the pile, the residual load at pile tip is about 20 MN. Once the loading starts, the residual load increased to 30 MN. This means that the residual load locked at pile tip is holding the pile tip causing higher tension capacity. However, in case of the 50g test, stopping the centrifuge reduced these residual stresses as discussed before. Figure (5.5) shows the axial load distribution along pile shaft at different load increments up to failure. This reduction in the residual stresses caused a reduction in the pile tension capacity to about 2.65 MN. Although this reduction in residual stresses, the pile tension capacity is in a good agreement when compared to the available design methods in the literature as ICP. There is only a little overprediction of pile capacity and an increase in the initial stiffness before the tension capacity is mobilized. This could be due to soil dilation. The measured tension capacity (V) can be compared to ICP design method given in Eq. (2.23). In this equation the stress change due to dilation effects during tension loading $\Delta\sigma'_{rd}$ is considered (where; $\Delta\sigma'_{rd} = 4G\ R_{calc}/d$; where R_{calc} is pile surface roughness). Jardine et al. (2005) reported that the change in radial effective stress during pile loading may contribute less than 5% of the capacity for piles with diameters greater than 1m. However, this dilation term is important with medium scale piles and can dominate the behavior of small model piles because of the inverse dependence of $\Delta\sigma'_{rd}$ on the diameter. The effect of soil dilation may also be one of the reasons of the high increase of pile tension capacity for the test at 70g.

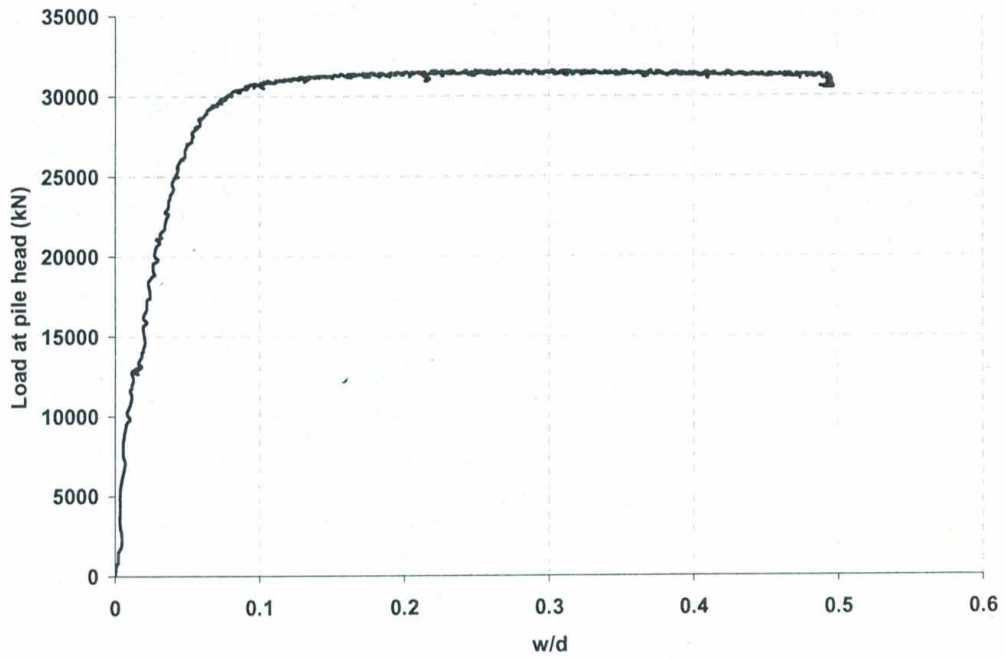

Figure (5.1) Vertical Load versus Normalized Vertical Displacement at pile head for a test at 70g

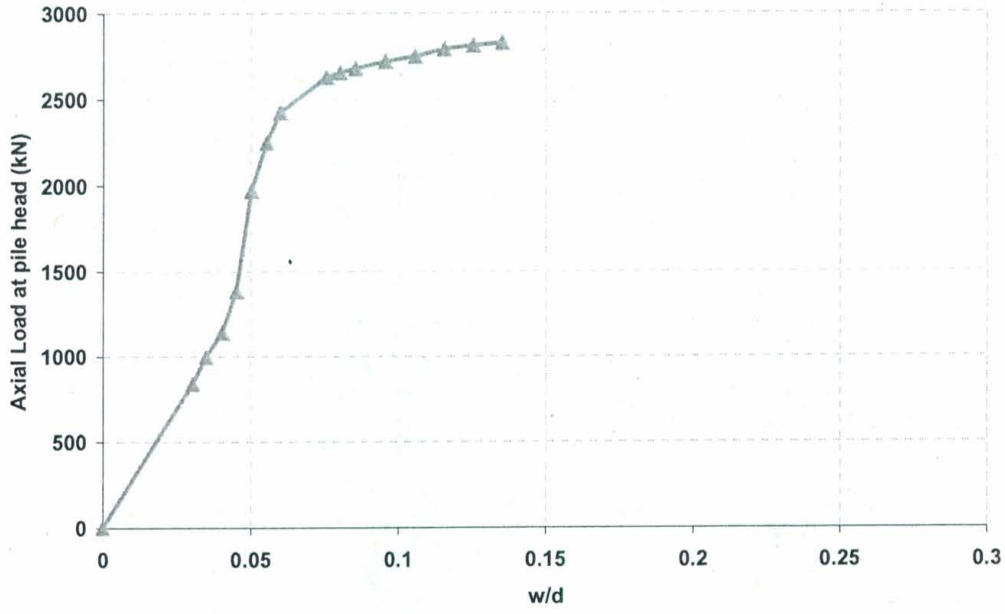

Figure (5.2) Vertical Load versus Normalized Vertical Displacement at pile head for a test at 50g

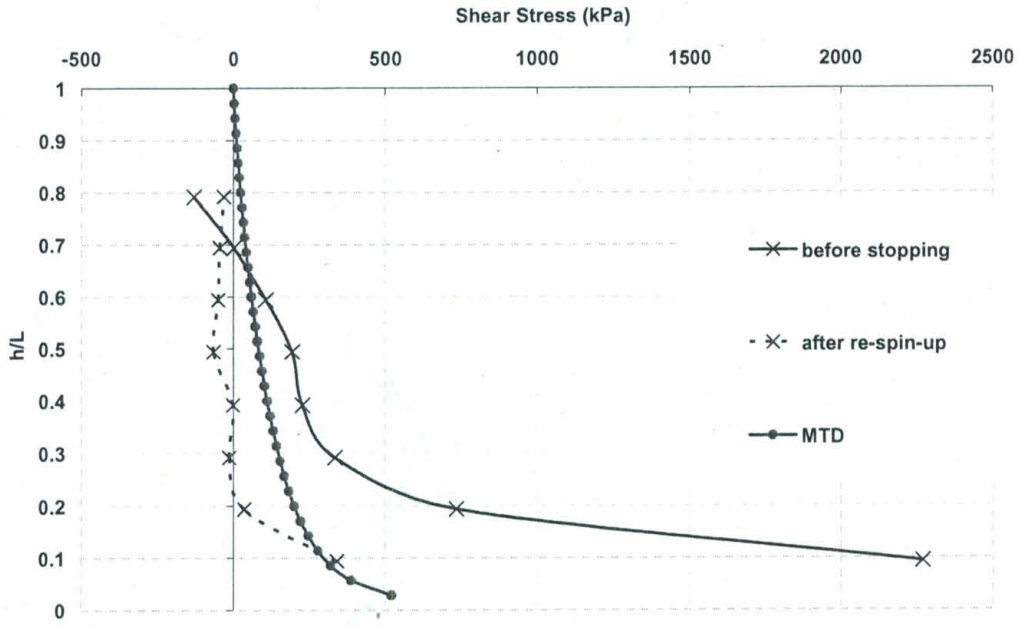

Figure (5.3) Shear Stresses along Pile Shaft before Spinning down and after Re-spinning up – 70g test

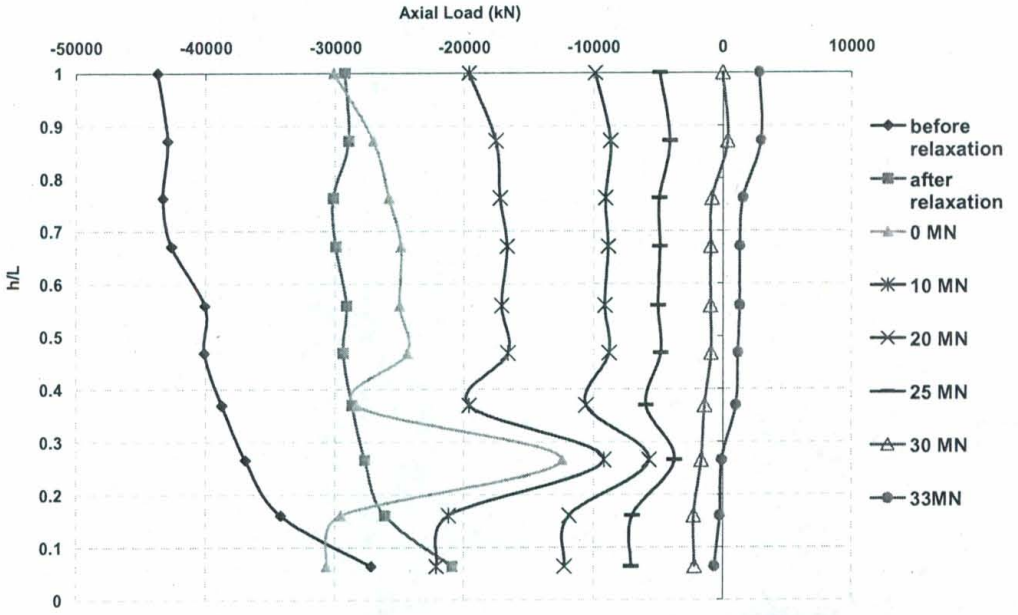

Figure (5.4) Axial Load Distribution along Pile Shaft for tests at 70g

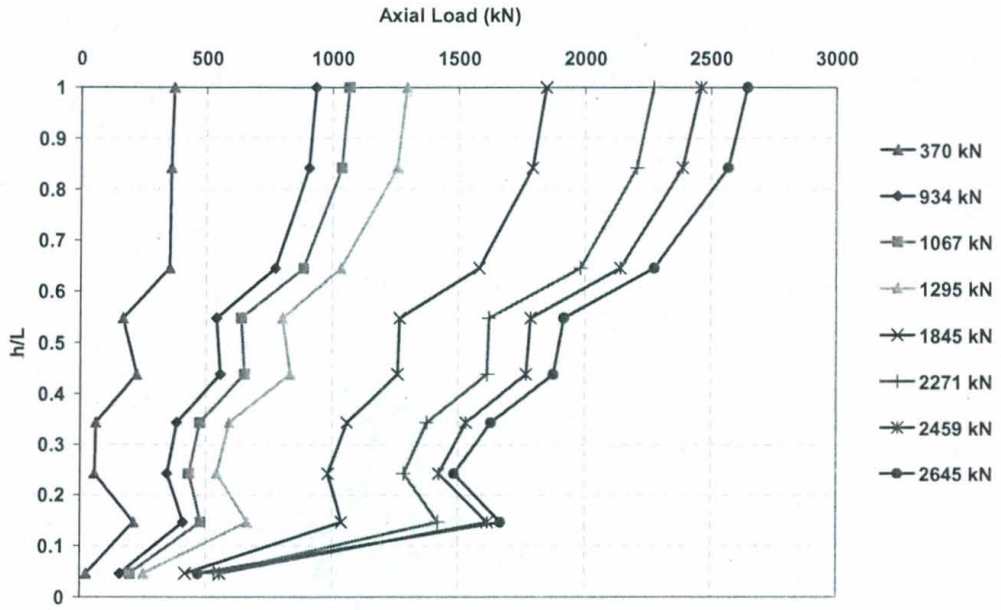

Figure (5.5) Axial Load Distribution along Pile Shaft for tests at 50g

5.2.2 Lateral Loading:

5.2.2.1 *Load-Displacement curves:*

Figures (5.6) and (5.7) show the horizontal load versus horizontal displacement curves for 70g and 50g tests, respectively. It can be seen from the figures that as the loading angle increases from 0° (pure lateral loading) to 30° the soil-pile system (the load-displacement curve) becomes stiffer. For the piles tested at 70g, at a pile head displacement of 10% of pile diameter, the carried load at the pile head increased 16.3% and 41.6% when the loading angle increased to 16° and 30°, respectively. The same trend is shown for the piles tested at 50g which show good repeatability between the tests.

5.2.2.2 Bending moment curves:

The strain gages attached to the model piles was used to record the strain in the pile during loading process. At each strain gage location, the total strain consists of an

axial and bending component. Of interest is the bending strain ε_b at any given section of the pile:

$$\varepsilon_b = \frac{\varepsilon_1 - \varepsilon_2}{2} \tag{5.1}$$

where ε_1 and ε_2 are the values of the strain on the opposite sides of the pile. Figure (5.8) shows in detail how the bending strain was obtained from the measured strain.

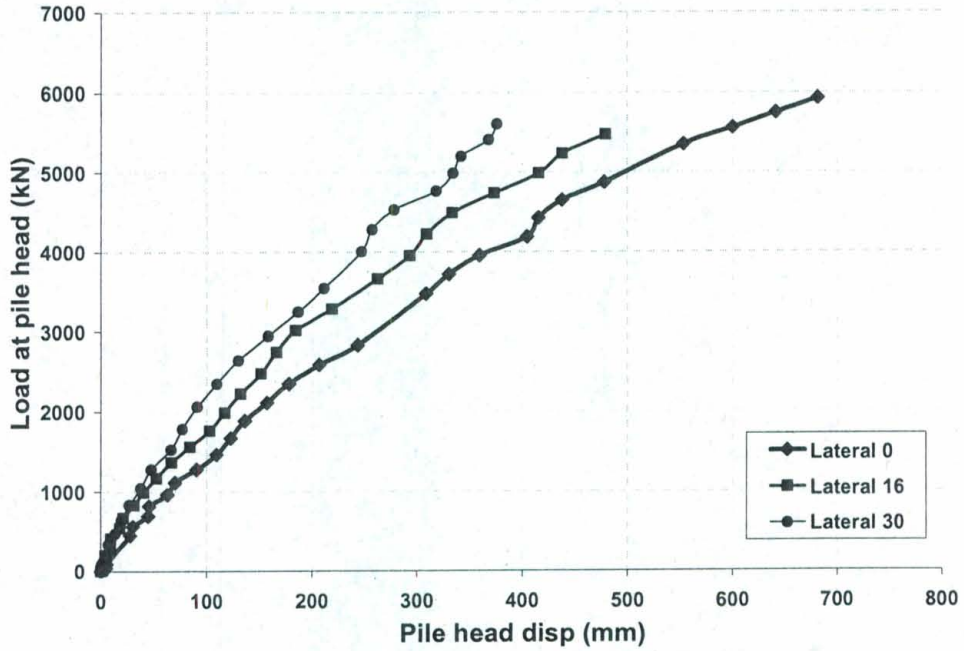

Figure (5.6) Horizontal Load versus Horizontal Displacement at pile head for tests at 70g

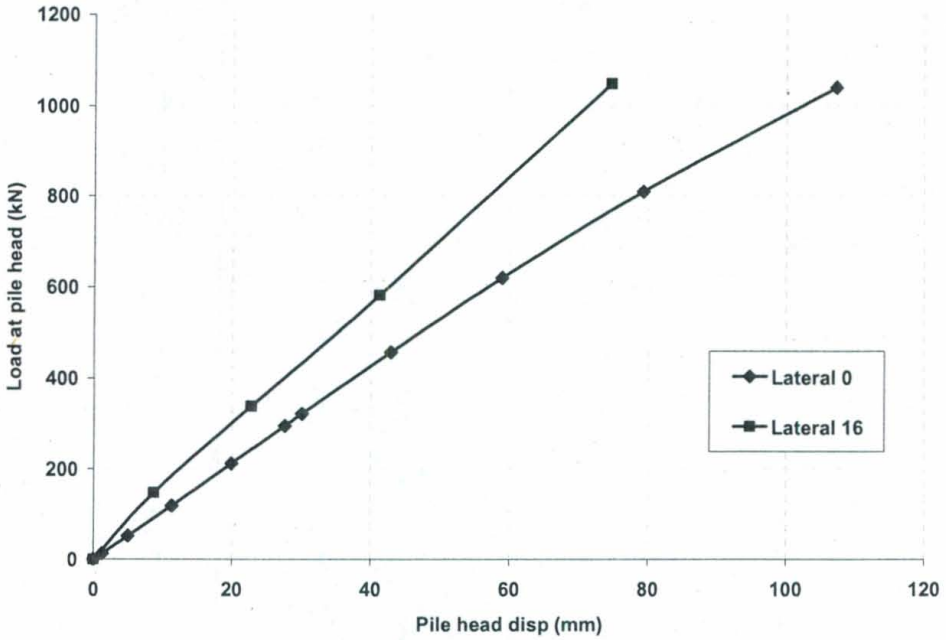

Figure (5.7) Horizontal Load versus Horizontal Displacement at pile head for tests at 50g

Strain is proportional to bending moment within the elastic stress range of the pile material. The strain measurements at 10 locations on the model pile were used to determine the bending moments at these locations as follows:

$$M = \frac{2\varepsilon_b E_p I_p}{d} \tag{5.2}$$

where E_p is the pile young's modulus and I_p is the pile second moment of inertia.

Figures (5.9) to (5.11) show the discrete measured bending moment at the successful strain gages for those piles tested at 70g and 50g. The fitted bending moment profiles, as will be discussed later, are shown on the same figures as solid lines. High agreement can be seen between the experimental data and the fitting profile. At the same gravity test level, the maximum bending moment values of all loading angles larger than 0° at the same horizontal load increment are very close.

Figure (5.12) shows the relation between the normalized horizontal load (H_n) on the pile head and the normalized maximum bending moment ($M_{n\text{-}max}$) for all piles. Both H_n and $M_{\text{n-max}}$ can be defined as follows:

$$H_n = \frac{H}{\gamma' d^3} \tag{5.3}$$

$$M_{n-\max} = \frac{M_{\max}}{\gamma' d^4} \tag{5.4}$$

where H is the horizontal load at the pile head, M_{max} is the maximum bending moment, γ' is the effective unit weight of sand, and d is pile diameter.

It can be seen that in both tests at loading angle 0° $M_{n\text{-}max}$ values are very close. Also $M_{n\text{-}max}$ values for all piles tested at angles larger than 0° are very close at the same normalized horizontal load component (H_n). This is made clear by Fig. (5.13) where all ($M_{n\text{-}max}$) values of these piles tested at 70g and 50g are plotted. All data show a linear increase of ($M_{n\text{-}max}$) as (H_n) increases. The data can be fitted to the following equation:

$$M_{n-\max} = 2.466 * H_n \qquad \text{[Pure lateral loading]} \tag{5.5a}$$

$$M_{n-\max} = 1.574 * H_n \qquad \text{[Inclined pullout loading]} \tag{5.5b}$$

From these results it can be seen that there is a reduction in $M_{n\text{-}max}$ for all cases where the loading angle is larger than 0° than that at 0° angle (pure lateral loading) of about 36%. This reduction is almost constant regardless of the loading angle value. This means that the reduction is due to a reduction in soil confining pressure around the pile. The tension load component of the pullout force at the pile head causes elastic 'Poisson' radial contractions of the shaft which is more significant with tubular pile as reported by Jardine and Chow (2005). This radial contraction of pile section will

cause a reduction in soil confining pressure around the pile. In addition, shear stress transfer during tension loading and the effects of principal stress axis rotation reduce the global compressive stress around the pile. So, even a very small loading angle (i.e. 3° as shown in Fig. (5.10)) will cause a reduction in the soil confining pressure on the pile due to the pullout vertical component.

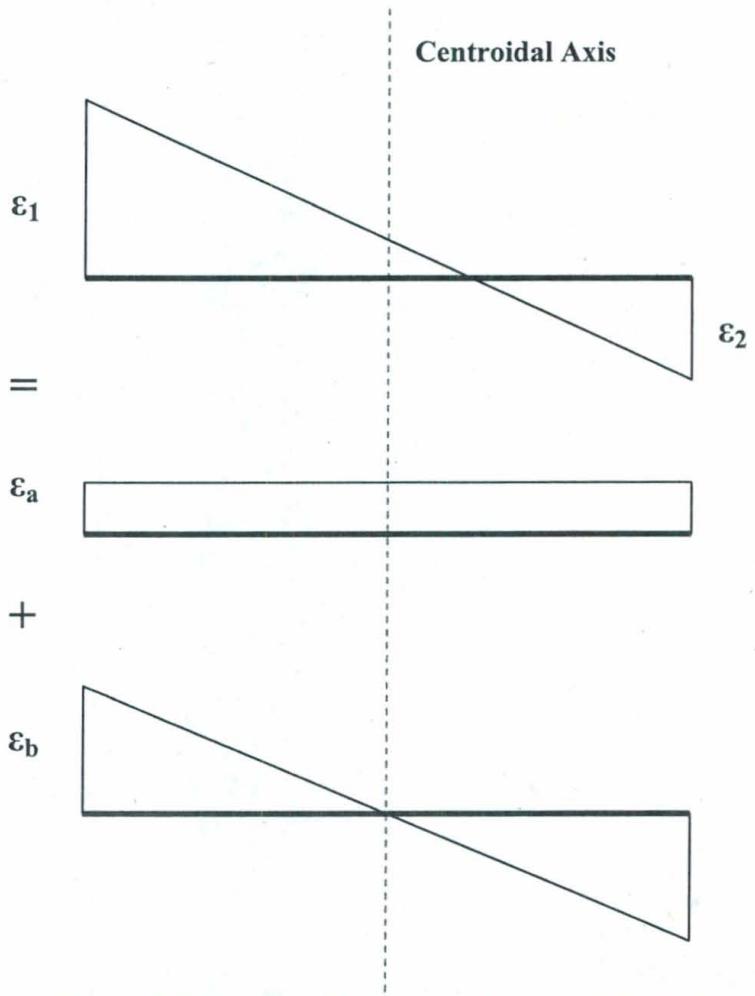

Figure (5.8) Method of Measuring Strain on Pile Shaft

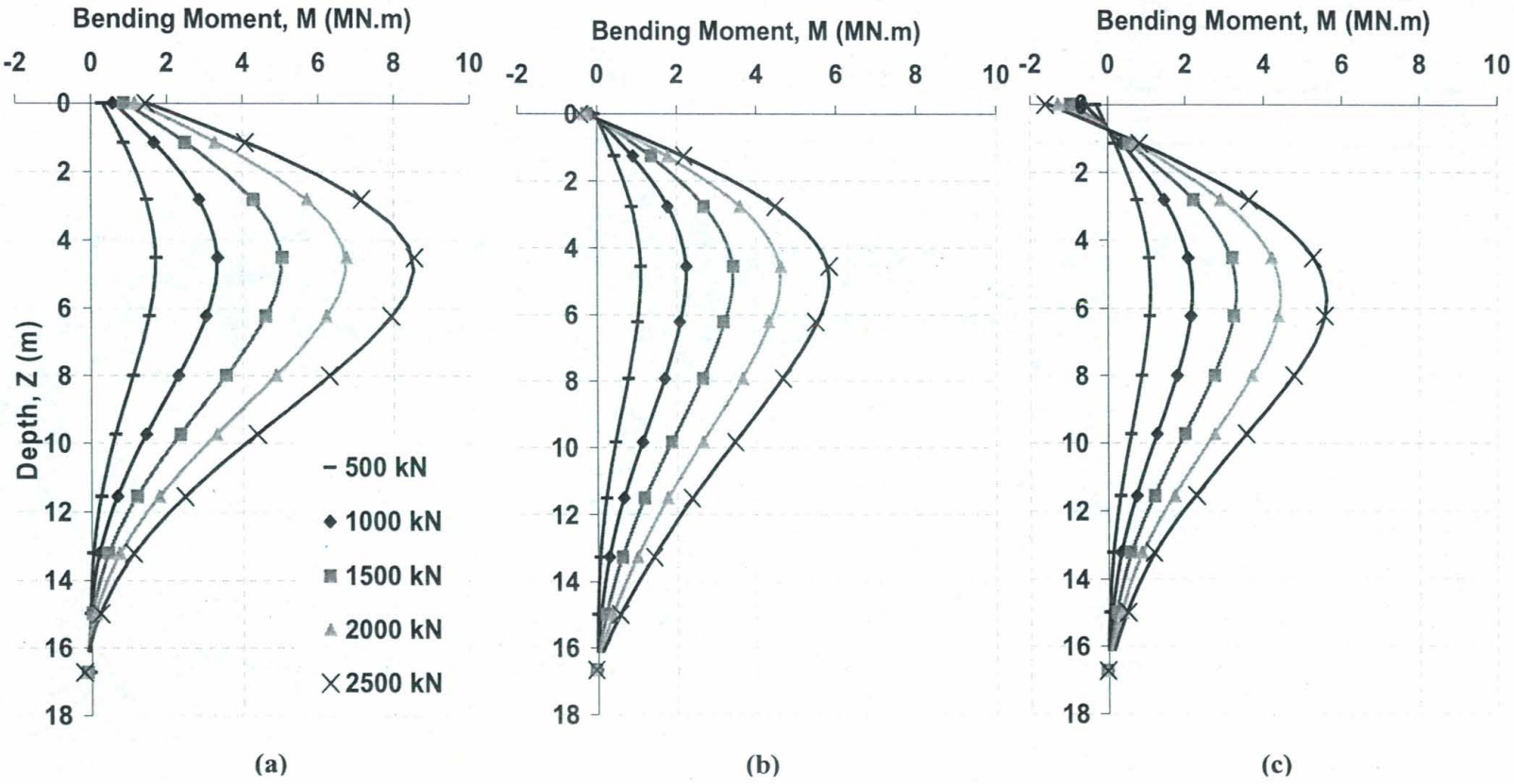

Figure (5.9) Bending Moment Distribution at Different Loading Angles (a) 0˚, (b) 16˚, (c) 30˚, [Fitting Curve is a Solid Line]- 70g tests

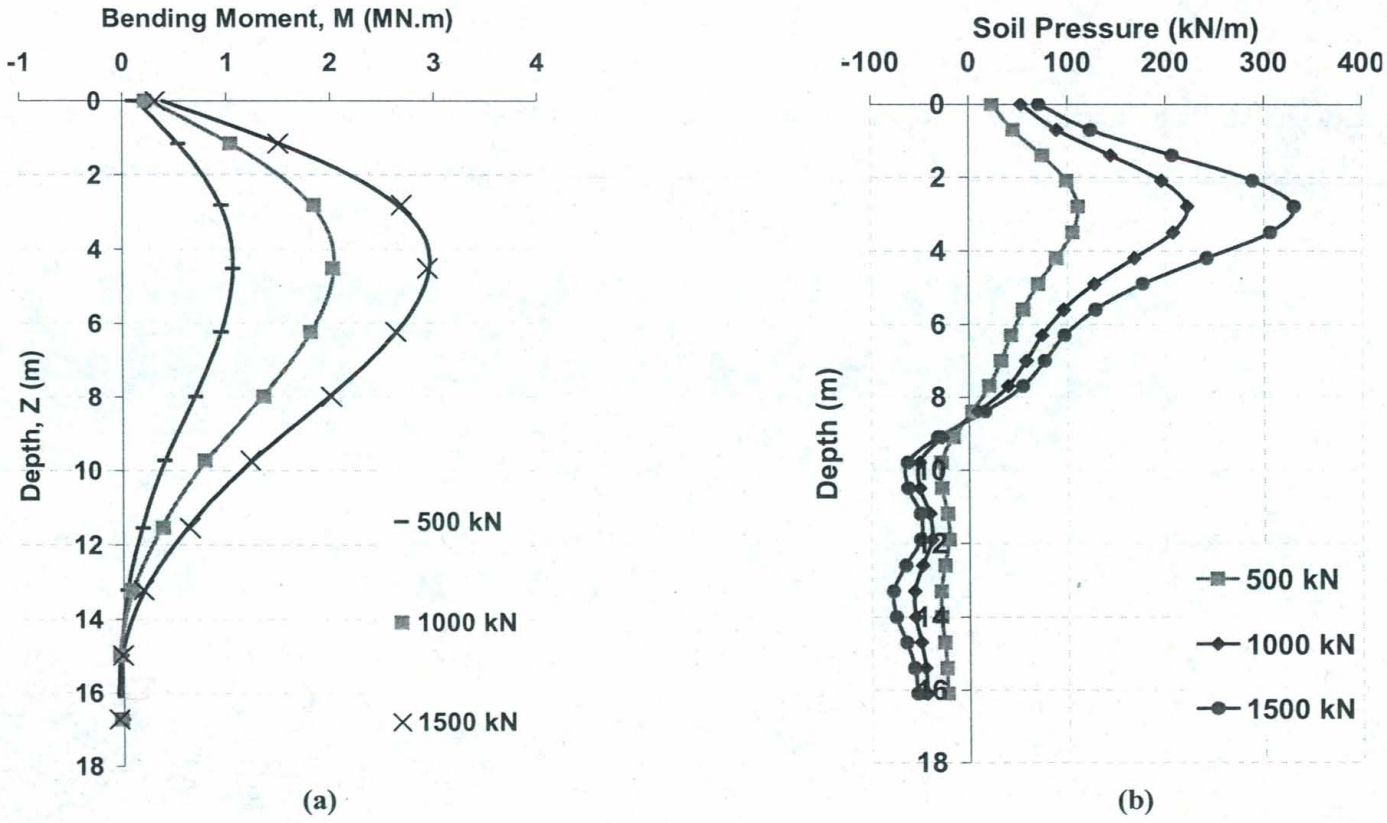

Figure (5.10) Test at Loading Angle 3° (a) Bending Moment Distribution [Fitting Curve is a Solid Line], (b) Soil Pressure Profile- 70g test

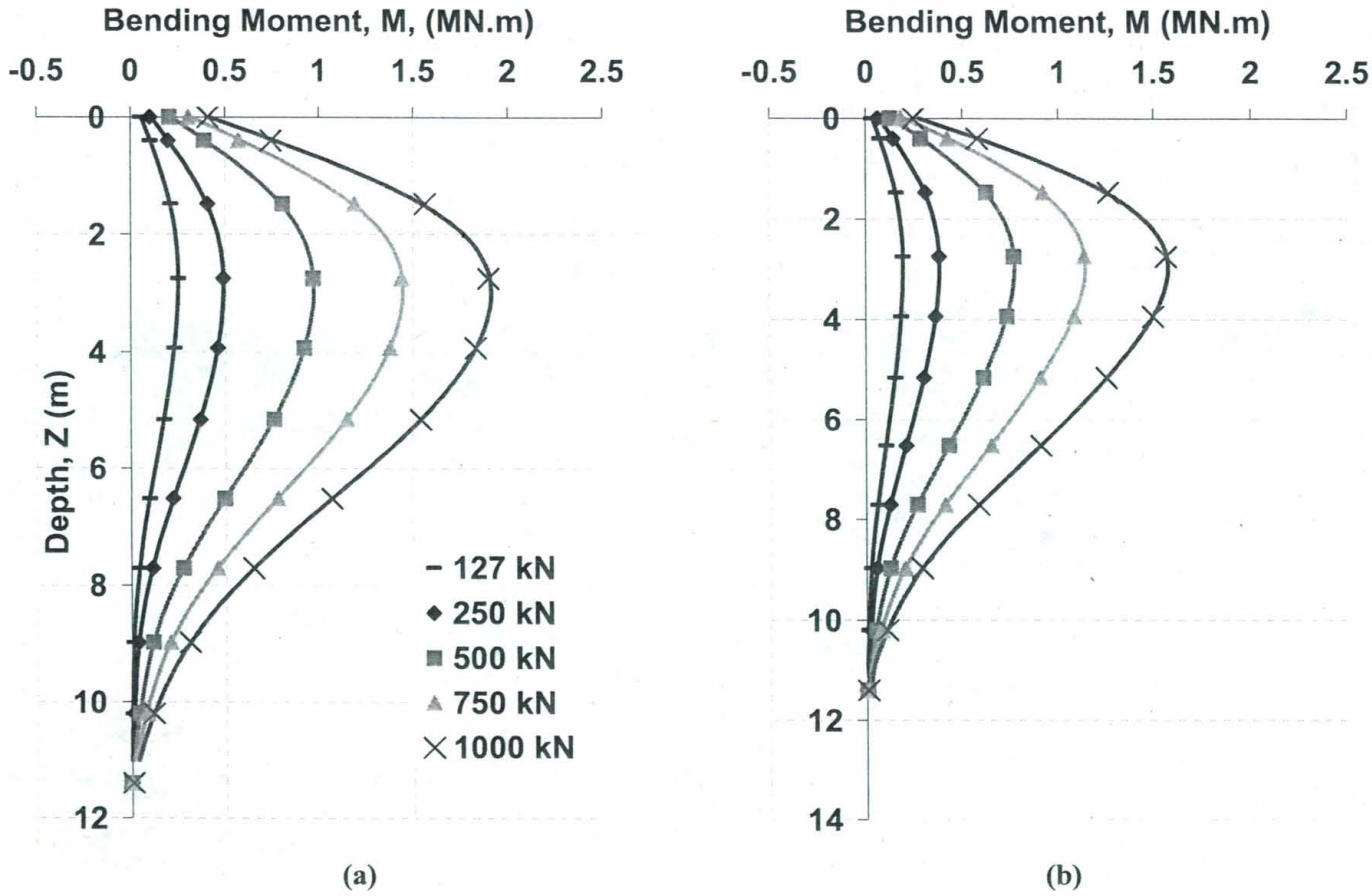

Figure (5.11) Bending Moment Distribution at Different Loading Angles (a) 0°, (b) 16°,, [Fitting Curve is a Solid Line]- 50g tests

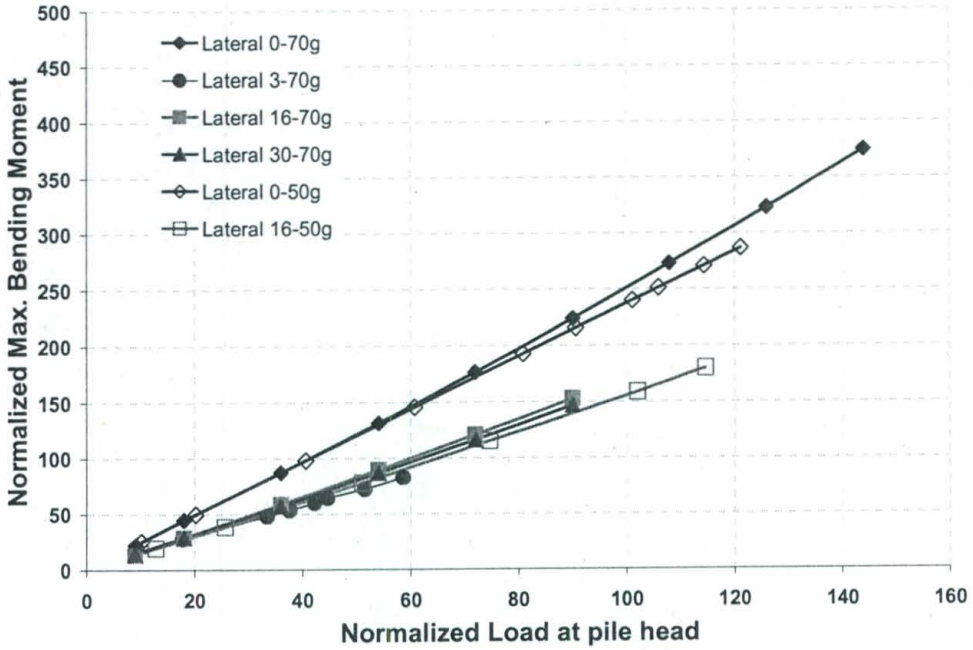

Figure (5.12) Normalized Horizontal Load versus Normalized Max. Bending Moment for All Tests.

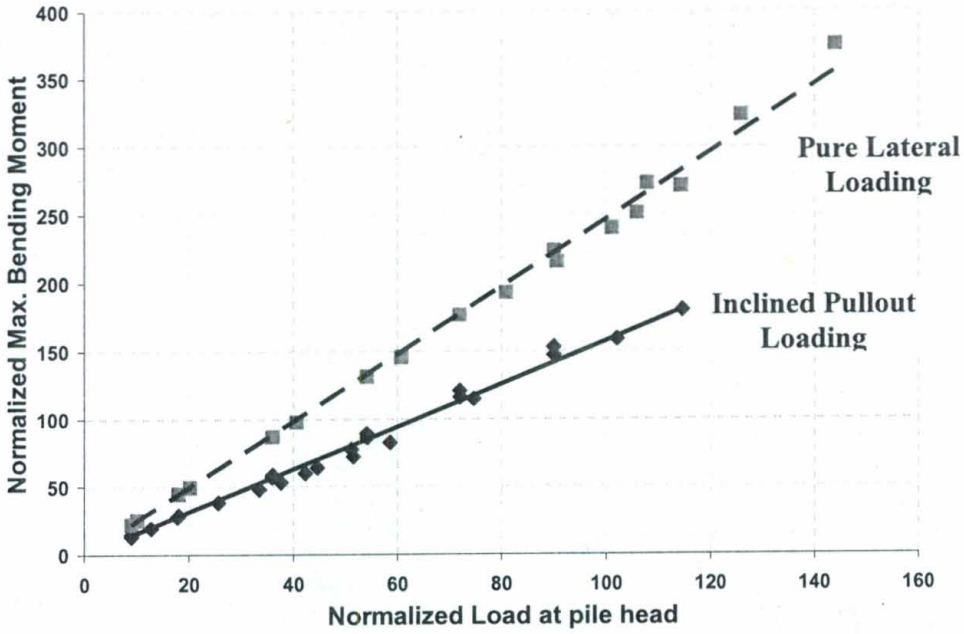

Figure (5.13) Fitting of Normalized Horizontal Load versus Normalized Max. Bending Moment

5.2.2.3 ***p-y curves:***

Many methods available in the literature had been tried to fit the experimental bending moment data. The fitted function should be integrated twice to get the pile curvature and displacement profile (y). In the present study, the integration constants were the rotation and horizontal displacement from the two laser displacement transducers at the pile head. The fitted function also should be differentiated twice to get the shear and soil pressure (p) along the pile length. The differentiation process is a much more difficult operation as it is very sensitive to the bending moment fitted function. It is important not to introduce additional conditions (zero pressure at the surface of the soil or at the pile tip, for example) during these smoothing and differentiation operations. These restrictive conditions can have a great influence on the shape of the reaction curves obtained, and may represent the researcher a priori idea of the p-y relation rather than the real physical relationship (Mezazigh and Levacher 1998).

Quintic spline functions were found to provide the best fit of the experimental bending moment data and give a smooth and an acceptable profile for the soil pressure (p) and displacement (y) along the pile. The fitting process was carried out using an adjustable smoothing parameter ρ. The value of this parameter controls the smoothness of the fitted bending moment profile. The value of ρ is selected by checking the static equilibrium of the pile. The resultant of the soil pressure determined after double differentiation of the bending moment curves is compared to the horizontal force component applied at the head of the pile. In all cases the difference between the measured horizontal force component and the horizontal force obtained by double differentiation of the bending moment curves did not exceed 15% as given by Mezazigh and Levacher (1998):

$$H + \int_0^L p(z).d.dz + V(z) \approx 0 \quad (5\text{-}15\%) \tag{5.5}$$

where $V(z)$ is the shear force at depth z. Once the soil pressure (p) and the displacement (y) profiles are obtained at different load increments on the pile head, p-y curves can be derived for all tests under lateral loading.. To obtain the pile deflection profile, the fitted bending moment data was integrated twice. The two integration constants are the pile head displacement and the rotation measured using the two displacement transducers at the pile head. Once the soil pressure (p) and the displacement (y) profiles are obtained at different load increments on the pile head, p-y curves can be derived for all tests under lateral loading. The pressure curves $P(z)$ are determined by double differentiation of the bending moment curves as:

$$p(z) = \frac{d^2 M(z)}{dz^2} \tag{5.6}$$

The pile deflection profiles $y(z)$ have been determined by double integration of the bending moment curves as:

$$y(z) = \frac{1}{E_p I_p} \iint M(z).dz^2 \tag{5.7}$$

Figures (5.14) to (5.17) show the soil pressure and pile deflection profile versus depth for the piles tested at 70g and 50g. It can be seen that the soil pressure at shallow depth and close to pile tip decreases as the loading angle increases. The location of the point of zero pressure at 0.54L (6.75d) and 0.56L (7d) for the piles tested at 70g and 50g, respectively, does not change as the loading angle changes.

The pile deflection profile is decreasing at shallow depths by increasing the loading angle. However, at deeper depths the deflection increases with a decrease in the pile rotation. This trend is expected as the vertical pullout load component causes this decrease in the pile rotation.

It should be noted that the calculated pile deflection profile shows a rigid pile behavior. According to Broms (1964) and Meyerhof (1995), the pile soil rigidity in

the present study should be flexible. This was also supported by the Finite Element Model (FEM) that will be discussed later. In most of the previous studies to calculate pile deflection profile, the displacement or the rotation at pile tip was assumed to be zero as one of the integration constants. However, this assumption could be valid for very long piles and it may cause some error at large loads (Kong and Zhang, 2005). In the present study, a trial was made to calculate pile deflection profile assuming the two integration constants are the pile head deflection and zero deflection at pile tip. It was found that the pile deflection has the same sign along the pile with no zero deflection at zero soil pressure as it should be. This means that the assumption of no deflection at pile tip is not valid in the present case. The small bending moment values measured close to the pile tip could have some error that lead to higher deflection values.

For each depth, the *p-y* curves have been plotted as shown in Figs. (5.18) to (5.22). When comparing these curves for different loading angles at the same Z/d ratio, where Z is the depth, as shown in Figs. (5.23) and (5.24), it can be seen that the initial stiffness of the *p-y* curves is same. However, at a higher deflection the curves of 16° and 30° divers from the pure lateral loading curve. It can be seen also that all *p-y* curves are nonlinear with no ultimate soil resistance for $Z/d > 0.5$.

In terms of fitting these *p-y* curves, many trials have been carried out to fit these curves. The obtained p-y curves of the pure lateral loading case were compared to *p-y* curves recommended by other authors (i.e. Yan and Byrne (1992), API (2000), and Dyson and Randolph (2001)) as shown in Figs. (5.25) to (5.30). Both of p-y curves provided by Yan and Byrne (1992) and Dyson and Randolph (2001) are of a parabolic shape same as the current *p-y* curves. There is no well-defined ultimate soil resistance at large deflection as recommended by API (2000). At small deflection, the API curves appear stiffer, whereas at large deflection they are softer, reaching ultimate resistances that are substantially lower than the experimental ones.

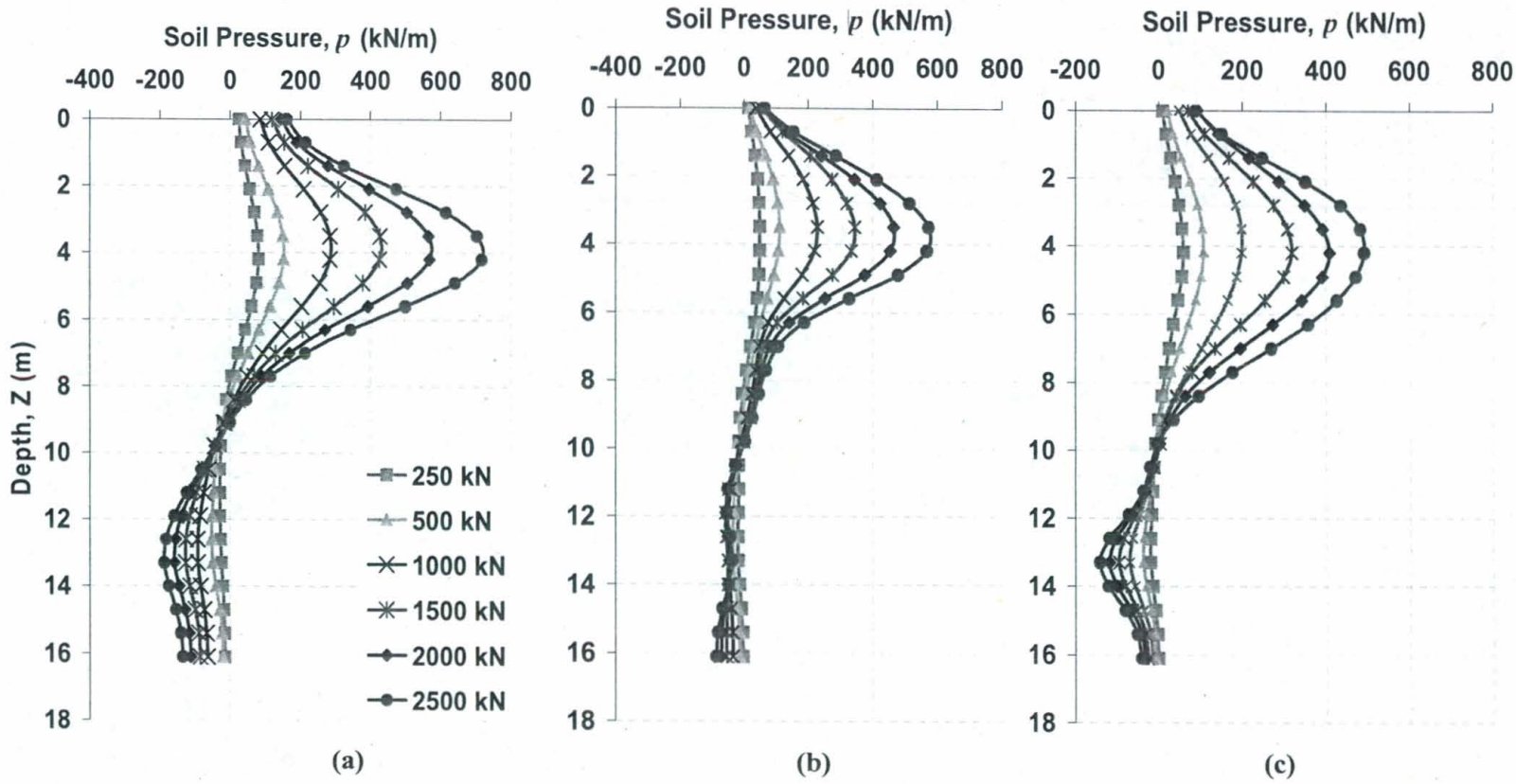

Figure (5.14) Soil Pressure Distribution at Different Loading Angles (a) 0°, (b) 16°, (c) 30°- 70g tests

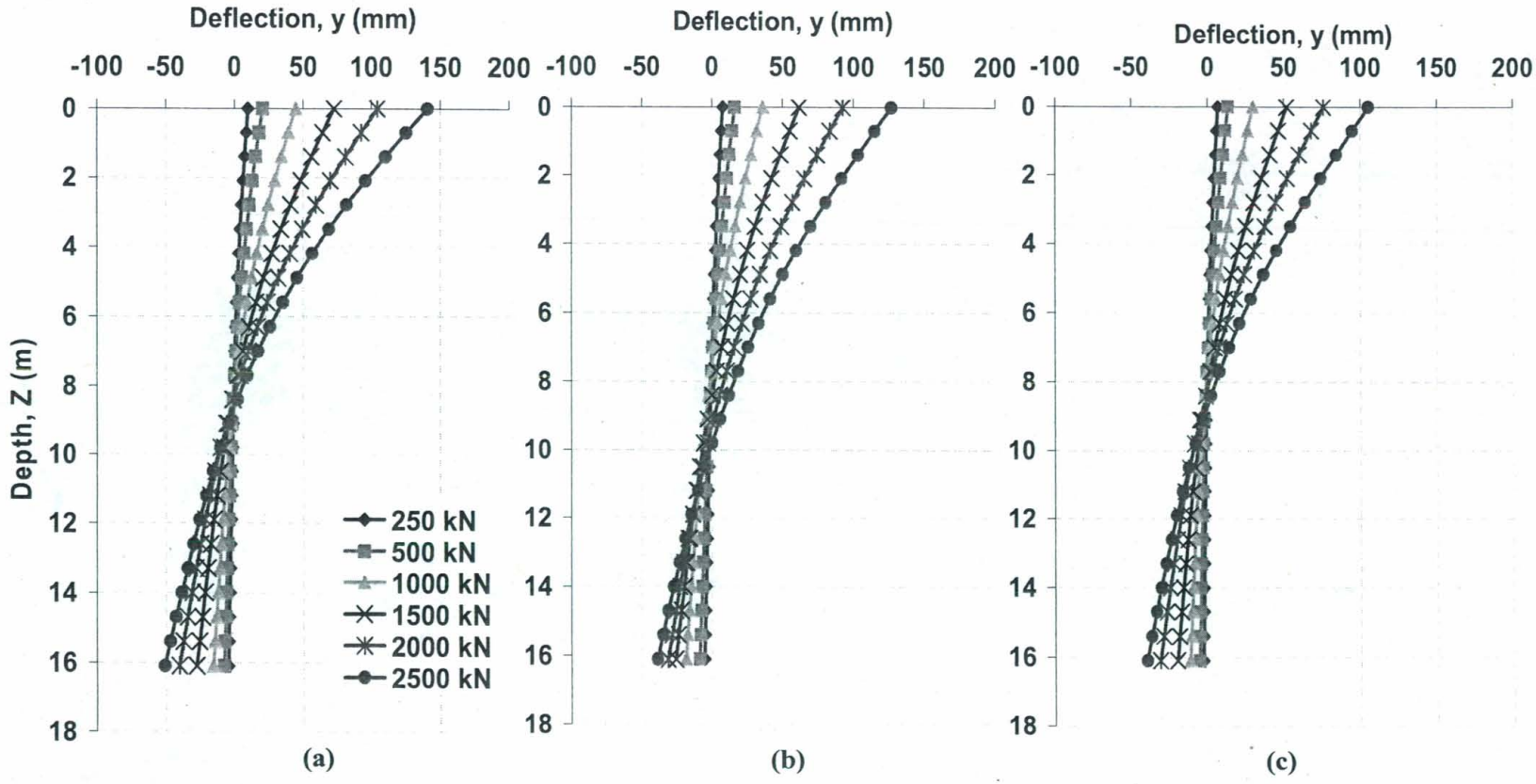

Figure (5.15) Pile Deflection Profile at Different Loading Angles (a) 0°, (b) 16°, (c) 30°- 70g tests

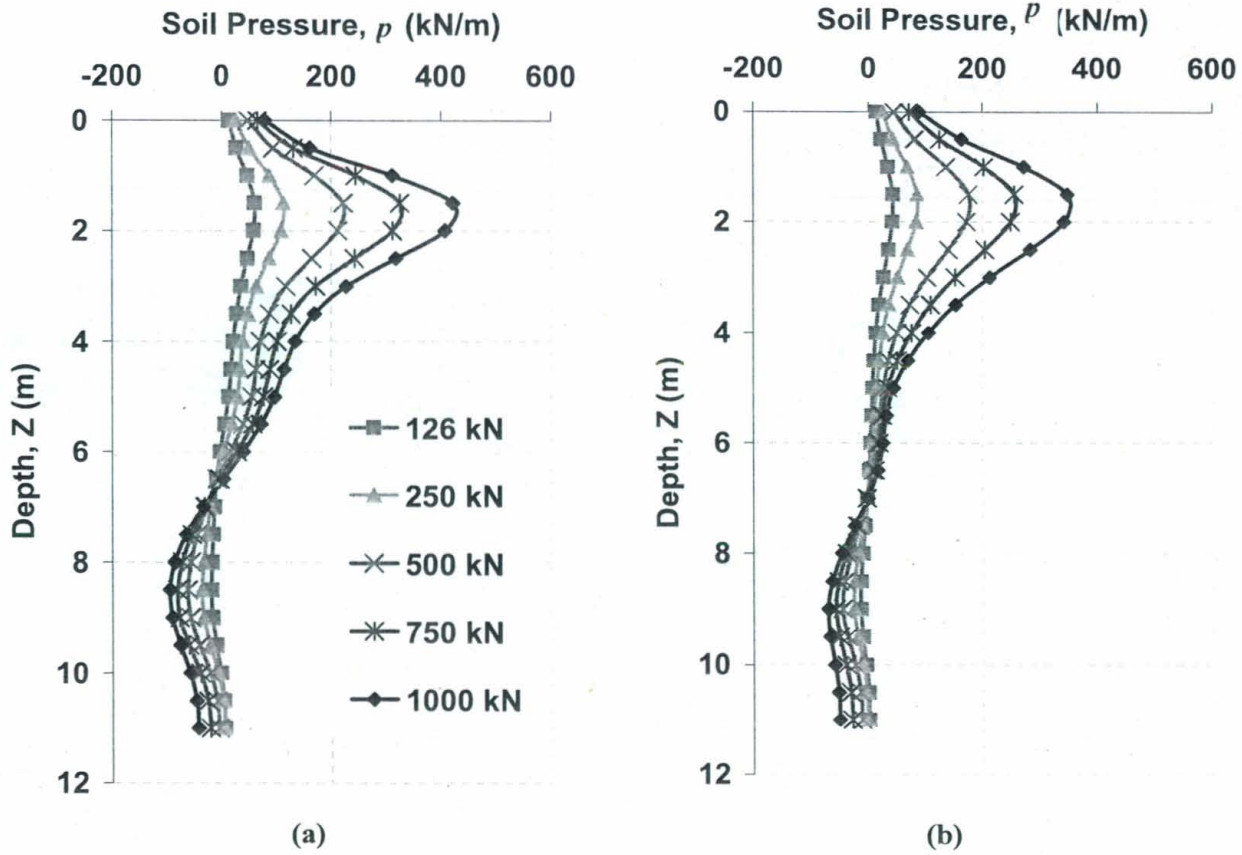

Figure (5.16) Soil Pressure Distribution at Different Loading Angles (a) 0°, (b) 16°- 50g tests

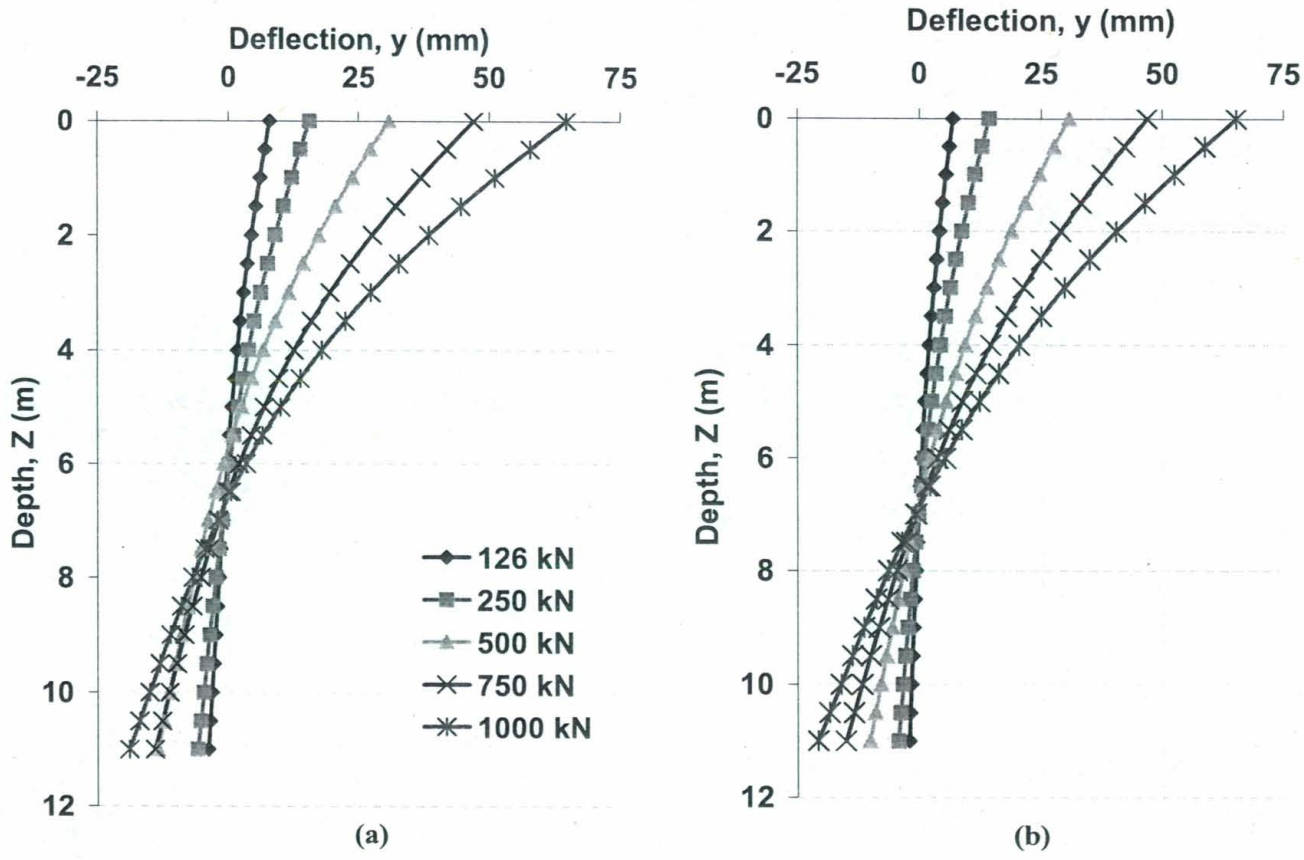

Figure (5.17) Pile Deflection Profile at Different Loading Angles (a) 0°, (b) 16°- 50g tests

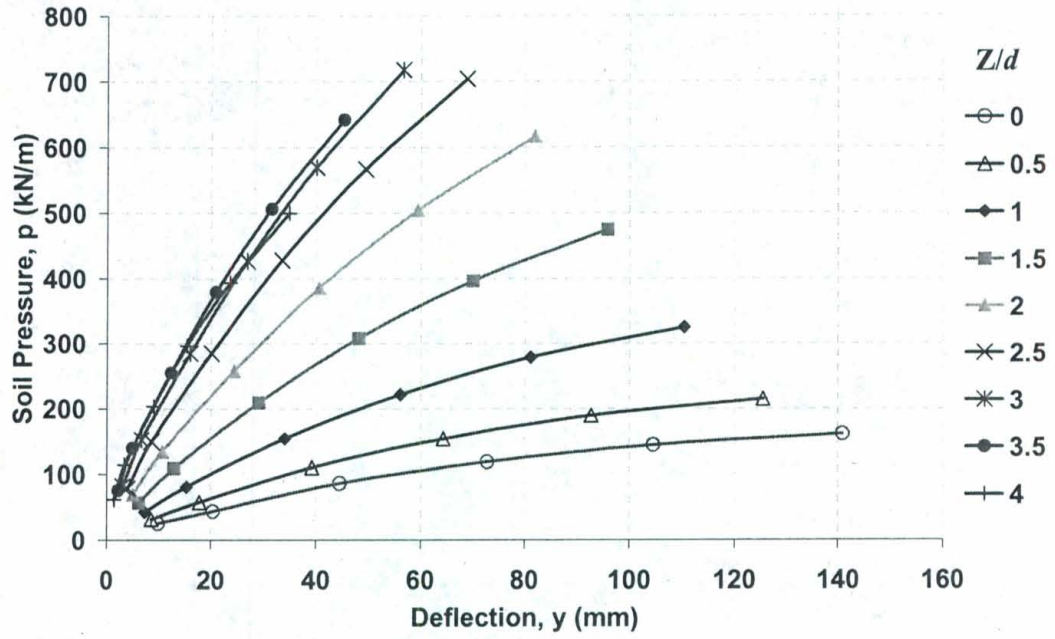

Figure (5.18) p-y Curves for 0° Loading Angle- 70g

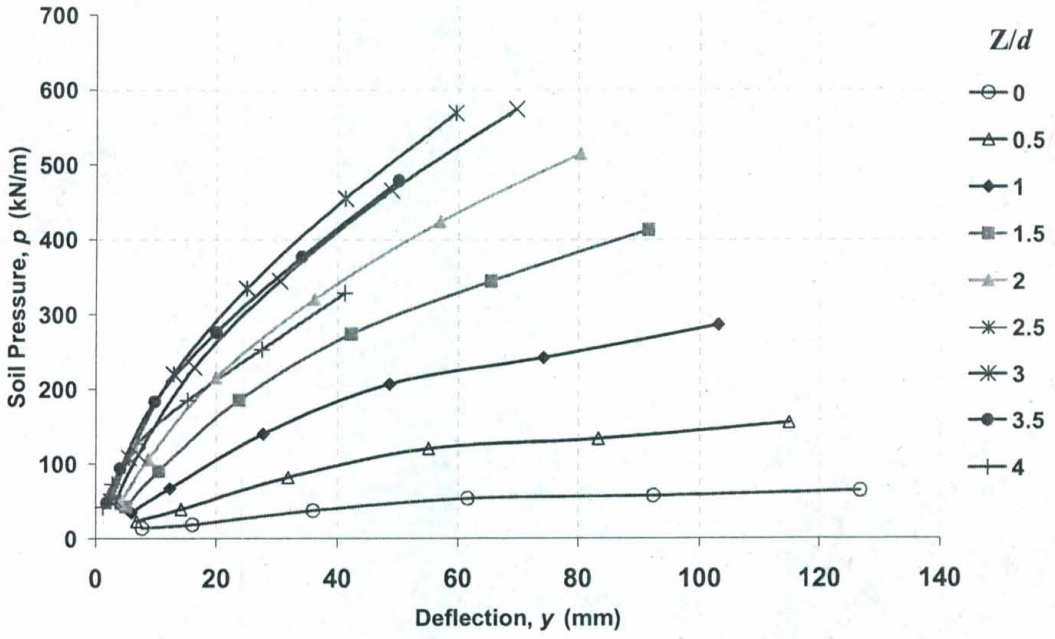

Figure (5.19) p-y Curves for 16° Loading Angle- 70g

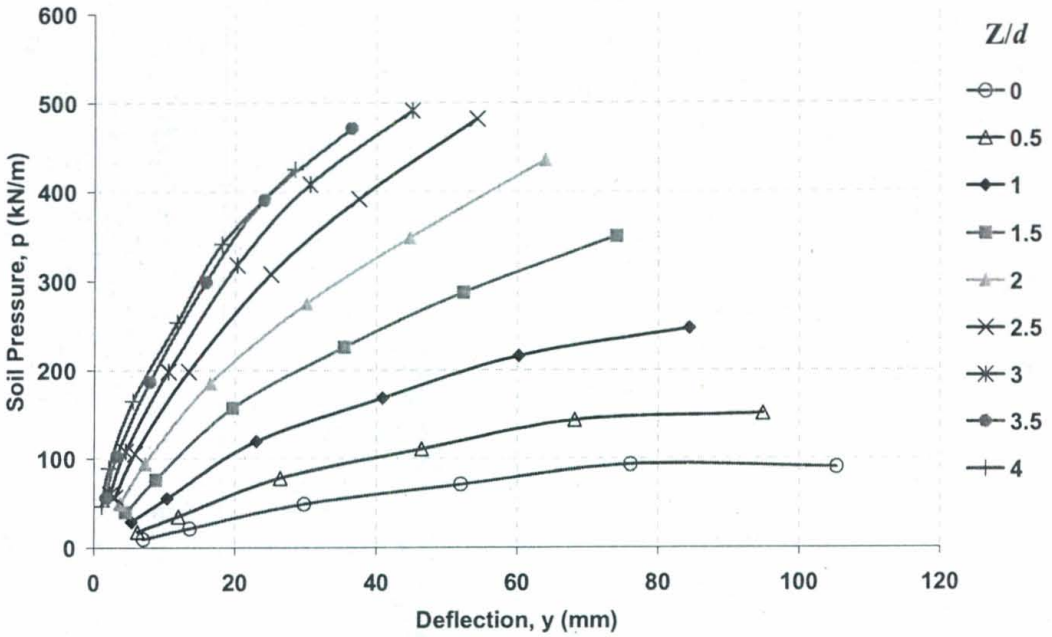

Figure (5.20) p-y Curves for 30° Loading Angle- 70g

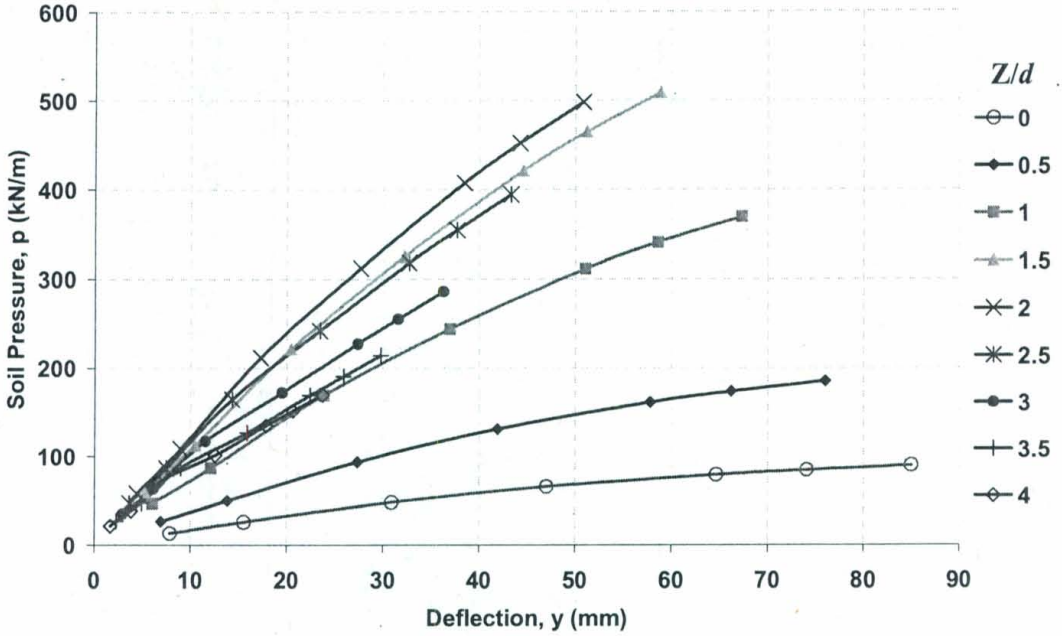

Figure (5.21) p-y Curves for 0° Loading Angle- 50g

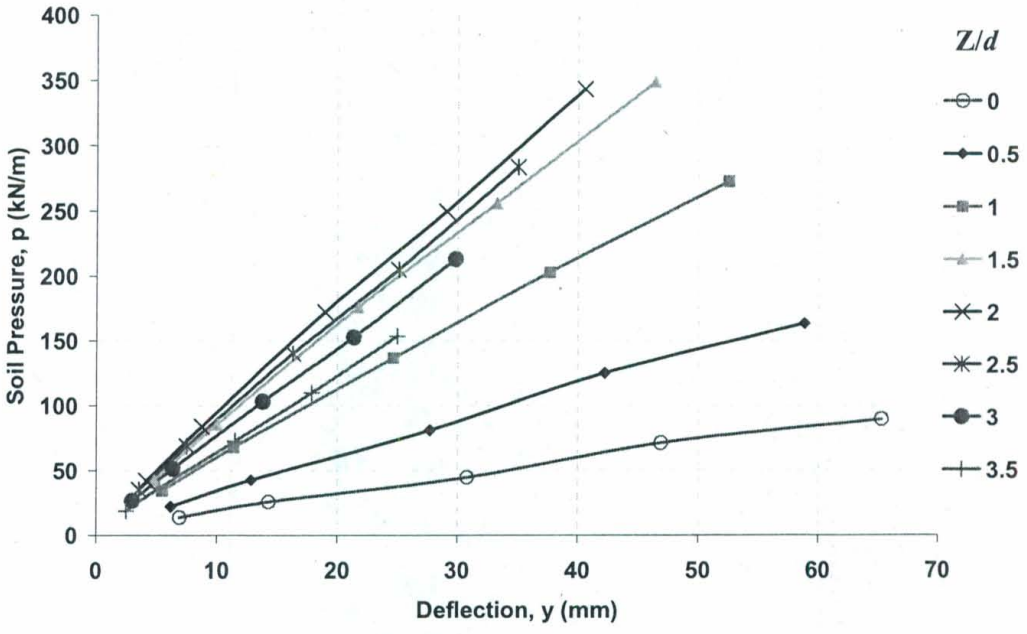

Figure (5.22) p-y Curves for 16° Loading Angle- 50g

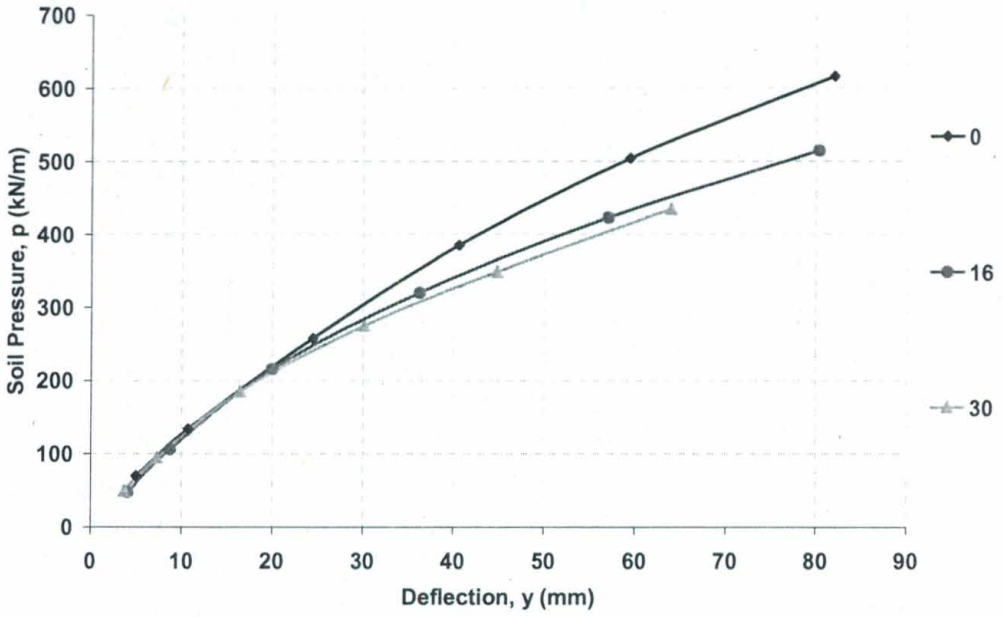

Figure (5.23) Comparison of experimental p-y Curves at 70g - Z/d= 2

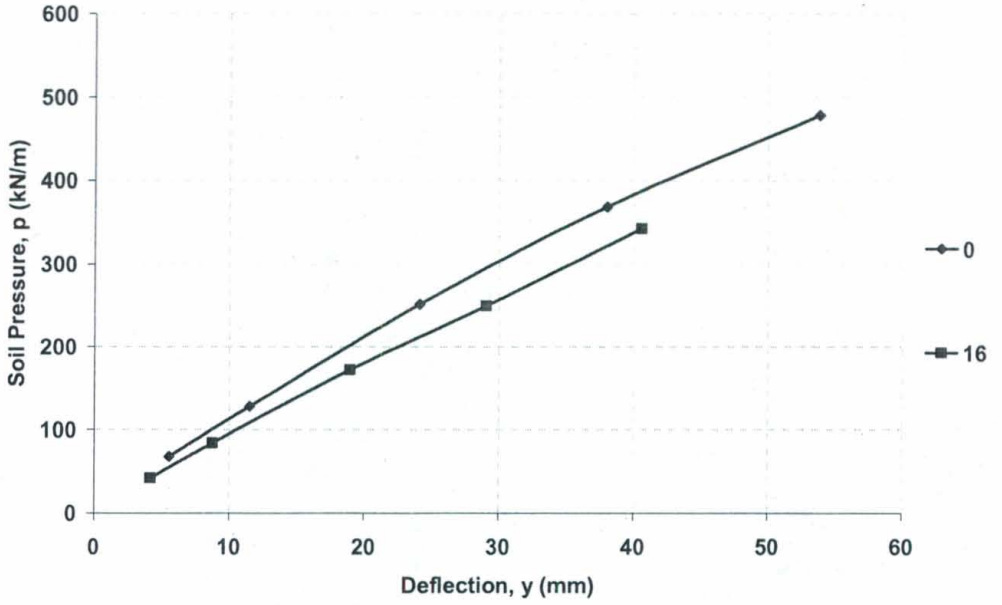

Figure (5.24) Comparison of experimental p-y Curves at 50g - Z/d= 2

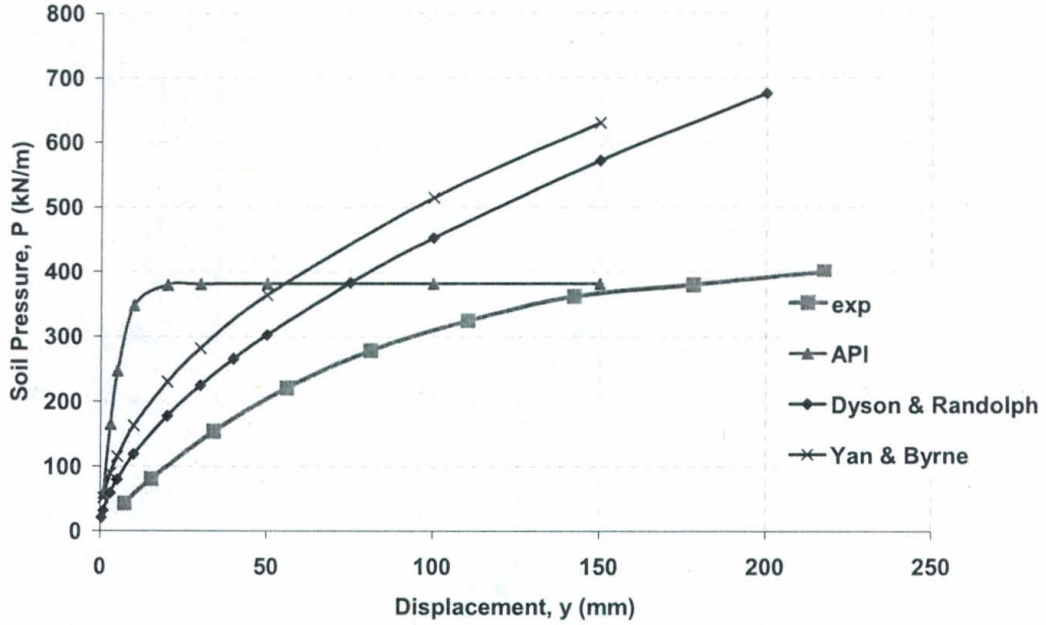

Figure (5.25) Comparison of experimental p-y Curves at 70g with others - Z/d= 1

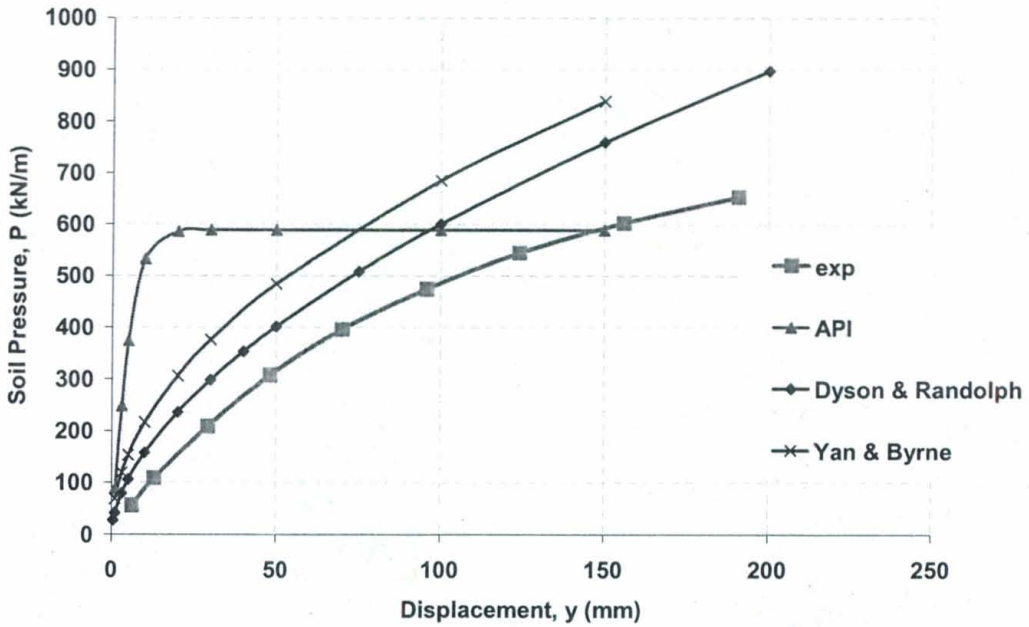

Figure (5.26) Comparison of experimental p-y Curves at 70g with others - Z/d= 2

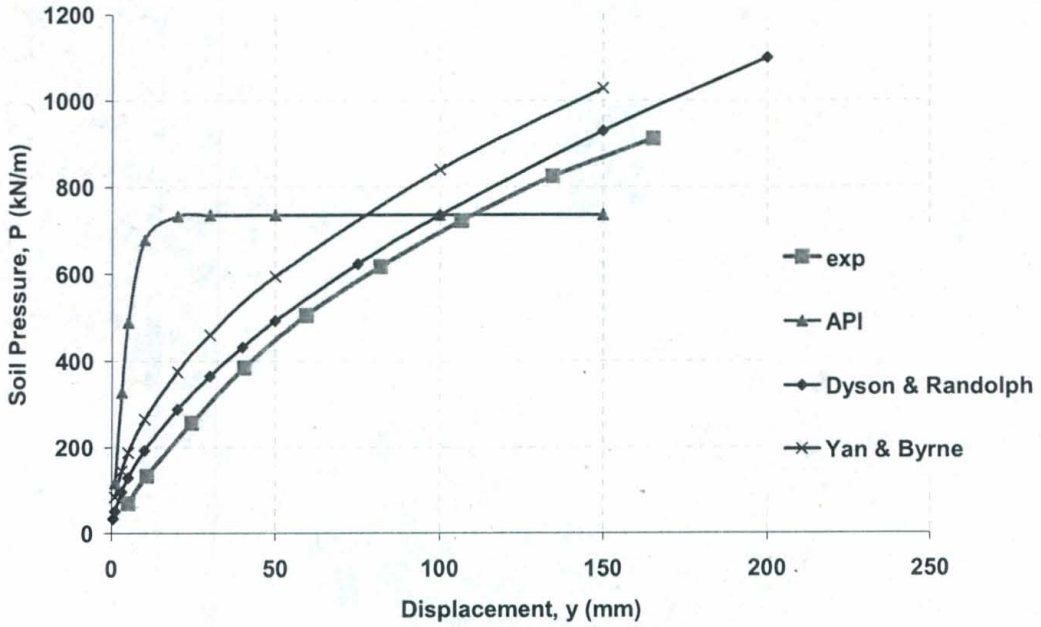

Figure (5.27) Comparison of experimental p-y Curves at 70g with others - Z/d= 3

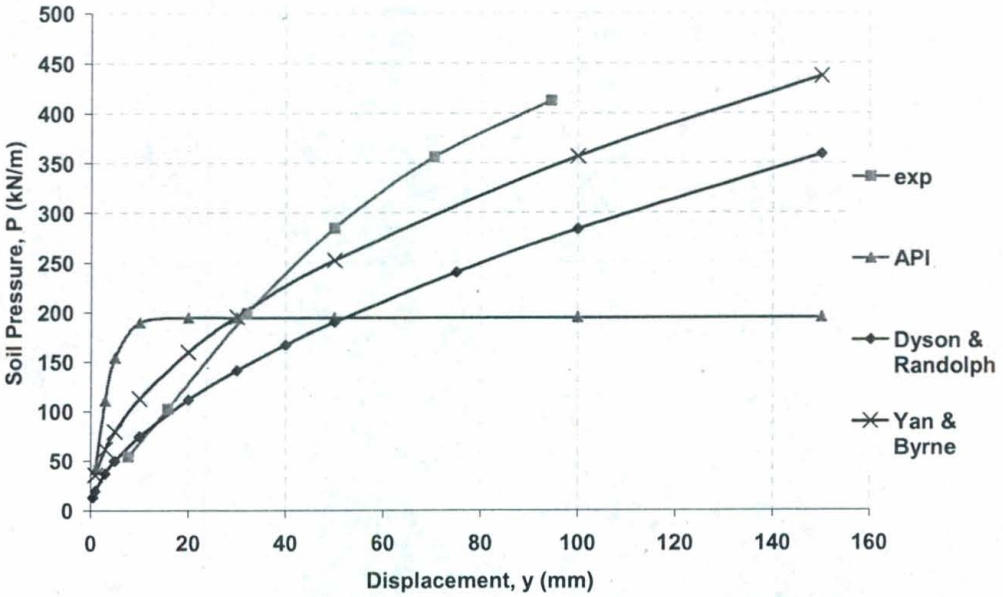

Figure (5.28) Comparison of experimental p-y Curves at 50g with others - Z/d= 1

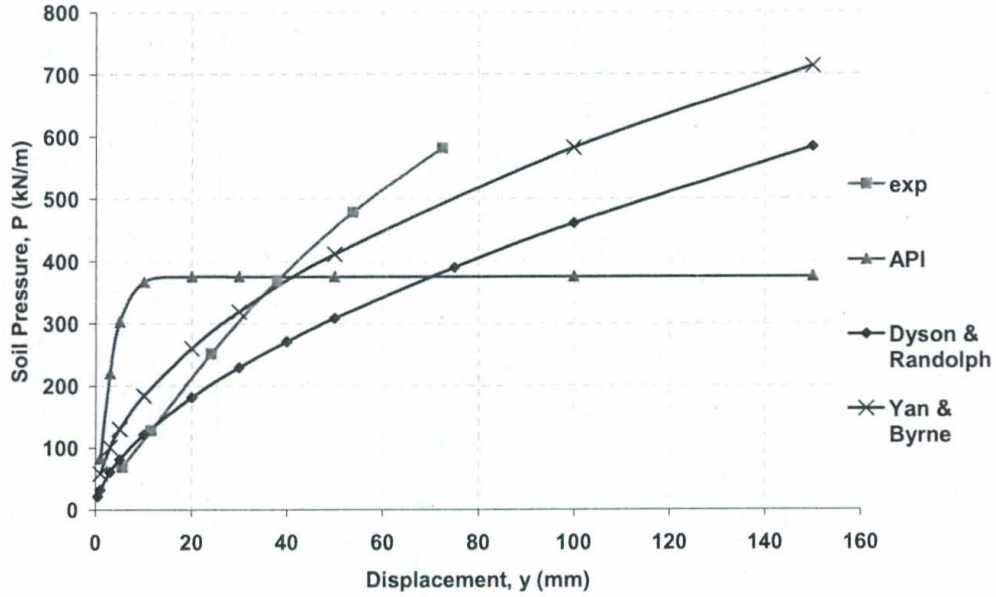

Figure (5.29) Comparison of experimental p-y Curves at 50g with others - Z/d= 2

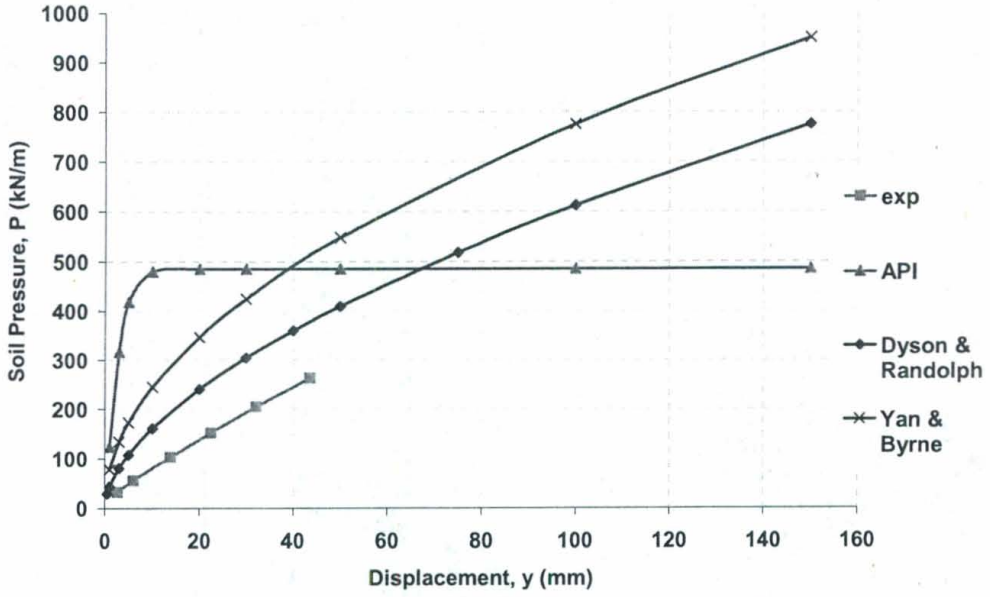

Figure (5.30) Comparison of experimental p-y Curves at 50g with others - Z/d= 3

It was found that the experimental *p-y* curves could be expressed by a soil parameter that is a function of stress level. The shear wave velocity of the sand (V_s) was measured in-flight bender elements at the three depths. The maximum shear modulus (G_{max}) and the maximum Young's modulus (E_{max}) had been calculated using the measured (V_s) and assuming Poisson's ratio of 0.25 for dense sand. The soil pressure, ($P = p/d$) can be normalized to the measured maximum Young's modulus (E_{max}).

It can be seen in Figs. (5.31) to (5.35) that after normalization all the experimental *p-y* curves of *Z/d* ratio of 1 to 3.5 collapse to a narrow band. The average fitting curve for all loading angles cases can be expressed as:

$$\frac{P}{E_{max}(Z/d)^n}\% = a\left(\frac{y}{d}\%\right)^b \tag{5.8}$$

The values of parameters n, a and b are given in Table (5.2). Similar equation was recommended by Yan and Byrne (1992) assuming n=0. The tests carried out by Yan and Byrne (1992) were for piles of small diameters around 0.5 m. For the current study, the pile diameters are 1 m and 1.4 m. So the parameter n is increasing by increasing the pile diameter. No functional form could be found for these parameters (n, a and b) from the current experimental results. Other factors (i.e. sand relative density, pile stiffness, and pile diameter) should be studied in an experimental parametric study to see how these parameters may change with other conditions. It should be noted that Eq. (5.8) with the suggested parameters values only valid for the current case of very dense sand.

Table (5.1) *a* and *b* Parameters Values

Loading angle	*n*	*a*	*b*
0°	0.6	0.081	0.756
16°	0.5	0.077	0.796
30°	0.7	0.07	0.747

From these *p-y* curves, it can be seen that the curves are becoming softer as the loading angle increases. This is opposite to the load displacement curves shown in Figs (5.6) and (5.7). This means that the interaction between the lateral and vertical resistance of a pile under inclined pullout should not be neglected. A pile subjected to an inclined pullout should not be designed as a pile loaded purely laterally. If we considered a constant value of the horizontal load component at any loading angle, the vertical pullout component will be increasing as the loading angle increases. At the mean time, the lateral soil pressure will decrease although the total load displacement behavior will be stiffer. This means that the interaction between the

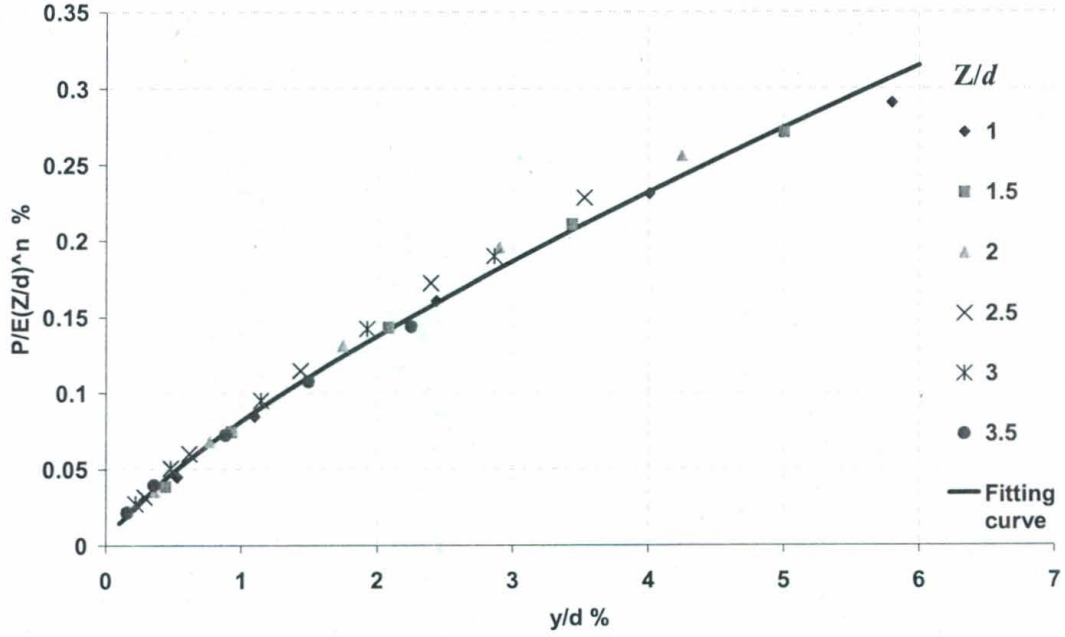

Figure (5.31) Normalized p-y Curves for 0° Loading Angle- 70g

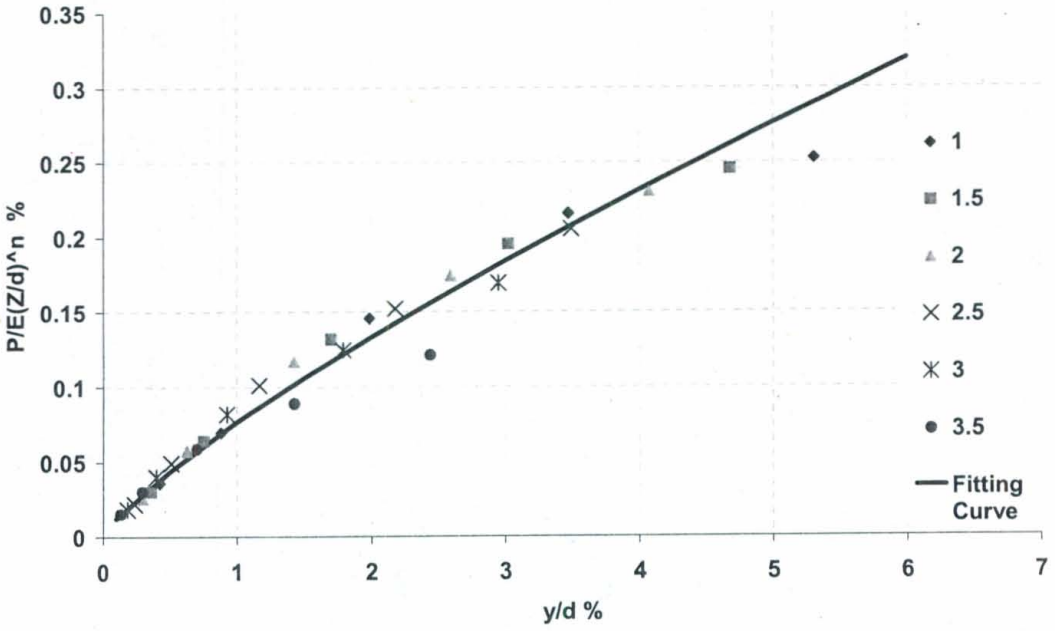

Figure (5.32) Normalized p-y Curves for 16° Loading Angle- 70g

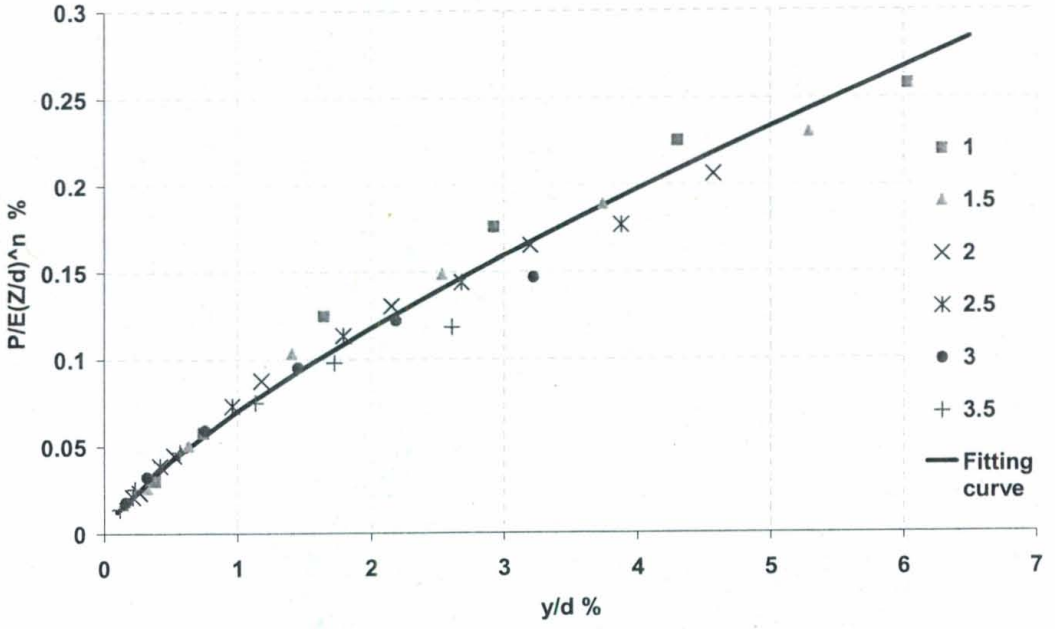

Figure (5.33) Normalized p-y Curves for 30° Loading Angle- 70g

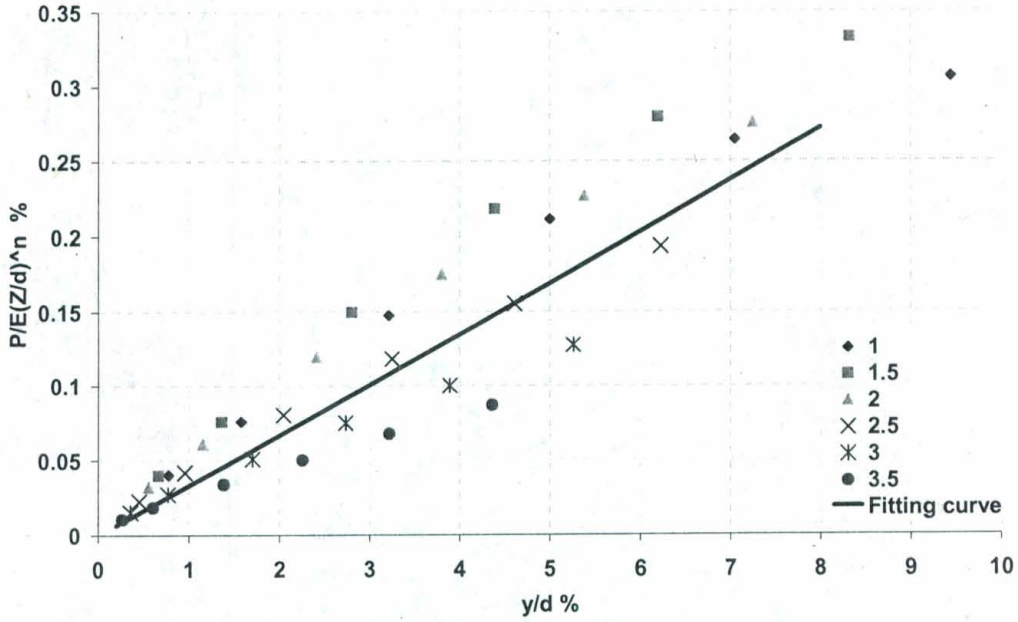

Figure (5.34) Normalized p-y Curves for 0° Loading Angle- 50g

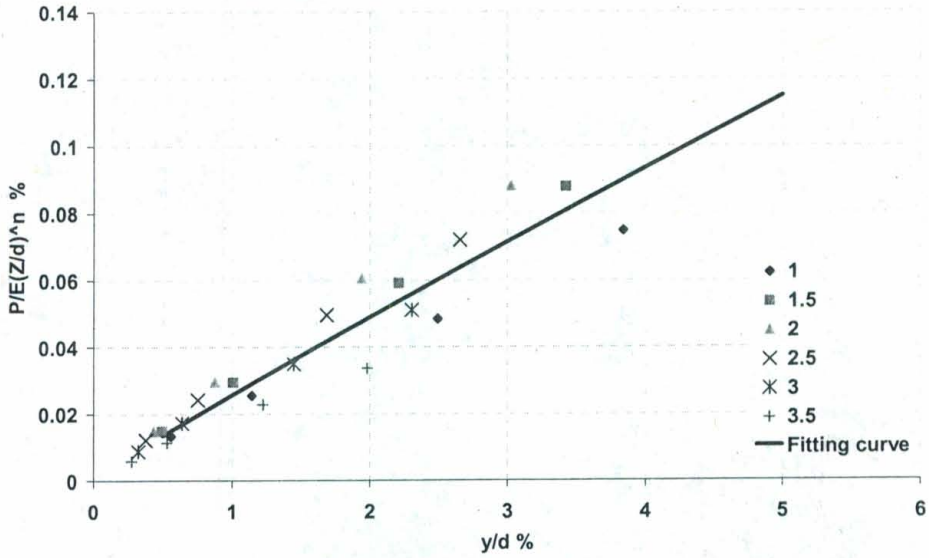

Figure (5.35) Normalized p-y Curves for 16° Loading Angle- 50g

lateral and vertical resistance of a pile under inclined pullout is significant. So to design a pile subjected to inclined pullout force, both lateral and vertical resistance should be considered even at small loading angles. Also, as discussed before, the pile tension capacity in the present inclined pullout tests are under-predicted. The interaction effect can be more significant at higher pile tension capacity.

In the present study we could not measure the vertical shear stress on the soil-pile interface from the strain gages readings. However, to well predict the behavior of the piles under inclined pullout, both the soil pressure and shear stress distributions should be considered in the analysis.

5.3. Conclusion:

In this chapter, the results of a series of centrifuge tests have been presented. The response of offshore anchor piles under mooring forces has been investigated. Bending moment profile has been measured along the pile. For design purpose a fitting equation was given to predict the maximum bending moment for any loading angle larger than 0° as a function of the horizontal component of the load at the pile head. *P-y* curves were calculated from the bending moment profiles. It was found that at the same *Z/d* ratio the *p-y* curves have the same initial stiffness and are becoming softer at large displacements as the loading angle increases. However, the total load displacement curves become stiffer as the loading angle increases. It can be concluded that to analyze anchor piles under inclined pullout forces using load transfer curves at soil-pile interface, the use of *p-y* curves alone is not enough. The shear stresses at the soil-pile interface (called *t-z* curves) should be considered in the analysis. Neglecting these shear stresses will overestimate the design of these anchor piles in terms of maximum bending moment and the expected total carried load at the pile head.

Chapter 6

Numerical Modeling Validation

6.1. Introduction:

The scope of centrifuge experimental results is extended by means of a parametric study, using the finite element method (FEM). FEM has been widely used for geotechnical engineering application. Many features have been developed in this method made it easy to use it including; coupled pore fluid elements for porous media, contact elements between two surfaces, large deformation analysis, etc. Also, one of the advantages of this method is the ability to use nonlinear elasto-plastic models that can model the soil behavior under different loading conditions.

In this chapter, a three dimensional (3-D) Finite Element Model (FEM) has been established to study the soil-pile interaction behavior under mooring forces. Numerical analysis was carried out using the ABAQUS / Standard 6.7 finite element analysis program (Hibbitt, et. al. 1998). Mohr-Coulomb plastic model has been used to model the soil. The model has been calibrated based on the centrifuge tests discussed before. The model parameters selection and the comparison with the centrifuge test results will be discussed.

6.2. Model Geometry and Meshing:

Figure (6.1) shows the geometry of the FEM. The soil boundaries extend horizontally 30 times the pile diameter. The bottom soil boundary is below pile tip 10 times the pile diameter. The dimensions of analysis domain have been selected larger than the centrifuge model to reduce boundary effects.

The finite element mesh used in the analysis is shown in Fig. (6.1). The elements used are 8-node continuum elements with porous properties (as shown in Table (6.2)) for those elements modeling the soil. Due to the symmetric loading condition only a half-cylinder representing the soil and the pile was considered. The elements are biased towards the pile to have finer mesh close to the pile where the stresses are expected to be higher. The mesh is coarser far from the pile to reduce the analysis processing time. A finer mesh was used to check the mesh refinement effect on the results. The fine mesh is shown in Fig. (6.2). Both the lateral load – lateral displacement curves of the coarse and fine mesh models are shown in Fig. (6.3). Both curves are very close.

The pile is modeled as a pipe pile as in the centrifuge test. The pile section has a flexural and axial stiffness same as given in Table (3.2). To have both the flexural and axial stiffness same as in the centrifuge test, pile wall thickness and Young's modulus of pile material were recalculated. Pile section dimensions and material properties are given in Table (6.1).

The model boundary at the bottom is restrained from displacement in all directions. The side boundary is restrained from the horizontal displacement. At the symmetry plane, the boundary is restrained from displacement in the perpendicular direction.

Table (6.1) Pile Section Properties for FEM

Characteristic	Prototype (70g)	Prototype (50g)
External diameter, d (m)	1.4	1.0
Wall thickness, t (m)	0.2725	0.195
Young's Modulus, E_p (MPa)	27609	27592
Poisson's ratio	0.3	0.3

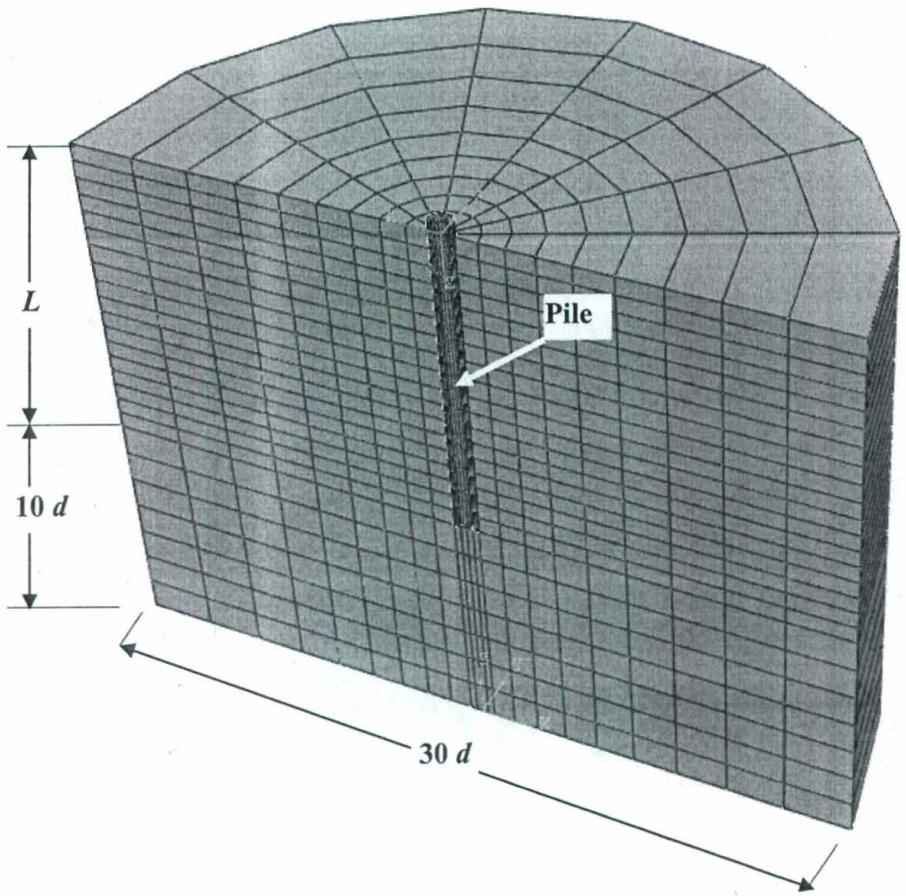

Figure (6.1) Finite Element Model with Coarse Mesh

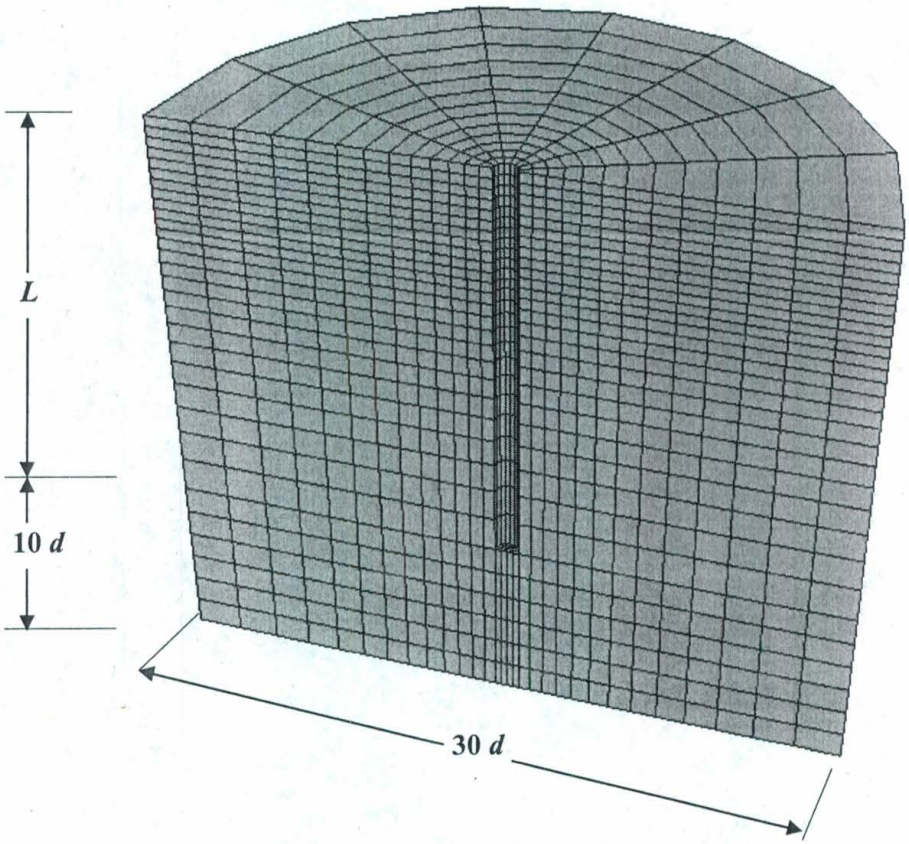

Figure (6.2) Finite Element Model with Fine Mesh

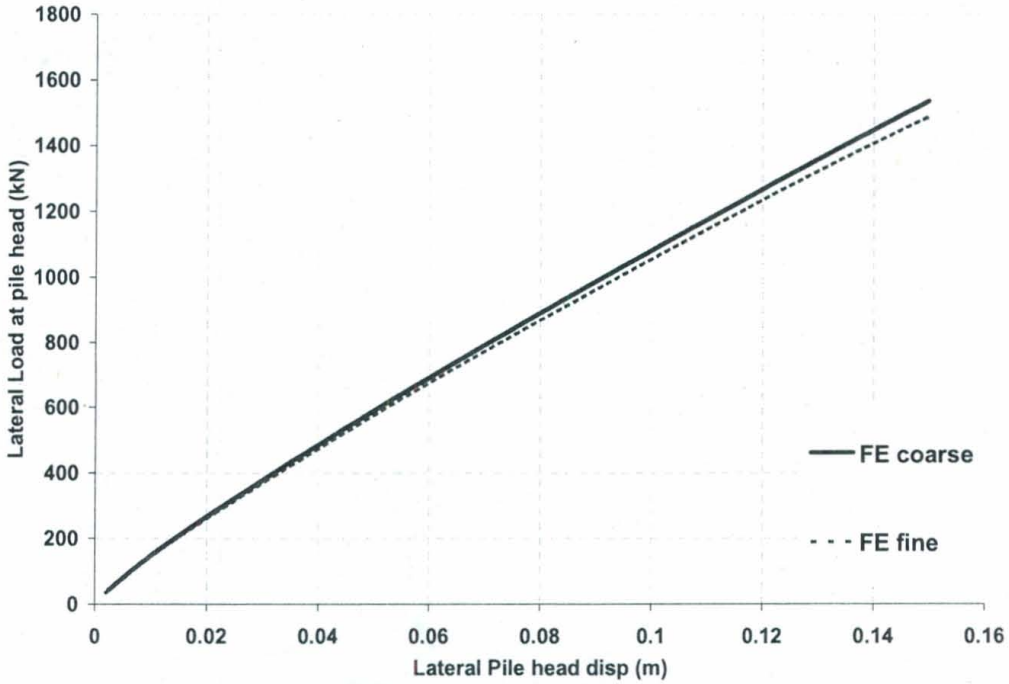

Figure (6.3) Lateral Load Displacement Curve of Coarse and Fine Mesh using FEM

6.3. Constitutive Models:

Different constitutive models have been used to model both the pile and soil. Both models will be discussed.

6.3.1 Pile Modeling:

The pile material is assumed to be linear elastic. This assumption is valid as the pile did not reach the yield bending moment during the centrifuge tests. The linear elastic material is defined by the elastic young's modulus of pile material (E_p) and Poisson's ratio (v_p). Offshore anchor piles are made usually of steel. Young's modulus of steel is 2.1 x 10^8 kN/m^2 and Poisson's ratio (v_p) of steel is about 0.3. However, to simulate both the flexural and axial stiffness of the pile in the centrifuge tests (based on the centrifuge scaling laws as discussed in chapter 3), an equivalent Young's modulus had been calculated. The values of E and v used in the analysis are given in Table (6.1).

6.3.2 Soil Modeling:

The sand is assumed to behave as an elastic perfectly plastic material obeying Mohr-Coulomb failure criterion. In the ABAQUS Mohr- Coulomb model, the yield behavior depends on the hydrostatic pressure. One of the consequences of this is that the material becomes stronger as the confining pressure increases. The yield behavior, as shown in Fig. (6.4), is mainly dependent on the major and minor principle stresses (σ_1, σ_3) and is independent of the value of the intermediate principal stress (σ_2). When mapped into three-dimensional stress space, a Mohr-Coulomb criterion resolves into an irregular hexagonal pyramid, as shown in Fig. (6.5). This pyramid forms the failure/yield envelope, which in turn governs how the soil will behave. The material will behave elastically if the stress point lies within the failure envelope. However, if the stress reaches the yield surface the material will undergo plastic deformation.

Mohr-Coulomb model parameters that are needed to calibrate the model are the effective unit weight of the soil, (γ'), soil Young's modulus (E_s), soil Poisson's ratio(ν), the effective angle of internal friction, (φ'), the dilation angle, (ψ), and the effective cohesion, (c').

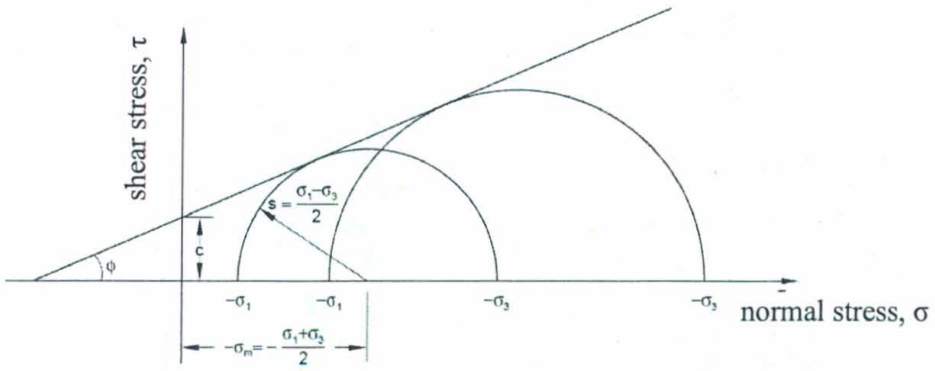

Figure (6.4) Mohr Coulomb's failure surface

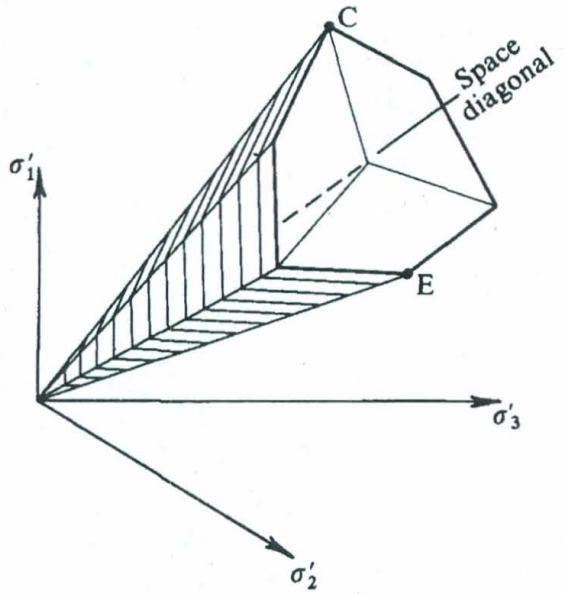

Figure (6.5) Mohr-Coulomb yield surface in principal stress space ($c = 0$)

These parameters were calculated using some available correlations of the Cone Penetration Tests (CPTs) carried out in the centrifuge. The correlation is usually based on the standard cone size of 36 mm. To simulate the standard cone in centrifuge, one should use a probe of less than 1mm diameter for centrifuge acceleration higher than 30g. This is impractical because this will lead to grain size effects which can affect the cone penetration results. However, using a cone of 10 mm diameter at 50g centrifuge acceleration will simulate a cone of 500 mm diameter in prototype scale which is more representing a pile not a cone. White and Bolton (2005) found from the database of field load tests assembled by Chow (1996), that no scale effect on q_b/q_c with absolute pile diameter is evident; where q_b is pile end bearing resistance and q_c is the standard cone resistance. They recommended q_b/q_c =0.9. This ratio can increase to unity if we excluded the effect of partial embedment and partial mobilization. Partial embedment is related to shallow depth and the presence of weak layers. Partial mobilization is the case where the pile capacity is not fully mobilized which is not the case for cone continuous penetration case. This means that the model cone in the centrifuge that is considered as a pile in prototype scale will have same resistance as the standard cone at deep penetration in

homogeneous soil. Van der Poel and Schenkeveld (1998) showed a good agreement between the cone penetration resistance in centrifuge and that predicted by Schmertmann (1978). Also as will be discussed later, the peak friction angle calculated using available correlation shows a good agreement with that calculated using author available correlations based on centrifuge tests.

6.3.2.1 Elastic Modulus:

Sand Young's modulus was calculated using the correlation suggested by Schmertmann (1970) and Robertson and Campanella (1983). Ferguson and Ko (1984) performed a series of centrifuge tests to examine the application of cone penetration test in sand in centrifuge. They concluded that Schmertmann's correlation is reasonably conservative for their centrifuge tests. Schmertmann (1970) related the constrained modulus (M) directly to the measured cone tip resistance (q_c), particularly in fine sandy soils:

$$M = \alpha \cdot q_c \tag{6.1}$$

where α is ranged between 3 to 9 as recommended by Baldi et al. (1982). In the present calibration a value of 5 was found to give good matching with the centrifuge results.

Young's modulus and constrained modulus are both related via elastic theory:

$$E_s = \frac{(1+\nu)\cdot(1-2\nu)}{(1-\nu)} \cdot M \tag{6.2}$$

6.3.2.2 Sand friction angle:

Robertson and Campanella (1983) recommended a relationship that correlates the cone penetration resistance (q_c) to the peak friction angle (φ') for unaged, uncemented quartz sand as:

$$\varphi' = \arctan[0.1 + 0.38 \cdot \log(q_c/\sigma'_v)] \tag{6.3}$$

Bolton (1986) reviewed extensive laboratory data on sands and developed a simplified relationship between relative density, effective mean stress (p') and peak friction angle (φ'). He introduced a new relative dilatancy index (I_R) of the form:

$$I_R = D_r(10 - \ln(p')) - 1 \tag{6.4}$$

He also correlated the peak friction angle (φ') and the critical state friction angle (φ'_c) to I_R:

$$\varphi' - \varphi'_c = 3I_R^{\circ} \tag{6.5}$$

To use Bolton's method to calculate the peak friction angle (φ') profile, both the sand relative density (D_r) and the critical state friction angle (φ'_c). Vaid et al. (2001) reported a value of 34° for the critical state friction angle (φ'_c) of Fraser River sand. To obtain relative density, density cubes were used during centrifuge tests sample preparation. The relative density was changing from 88% at the bottom of the model to about 84% at the top of the model. Bolton and Gui (1993) correlated the normalized cone tip resistance ($Q = \frac{q_c - \sigma_v}{\sigma'_v}$) to the relative density (D_r) from a series of centrifuge tests as:

$$D_r(\%) = 0.2831 + 32.964 \cdot Q \tag{6.6}$$

Figure (6.6) shows the calculated sand relative density profile using Eq. (6.6). The calculated peak friction angle of sand using Eq. (6.3) and Eq. (6.5) are plotted in Fig. (6.7). There is a good agreement between the two equations. At deep depths, both equations suggest a peak friction angle ranges between 43° and 44°. Chakraportty (2008) suggested a value of 43° for Fraser River sand at a relative density of 80%.

However, it can be seen that there is an obvious reduction in the relative density and consequently sand shear strength at shallow depths less than 80 mm and 60 mm (in centrifuge model scale) for 50g and 70g tests, respectively. This underestimation at low confining stress using CPT method was observed by many authors (Bolton and Gui, 1993, Puech and Foray, 2002, Robertson, 2010, and others). At shallow penetrations in sands (less than 3m in prototype scale), the increase of the cone resistance with depth is strongly affected by the low confining pressures, Puech and Foray (2002). Figure (6.6b) shows that this underestimation in both 50g and 70g tests happens at vertical effective stress of 40 kPa which is same as recommended by Puech and Foray (2002). To correct this underestimation, the relative density for vertical effective stresses at 40 kPa was taken as a constant value for all vertical effective stresses less than 40 kPa. The modified profile of relative density is shown in Fig. (6.6) as a constant value above 40 kPa vertical stress. The peak friction angle profile calculated using the modified relative density profile is shown in Fig. (6.8). It can be seen that peak friction angle using this modified relative density increases rapidly by decreasing depth or confining stress. This behavior has been observed by many researchers (Turner and Kulhawy, 1994, Zhu, 1998, Gay et al., 2003, and Lancelot et al., 2006).

The calculated internal friction angle profile was implemented in the FEM (as function of depth). A comparison between the present method and that given by Zhu (1998) is shown in Fig. (6.9). There is a good agreement between both methods. The high value of internal friction angle of dense sand at shallow depth (low confining stress) was also observed offshore at the Grand Bank as reported by Thompson and Long (1989). It was also observed by Lancelot et al. (2006) in dense sand for Hostun sand at low confining stresses. It can be concluded that these high values of internal friction angle can be observed for angular to subangular dense sand which is the case of Fraser River sand used in the present centrifuge study.

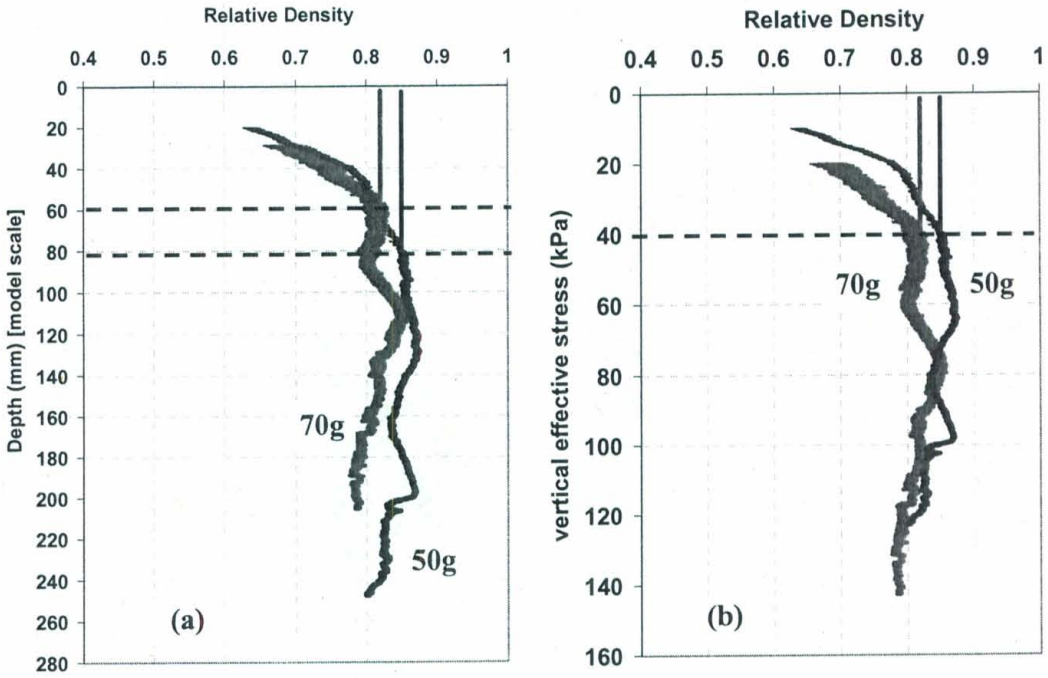

Figure (6.6) Relative density profile along depth: (a) versus depth (in model scale), (b) versus vertical effective stress

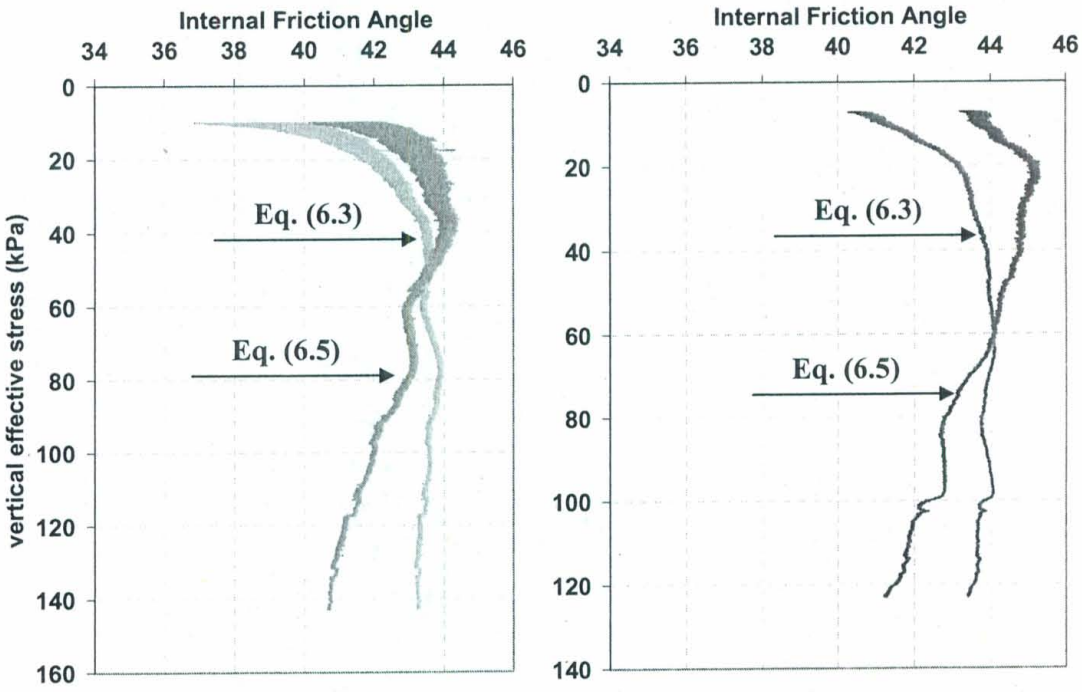

Figure (6.7) Sand friction angle profile along depth: (a) 70g test, (b) 50g test

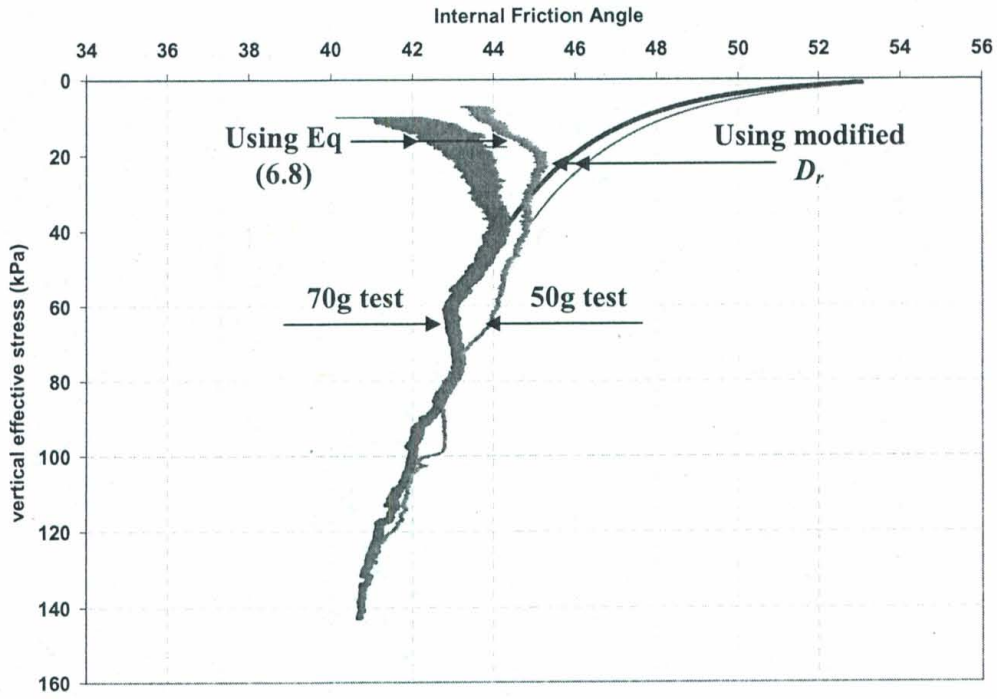

Figure (6.8) Sand friction angle profile along depth using relative density by Eq. (6.6) and the modified one

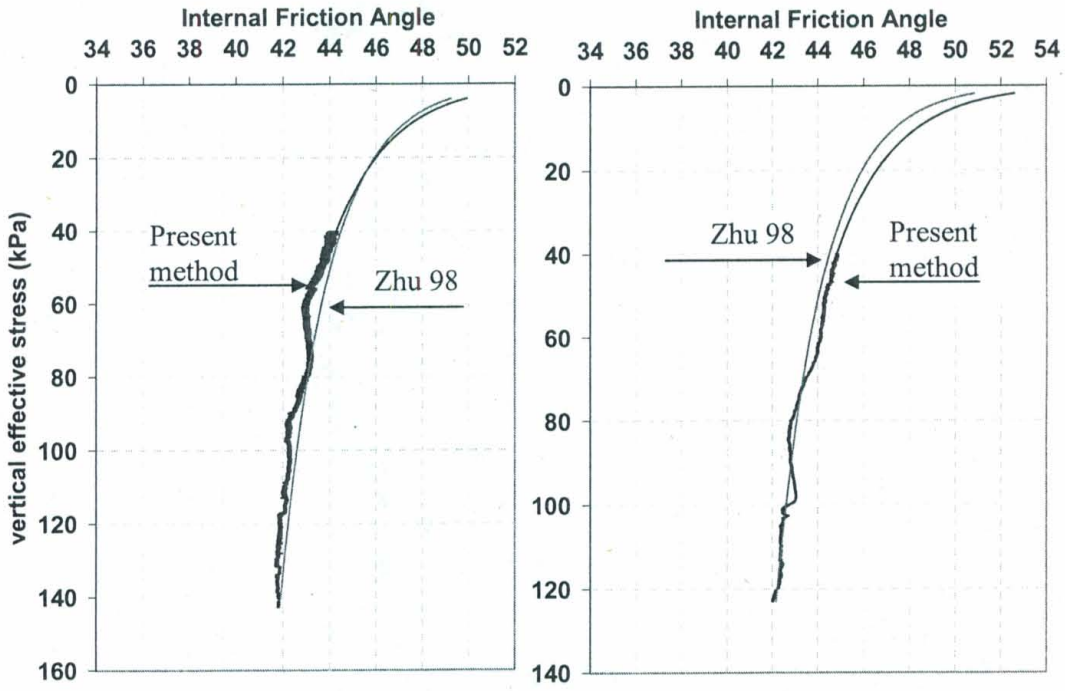

Figure (6.9) Sand friction angle profile along depth using the modified relative density and Zhu (1998): (a) 70g test, (b) 50g test

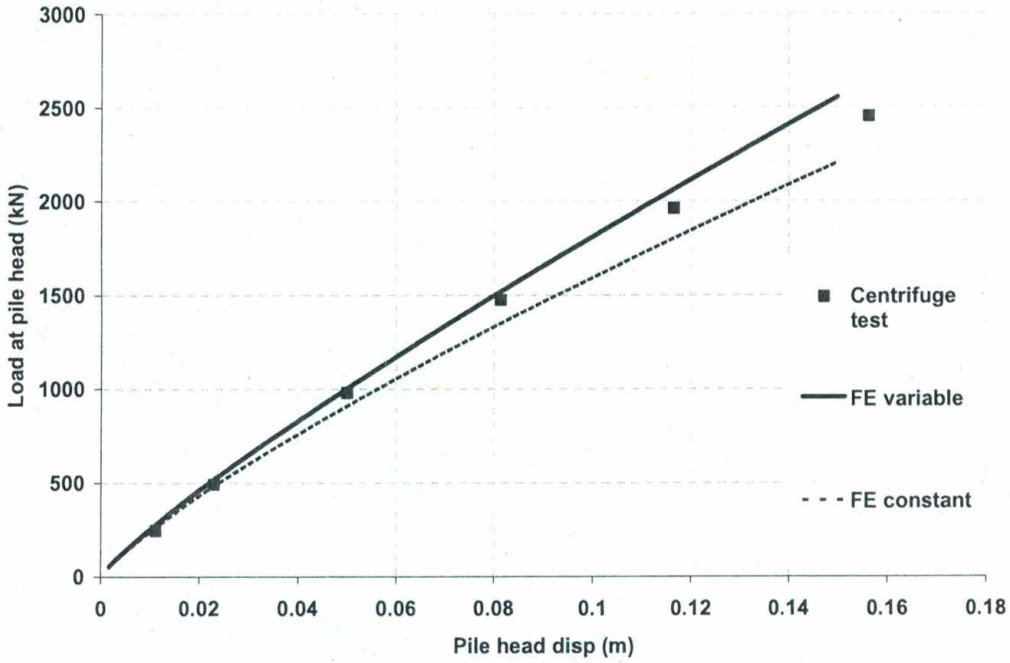

Figure (6.10) Lateral Load Displacement Curve using Variable and Constant Profile of Peak Friction Angle with Depth

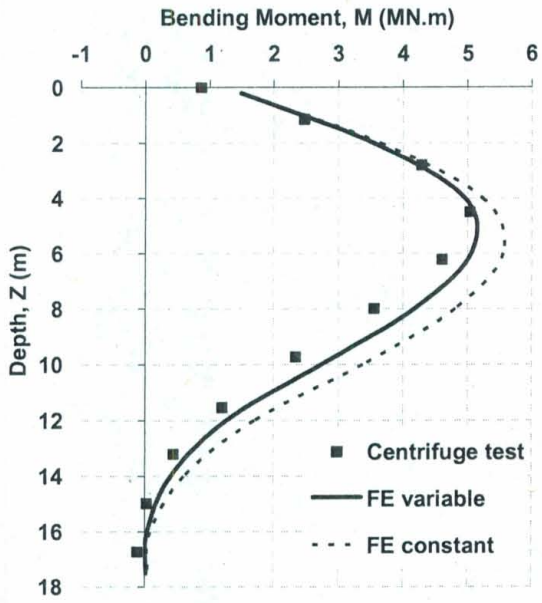

Figure (6.11) Bending Moment Profile at $H = 1000$ kN using Variable and Constant Profile of Peak Friction Angle with Depth

The importance of the profile of peak friction angle at shallow depths rises for laterally loaded flexible pile analysis. The present method and a constant value of peak friction angle (average value of values at vertical effective stresses > 40 kPa) have been used in the present FEM. The present method provided results of good agreement with the centrifuge test results in terms of load displacement curve and bending moment profile of the pile. The constant peak friction angle underpredicted the load displacement curve and overpredicted the pile bending moment profile. The comparison is shown in Figs. (6.10) and (6.11).

6.3.2.3 Sand dilation angle:

Non-associated flow was considered in Mohr Coulomb Model. Sand dilation angle was calculated using the equation suggested by Bolton (1986):

$$\psi = \frac{\varphi' - \varphi'_c}{0.8} \tag{6.7}$$

6.3.3 Soil-Pile Interaction:

A basic Coulomb frictional model was used to govern the interaction between the pile and sand surfaces (Hibbitt, Karlsson, Sorensen, Inc., 1998). The interaction at the pile-soil surface can range from perfect contact where no relative sliding between soil and pile occurs to perfect sliding conditions where no friction develops along the shaft of the pile. It was assumed that the soil and pile are both deformable bodies and can undergo finite relative sliding.

The contact surface approach implemented in ABAQUS allowed for separation and sliding of finite amplitude and arbitrary rotation of the contact surface. When surfaces are in contact, they usually transmit shear as well as normal forces across their interface. There is generally a relationship usually expressed in terms of the stresses at the interface of bodies:

$$\tau = \mu \cdot \sigma_h \tag{6.8}$$

where τ is the shear stress on the contact surface μ is the friction coefficient = tanδ; where δ is the interface angle between sand and pile, and , σ_h is the normal stress on the contact surface.

Fioravante (2002) defined the normalized roughness ($R_n = R_t/d_{50}$; where, R_t = maximum pile surface roughness, measured as peak to peak over a skin length L_m = 0.8 to 2.5 mm). The interface is considered smooth if the normalized roughness $R_n <$ 0.02. The interface is rough if R_n >0.1. He did a series of centrifuge tests and direct shear constant stiffness tests to evaluate the effects of the interface roughness on the shaft friction mobilized. He provided a relationship between R_n and the friction coefficient μ for two sands, medium fine quartz sand and very fine quartz sand. It was found from his results that for smooth interface μ ranges from 0.25 to 0.75 for R_n between 0.01 to 0.1. For the centrifuge tests in the current study, the pile was coated with epoxy layer. The epoxy layer provided a smooth surface for the pile surface. However, due to pile driving at high stresses, the lower one third of the pile length was abraded. The roughness of this part could not be measured. De Nicola and Randolph (1999) used model piles in centrifuge coated with epoxy. They recommended a value of 0.53 for the friction coefficient between epoxy surface and sand. In the FEM analysis a value of 0.55 was assumed along the soil-pile interface.

The pile installation method has a major effect on the pile loading behavior. For offshore driven piles as discussed before, the lateral stresses will increase in the soil in a limited zone adjacent to the pile (1.5 to 2 times pile diameter from pile surface). The lateral earth pressure coefficient K after pile installation was calculated based on ICP' (2005) method. The soil model has been divided into layers. The lateral earth pressure coefficient (K) values have been assigned to each layer. Although the increase in the lateral stress should be limited to a limited zone around the pile, it has been found, to simplify the model and due to the analysis convergence, that

increasing the lateral stress along the full width of the soil model has little effect on the results as the main increase in the lateral stresses is concentrated to the pile tip vicinity which will have a negligible movement for a flexible pile.

In ABAQUS, the elastic slip stiffness is by default a function of the contact pressure and a critical value of elastic slip at which the slip occurs. This value, by default in ABAQUS, is 0.005. However, this default value leads to a very stiff slip interface response as was also observed by Merifield et al. (2008). The elastic slip stiffness is adjusted to match the stiffness observed in the centrifuge tests. Table (6.2) summarize the input parameters used in the FEM validation.

Table (6.2) Soil Input Parameters in the FEM

Characteristic	Value
Sand Young's Modulus (E), (MN/m^2)	3.7 q_c
Sand effective friction angle (φ')	Fig. (6.9) – ranges: 52° to 42°
Sand dilation angle (ψ)	Eg. (6.7) – ranges: 22.5° to 10°
Soil-Pile friction coefficient (μ)	0.55
Lateral earth pressure coefficient (K)	Using ICP'2005
Poisson's ratio	0.3
Sand hydraulic conductivity (k) (m/sec)	0.0001
Sand saturation (S)	1
Cohesion, c' (kPa)	0.1

6.4. FEM Outputs Computations:

Bending moment of the pile was computed at the outermost nodes of the pile in the loading direction. Equation (6.9) was used to calculate bending moment (M):

$$M = \frac{2 \cdot \sigma_b . I_p}{d} \tag{6.9}$$

where $\sigma_b = (\sigma_1 - \sigma_2)/2$; where σ_1 and σ_2 are the axial stress at both the tension and compression sides of the pile at the same depth, respectively, I_p is the moment of inertia of the pile cross section, and d is pile diameter.

Soil pressure can be directly obtained from ABAQUS as the contact pressure at the contact surface between pile and soil. Also, the calculated bending moment profile of the pile was fitted using quintic spline as explained in chapter (4). The fitted function was differentiated twice to get the soil pressure profile along the pile. A comparison between soil pressure profile obtained from ABAQUS and calculated from bending moment profile shows a very good agreement between both methods as shown in Fig. (6.12). Pile deflection profile was directly obtained from ABAQUS at pile nodes along the pile.

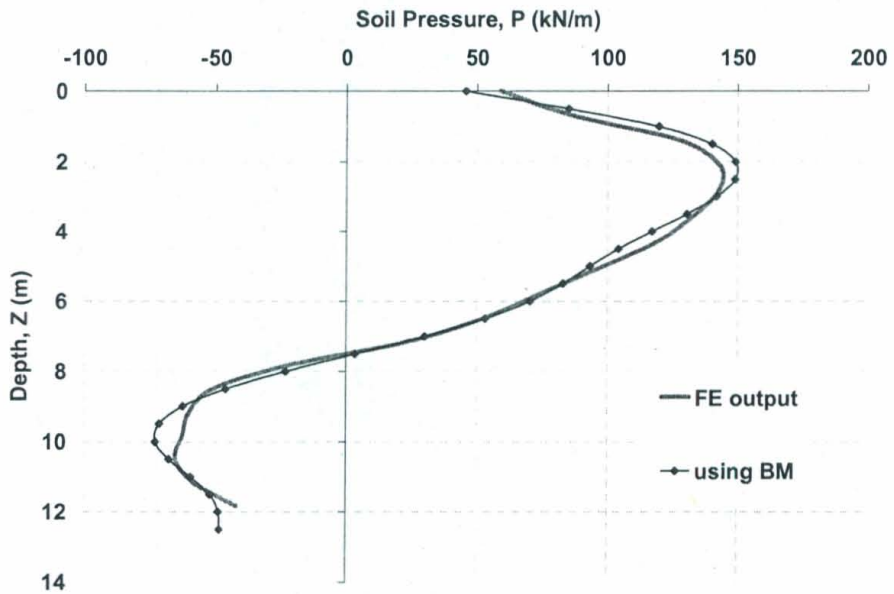

Figure (6.12) Soil Pressure Profile at H = 500 kN using ABAQUS output and Bending Moment Profile Double Differentiation- 50g test

6.5. Results and Discussion:

In this section a comparison between the centrifuge tests results and the FEM will presented. The comparison will be divided to pure tension loading case, pure lateral loading, and inclined pullout loading cases with loading angles (0°, 16°, and 30°) to horizontal.

6.5.1 Pure Tension Loading:

Figure (6.13) shows the vertical load – vertical displacement relationship at pile head for the test at 50g. The 70g test, for tension loading case, was not simulated using FEM as the calculated K profile was very high (value of 20 at pile tip) which caused convergence problems. It can be seen that there is a good agreement between FEM and the centrifuge test result in terms of the ultimate tension capacity and the initial stiffness. There is a change in the stiffness of the centrifuge test results because of soil dilation at soil-pile interface which is due to small model scale as discussed in the previous chapter.

6.5.2 Pure Lateral Loading:

Figure (6.14) shows the lateral load – lateral displacement relationship comparing both the centrifuge test and FEM for 70g and 50g tests. It can be seen that there is a good agreement between the centrifuge test and the predicted results using FEM. FEM predicts the initial stiffness same as that in the centrifuge tests. FEM predicts the bending moment profile in a good agreement especially the maximum bending moment values and depths for 70g test as shown in Fig. (6.15-a). However, for 50g tests, FEM load displacement curve becomes little stiffer than the centrifuge tests at higher loads with the maximum bending moment location at deeper depth than that at centrifuge test as shown in Fig. (6.15-b).

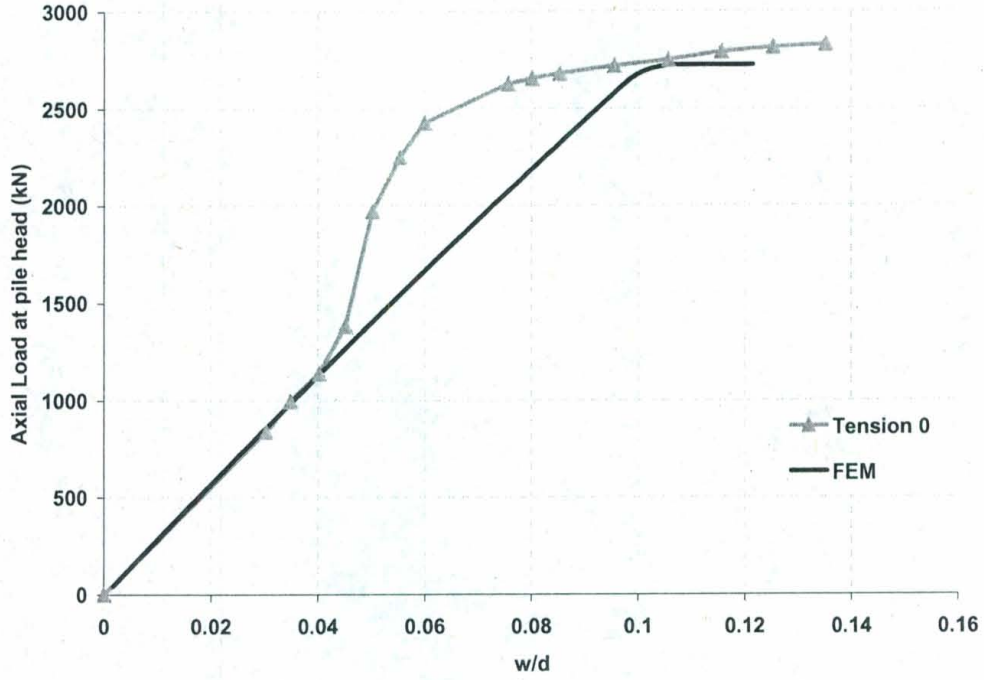

Figure (6.13) Vertical Load – Normalized Vertical Displacement Relationship – Comparison between FEM and Centrifuge Test Result

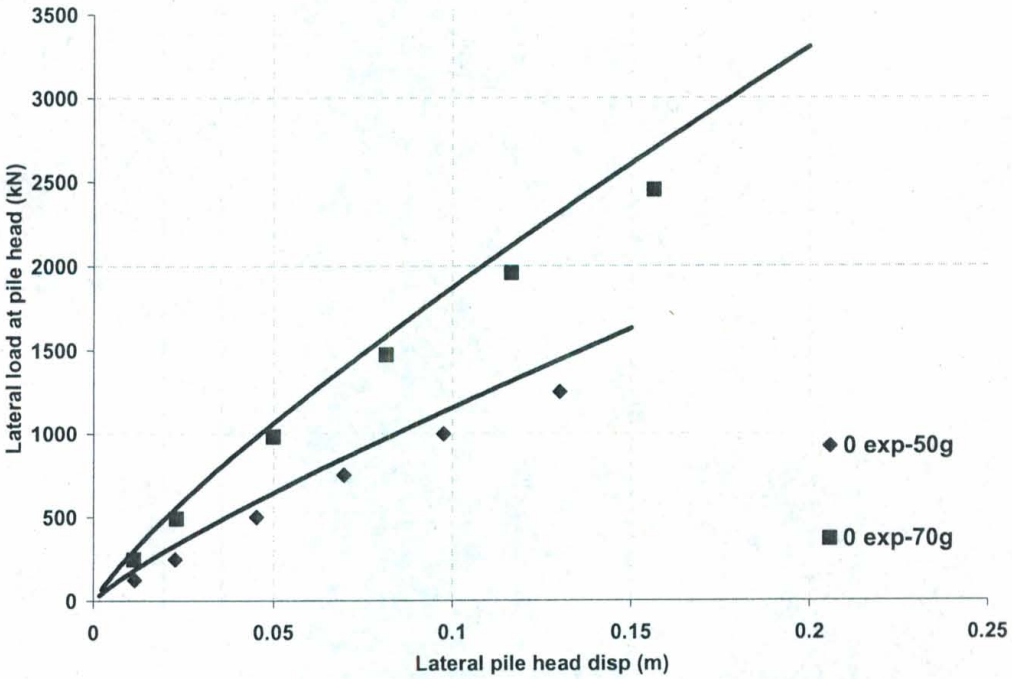

Figure (6.14) Lateral Load – Lateral Displacement Relationship at Pile Head– Comparison between FEM and Centrifuge Test [FEM is a Solid Line]

Figure (6.16) shows soil pressure distribution along pile at different load increments for 70g and 50g tests. At 70g test, FEM predicts well soil pressure at shallow depths at small load increments. However, by increasing the load at pile head, FEM under-predicts the maximum soil pressure. The same behavior can be seen for 50g test with more under-prediction of soil pressure. This under-prediction in case of 50g test could be due to the deeper prediction of maximum bending moment location. This miss prediction of maximum bending moment location caused an under-prediction of bending moment at shallow depth and consequently under-prediction in soil pressure. Also, this under-prediction, in both 70g and 50g tests, could be due to a disadvantage in Mohr-Coulomb model (MC). MC model in ABAQUS is an elastic perfectly plastic model. It does not harden as the stresses in the soil reach the yield stage which causes this under prediction in soil pressure at high loads.

For pile deflection profile, FEM gives good prediction above the rotation point observed in the centrifuge tests results. FEM profile shows a flexible pile behavior in contrast to a rigid pile behavior observed in the centrifuge tests. According to Broms (1964) and Meyerhof (1995), the pile soil rigidity in the present test should be flexible. This is supported by the FEM results.

For design purposes, load-displacement curve and maximum bending moment are used. In the present study, it can be seen that FEM predicts well the load-displacement curve. Maximum bending moment values predicted by FEM are in a very good agreement with the centrifuge tests results as shown in Fig. (6.18). It can be concluded that FEM can simulate the behavior of laterally loaded piles with a good agreement.

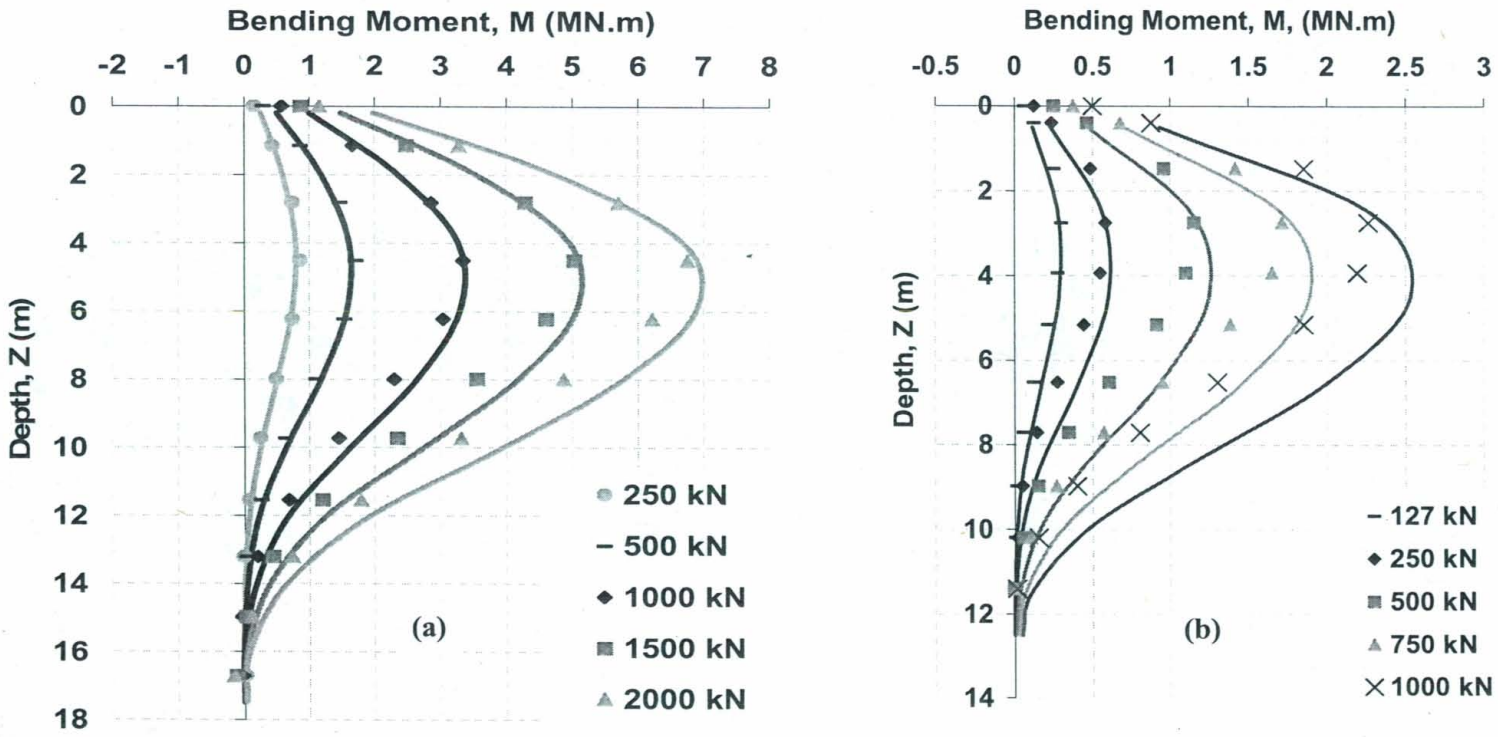

Figure (6.15) Bending Moment Distribution for Pure Lateral Loading Case (a) 70g test, and (b) 50g test, [FEM Curve is a Solid Line]

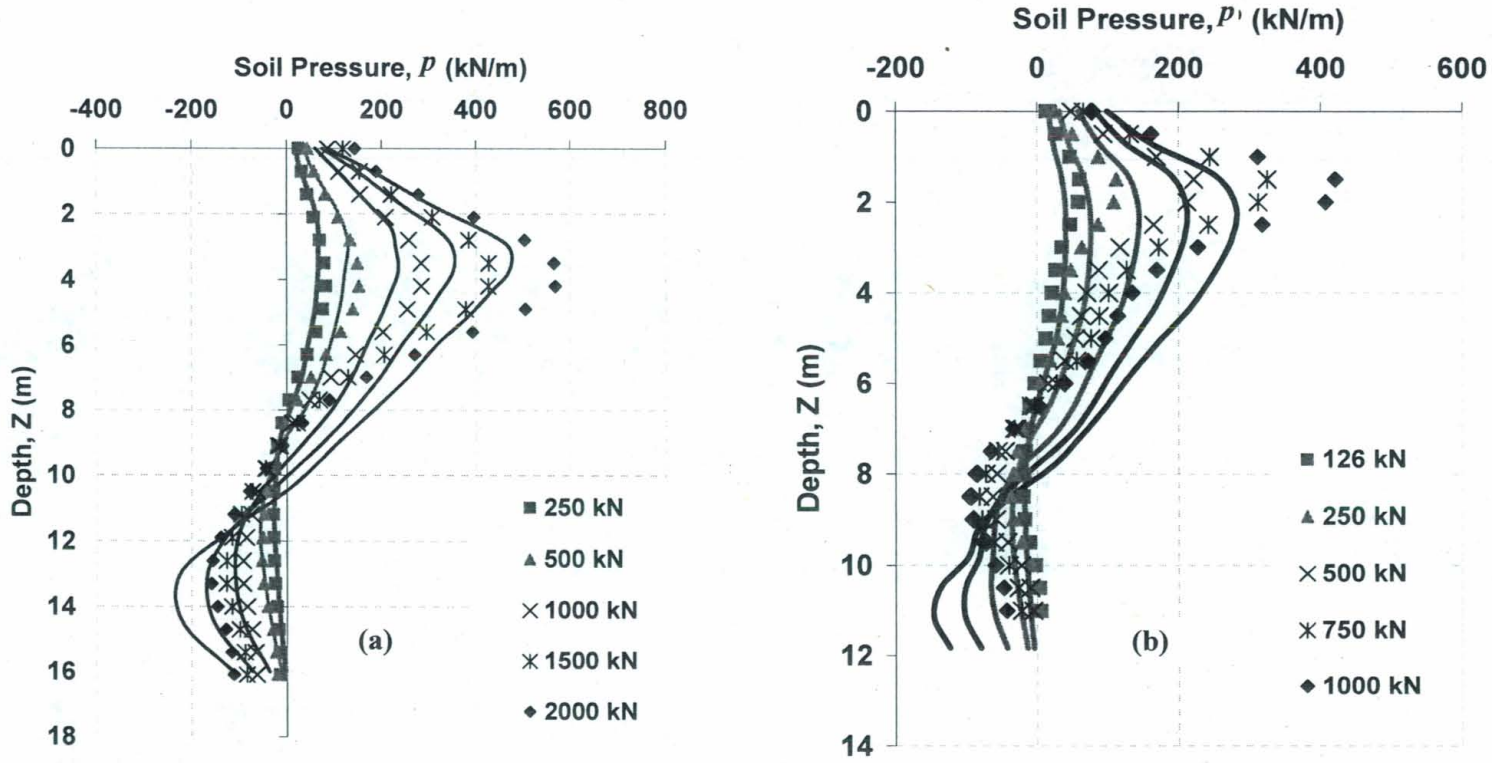

Figure (6.16) Soil Pressure Profile for Pure Lateral Loading Case (a) 70g test, and (b) 50g test, [FEM Curve is a Solid Line]

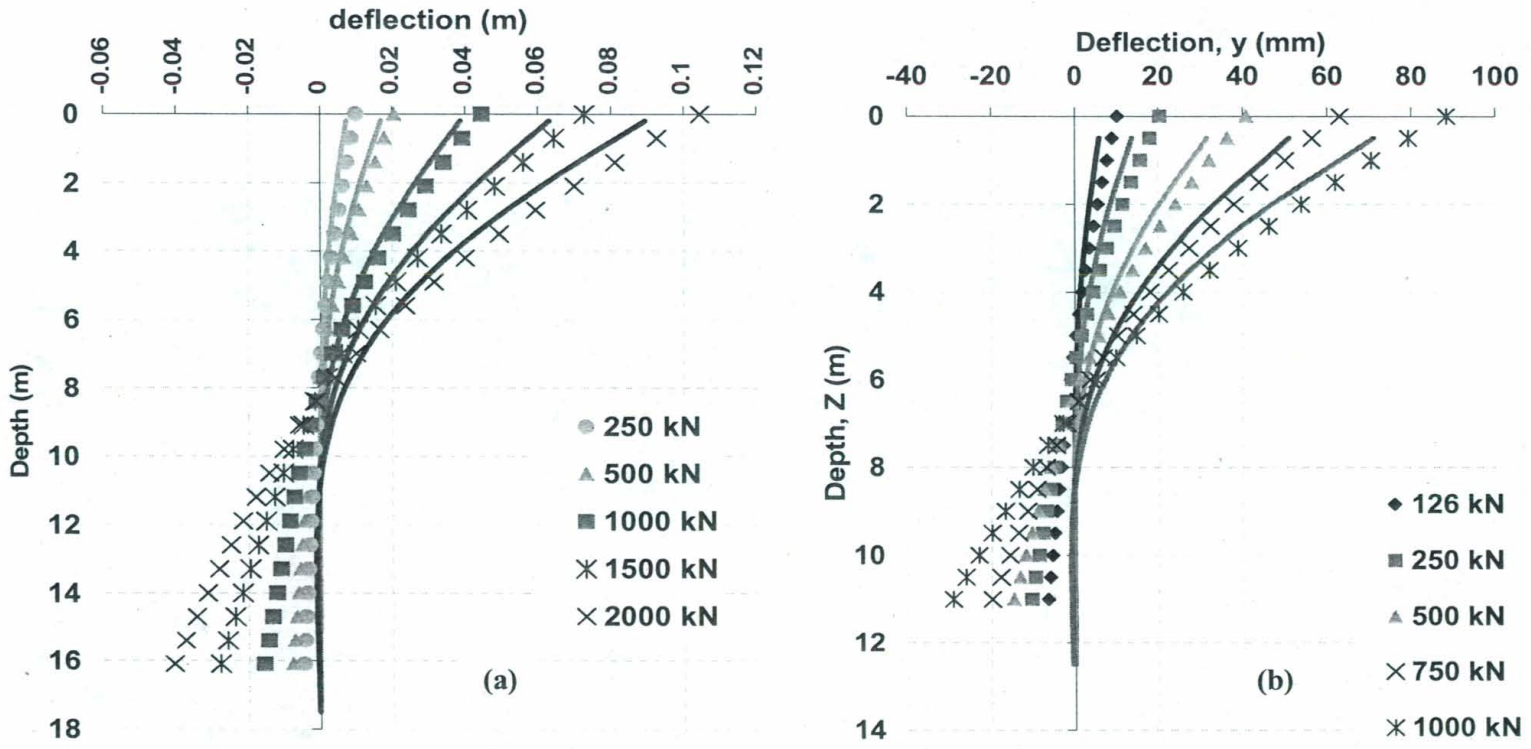

Figure (6.17) Pile Deflection Profile for Pure Lateral Loading Case (a) 70g test, and (b) 50g test, [FEM Curve is a Solid Line]

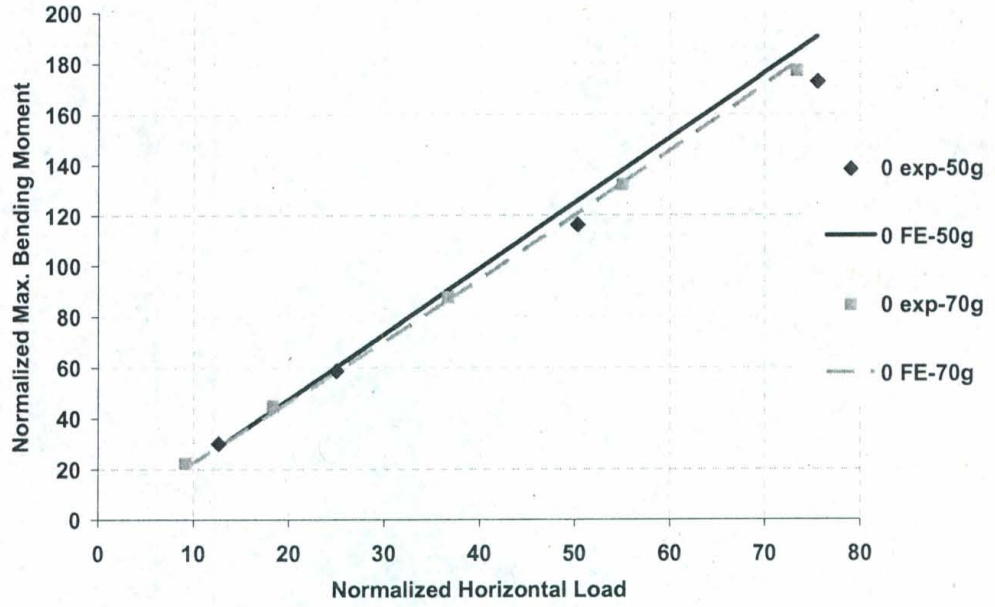

Fig. (6.18) Normalized Horizontal Load versus Normalized Max. Bending Moment for Pure Lateral Loading Tests.

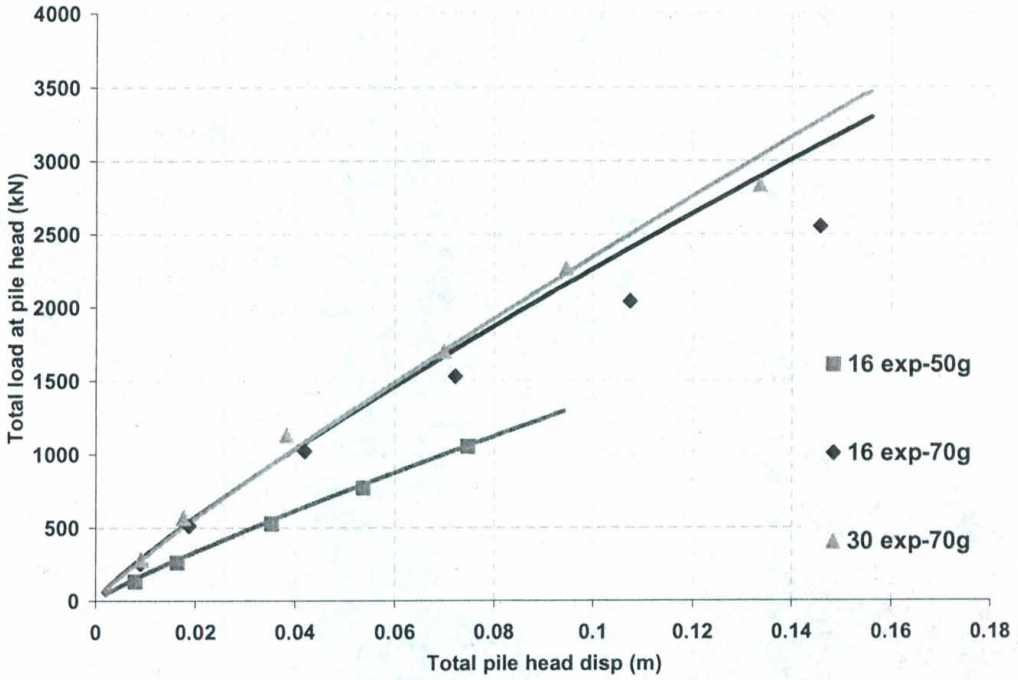

Figure (6.19) Total Load – Total Displacement Relationship at Pile Head– Comparison between FEM and Centrifuge Test [FEM is a Solid Line]

6.5.3 Inclined Pullout Loading:

Total load-total displacement relationship is shown in Fig. (6.19). There is a very good agreement between FEM and centrifuge test results at 50g tests. The FEM results for the 70g tests show the same initial stiffness as the centrifuge tests for both tests at loading angles 16° and 30°. At higher deflection, FEM with loading angle at 16° shows stiffer response than centrifuge test. However, both FEM and centrifuge tests results show stiffer pile response by increasing loading angle.

The comparison extended to the bending moment profile, soil pressure distribution, and pile deflection profile as shown in Figs. (6.20) to (6.23). FEM predicts soil pressure at shallow depths and pile deflection above the rotation point in a good agreement. There is an overprediction in bending moment profile. This overprediction is more than that in the case of pure lateral loading. Figure (6.24) shows the relationship between the normalized lateral load at pile head and the normalized maximum bending moment. It can be seen that all the centrifuge tests at 70g and 50g have a constant slope regardless of the loading angle. This is also the same observation for FEM although it has a higher slope than that of the centrifuge tests. This means that FEM supports that the normalized maximum bending moment does not change by changing the loading angle. The difference in the slope between both FEM and the centrifuge tests results could be due to soil dilation as discussed before. At small vertical pullout load component FEM results are very close to the centrifuge tests results. By increasing the vertical pullout load component soil dilation increases. This increase in soil dilation causes a decrease in pile bending moment. As discussed before, the effect of dilation is higher in case of small scale model pile as in the centrifuge tests case. However, for large diameter piles (larger than 1m), the effect of soil dilation is small. This interprets the deviation of the FEM results from the centrifuge tests results by increasing the load at pile head which was not observed in case of pure lateral loading.

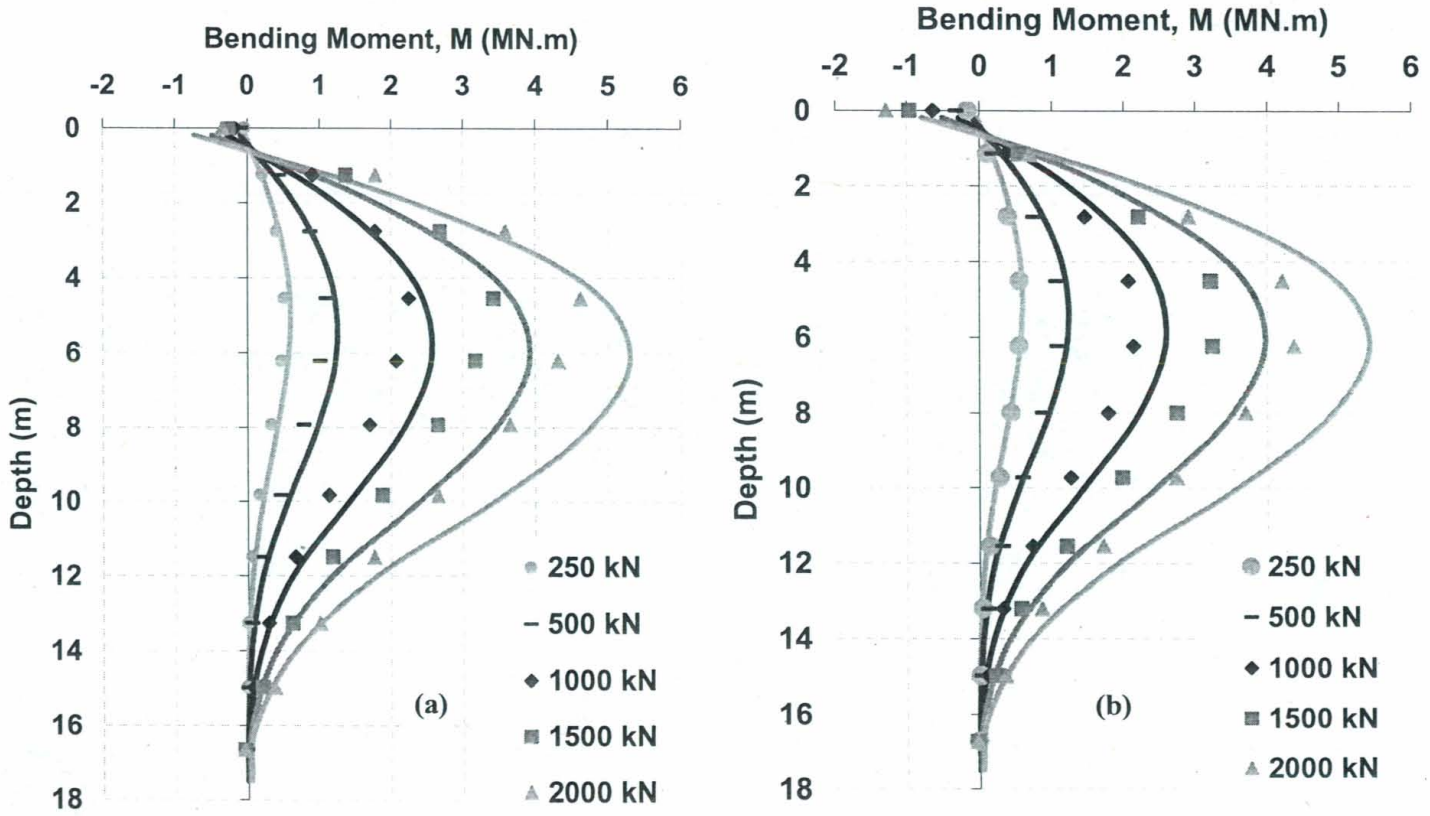

Figure (6.20) Bending Moment Distribution for Inclined Pullout Loading Case (a) 16°, and (b) 30°, [FEM Curve is a Solid Line]-70g tests

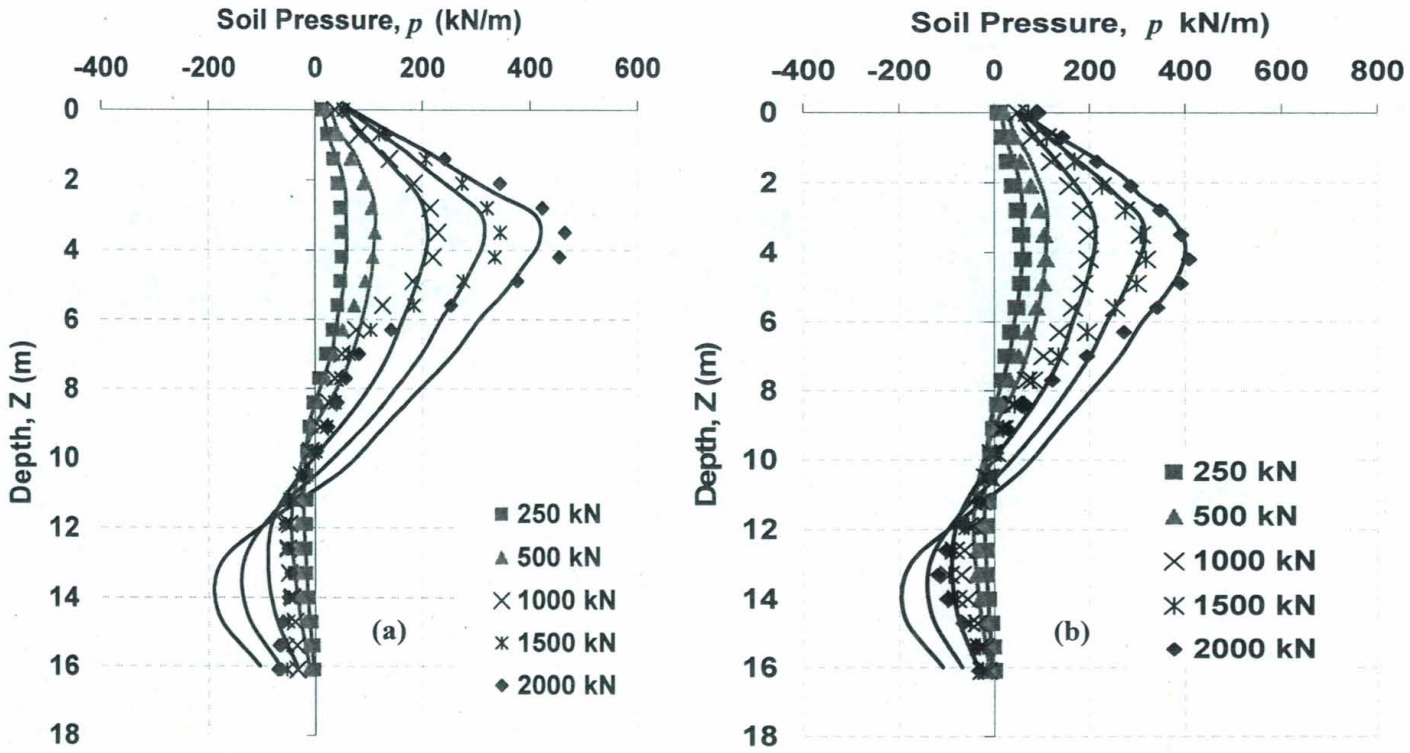

Figure (6.21) Soil PressureDistribution for Inclined Pullout Loading Case (a) 16°, and (b) 30°, [FEM Curve is a Solid Line]-70g tests

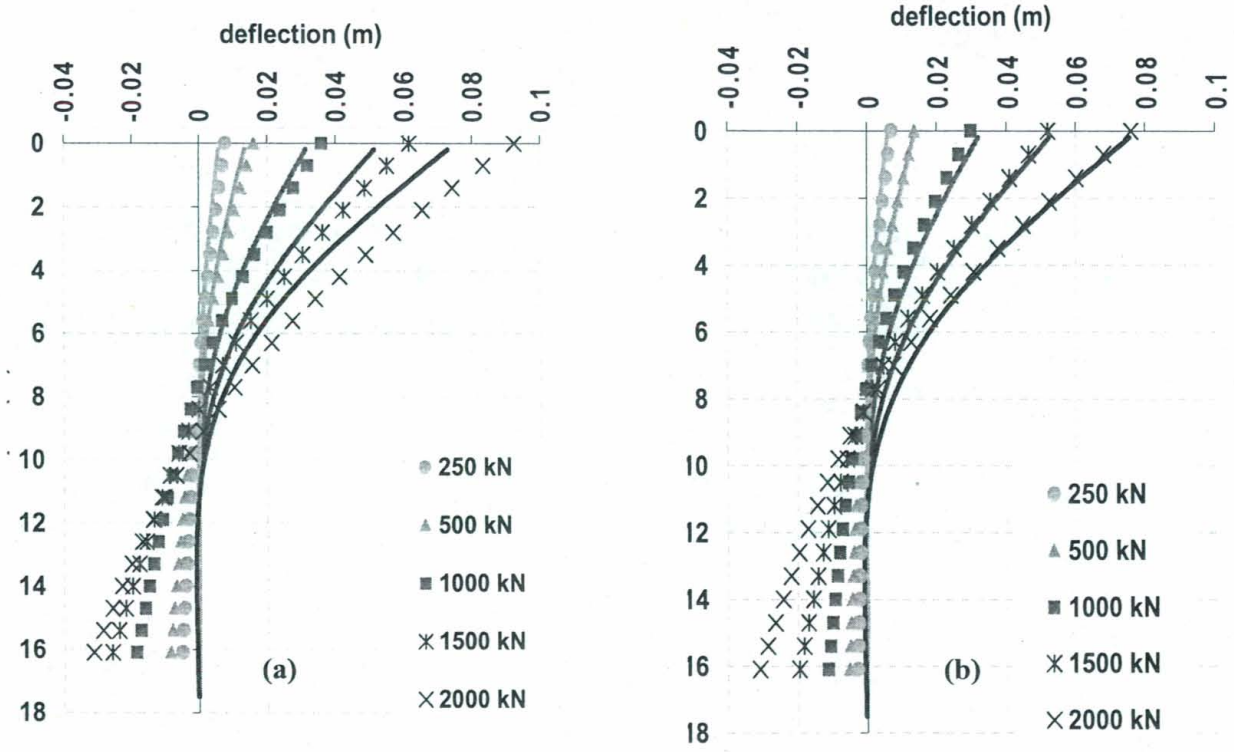

Figure (6.22) Pile Deflection Profile for Inclined Pullout Loading Case (a) 16°, and (b) 30°,
[FEM Curve is a Solid Line]-70g tests

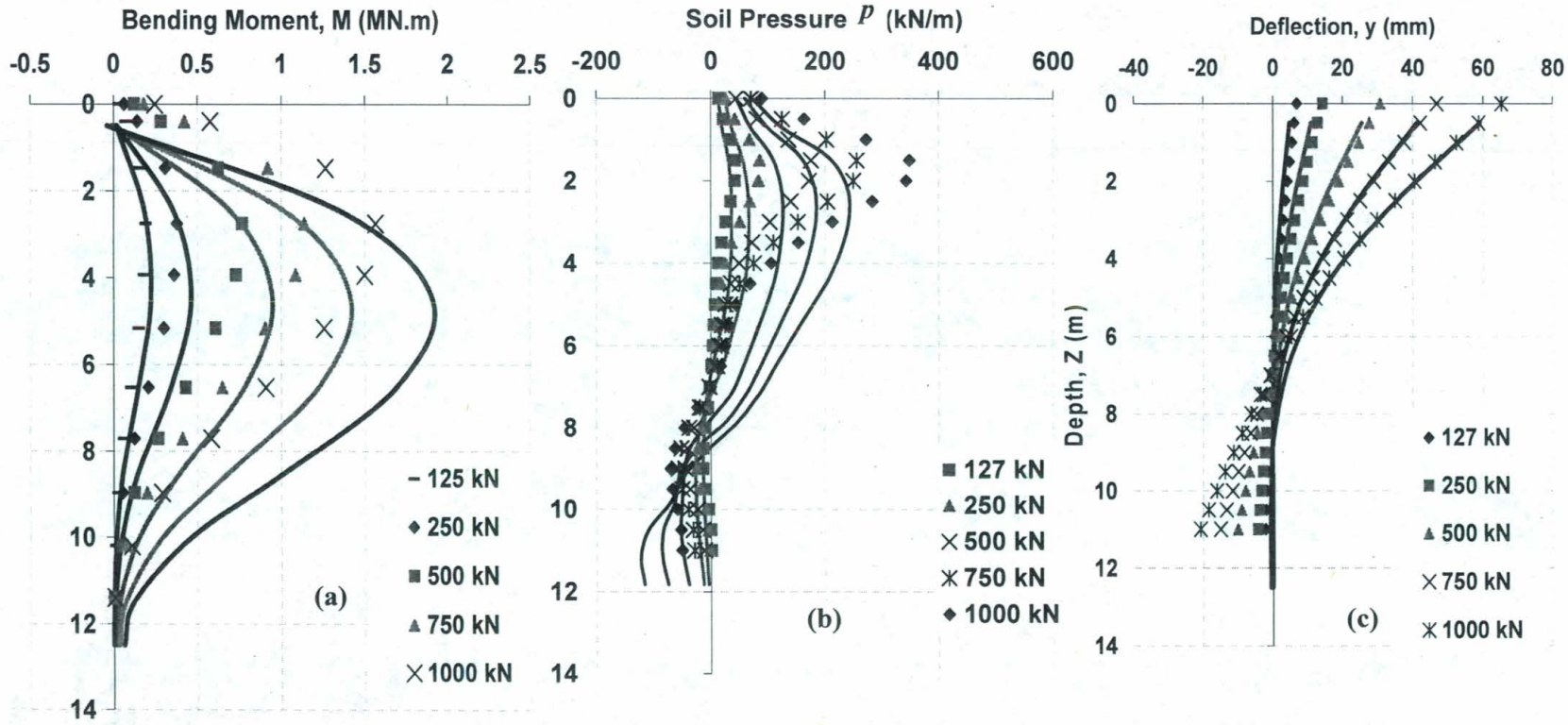

Figure (6.23) Inclined Pullout Loading Case 16° (a) Bending Moment, (b) Soil Pressure, (c) Pile Deflection [FEM Curve is a Solid Line]-50g tests

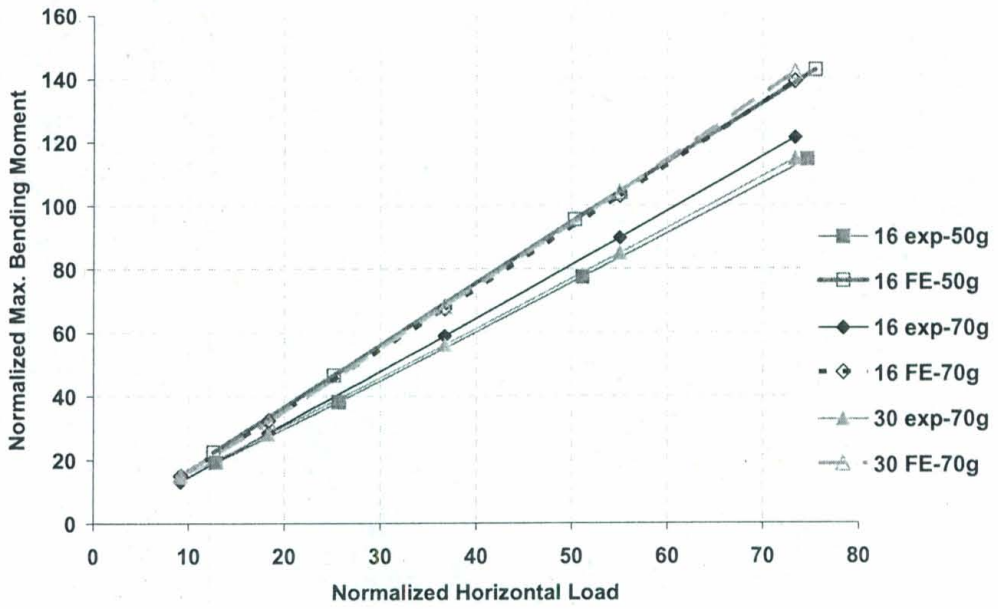

Fig. (6.24) Normalized Horizontal Load versus Normalized Max. Bending Moment for Inclined Pullout Loading Tests.

Figure (6.25) shows soil pressure distribution at depths 1.2m ($\approx 1d$) and 3m ($\approx 2d$). It can be seen that there is a reduction in soil pressure by applying tension load component from that at pure lateral loading. The soil pressure is almost same for both loading angles 16° and 30° at different horizontal load increments at pile head. There is only small reduction by increasing loading angle at high load increment as can be seen at H = 2000 kN. This is the same observation from centrifuge tests as shown in Fig. (5.25).

6.6. Conclusion:

A three dimensional (3-D) Finite Element Model (FEM) has been established to study the soil-pile interaction behavior under mooring forces. Mohr-Coulomb plastic model has been used to model the soil. The model has been calibrated based on the centrifuge tests discussed before. CPTs were carried out in the centrifuge. The results of CPTs were used to calculate soil parameters needed for the FEM using some

available correlations in the literature. The effect of pile installation was considered by increasing the lateral stress based on the recommendations of ICP' (2005). FEM predicts the tension capacity of the pile in a good agreement with ICP method. However, it slightly under-predicts the tension capacity in comparison to the centrifuge test due to the effect of soil dilation when using small scale model pile. FEM predicts well the behavior of pure laterally loaded pile in terms of load-displacement curve at pile head and maximum bending moment of the pile. For inclined pullout loading, FEM shows the same trend as the centrifuge tests. There is a little overprediction in the normalized maximum bending moment which could be due to the soil dilation effect as in the tension loading case. In general, FEM shows a good agreement with the centrifuge tests results.

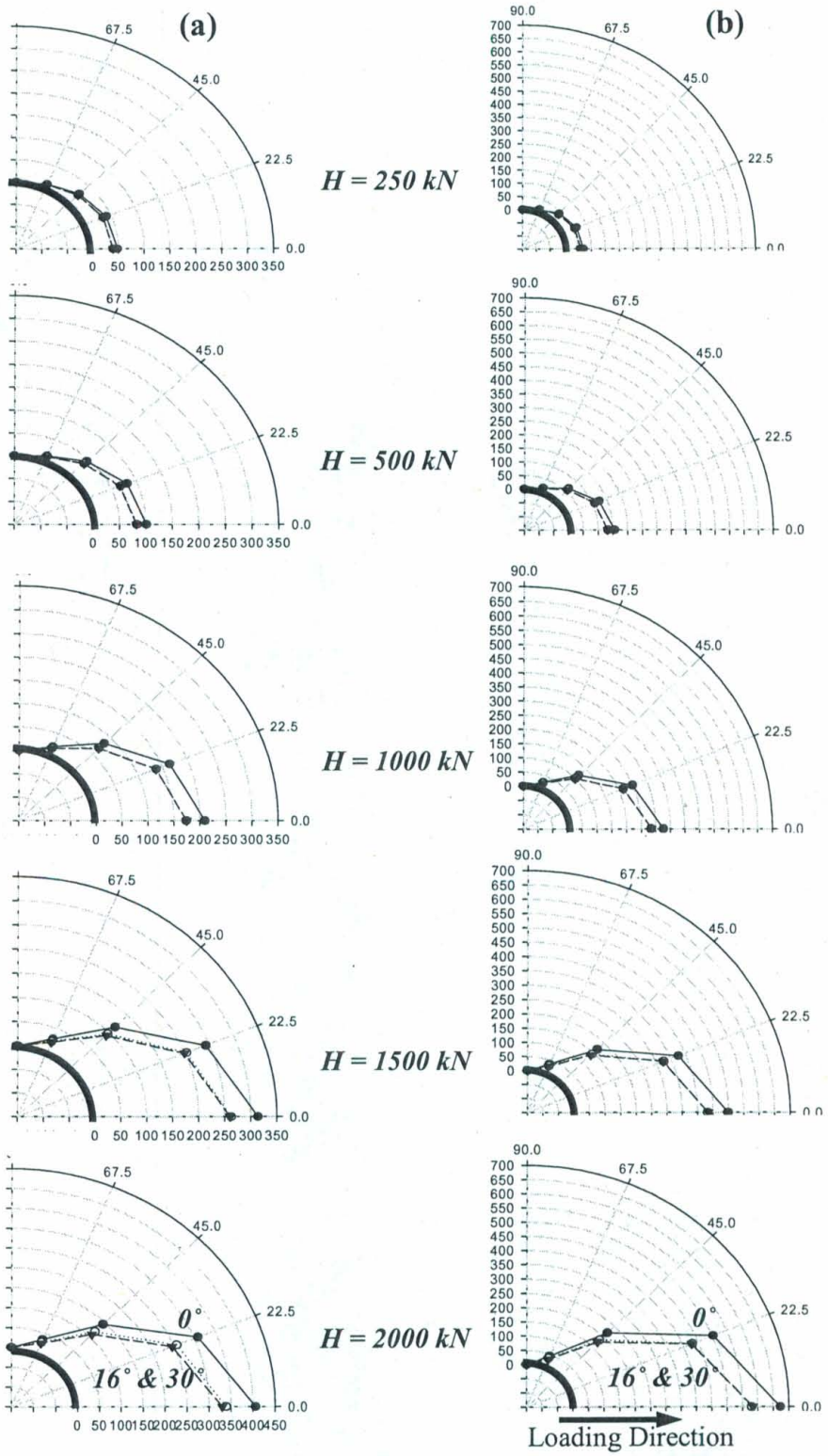

Fig. (6.25) Soil Pressure Distribution for Different Loading Angles at Depths (a) 1.2m, and (b) 3m – 70g tests

Chapter 7

Behavior of Offshore Anchor Piles in Dense Sand – Numerical Parametric Study

7.1. Introduction:

In this chapter, a parametric study was carried out to study the behavior of offshore anchor piles under mooring forces in dense sand using FEM. The FEM was calibrated based on the centrifuge tests results as discussed before. In the current parametric study, only pile geometry and loading conditions were changed. Soil properties were the same as that for dense sand used in the FEM calibration. Different pile lengths and diameters were considered to have different pile-soil rigidities. The pile was loaded at different load inclination angles to examine a wide range of loading conditions. Also, different padeye depths were tested to check its effect on offshore anchor piles behavior. From the current parametric study, design methods and design recommendations are given to help in improving the design of offshore anchor piles under monotonic mooring forces.

7.2. Parametric Study:

The parametric study was carried out in two parts. In the first part, pile geometry was considered by changing both pile diameter and length to have different pile-soil rigidities. In all cases the pile was loaded at the ground surface (no eccentricity) at loading inclination angles, θ = 0°, 5°, 10°, 15°, 30°, 60°, 90° to horizontal. Although offshore anchor piles are usually subjected to mooring forces with maximum loading angles of about 30° as reported by Randolph et al. (2005), higher loading angles were examined in the present study to understand the effect of the interaction between

vertical and horizontal pullout loading on offshore anchor piles behavior. In the second part of the current parametric study, the padeye depth (e) was changed to check its effect on the ultimate capacity of the pile and on the pile-soil interaction. The parameters combinations used in the parametric study for the first and second parts are shown in Tables (7.1) and (7.2), respectively. All piles have the same wall thickness (t) of 30 mm (to have an average ratio of d/t of 50 that is being used for offshore piles) and Young's modulus of steel 2.1 x 10^8 kN/m^2.

Pile-Soil flexibility was calculated as the ratio of pile length (L) to the elastic length (T). The elastic length was calculated using equation (2.1) (as discussed in chapter 2). In equation (2.1), the parameter n_h was assumed as 40 MN/m^3 as recommended by API (2000) for dense sand and as shown in Fig. (2.5).

A total of 98 runs were carried out in the current parametric study. All piles were loaded using displacement control and under drained conditions. For some cases, the pile was pulled out to a large displacement to get the ultimate capacity of the pile. In the next sections, the results of the parametric study will be discussed. The soil-pile interaction will be discussed in terms of pile bending moment profile, soil pressure along the pile, soil shear stress along pile, and pile deflection profile. Design methods will be suggested to predict pile ultimate capacity maximum bending moment.

7.3. Results Analysis and Discussion:

In the following sections, the results of cases 1 to 8 (Table 7.1) are presented. The results will be discussed and suggested design methods will be recommended.

7.3.1 Load – Displacement Relationship:

Figures (7.2) to (7.9) show load-displacement relationship at pile head for some cases where pile was loaded at the ground surface. The figures show the horizontal load versus horizontal displacement relationship, vertical load versus vertical displacement relationship, and total load versus total displacement relationship. The results are for

Table (7.1) Parameters of the Parametric Study for loading cases at ground surface

Case #	*Diameter, d (m)*	*Length, L (m)*	*L/d*	E_pI_p *(MN m²)*	*T (m)*	*L/T*	*θ*	*e (m)*
1	2	8	4	18919	3.43	2.33	0°, 5°, 10°, 15°, 30°, 60°, 90°	0
2		12.5	6.25			3.65		
3		15	7.5			4.38		
4		17.5	8.75			5.1		
5	1	12.5	12.5	2260	2.24	5.58		
6	1.4	17.5	12.5	6365	2.76	6.35		
7	2	25	12.5	18919	3.43	7.3		
8		35	17.5			10.2		

Table (7.2) Parameters of the Parametric Study - cases of different padeye depths

Case #	*Diameter, d (m)*	*Length, L (m)*	*L/d*	*E_pI_p ($MN m^2$)*	*T (m)*	*L/T*	*θ*	*e (m)*
9	2	12.5	6.25	18919	3.43	3.65	15°	(1, 2, 3, 4, 4.5, 5, 5.5) *d*
10		17.5	8.75			5.1		(1, 2, 3, 4) *d*
11		25	12.5			7.3		(1, 2, 3, 4) *d*

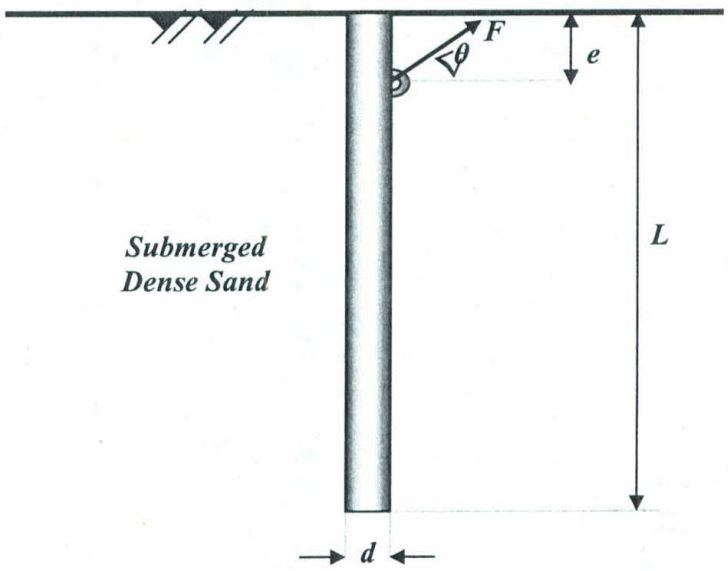

Fig. (7.1) Problem under Consideration: Pile Subjected to Mooring Force

piles of a wide range of flexibility (*L/T*). It can be seen from these figures that there is a significant interaction between lateral and vertical pullout loading conditions. The lateral load component is affected by the vertical pullout loading. The vertical pullout load component increases the initial stiffness of the lateral load – lateral displacement relationship. This increase of the initial stiffness can be seen at very small loading angle (i.e. 5°). This initial stiffness is almost constant for all loading angles more than 0°. By increasing the lateral displacement at pile head the lateral load at the pile head starts to increase at lower rate than the initial one. However, this deviation from the initial stiffness of the lateral load component happens when the pile starts to fail in tension. This is observed for all piles regardless of the soil-pile flexibility (*L/T*). This means that by reaching the pile to the tension failure, the lateral load – lateral displacement relationship becomes nonlinear which is the case of rigid pile. From the vertical load – vertical displacement relationships, it can be seen that pile tension capacity decreases by decreasing loading angle. This reduction in pile tension capacity is significant at small loading angles and up to almost loading angle of 30°. For loading angles larger than 30°, pile tension capacity is close to the case of pure vertical pullout loading.

For the total load – total displacement relationship, pile response becomes stiffer by increasing the loading angle from 0° (pure lateral loading) to 90° (pure tension loading). **The ultimate capacity of pile was taken as the total load corresponding to failure in tension.** In all cases, it was found that the pile reached the ultimate tension capacity before reaching the ultimate lateral capacity of a rigid pile has the same dimensions. The ultimate capacity of pile increases by decreasing loading angle. The pile head displacement at the ultimate capacity increases by decreasing loading angle. A design method to predict pile ultimate capacity will be discussed later.

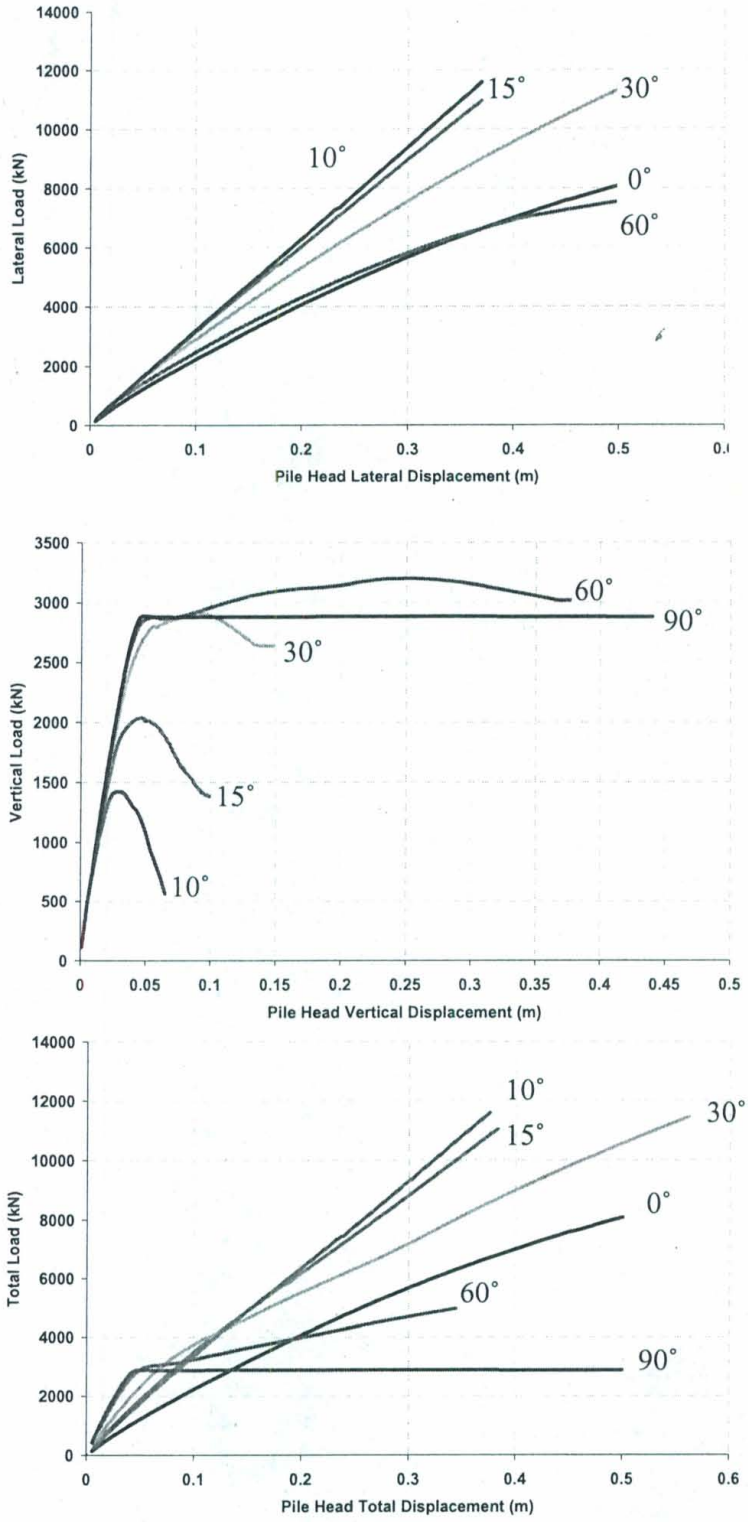

Fig. (7.2) Load – Displacement Curves at Pile Head – Case # 1 - (a) Lateral Component, (b) Vertical Component, (c) Total Component

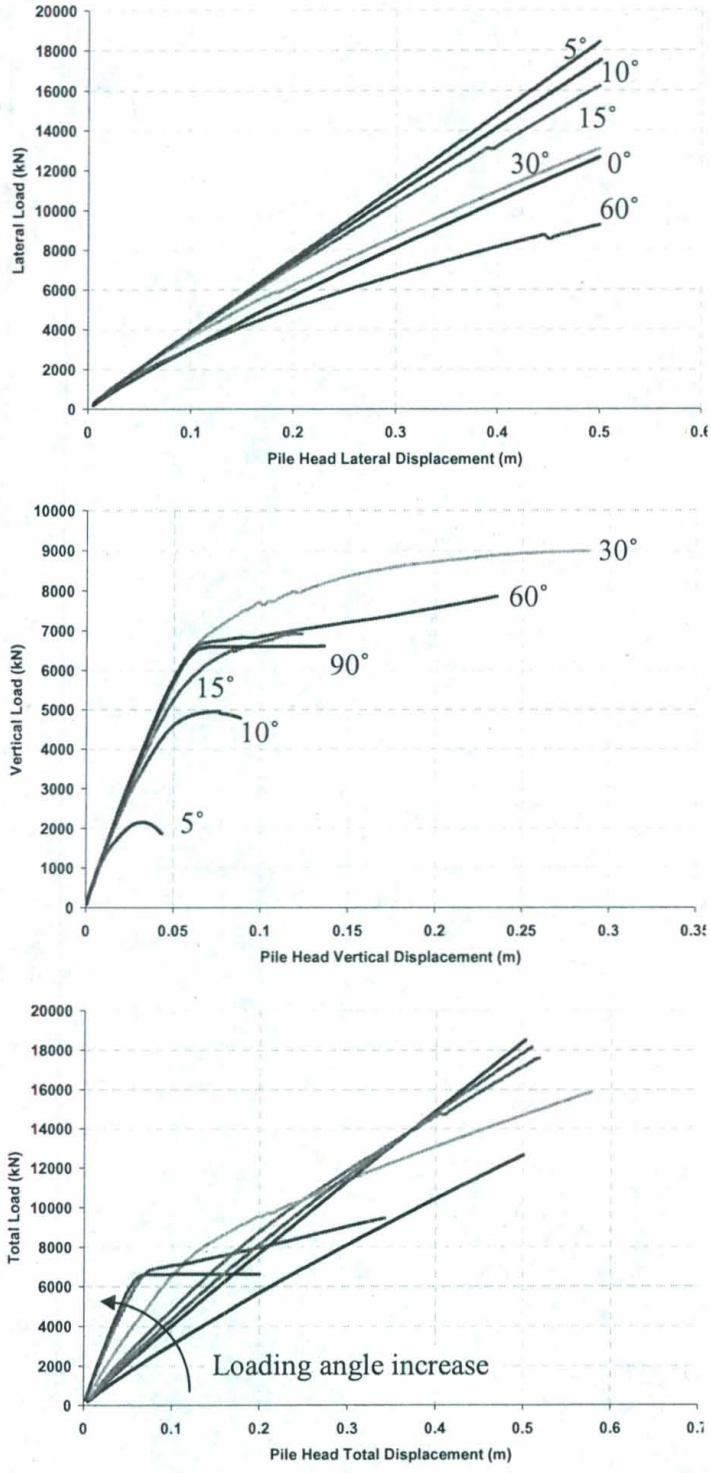

Fig. (7.3) Load – Displacement Curves at Pile Head – Case # 2 - (a) Lateral Component, (b) Vertical Component, (c) Total Component

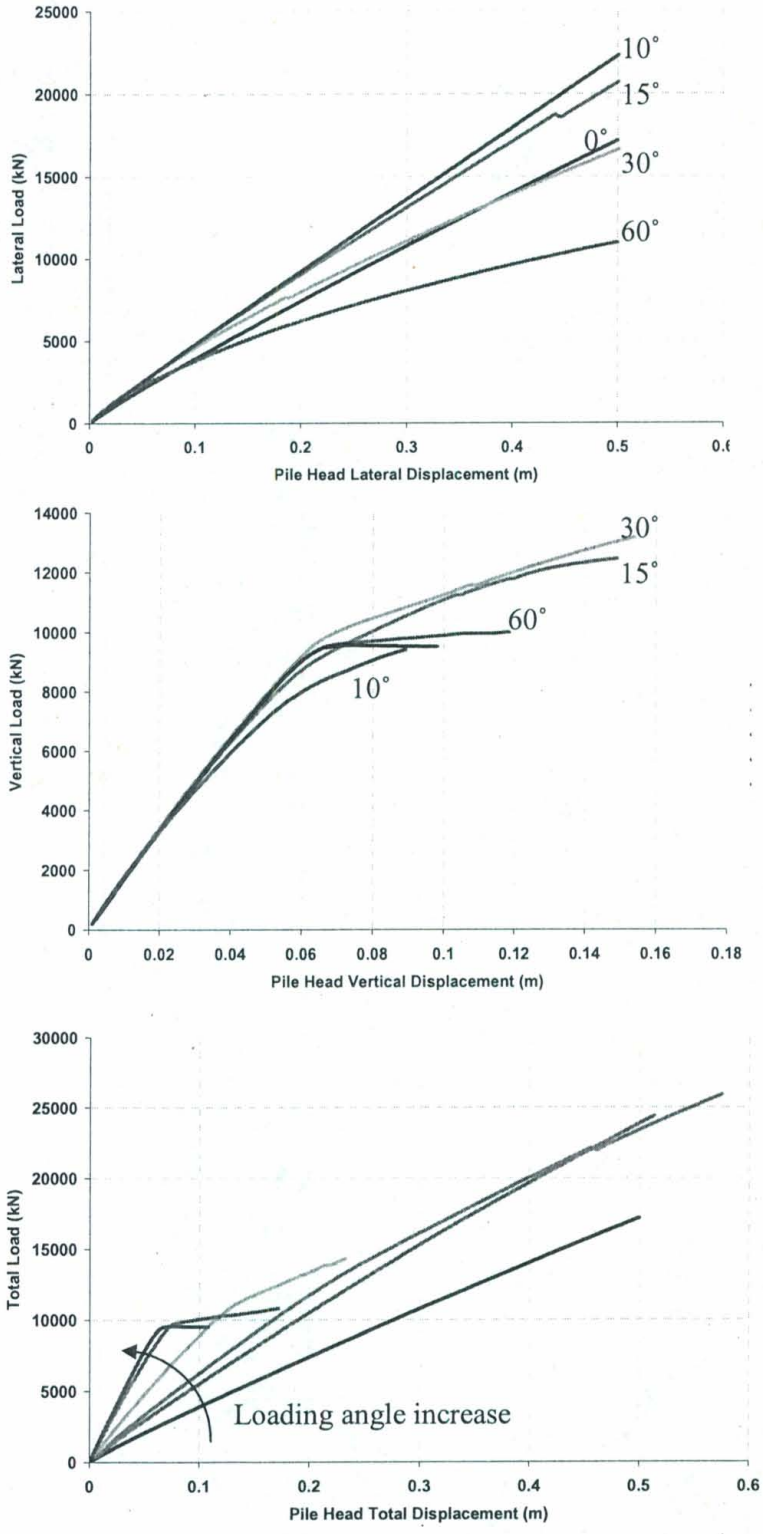

Fig. (7.4) Load – Displacement Curves at Pile Head – Case # 3 - (a) Lateral Component, (b) Vertical Component, (c) Total Component

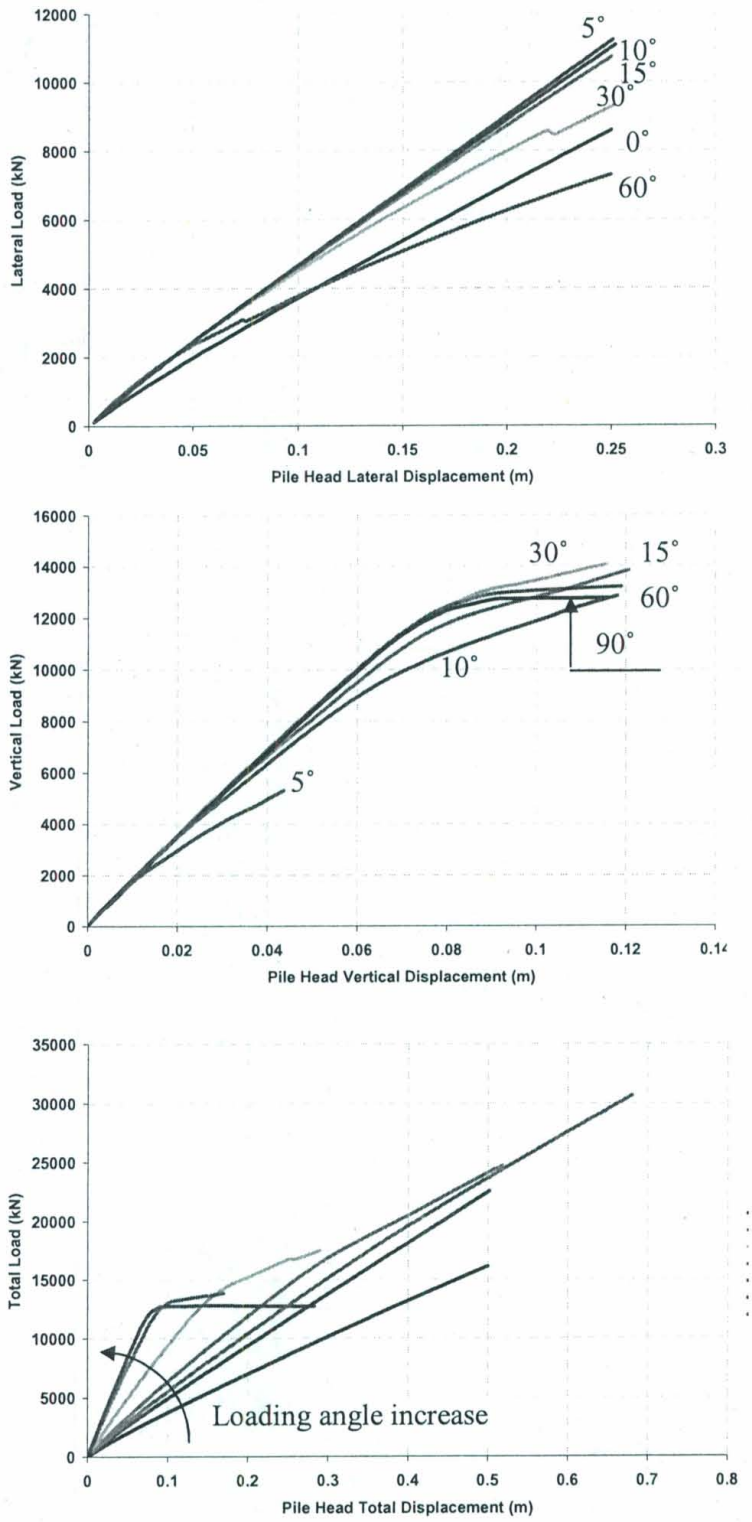

Fig. (7.5) Load – Displacement Curves at Pile Head – Case # 4 - (a) Lateral Component, (b) Vertical Component, (c) Total Component

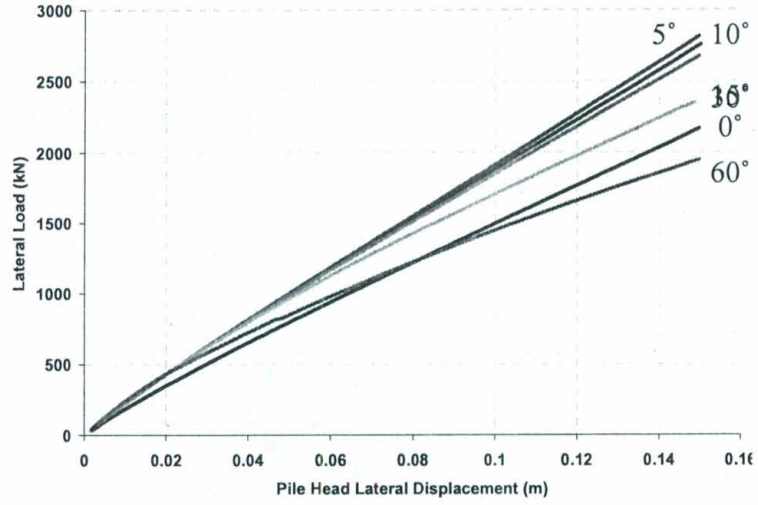

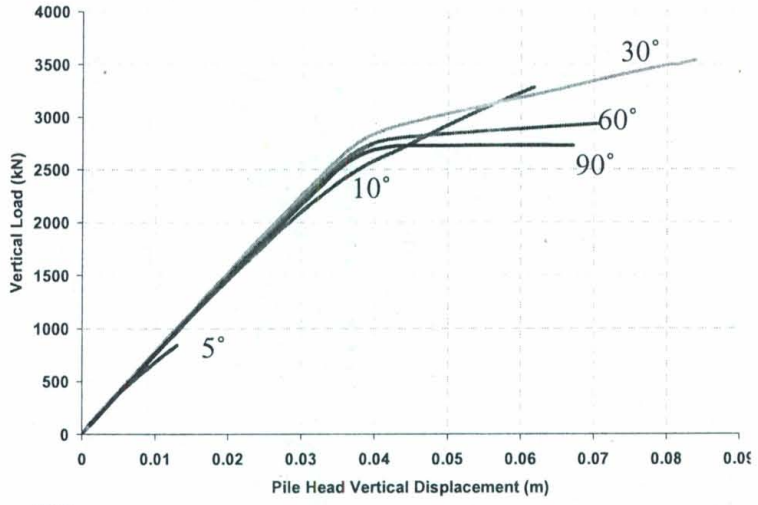

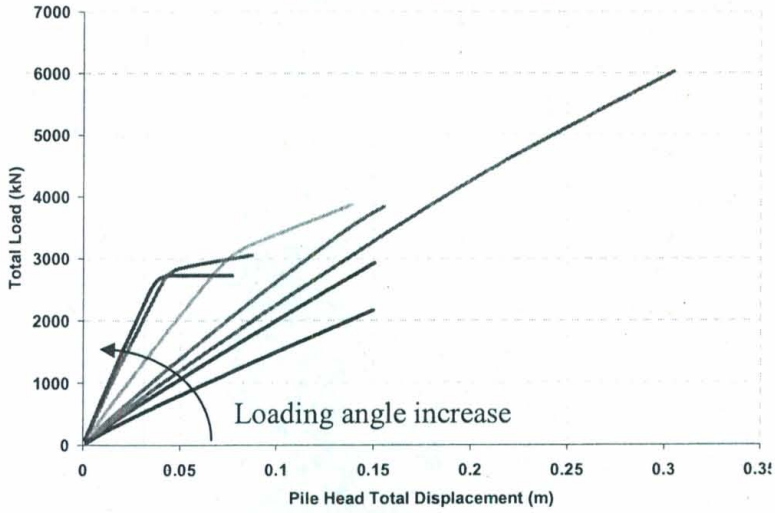

Fig. (7.6) Load – Displacement Curves at Pile Head – Case # 5 - (a) Lateral Component, (b) Vertical Component, (c) Total Component

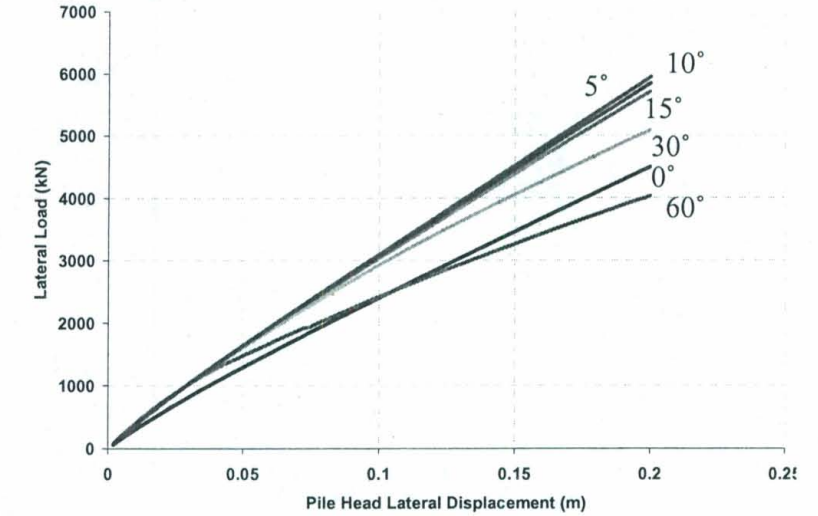

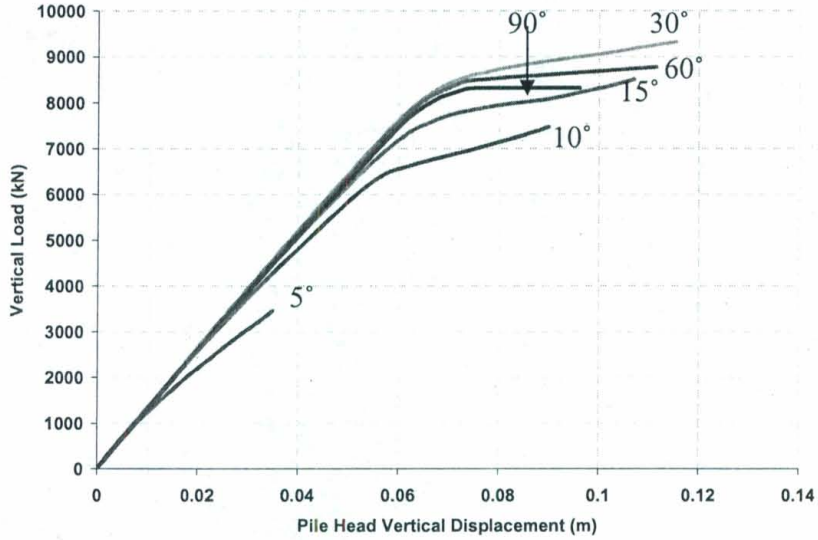

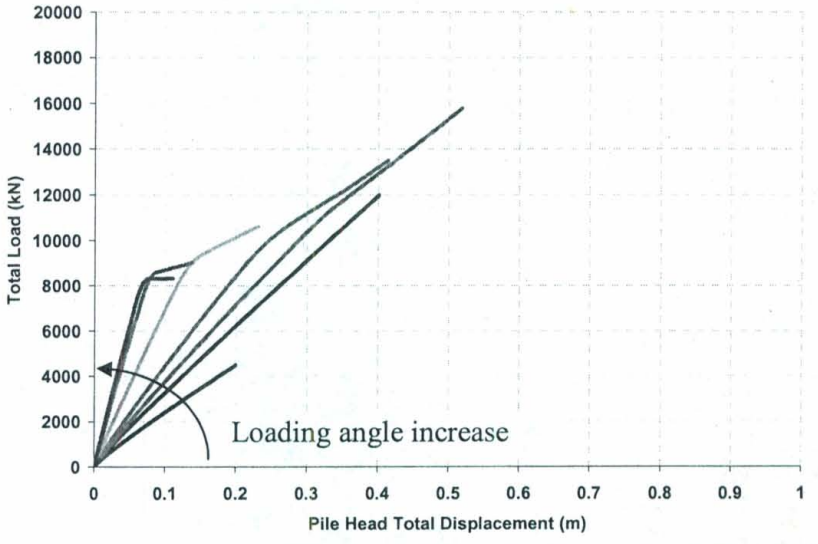

Fig. (7.7) Load – Displacement Curves at Pile Head – Case # 6 - (a) Lateral Component, (b) Vertical Component, (c) Total Component

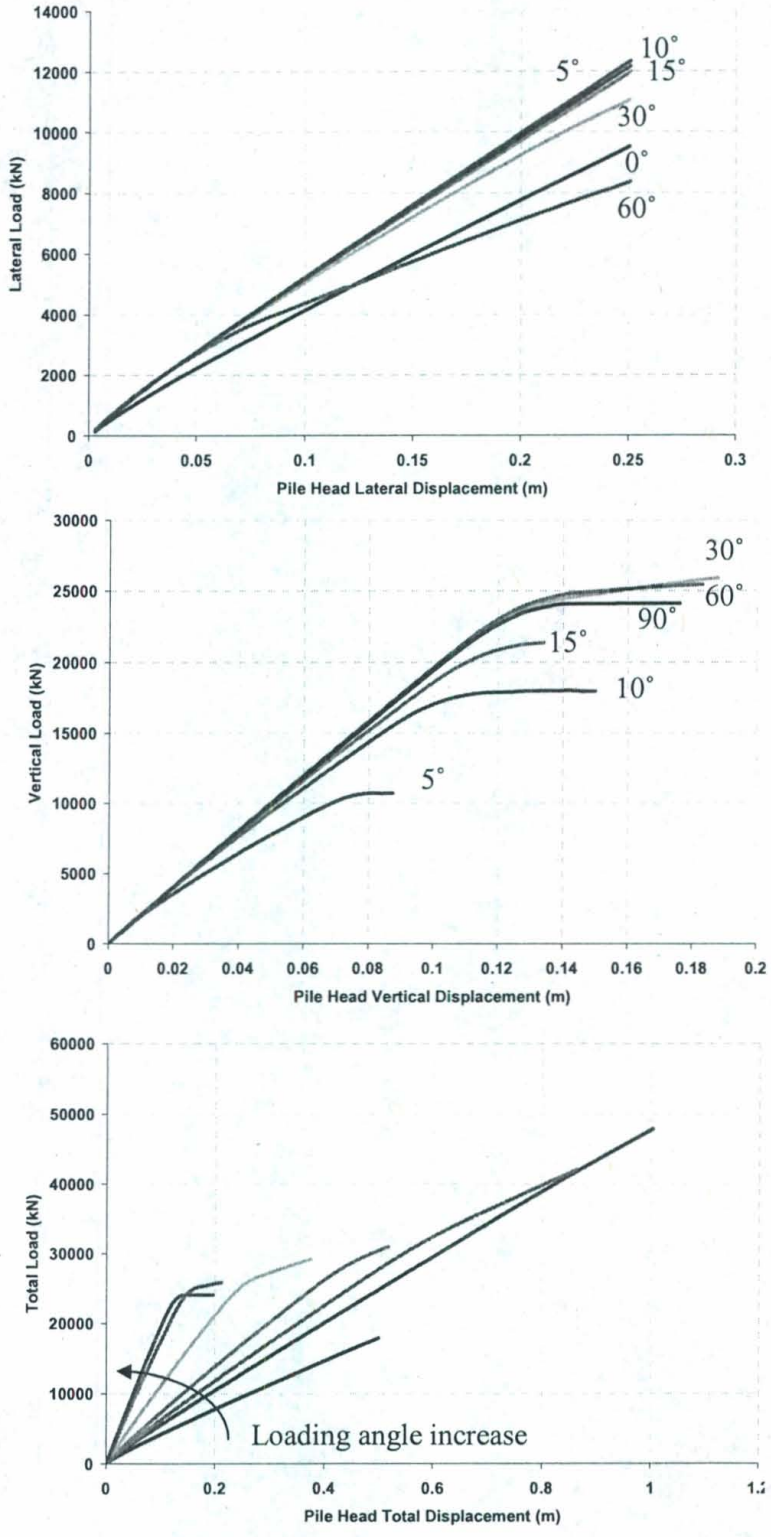

Fig. (7.8) Load – Displacement Curves at Pile Head – Case # 7 - (a) Lateral Component, (b) Vertical Component, (c) Total Component

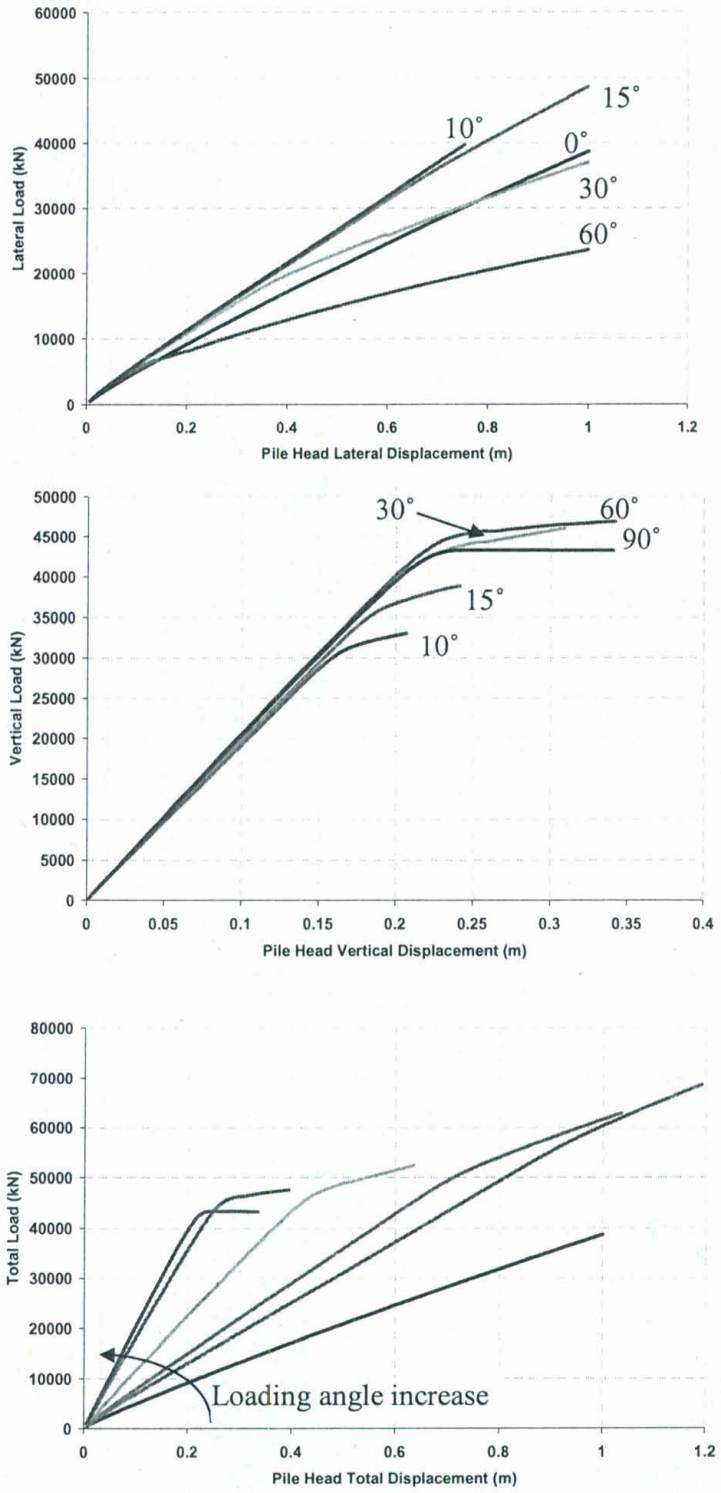

Fig. (7.9) Load – Displacement Curves at Pile Head – Case # 8 - (a) Lateral Component, (b) Vertical Component, (c) Total Component

7.3.2 Pile Lateral Deflection Profile:

Pile lateral deflection profiles are shown in Figs. (7.10) to (7.14). It clear for all plotted cases that vertical pullout load component has a significant effect on pile lateral deflection. Before failure in tension, there is a reduction in the lateral deflection. The same pile loaded at different loading angles larger than 0° and at the same lateral load increment has the same lateral deflection profile before the pile fails in tension. What happens before tension failure is that the tension stresses in the pile result in pile elongation and decrease in pile curvature. When the pile starts to fail in tension the elongation reaches its ultimate and the pile bending stiffness increases. This increase in pile bending stiffness is more obvious for cases of loading angle of 60° where the pile reaches the ultimate capacity in tension at relatively small lateral load components. This is clear for cases of small *L/T* (case# 2 and case# 4). At which the pile rotates and behaves as a rigid pile after failing in tension. For other cases have higher *L/T* values, which means piles of higher flexibility, the curvature of the pile at shallow depths decreases and lateral deflection increases. However, the effect of pile bending stiffness increase decreases by decreasing loading angle. The reason for that is that by decreasing loading angle the pile reaches high curvature before failing in tension at larger lateral deflection.

For design purposes, the interest should be before reaching failure in tension. This means that before failure there is a constant reduction in pile lateral deflection for all loading angles larger than 0° regardless of the angle value. This reduction in pile lateral deflection causes a stiffer response of pile as shown in load – displacement relationships and as will be discussed later also.

7.3.3 Bending Moment Profile:

Figures (7.15) to (7.19) show bending moment profile for some cases of the parametric study. It can be seen that for the same pile and at the same lateral load

increment at pile head there is a constant reduction in bending moment once the loading angle becomes larger than 0° (pure lateral loading). For all loading angles larger than 0° bending moment profile is same until the pile fails in tension. When the pile fails in tension, bending moment profile changes. This is similar to what observed from pile lateral deflection profiles. This can be seen in Figs. (7.15) to (7.19) where in all cases of loading angle 60° the piles fail in tension at smaller lateral load components than that in smaller loading angles. It can be seen that after failing in tension maximum bending moment increases and goes deeper. Figure (7.15) shows bending moment profile of case #2 where the pile has low value of (L/T) that means it is close to rigid pile behavior. For this case as the pile fails in tension bending moment decreases to negative values. The reason for this is that as the soil fails in tension, the soil contribution to support the lateral forces decreases. When this soil contribution goes down, more load transfers to the pile. This can be seen as a decrease in soil-pile flexibility and the pile behaves as a rigid pile that rotates with less curvature as shown in pile lateral deflection profiles. This decrease in pile curvature increases pile bending stiffness and decreases bending moment.

7.3.4 Soil Pressure and Shear Stress Profile:

Soil pressure and soil shear stress profiles help to understand the interaction between lateral and vertical pullout loading. However, before this discussion, soil pressure and shear stress profiles for cases of pure lateral and pure tension loading should be discussed first to understand the interaction between both loading cases. It should be noted that the plotted soil pressure is a soil reaction. This means that it is a change from the initial soil pressure before loading and it is zero before loading.

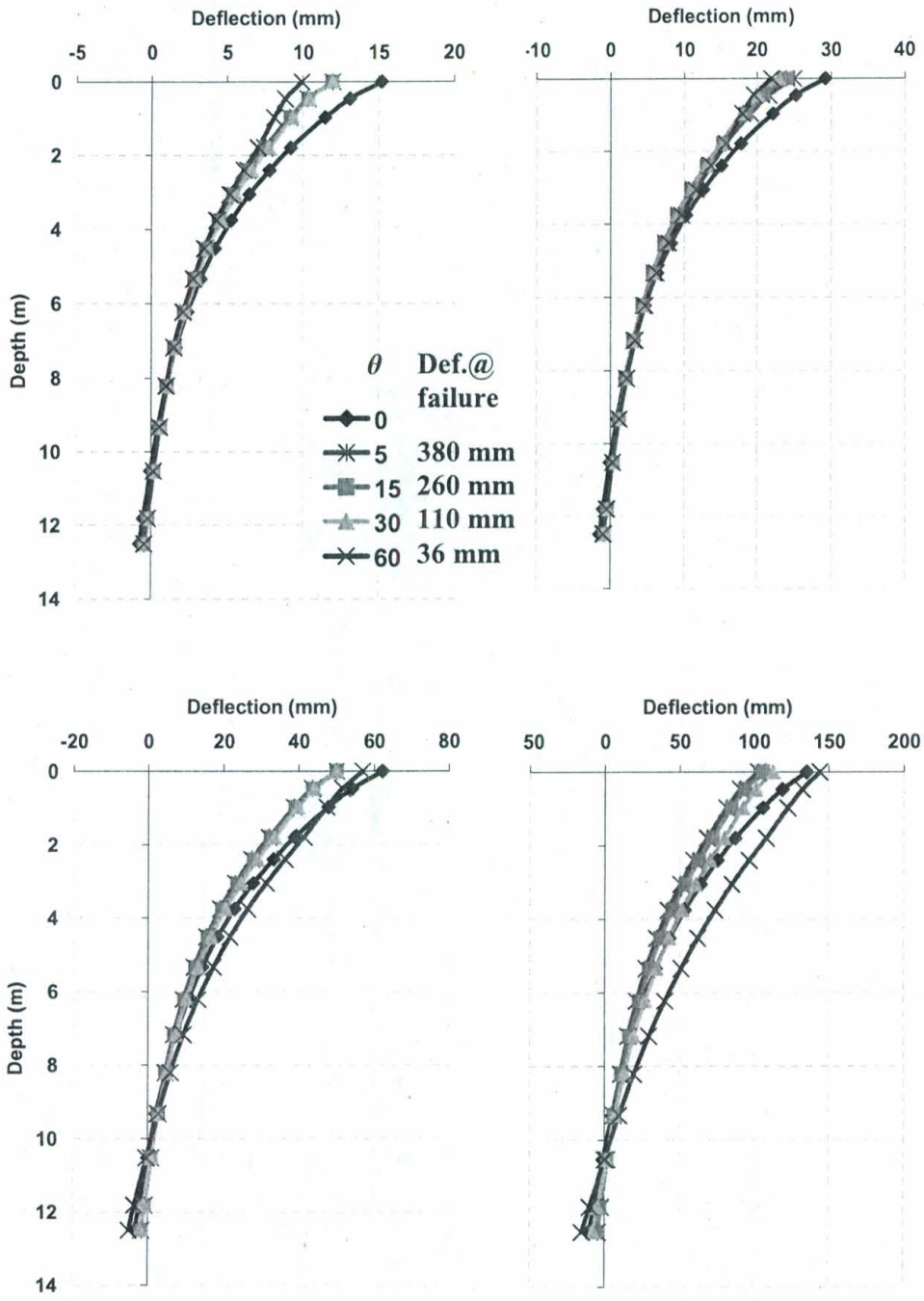

Fig. (7.10) Pile Lateral Deflection Profile – Case # 2 – at Lateral Load Increments (a) 500 kN, (b) 1000 kN, (c) 2000 kN, (d) 4000 kN

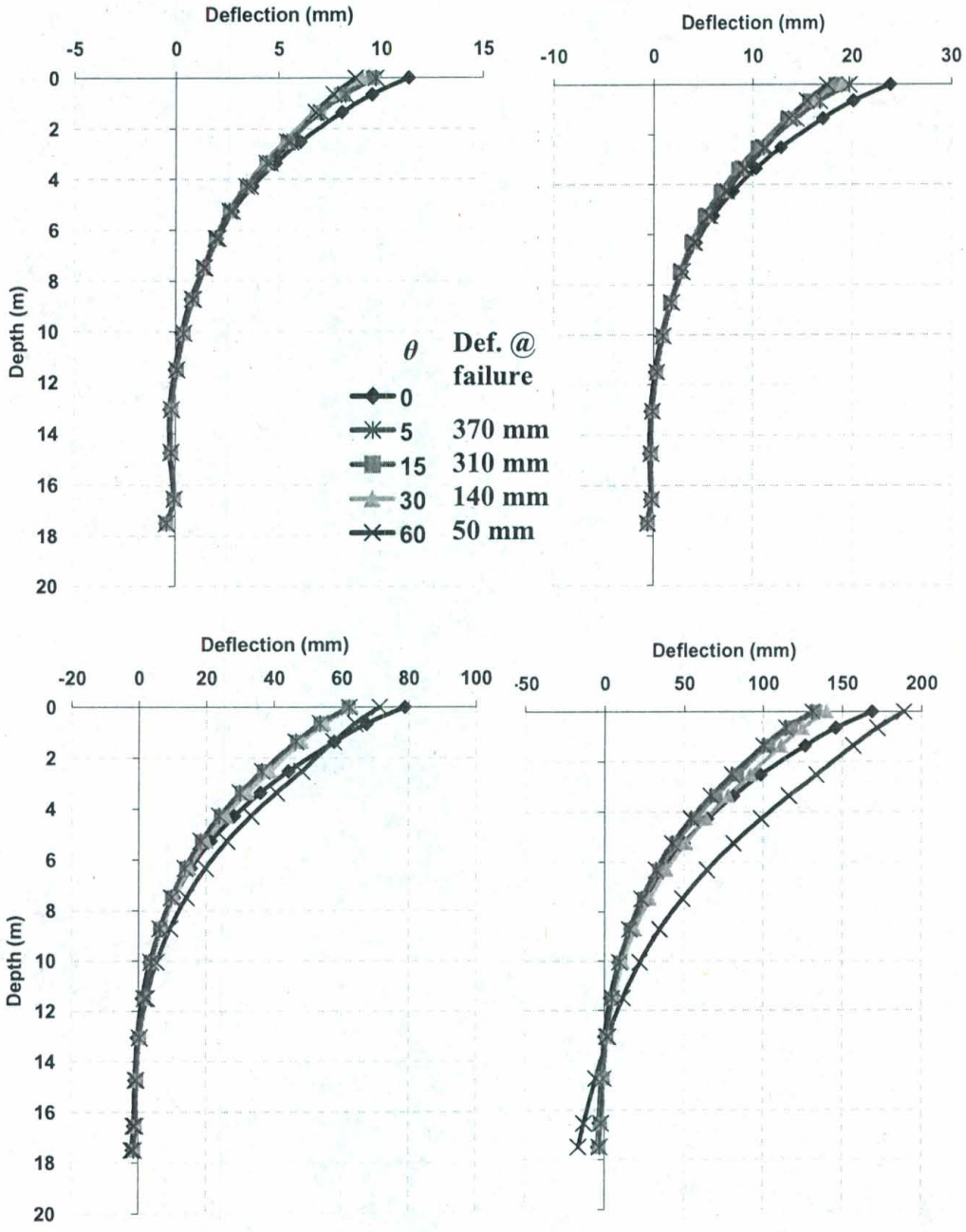

Fig. (7.11) Pile Lateral Deflection Profile – Case # 4 – at Lateral Load Increments (a) 500 kN, (b) 1000 kN, (c) 3000 kN, (d) 6000 kN

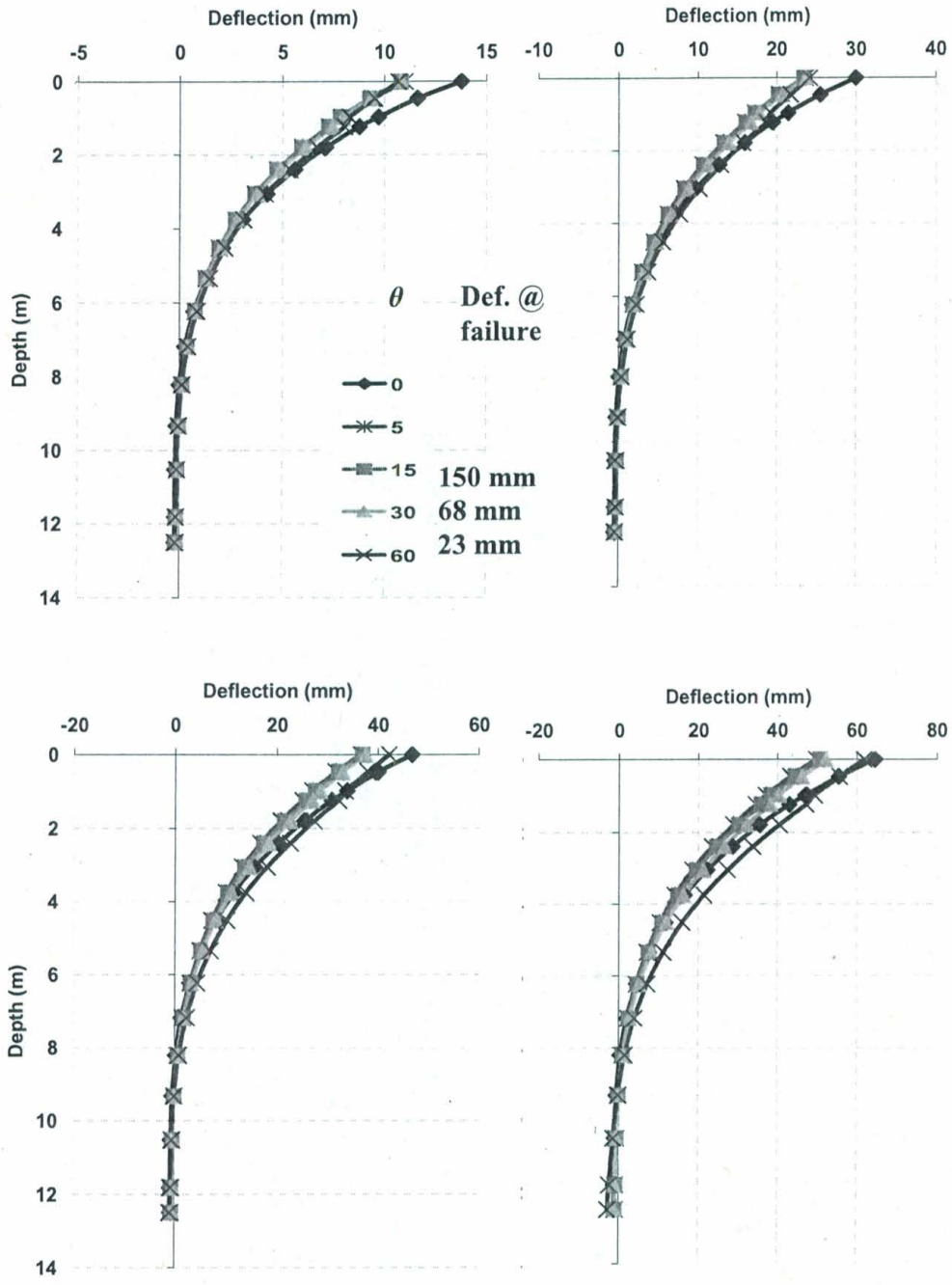

Fig. (7.12) Pile Lateral Deflection Profile – Case # 5 – at Lateral Load Increments
(a) 250 kN, (b) 500 kN, (c) 750 kN, (d) 1000 kN

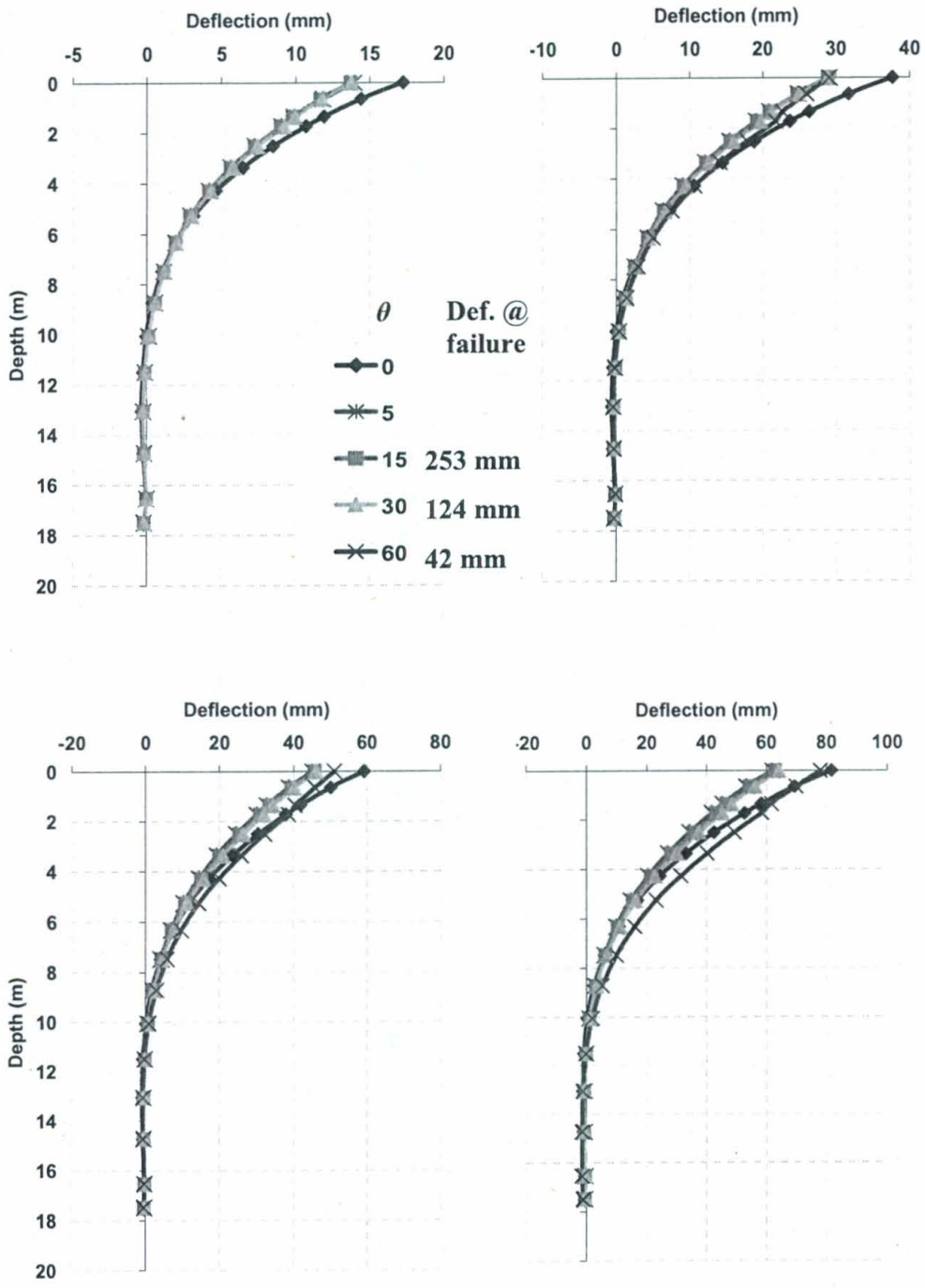

Fig. (7.13) Pile Lateral Deflection Profile – Case # 6 – at Lateral Load Increments (a) 500 kN, (b) 1000 kN, (c) 1500 kN, (d) 2000 kN

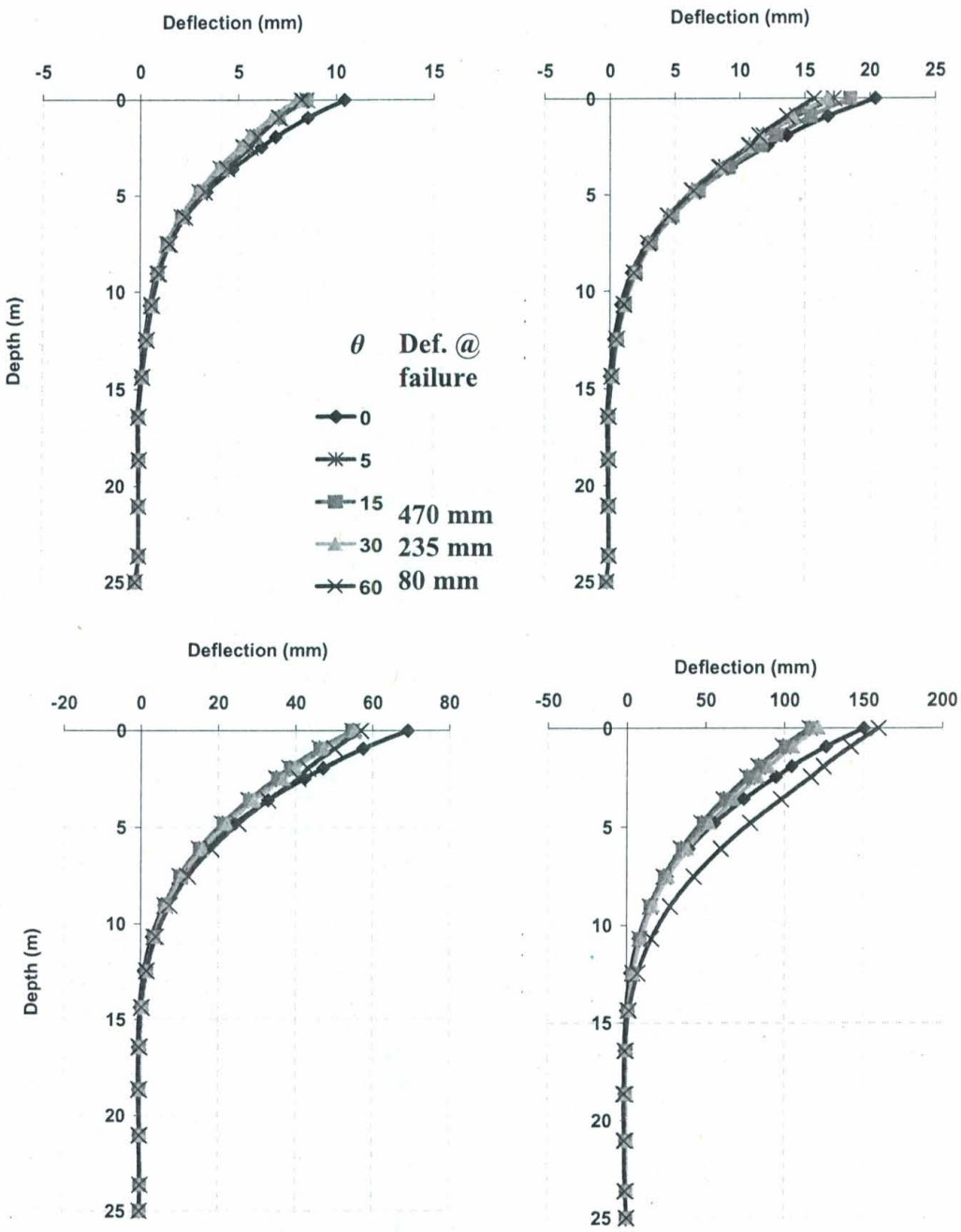

Fig. (7.14) Pile Lateral Deflection Profile – Case # 7 – at Lateral Load Increments (a) 500 kN, (b) 1000 kN, (c) 3000 kN, (d) 6000 kN

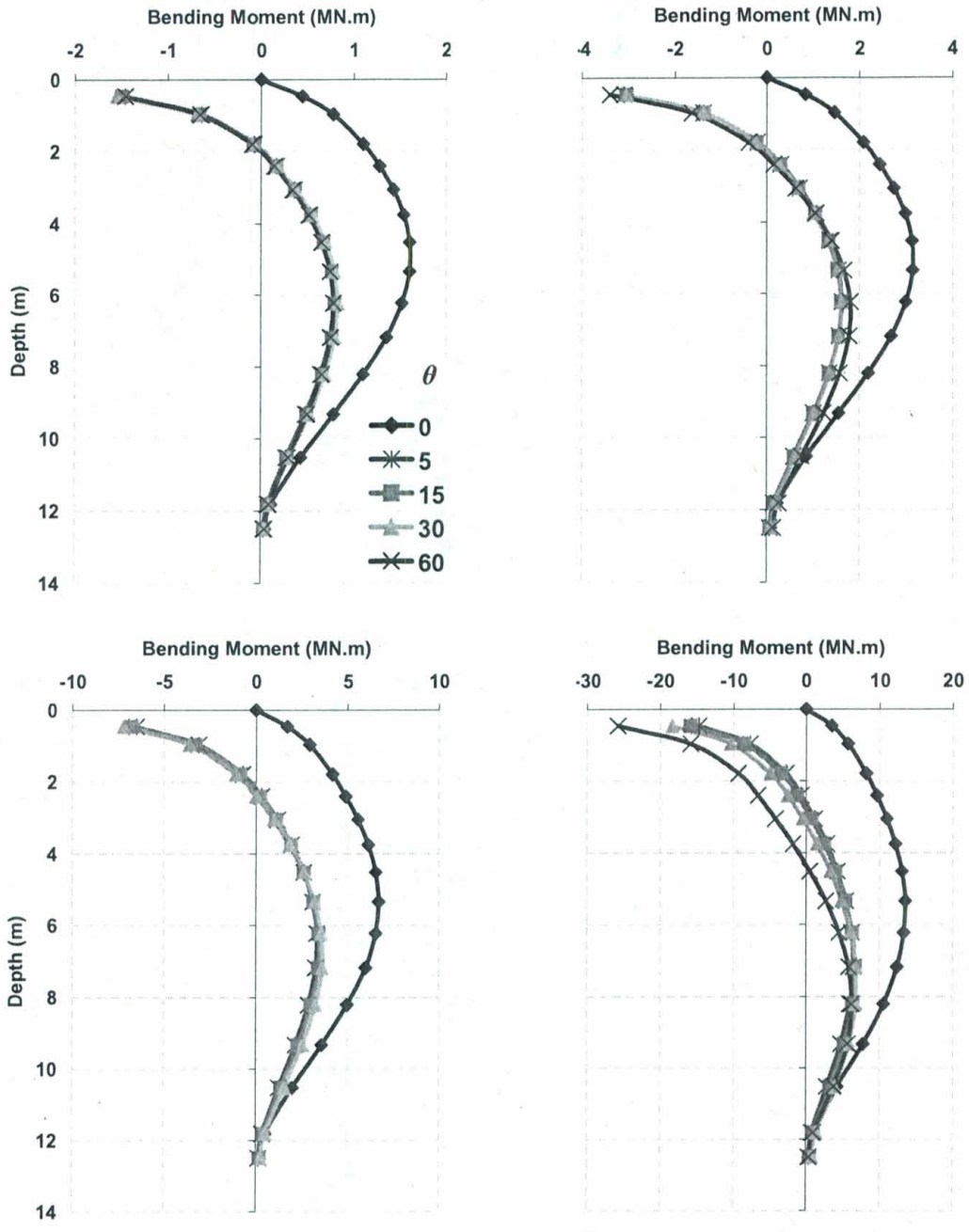

Fig. (7.15) Bending Moment Profile – Case # 2 – at Lateral Load Increments (a) 500 kN, (b) 1000 kN, (c) 2000 kN, (d) 4000 kN

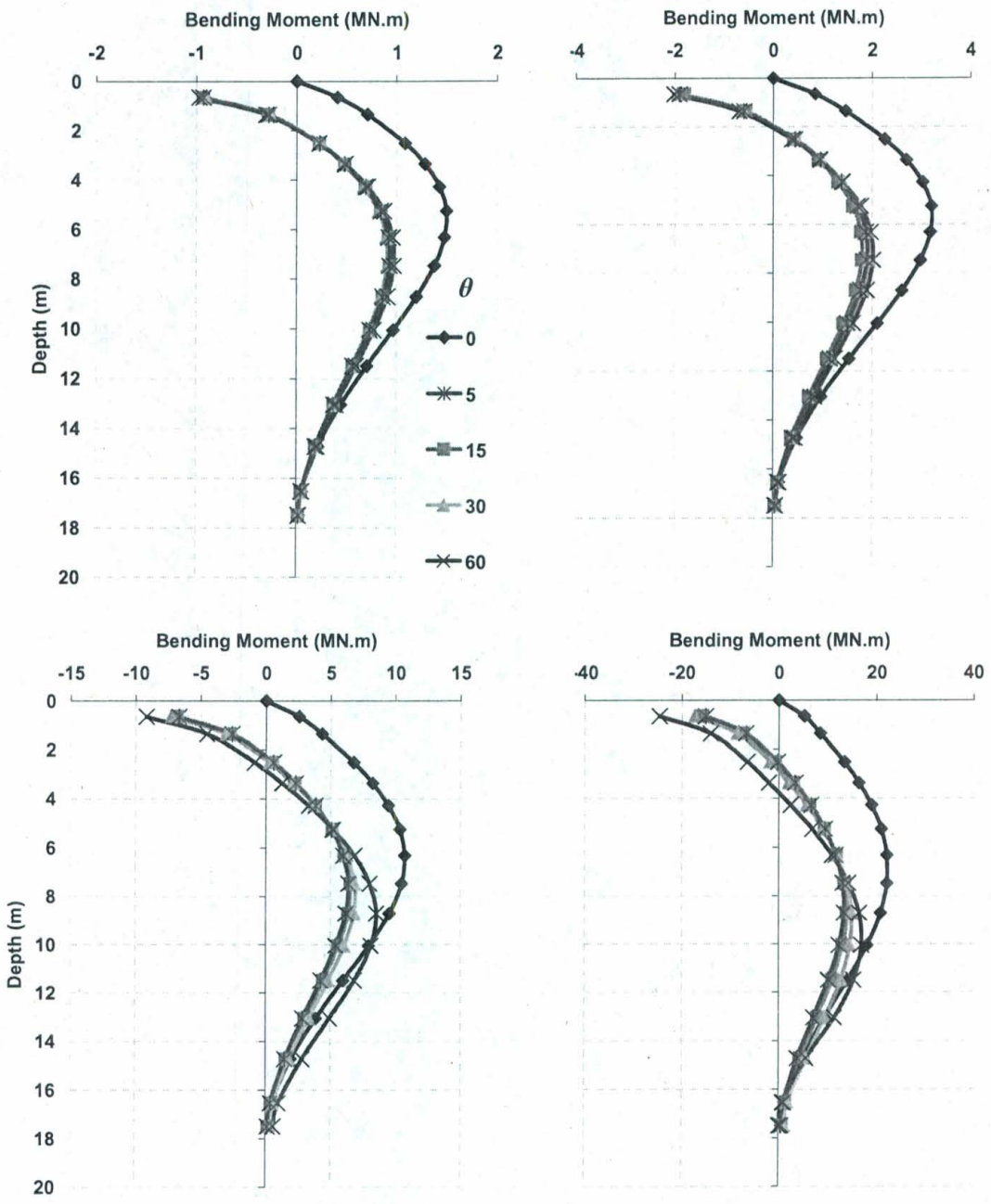

Fig. (7.16) Bending Moment Profile – Case # 4 – at Lateral Load Increments (a) 500 kN, (b) 1000 kN, (c) 3000 kN, (d) 6000 kN

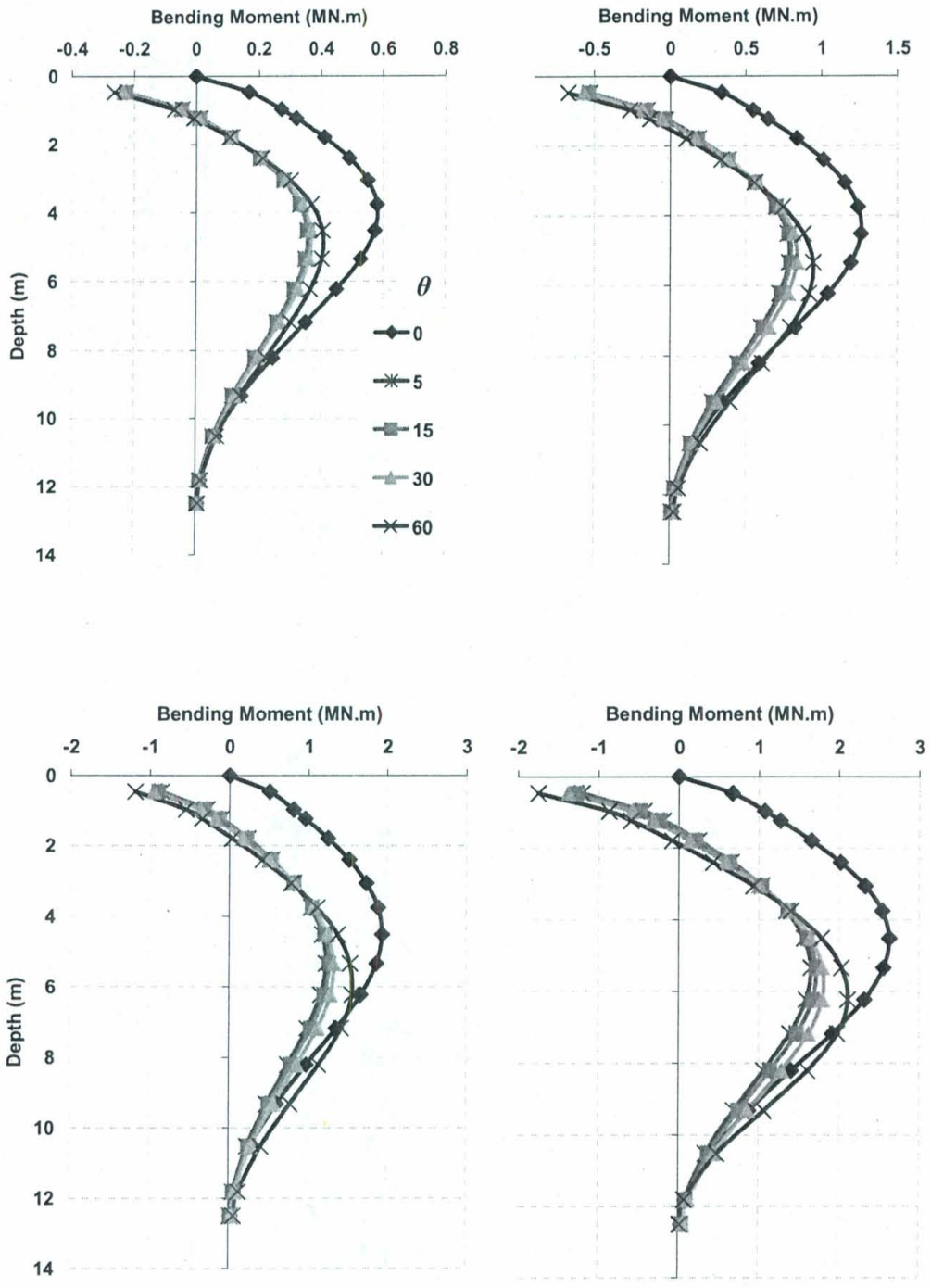

Fig. (7.17) Bending Moment Profile – Case # 5 – at Lateral Load Increments (a) 250 kN, (b) 500 kN, (c) 750 kN, (d) 1000 kN

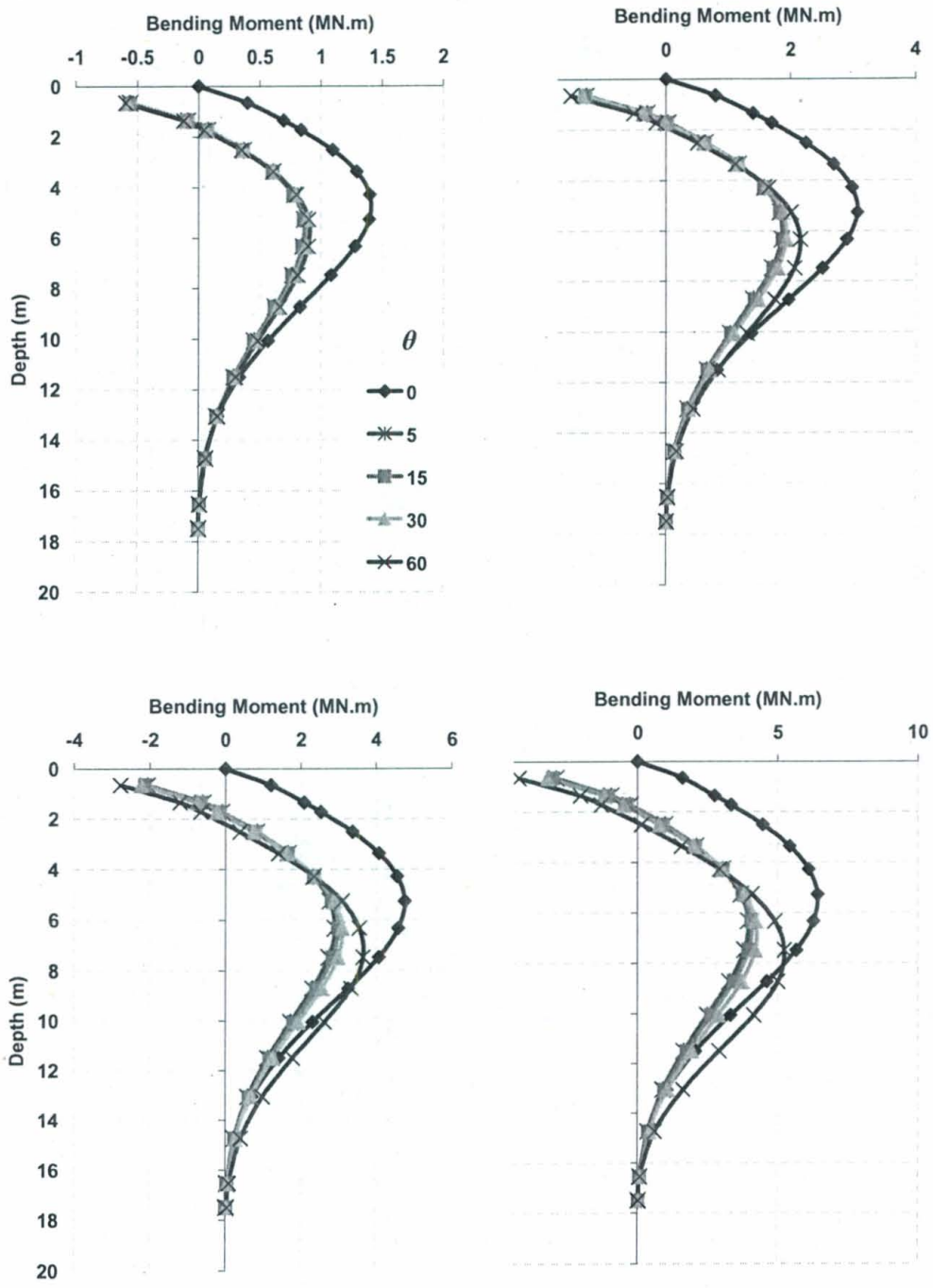

Fig. (7.18) Bending Moment Profile – Case # 6 – at Lateral Load Increments (a) 500 kN, (b) 1000 kN, (c) 1500 kN, (d) 2000 kN

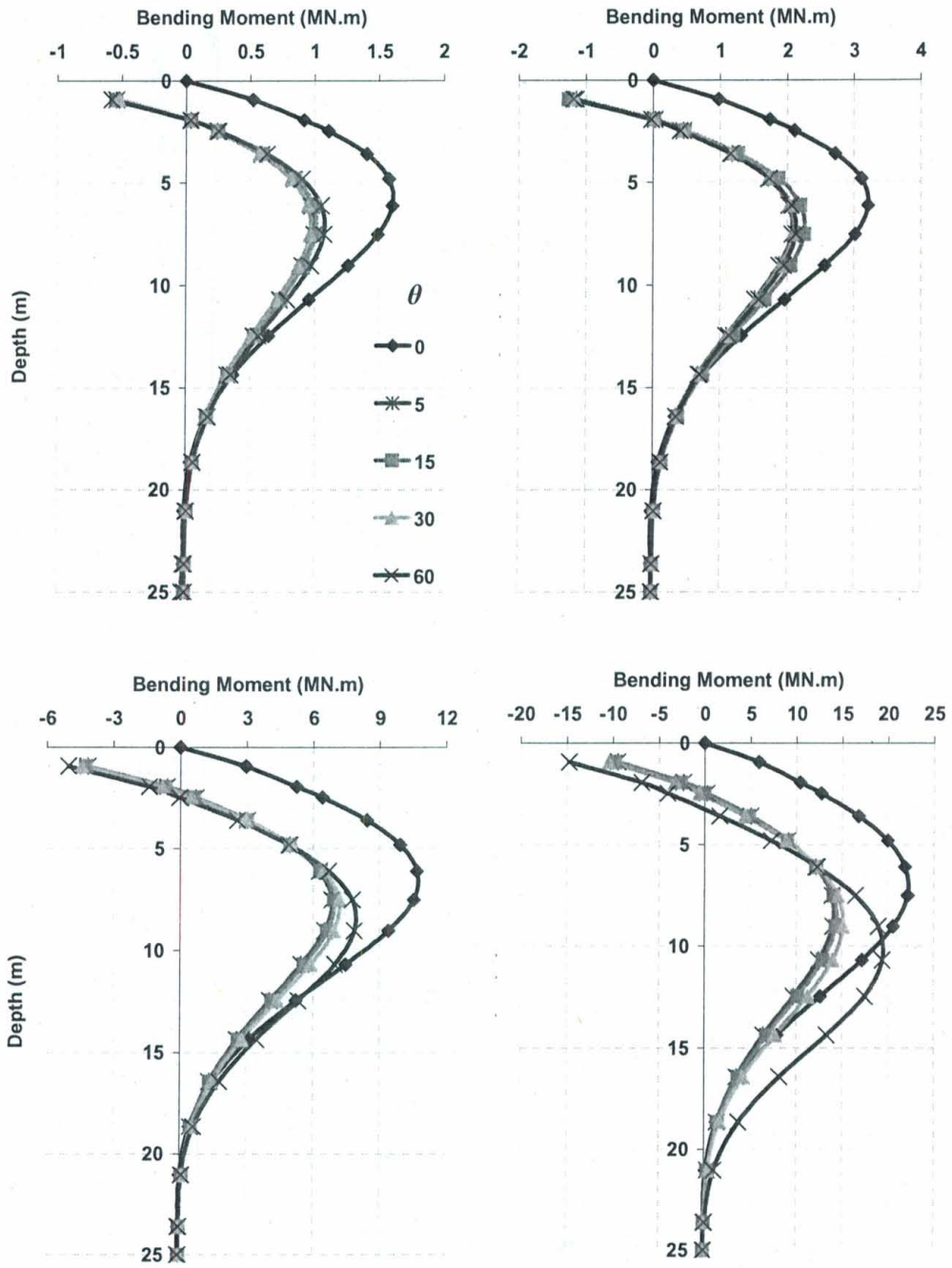

Fig. (7.19) Bending Moment Profile – Case # 7 – at Lateral Load Increments (a) 500 kN, (b) 1000 kN, (c) 3000 kN, (d) 6000 kN

Soil pressure and soil shear stress profiles for different cases under pure lateral loading are shown in Figs. (7.20 a) to (7.24 a). Soil Pressure increases by increasing lateral load at pile head. It reaches maximum value at a depth of $2D$ to $3D$. Below this depth the pressure decreases and reaches zero value at a depth corresponding to zero lateral pile deflection shown in Figs. (7.10) to (7.14). Below this level, soil pressure increases in a manner that depends on pile flexibility. For piles of small L/T (cases# 2, 4, and 5), soil pressure increases by increasing depth up to pile tip. For pile of higher L/T values (cases# 6 and 7); pile of more flexibility; the pressure increases by increasing depth then decreases until reaching small values at pile tip. The plotted soil shear stress in the same figures is in the longitudinal direction (direction of pile length). It shows that under pure lateral loading soil shear stress is negative at shallow depth reaching minimum value at the same depth of maximum soil pressure. By increasing depth, soil shear stress increases and being positive until reaching maximum value at pile tip. The negative shear stress at shallow depth means that soil is moving up relative to the pile (heaving due to the lateral loading) where the zone of soil pressure increases on the front side of the pile. Below this depth soil shear stress increases to positive values. The positive shear stress increases by decreasing L/T. By increasing pile rigidity the pile tends to rotate and pile tip moves backward. This pile movement will increase soil shear stress close to pile tip.

For cases of pure tension loading, both soil pressure and soil shear stress distributions are shown in Figs. (7.20 b) to (7.24 b). As the pile is subjected to pure tension load, there will be high resistance close to the pile tip where soil stresses are high due to pile driving. This tension loading process and the resistance at pile tip will cause pile elongation. The elongation effect of soil pressure distribution along the pile is clear in the figures. There is a reduction in soil pressure along the pile length up to a depth close to pile tip. As the pile elongate, pile section contract causing soil confining pressure to decrease. However, close to the pile tip, the developed resistance against pulling the pile out cause soil dilation and increase in soil pressure. In the mentioned figures, it can be seen that at high tension loads up to failure there is a significant reduction at pile tip. This reduction happens when the pile starts to be pulled out and

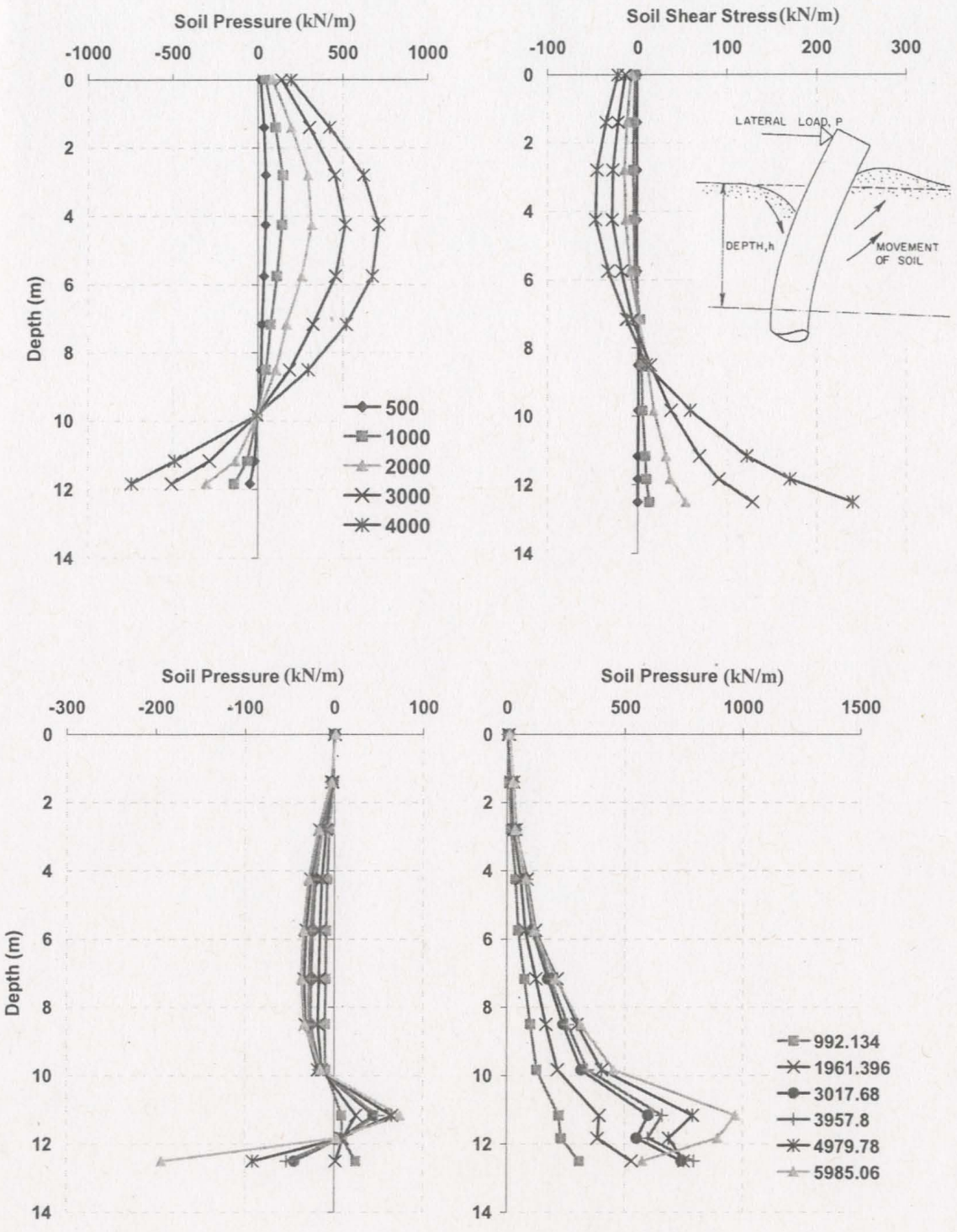

Fig. (7.20) Soil Pressure and Soil Shear Stress – Case #2 (a) Pure Lateral Loading ($\theta = 0^{\circ}$), (b) Pure Tension Loading ($\theta = 90^{\circ}$)

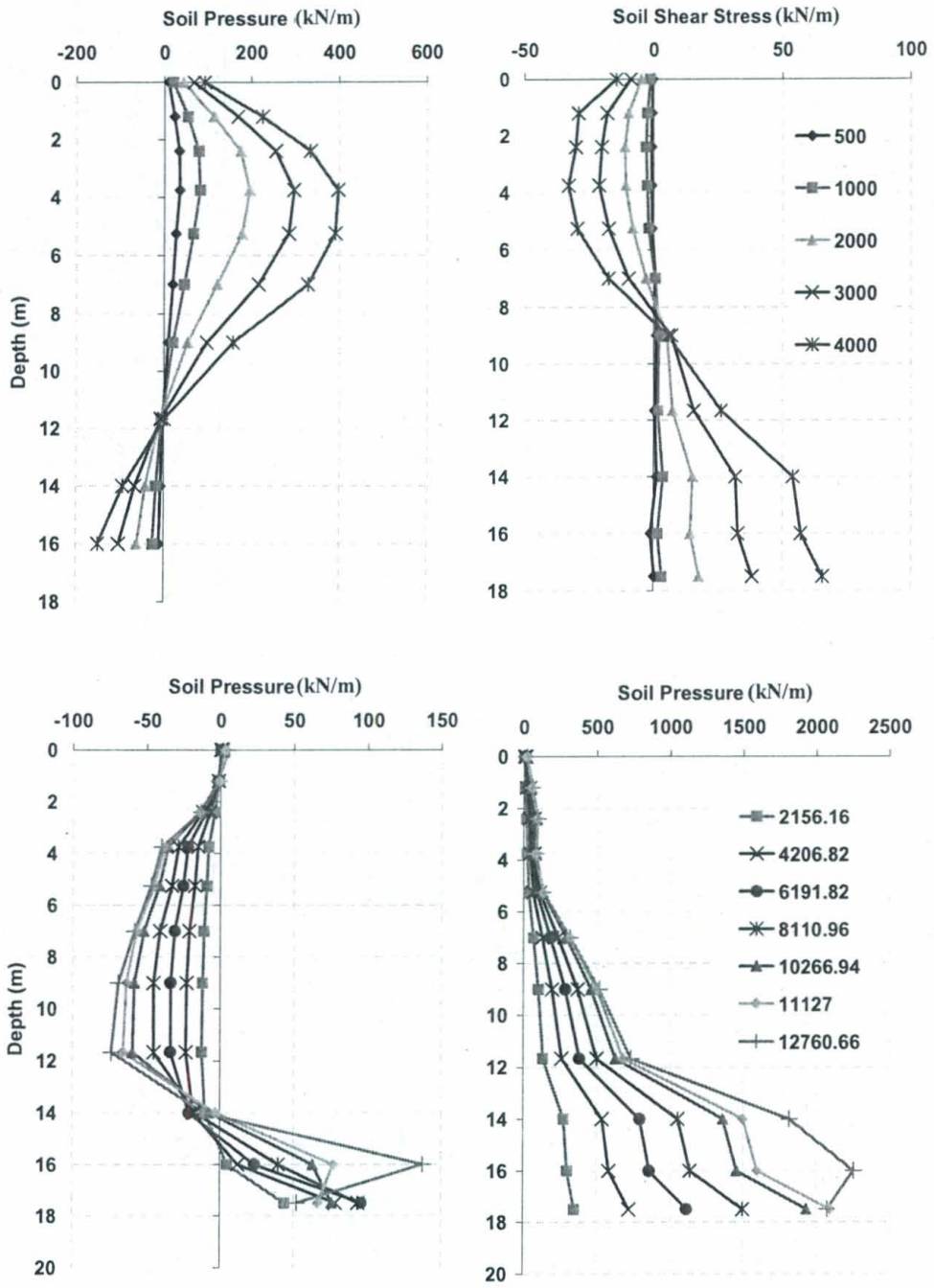

Fig. (7.21) Soil Pressure and Soil Shear Stress – Case #4 (a) Pure Lateral Loading ($\theta = 0°$), (b) Pure Tension Loading ($\theta = 90°$)

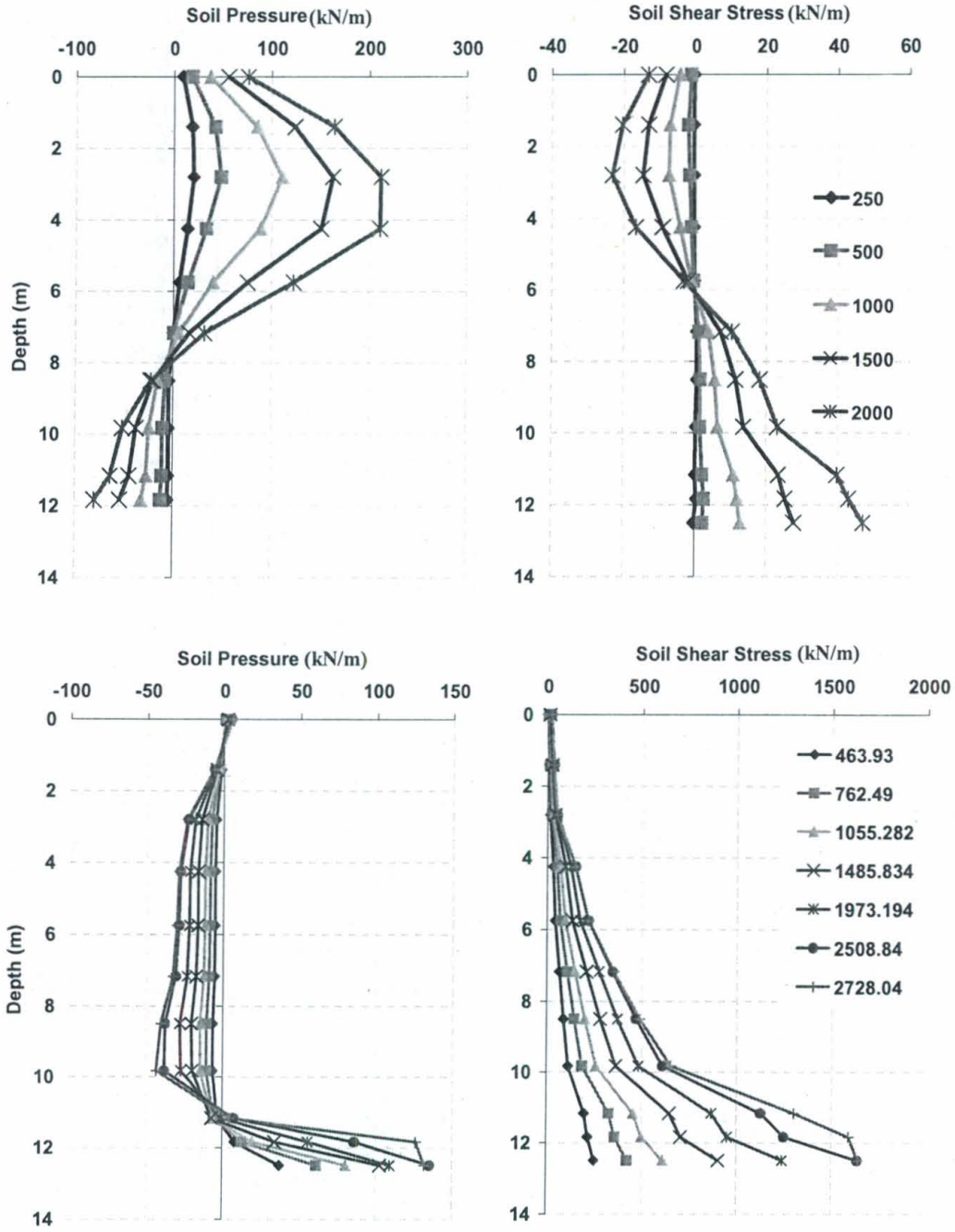

Fig. (7.22) Soil Pressure and Soil Shear Stress – Case #5 (a) Pure Lateral Loading ($\theta = 0°$), (b) Pure Tension Loading ($\theta = 90°$)

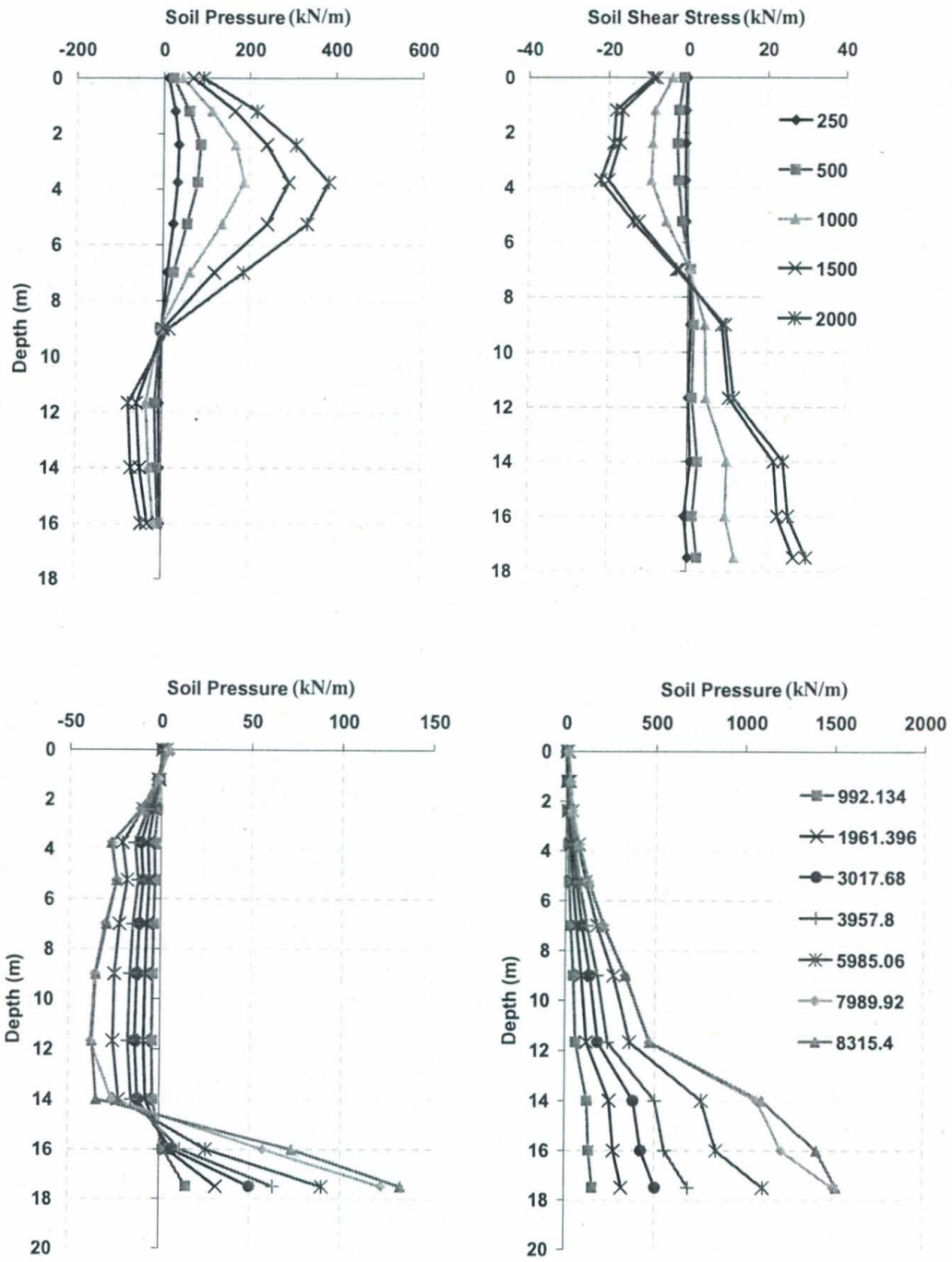

Fig. (7.23) Soil Pressure and Soil Shear Stress – Case #6 (a) Pure Lateral Loading ($\theta = 0°$), (b) Pure Tension Loading ($\theta = 90°$)

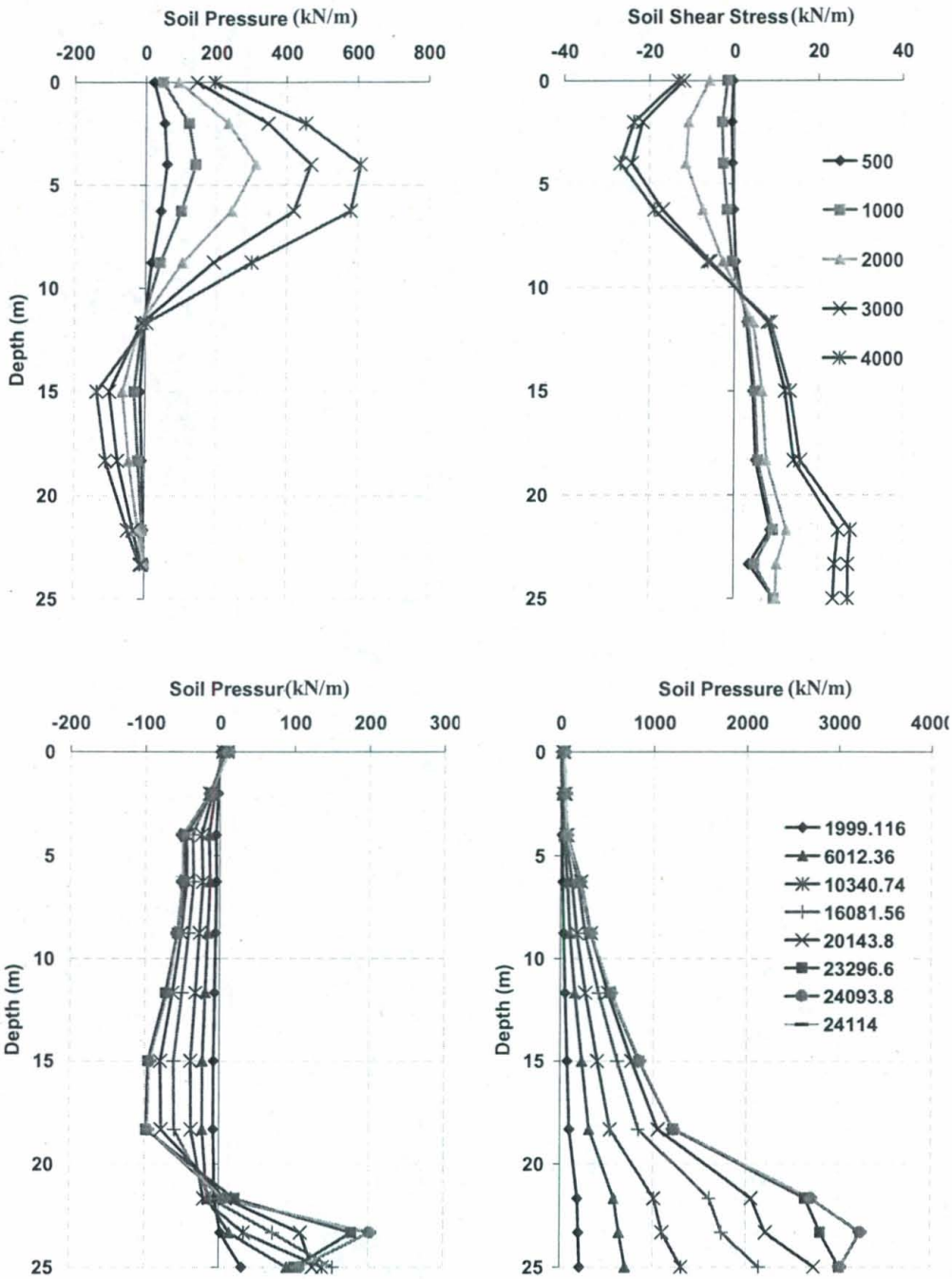

Fig. (7.24) Soil Pressure and Soil Shear Stress – Case #7 (a) Pure Lateral Loading ($\theta = 0°$), (b) Pure Tension Loading ($\theta = 90°$)

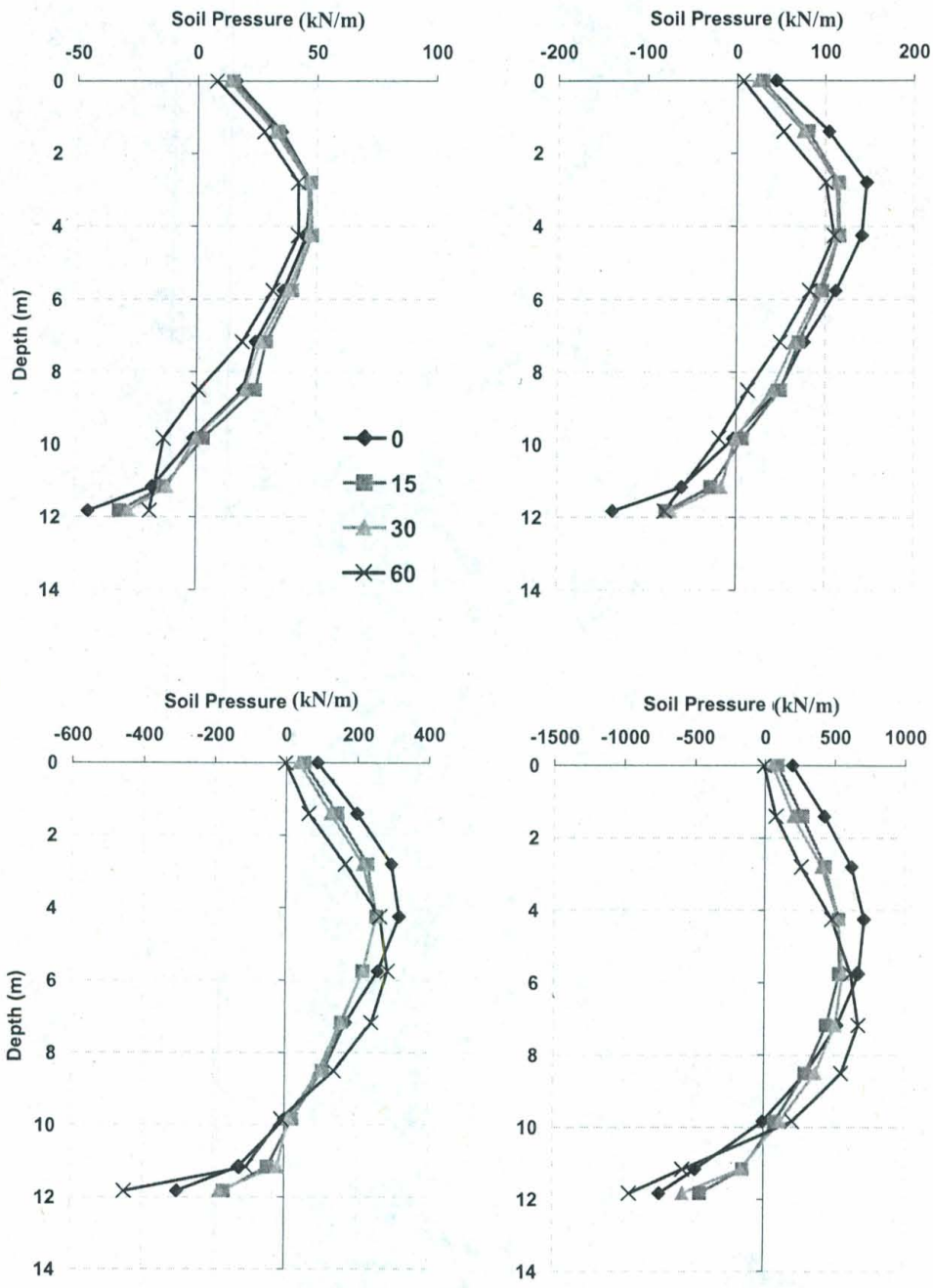

Fig. (7.25) Soil Pressure Profile – Case #2 at Lateral Load Increment (a) 500 kN, (b) 1000 kN, (c) 2000 kN, (d) 4000 kN

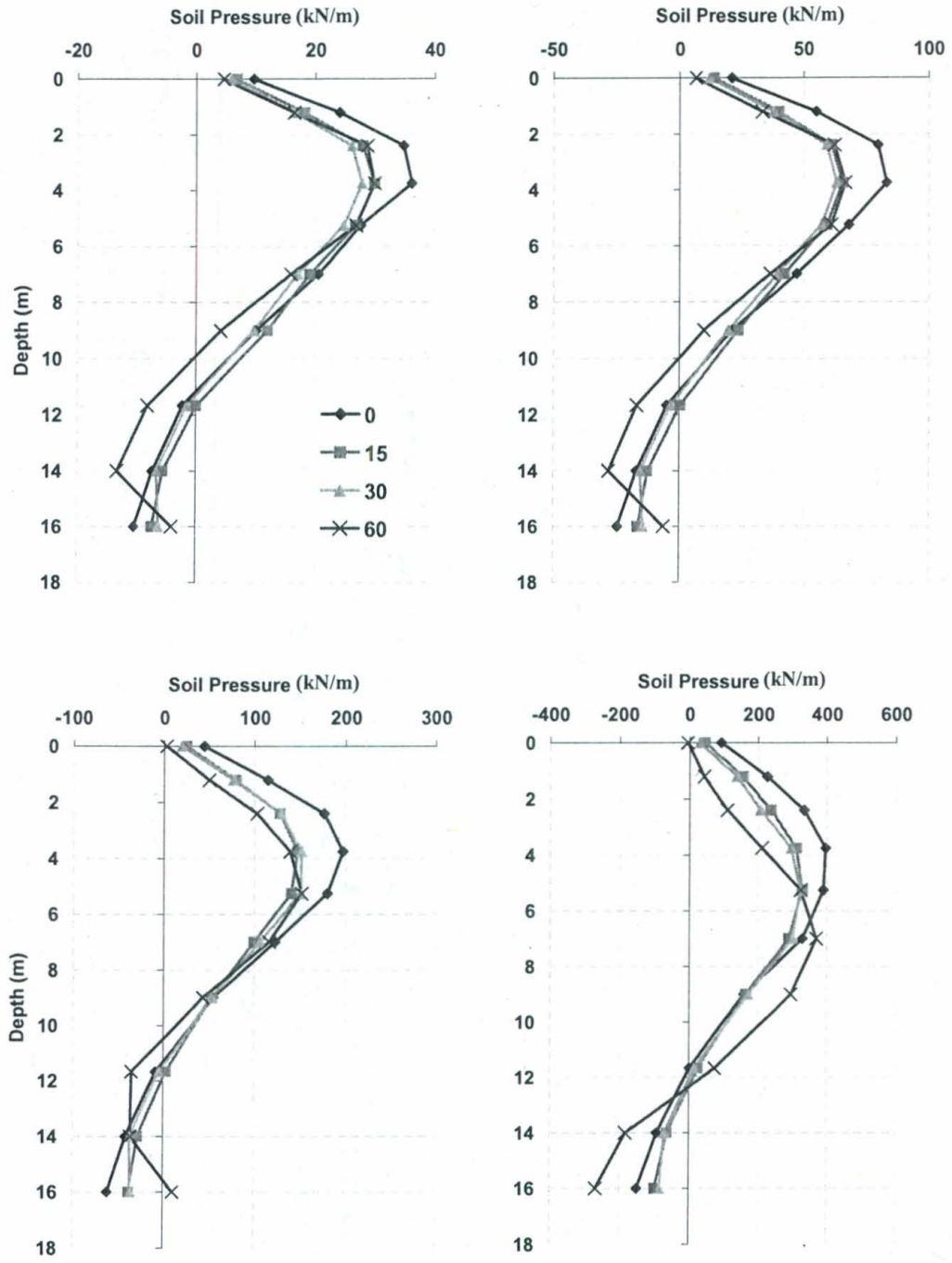

Fig. (7.26) Soil Pressure Profile – Case #4 at Lateral Load Increment (a) 500 kN, (b) 1000 kN, (c) 2000 kN, (d) 4000 kN

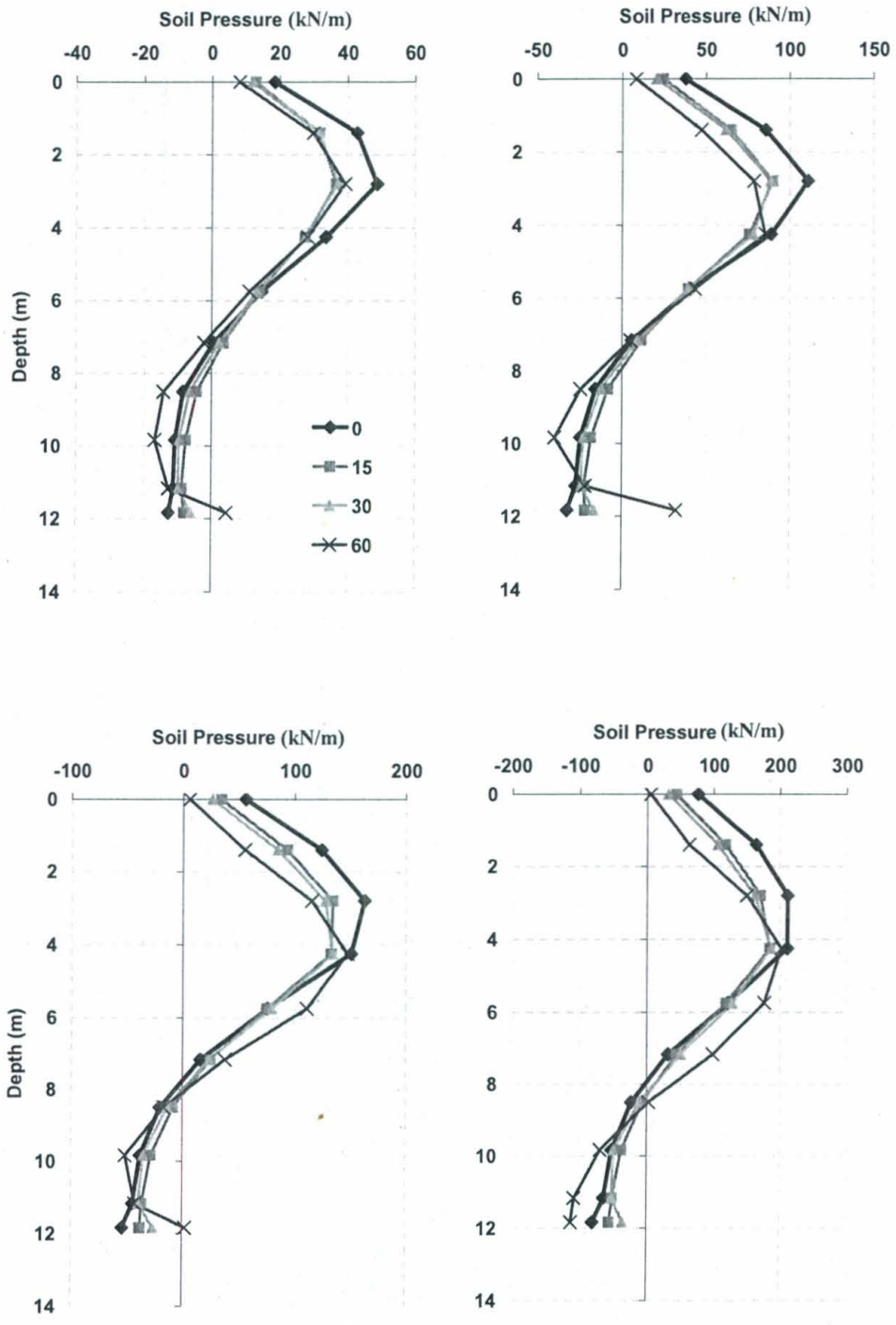

Fig. (7.27) Soil Pressure Profile – Case #5 at Lateral Load Increment (a) 250 kN, (b) 500 kN, (c) 750 kN, (d) 1000 kN

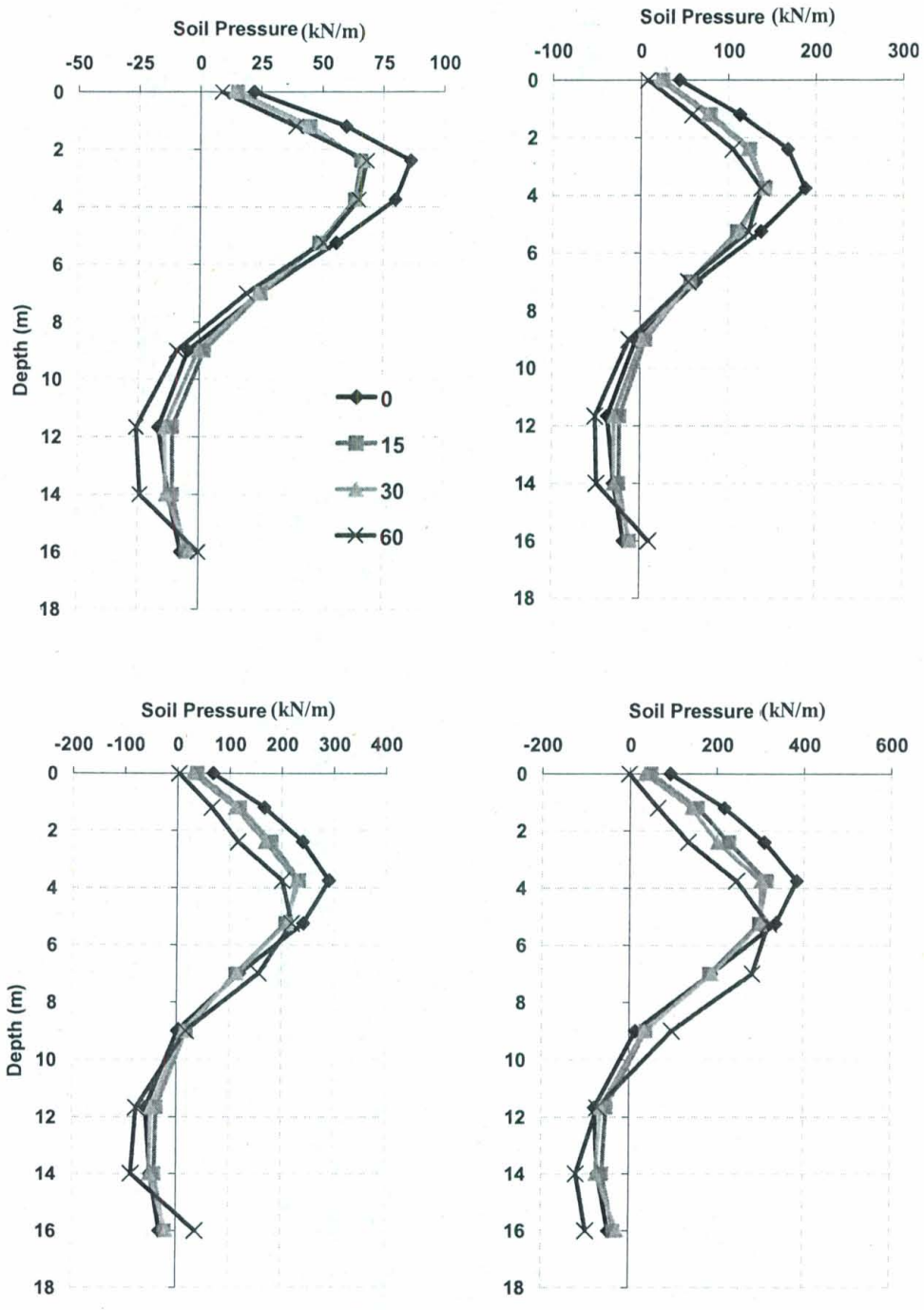

Fig. (7.28) Soil Pressure Profile – Case #6 at Lateral Load Increment (a) 500 kN, (b) 1000 kN, (c) 1500 kN, (d) 2000 kN

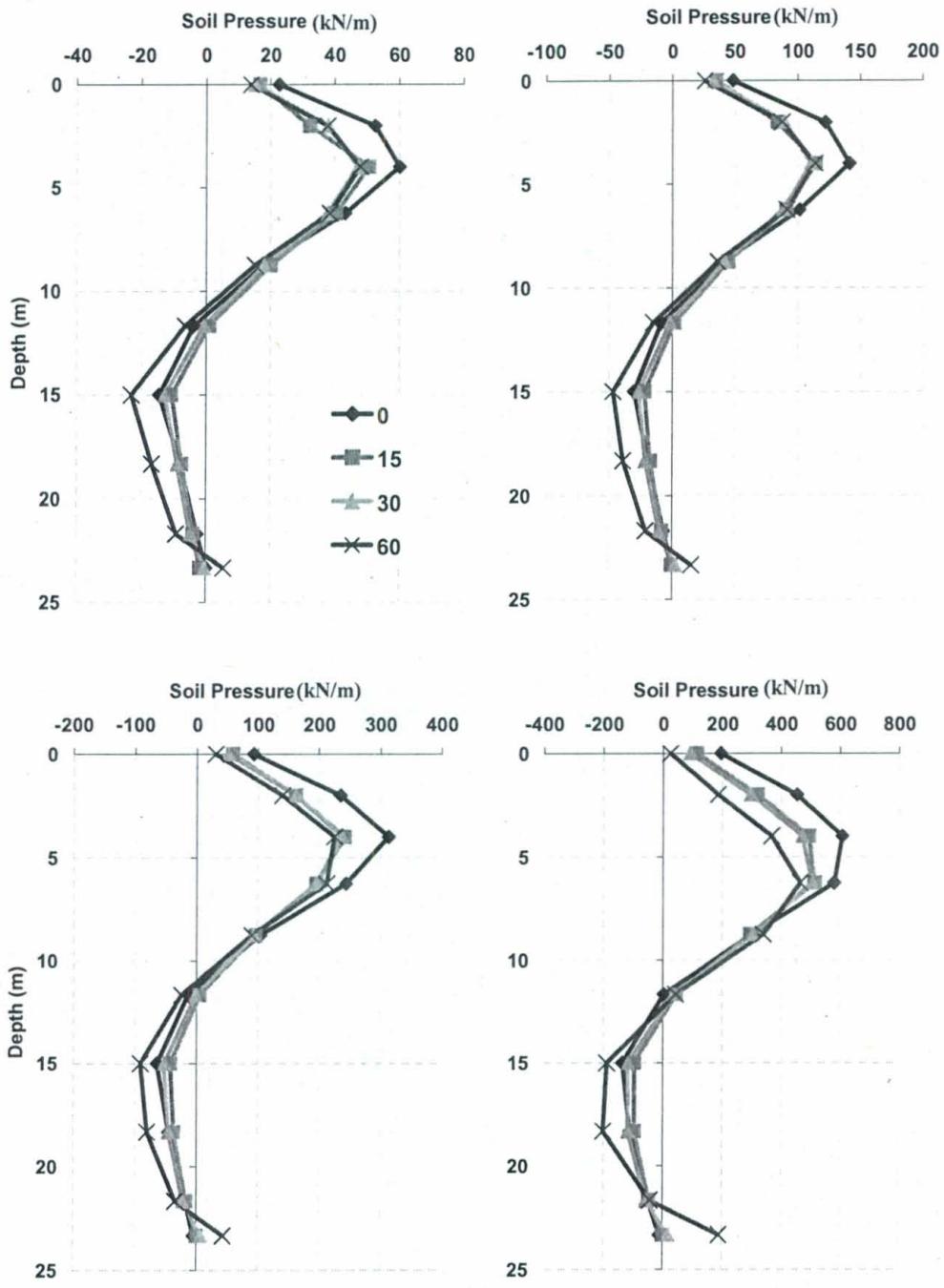

Fig. (7.29) Soil Pressure Profile – Case #7 at Lateral Load Increment (a) 500 kN, (b) 1000 kN, (c) 2000 kN, (d) 4000 kN

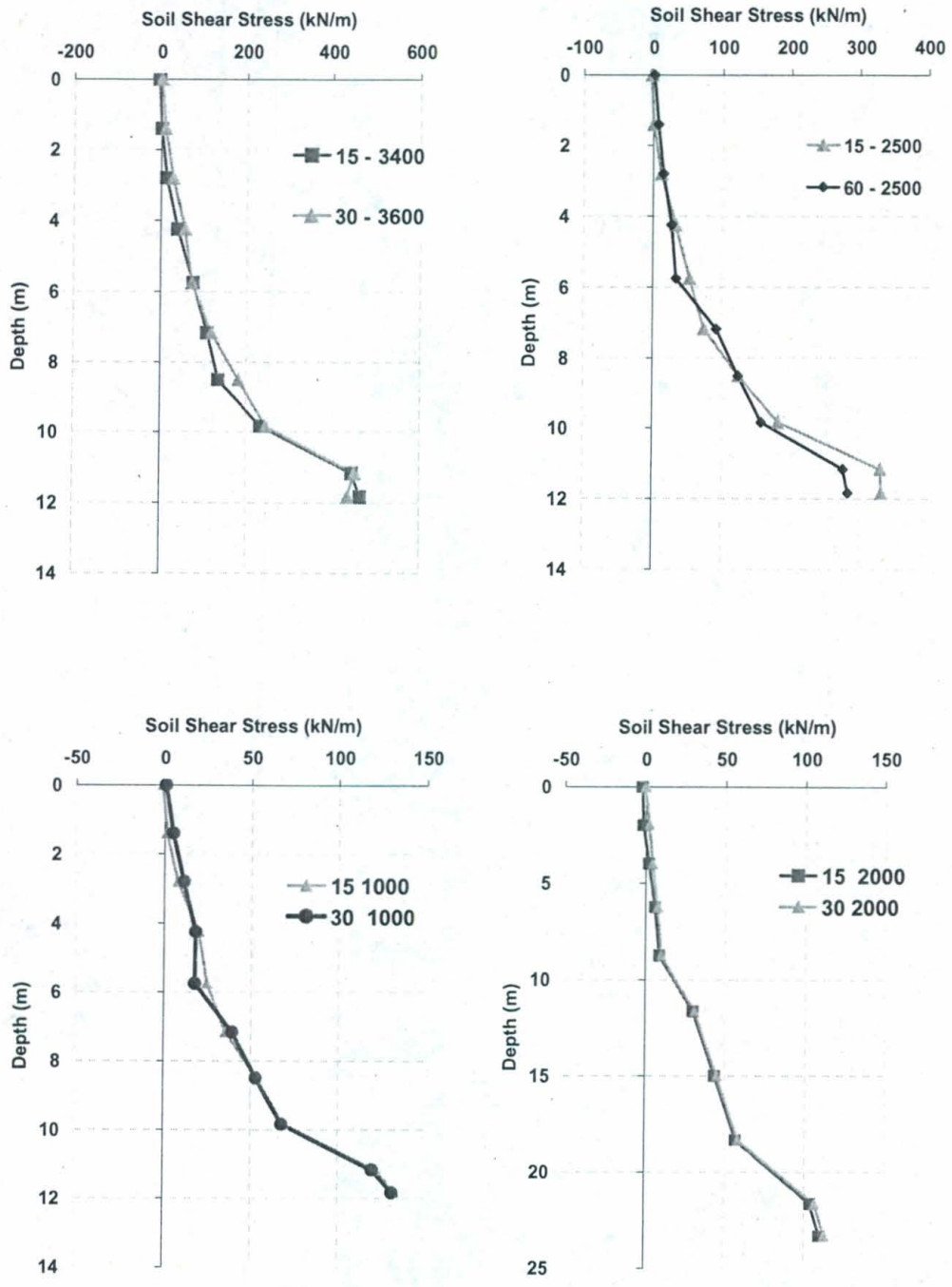

Fig. (7.30) Soil Shear Stress Profile –at Selected Tension Load Increments (a) casé# 2, (b) case# 2, (c) case# 5, (d) case# 7

there is no more contact between pile tip and the soil. In terms of soil shear stress distribution along the pile, it can be seen that it increases by depth. Also soil shear stress increases in a rate that increases by increasing depth which is similar to what recommended by ICP (2005) design method for offshore piles.

After discussing the response of soil to both pure lateral and pure tension loading cases in terms of soil pressure and soil shear stress along the pile, we can better understand how soil will behave under combined loading cases. Soil pressure distributions are shown in Figs. (7.25) to (7.29) for different loading angles at different lateral load increments at pile head. For all loading angles more than 0° (pure lateral loading), there is a constant reduction in soil pressure from that of pure lateral loading case at shallow depths before the pile fails in tension. This reduction that was observed also in bending moment profiles is due to pile elongation as a result of tension load component at pile head as discussed before. At deeper depths, there is also a reduction in soil pressure at small loading angles. However, by increasing loading angles the tension load component increases causing an increase in soil pressure due to soil dilation as discussed in the case of pure tension loading. When the pile fails in tension, no more soil shear stress will be developed. This will lead to a reduction in soil pressure at shallow depth and an increase at deeper depths as the resistance is going to deeper soil layers which can resist more. This is significant to what observed in bending moment profiles where maximum bending moment moved to deeper depths.

Soil shear stress distributions are shown in Fig. (7.30) for some cases at different vertical pullout load increments. It can be seen that for small loading angles soil shear stresses are the same at the same vertical pullout load increments. However, there is a small difference between small and large loading angles at the same vertical load increment especially for piles of less flexibility as shown in Fig. (7.30 b). To mobilize the same vertical load increment, piles loaded at small loading angle will be already subjected to higher lateral load and lateral deflection than that loaded at larger loading angle. This higher lateral deflection will cause a reduction in the initial soil confining

pressure on the backward side of loading direction. This will lead to less contact pressure on the back side which causes less shear stress at shallow depth. Close to pile tip and when the pile is less flexible and tends to rotate, high soil pressure will be developed at pile tip which will be higher in case of small loading angle than that of large loading angle. The higher soil pressure at pile tip will cause higher soil shear stress to be developed in case of small loading angle than that of large loading angle. For more flexible piles there will be no much deference at pile tip between different loading angles. However, the reduction in contact pressure on the back side at shallow depths will cause a reduction in soil shear stress and on the total pile tension capacity as discussed before in the section of load displacement curves.

From the previous discussion based on load – displacement relationships, pile lateral deflection profile, bending moment profile, and soil pressure and soil shear stress distributions, it can be concluded that there is a significant interaction between both lateral and vertical pullout loading cases. Such interaction should be considered in the design of offshore piles. Ignoring this interaction will lead to uneconomic design. In the following sections, a recommended design method for pile ultimate capacity and maximum bending moment will be presented.

7.3.5 Ultimate Pile Capacity Proposed Method:

The ultimate capacity of an offshore anchor pile subjected to inclined pullout load was obtained when the pile failed in tension. The ultimate tension pile capacity for different loading angles was determined by plotting the load – displacement curves on log-log scale and pick the point of maximum curvature to be the failure load. The present design method can predict the ultimate pile capacity (F_o) as:

$$F_o = \sqrt{H_f^2 + V_f^2} \tag{7.1}$$

where H_f is the lateral load at failure and V_f is the failure tension load. By predicting both H_f and V_f, the ultimate capacity of the pile (F_o) can be obtained.

To predict the lateral load at failure (H_f), it was normalized to (H_R); the ultimate lateral capacity of a rigid pile has the same pile diameter and length as the current cases; and plotted versus loading angles as shown in Fig. (7.31). The curves are shown for a wide range of L/T that ranges from rigid pile case of $L/T = 2.33$ to pile of high flexibility of $L/T = 10.2$. It can be seen from the figure that for all cases (H_f / H_R) decreases in an exponential decay manner by increasing loading angle. However, the rate of decay is decreasing by increasing pile flexibility (L/T). All curves were fitted to follow a decay exponential function as:

$$H_f / H_R = \alpha_H \cdot e^{-\beta_H \theta} \tag{7.2}$$

where α_H and β_H are fitting parameters. It was found that the parameter β_H has almost a constant value of 0.046. The parameter α_H was found to be a function of pile flexibility (L/T). Figure (7.32) shows the change of α_H with L/T. The plotted points were fitted as:

$$\alpha_H = \alpha_{H\min} + \frac{\alpha_{H\max} - \alpha_{H\min}}{1 + \left(\frac{L/T}{4.67}\right)^{9.2}} \tag{7.3}$$

where $\alpha_{H\,min} = 0.71$ and $\alpha_{H\,max} = 1.31$.

The ultimate lateral capacity of rigid pile can be determined based on the equation recommended by Zhang et al. (2005). They suggested the following equation:

$$H_R = 0.3\left(\eta K_P^2 + \zeta \cdot K \tan\delta\right) \cdot \gamma \cdot a \cdot d\left(2.7x - 1.7L\right) \tag{7.4 a}$$

where K_P is the passive earth pressure coefficient and equals to $\tan(45° + \varphi/2)$, for circular pile $\eta = 0.8$ and $\zeta = 1$ and x is the depth to the point of rotation can be calculated as:

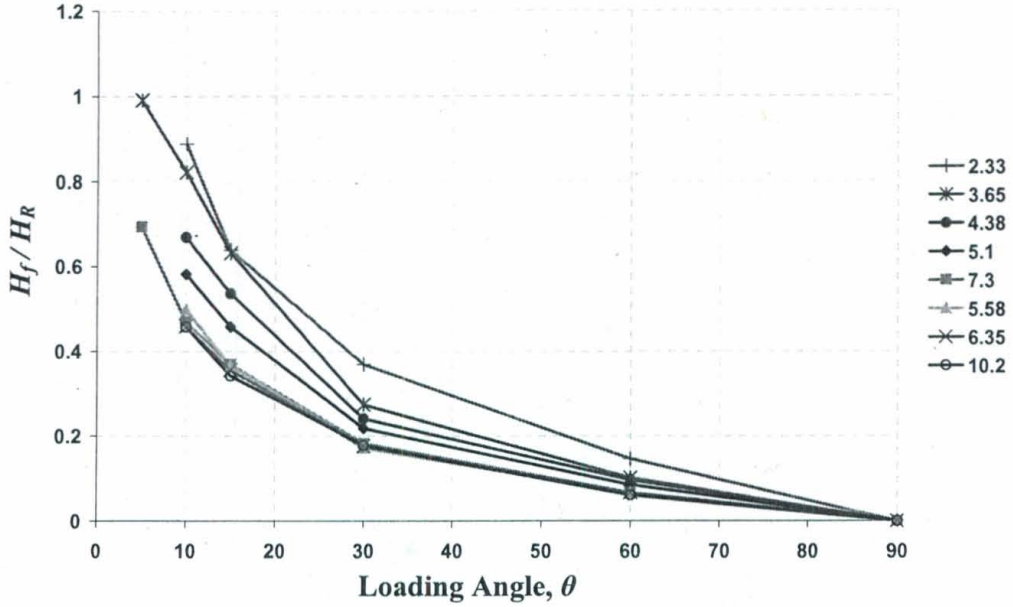

Fig. (7.31) Normalized Lateral Load Capacity (H_f / H_R) versus Loading Angle

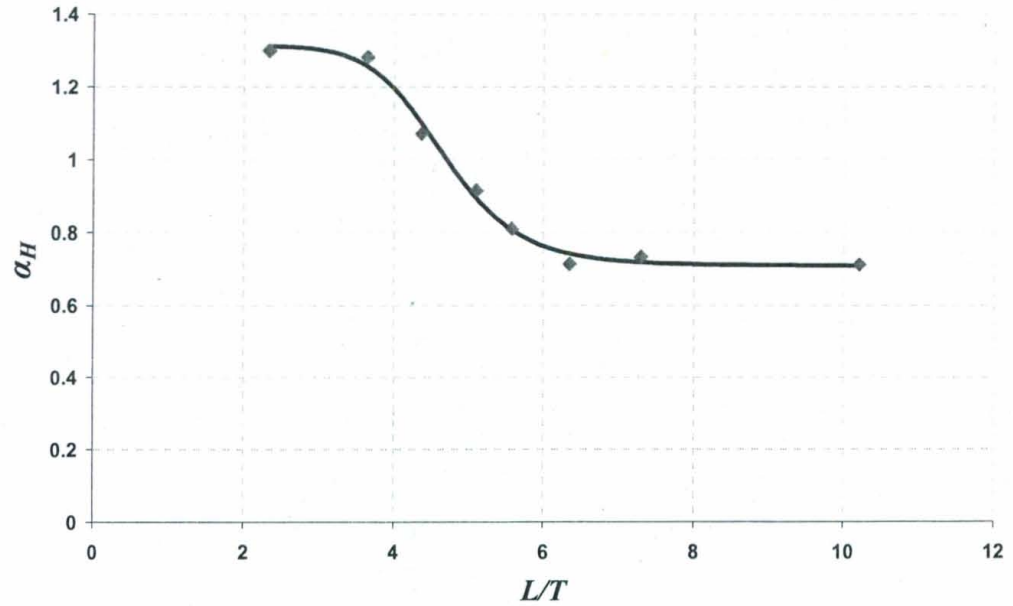

Fig. (7.32) Relationship between α_H and L/T

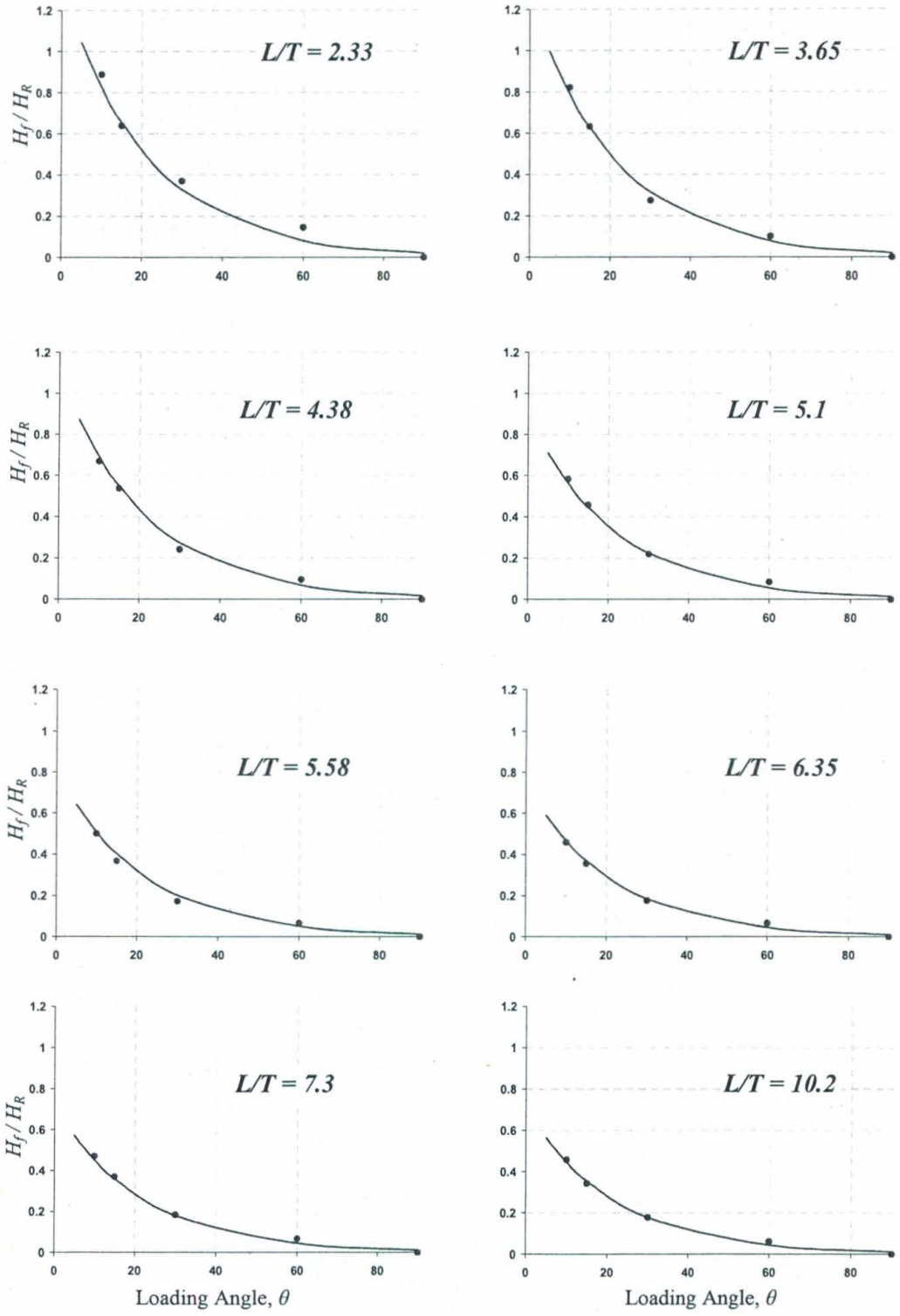

Fig. (7.33) Normalized Lateral Load Capacity (H_f / H_R) versus Loading Angle – Comparison between FEM results and the proposed design method

$$x = \left[-(0.567 \cdot L + 2.7 \cdot e) + \left(5.307 \cdot L^2 + 7.29 \cdot e^2 + 10.541 \cdot eL\right)^{0.5} \right] / 2.1996 \qquad (7.4\text{ b})$$

By calculating the parameter α_H using Eq. (7.3) and using a value of 0.046 for the parameter β_H, the lateral load at failure can be determined. Fig. (7.33) shows the comparison between the proposed method using Eq. (7.2) and the data obtained from the FEM results. There is high agreement between the proposed design method and the results obtained from the FEM.

Fig. (7.34) shows the relationship between (V_u / V_f) and loading angles. It can be seen that all plotted cases follow the same trend. All data follow one function as:

$$V_u / V_f = 1 + 8.8 \cdot e^{-0.33 \cdot \theta} \qquad (7.5)$$

where V_u is the ultimate tension capacity under pure tension loading case ($\theta = 90°$). It can be observed from Fig. (7.34) that almost a loading angle of 20° is a critical angle below which the ultimate tension capacity decreases from the case of pure tension loading. Using Eqs. (7.2) and (7.5) to calculate H_f and V_f, respectively, the ultimate capacity of the pile (F_o) can be obtained using Eq. (7.1) at different loading angles.

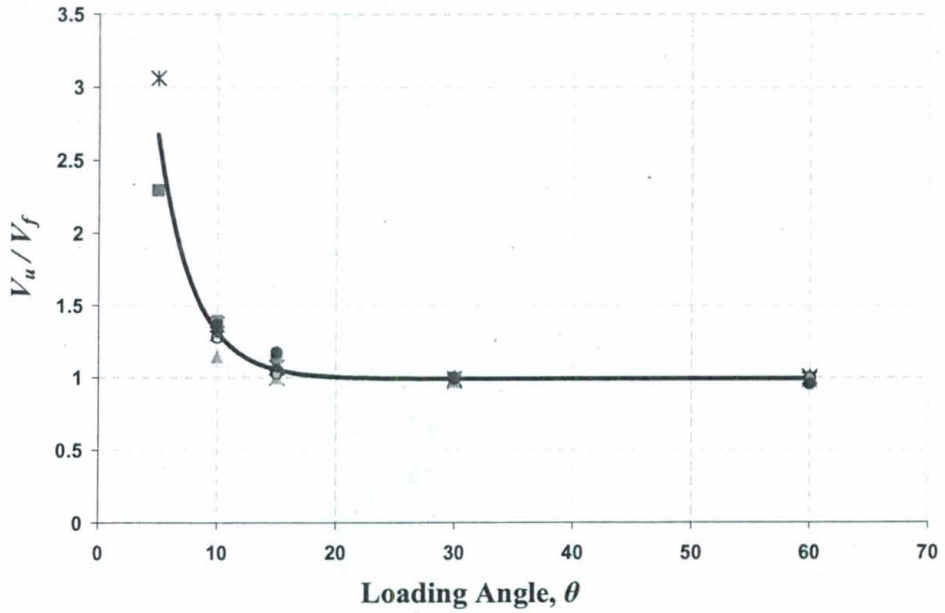

Fig. (7.34) Normalized Tension Load Capacity (V_u / V_f) versus Loading Angle

7.3.6 Maximum Bending Moment Proposed Method:

As discussed before that for the same pile and at the same lateral load increment at pile head there is a constant reduction in bending moment once the loading angle becomes larger than 0° (pure lateral loading). For all loading angles larger than 0° bending moment profile is same until the pile fails in tension. This can also be seen in Figs. (7.35) to (7.39). In these figures, the normalized horizontal load (H_n) on the pile head and the normalized maximum bending moment ($M_{n\text{-}max}$), defined by Eqs. (5.3) and (5.4), respectively, are plotted. It can be seen that the relationship between (H_n) and ($M_{n\text{-}max}$) is linear in all cases. This is same to what observed from the centrifuge tests results. For the same pile, the relationship is the same for all loading angles larger than 0° (pure lateral loading) and before the pile fails in tension. The plotted data were fitted by a linear function as:

$$M_{n-\max} = m \cdot H_n$$

where the slope m can be considered as m_0 for pure lateral loading cases and m_θ for inclined pullout loading cases. The ratio of (m_0 / m_θ) for different cases are plotted versus (L/T) in Fig. (7.40). The plotted data were fitted as:

$$m_0 / m_\theta = 1.55 + 1029 \cdot e^{-2.077(L/T)} \tag{7.6}$$

Using Eq. (7.6) the maximum bending moment of offshore anchor piles subjected to inclined pullout loading can be predicted at any stage during loading up to failure. Bending moment of pile under pure lateral loading is needed to use Eq. (7.6). That bending moment can be calculated using some available codes or methods that are being used in industry as LPile software. It should be noted that maximum bending moment that can be predicted from the current proposed method is the positive bending moment. In most cases the maximum negative bending moment close to pile head is less than or equal to the maximum positive bending moment before the pile fails in tension. The maximum negative bending moment should be less than what observed in the current study. The offshore anchor pile is usually loaded at a padeye.

This padeye is fixed in another ring of steel has an inside diameter same as the pile outside diameter. This means that the pile stiffness at loading level is higher than pile stiffness at along the pile. Also, the stress localization at pile head where the displacement is applied in the FEM could cause some increase in the maximum negative stress at pile head.

From the current parametric study, it was proposed two design methods to predict the ultimate pile capacity and maximum bending moment of offshore anchor piles subjected to mooring forces in dense sand. The proposed methods can be used at different loading angles. Also the methods are valid for piles of *L/T* larger than 2 which are not rigid piles. However, these methods did not consider the loading eccentricity (*e*). It considered that the loading at the ground surface. Offshore anchor piles are usually loaded at the ground surface or below. The padeye can be below the ground surface to increase pile lateral capacity. In the next section, the effect of padeye depth will be discussed. A design recommendation will be suggested.

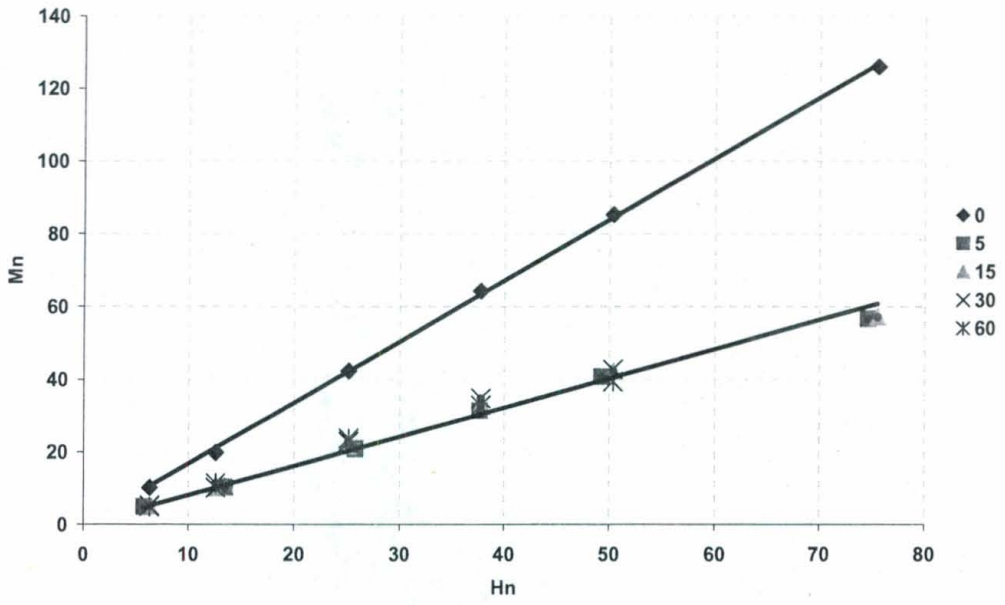

Fig. (7.35) Normalized Horizontal Load versus Normalized Max. Bending Moment for All Tests – Case# 2

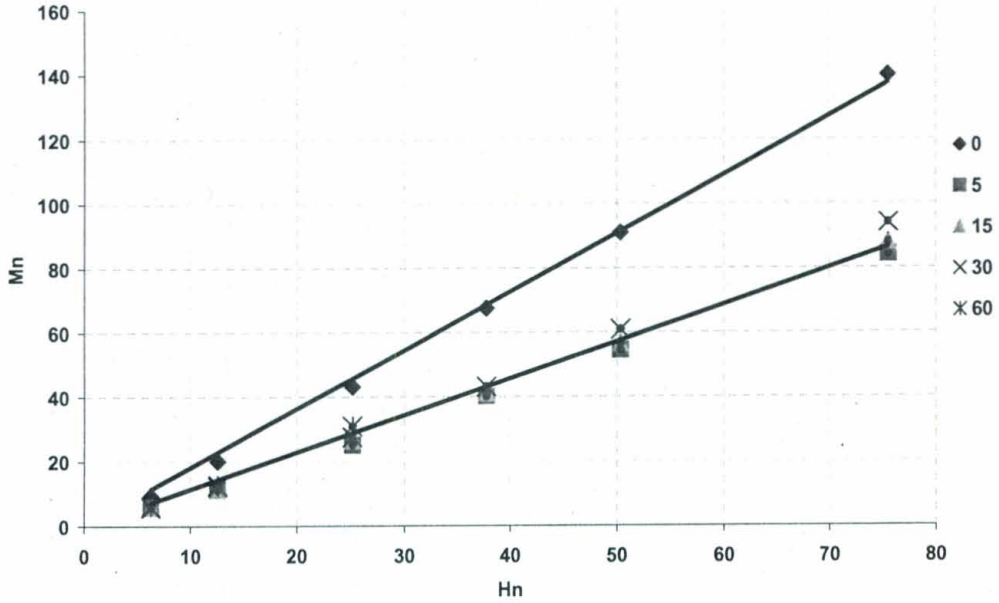

Fig. (7.36) Normalized Horizontal Load versus Normalized Max. Bending Moment for All Tests – Case# 4

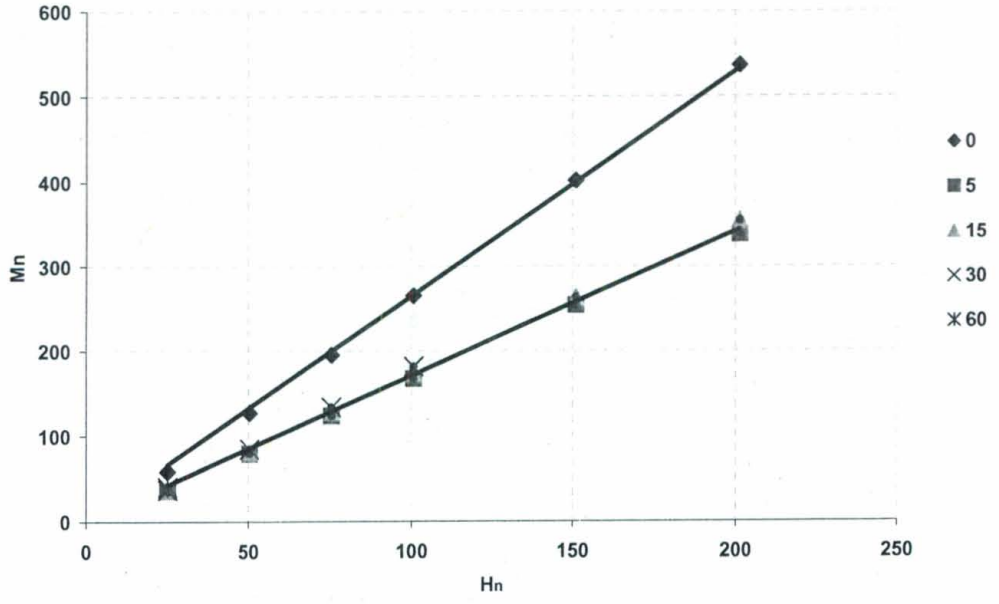

Fig. (7.37) Normalized Horizontal Load versus Normalized Max. Bending Moment for All Tests – Case# 5

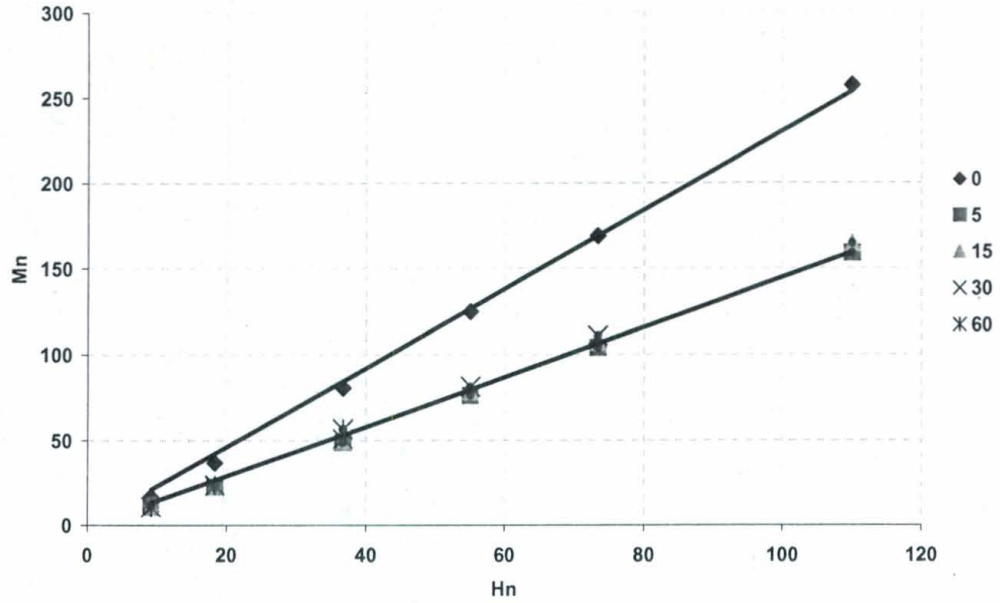

Fig. (7.38) Normalized Horizontal Load versus Normalized Max. Bending Moment for All Tests – Case# 6

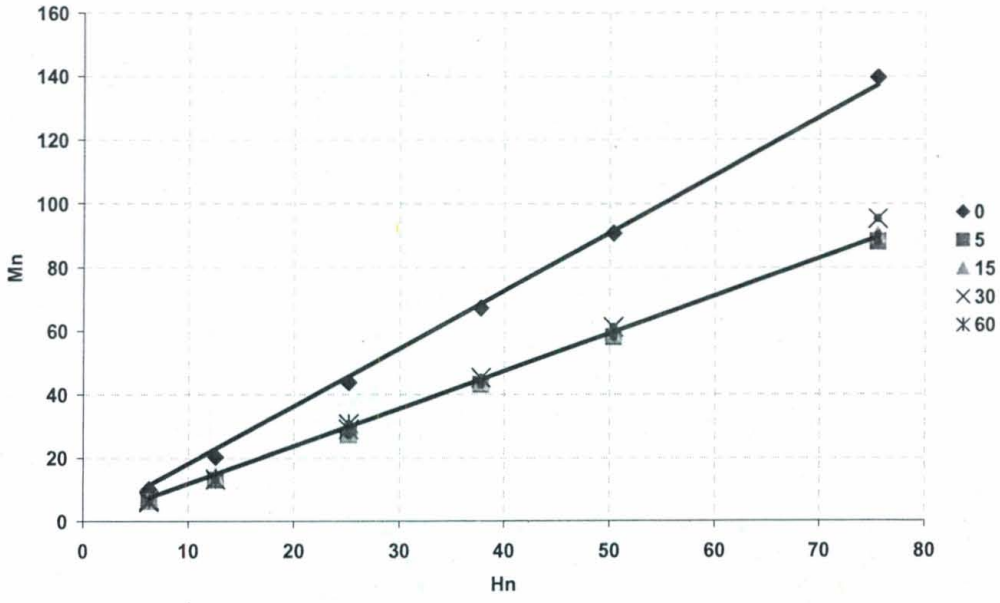

Fig. (7.39) Normalized Horizontal Load versus Normalized Max. Bending Moment for All Tests – Case# 7

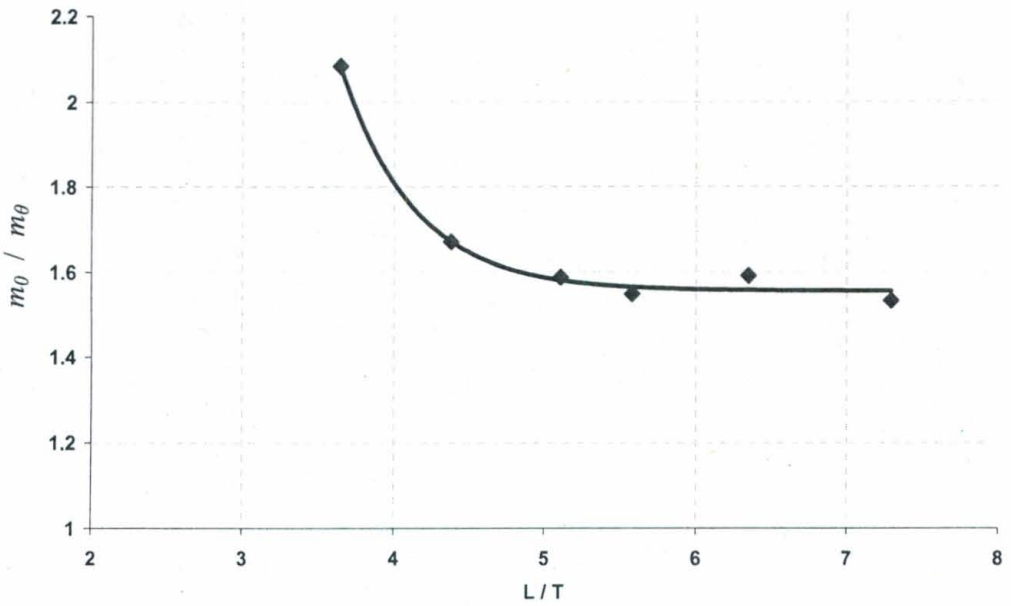

Fig. (7.40) Maximum Bending Moment Ratio versus *L/T*

7.4. The Effect of Padeye Depth:

Offshore anchor piles are usually loaded from a padeye at pile surface. The padeye depth can be at the ground surface or below the ground surface. Using a padeye below the ground surface is widely used in case of suction caissons. Suction caissons are same as rigid piles. It moves as one unit and so the failure in soil governs the design. Supachawarote et. al (2004) found that for normally or lightly overconsolidated clay, where the strength gradient is significant, the optimal depth is for $e/L \approx 0.65$ to 0.7. The optimal depth occurs when the failure mode changes from rotation to translation mode. At the translation mode, the caisson will drag horizontally in the soil so that the whole front side of the caisson (in the direction of loading) is in contact with the soil causing the highest soil reaction. Also as the soil strength increases with depth, soil reaction resultant should be at about two third of the caisson length. However, anchor piles are more flexible and the mode of failure

will be different from that for suction caissons or rigid piles. In the current parametric study, the effect of padeye depth is studied. Table (7.2) shows the parameters combinations used in this study. Three piles of different *L/T* that covers a wide range of pile flexibility were selected. The piles were pulled out at angle of 15°. The loading angle of 15° was selected as it is close to the case of offshore conditions. In all cases the padeye depth was changed from at the ground surface to a depth of 4*d*. For the case of *L/T* = 3.65 where pile is relatively rigid, deeper locations of padeye were tested. We faced some convergence problems to pull out piles of higher flexibility at padeye depths of deeper depth than 4*d*. This could be due to pile flexibility and a problem of pulling the pile out at a depth of high stresses. From this parametric study, it was found that pulling an offshore anchor pile at a level below the ground surface has some advantages of increasing the ultimate capacity of the pile, decreasing pile deflection, and decreasing bending moment.

7.4.1 Load – Displacement Relationships:

Load – displacement relationships of lateral, vertical, and total components are shown in Figs. (7.41) to (7.43). For all cases of different *L/T*, lateral pile capacity increases by increasing padeye depth. However, for the case of *L/T* = 3.65 (case # 9) which is relatively rigid, maximum lateral capacity was observed at padeye depth of 4 to 4.5 *d* which is corresponding to *e/L* of 0.64 to 0.72. This ratio of *e/L* is similar to what observed by Supachawarote et. al (2004) for clay. Deeper than this level the lateral capacity of the pile decreases gradually. For the same pile, the tension pile capacity decreases as the padeye depth changed from at the ground surface to a depth of 4*d*. Below that depth the tension capacity of the pile increases. The same trend can be observed for the pile of *L/T* = 5.1 (case # 10) where the tension capacity is decreasing up to a padeye depth of 4*d*. However, for the case of pile of *L/T* = 7.3 (case # 11), the tension capacity of the pile decreases at less rate than other cases. The total capacity of the pile increases by increasing padeye depth up to 4*d* (the deepest studied depth for cases # 10 and 11). For case # 9, which is relatively rigid pile, the total capacity reached its maximum at a padeye depth of 4.5*d*.

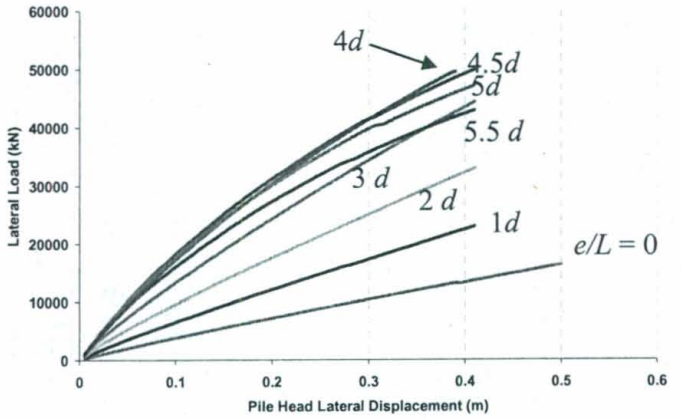

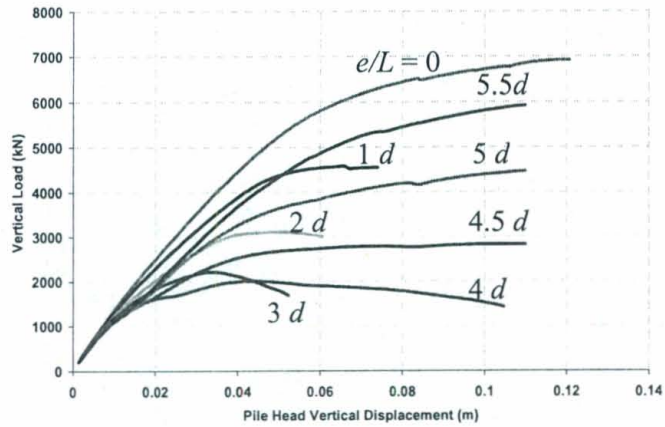

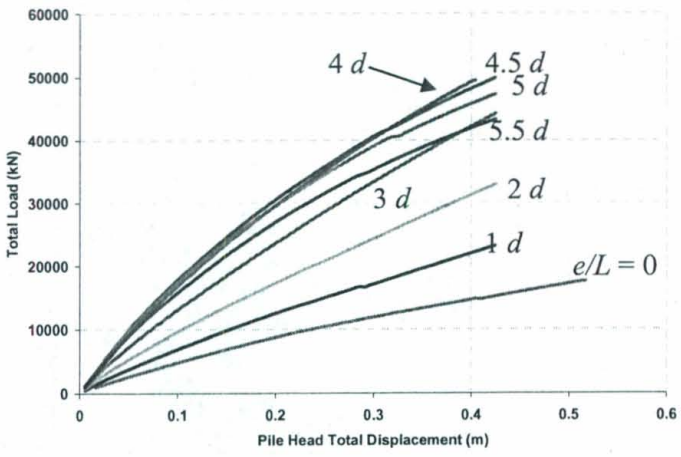

Fig. (7.41) Load – Displacement Curves at Pile Head – Case # 9 - (a) Lateral Component, (b) Vertical Component, (c) Total Component

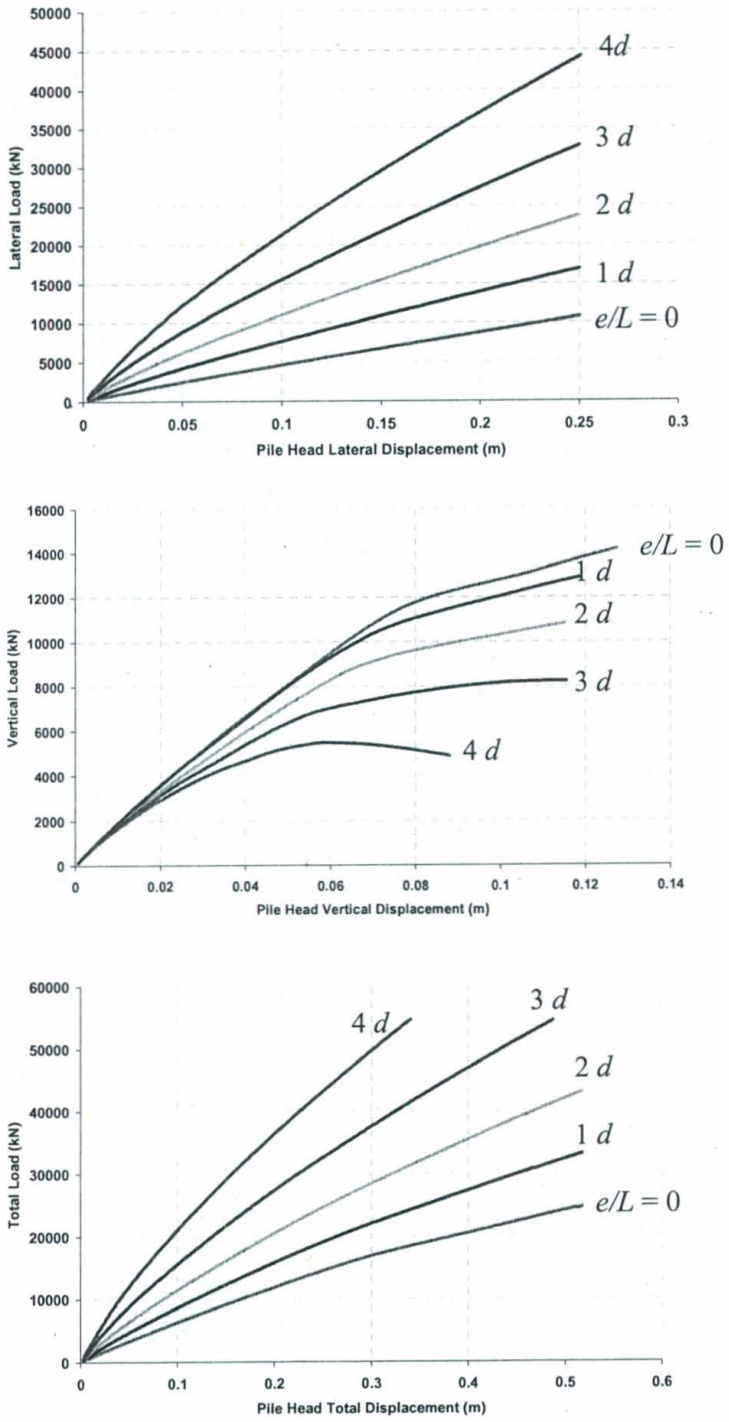

Fig. (7.42) Load – Displacement Curves at Pile Head – Case # 10 - (a) Lateral Component, (b) Vertical Component, (c) Total Component

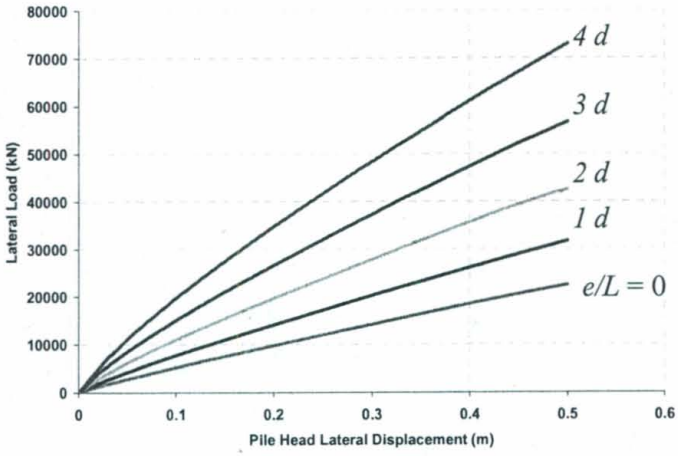

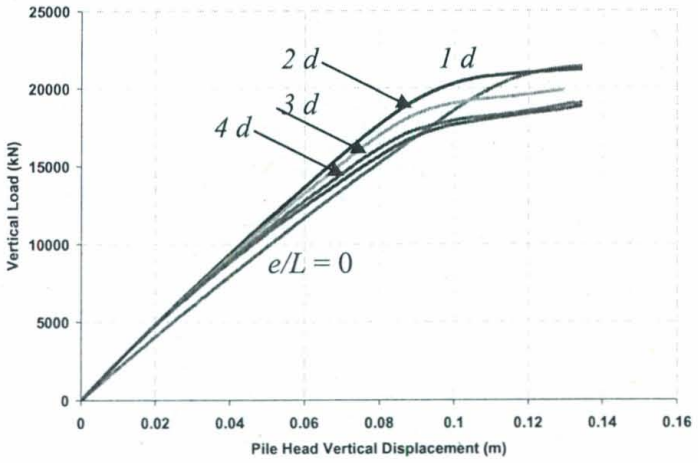

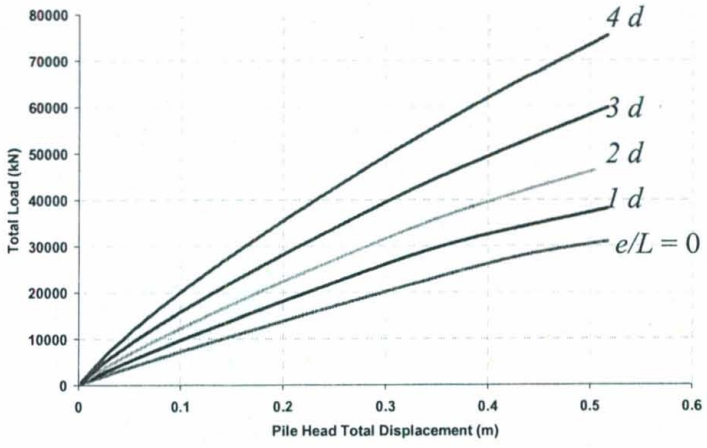

Fig. (7.43) Load – Displacement Curves at Pile Head – Case # 11 - (a) Lateral Component, (b) Vertical Component, (c) Total Component

7.4.2 Pile Lateral Deflection Profile:

Pile lateral deflection profiles are shown for pile of different flexibility and for different depths of padeye at different load increments in Figs. (7.44) to (7.46). There is a significant reduction in lateral deflection of the pile at and above the padeye depth for all cases by increasing the padeye depth. The lateral deflection increases below the padeye depth by increasing the depth of the padeye and by increasing the load. For the case # 9, there is a significant increase in pile lateral deflection below the padeye depth at a depth of $4d$. It is clear that at a padeye depth of $4d$, the pile starts to drag horizontally with almost constant lateral deflection along the pile length except at the padeye location due to stresses localization. This interprets reaching maximum pile capacity at that depth. When the pile deflection changes from the rotation mode to the translation mode soil reaction against the pile will reach its maximum and consequently the capacity of the pile. For the other cases, there is an increase in pile deflection below the padeye depth by increasing its depth. However, the flexibility of the pile prevents the pile from changing to translation mode.

7.4.3 Bending Moment Profile:

Figures (7.47) to (7.49) show bending moment profiles of all cases. There is a significant reduction in bending moment by increasing padeye depth. The reduction rate is high for the positive bending moment and almost vanishes at padeye depth of $4d$. The negative bending moment decreases rapidly by increasing the padeye depth up to about a depth of $2d$. Below a depth of $2d$, there is almost no change in the maximum negative bending moment. This significant reduction in bending moment is due to the reduction in pile curvature. The decrease in pile curvature above padeye depth caused that significant reduction in bending moment.

From all these results, it can be concluded that increasing padeye depth has a significant effect on offshore anchor pile behavior. As dense sand strength increases with depth, increasing padeye depth will increase the ultimate pile capacity and will

decrease lateral deflection and bending moment. The effect of padeye depth is more obvious for piles of low flexibility. The optimum depth of padeye for relatively rigid pile is at about *e/L* of 0.7. At this depth ratio the pile changes from rotation mode to translation mode which causes the whole front side of the pile to be in contact with soil. This will increase soil reaction and the total ultimate capacity of the pile. Although the total capacity of the pile increases by increasing padeye depth, the tension capacity decreases. This reduction in tension capacity increases by decreasing pile flexibility as can be seen in Fig. (7.50). As the padeye depth increases, soil confining pressure on the back side of the pile (opposite of the loading direction) decreases. This reduction will reach its optimum when the pile deflection mode changes from rotation to translation. Below that depth the tension capacity increases. This is because of the change in pile deflection again from translation to backward rotation which will increase that soil contact pressure at shallow depth on the backside of the pile. From this observation, the tension capacity will increase by increasing the contact pressure.

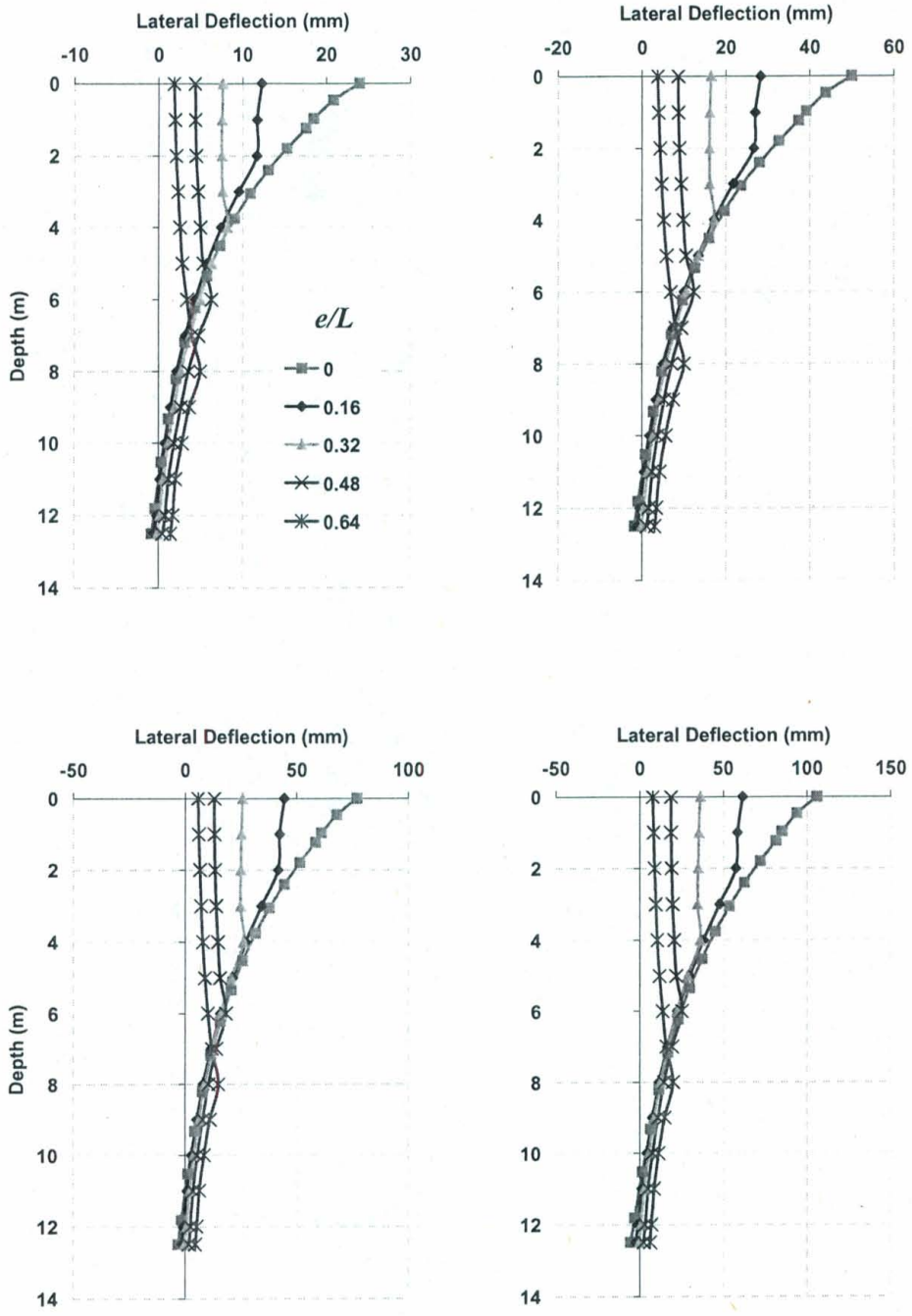

Fig. (7.44) Pile Lateral Deflection Profile – Case # 9 – at Lateral Load Increments (a) 1000 kN, (b) 2000 kN, (c) 3000 kN, (d) 4000 kN

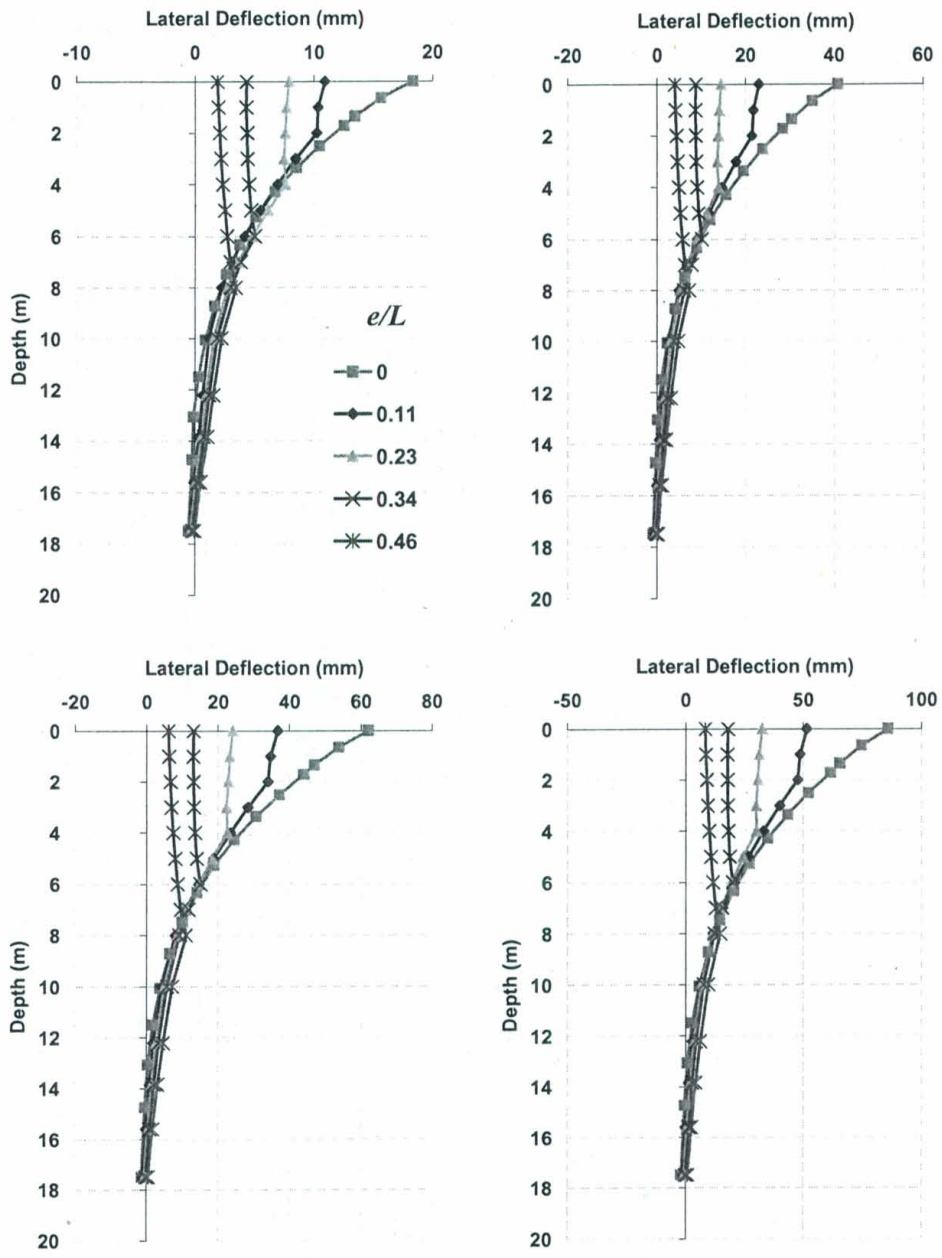

Fig. (7.45) Pile Lateral Deflection Profile – Case # 10 – at Lateral Load Increments (a) 1000 kN, (b) 2000 kN, (c) 3000 kN, (d) 4000 kN

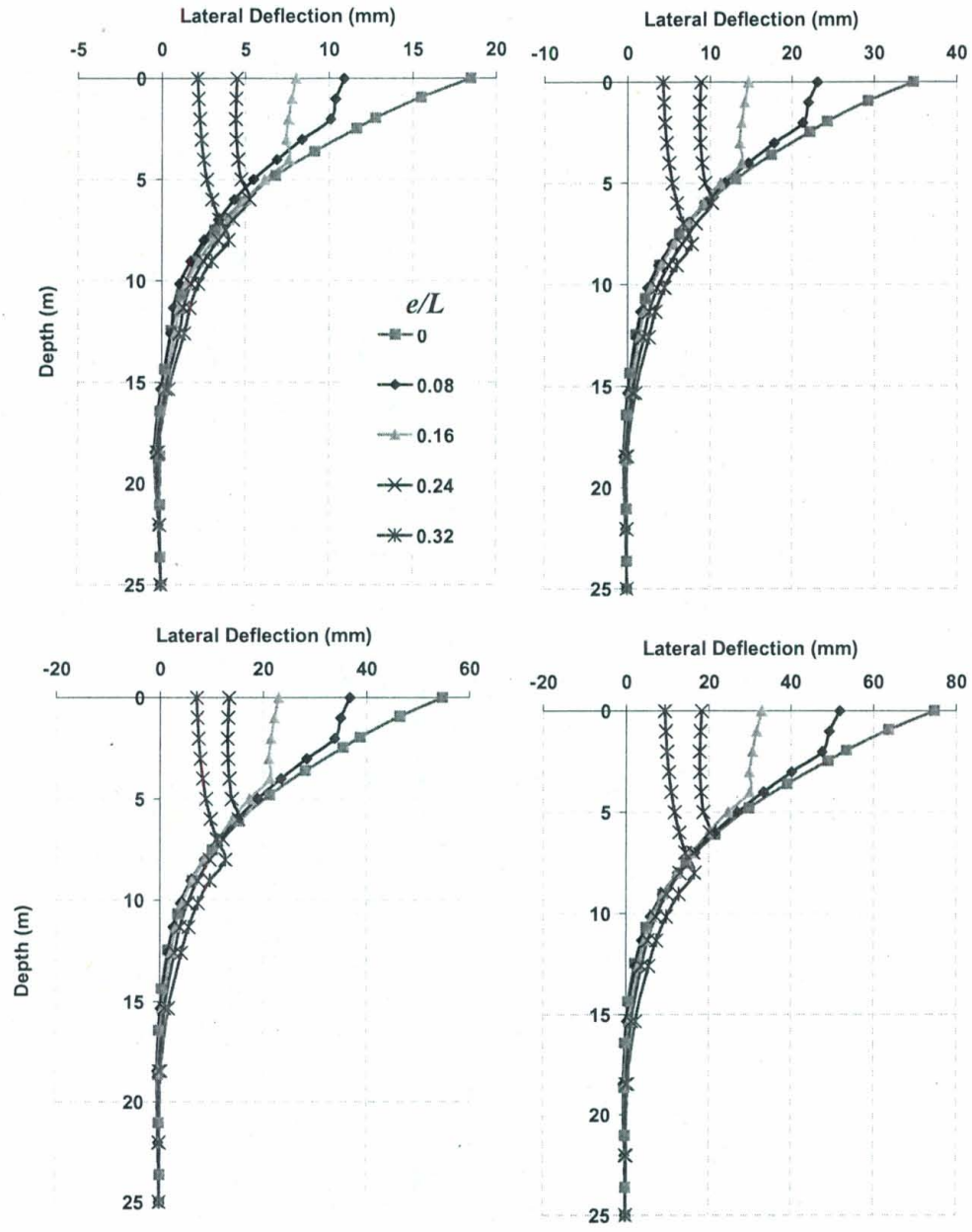

Fig. (7.46) Pile Lateral Deflection Profile – Case # 11 – at Lateral Load Increments (a) 1000 kN, (b) 2000 kN, (c) 3000 kN, (d) 4000 kN

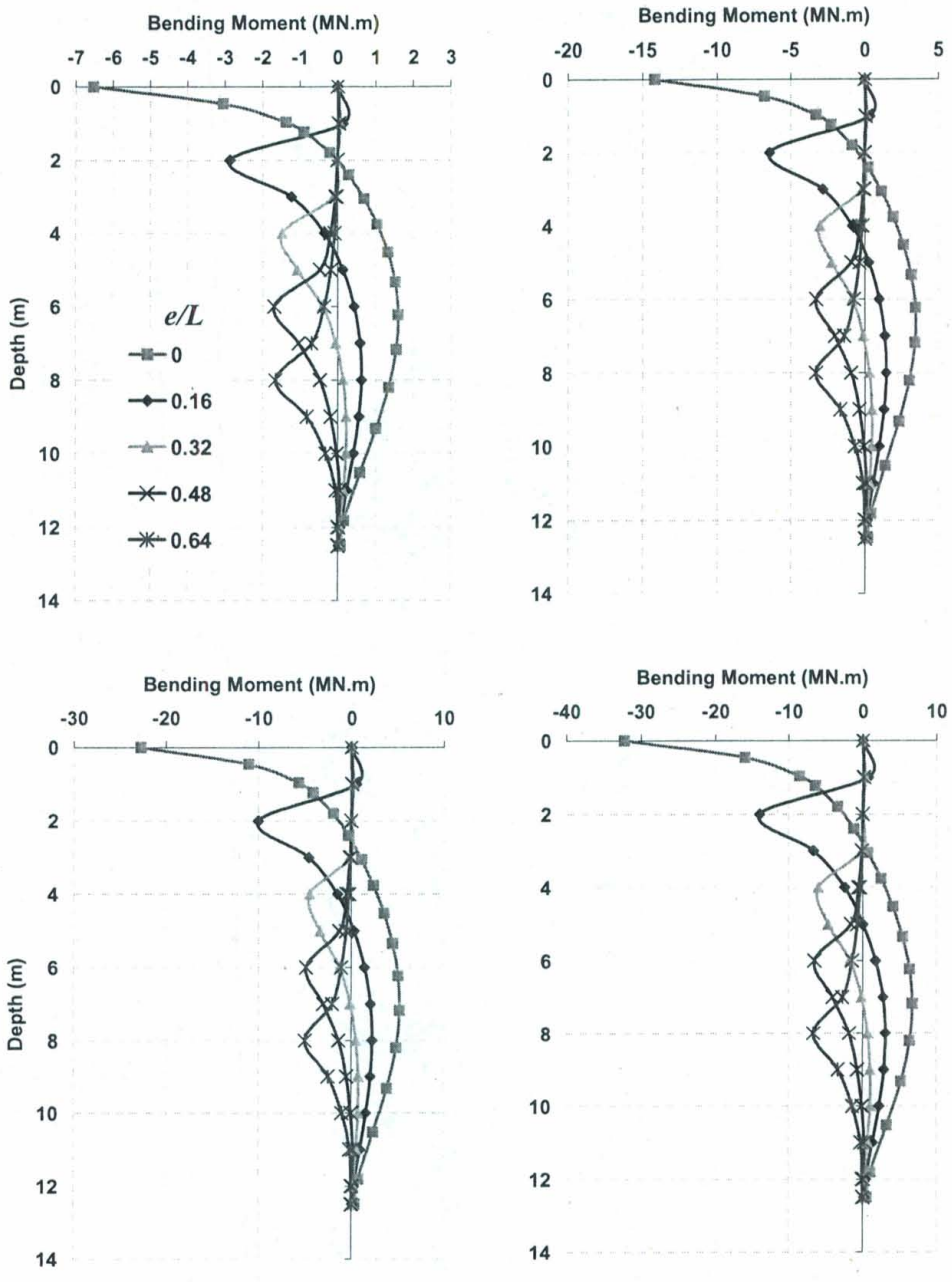

Fig. (7.47) Bending Moment Profile – Case # 9 – at Lateral Load Increments
(a) 1000 kN, (b) 2000 kN, (c) 3000 kN, (d) 4000 kN

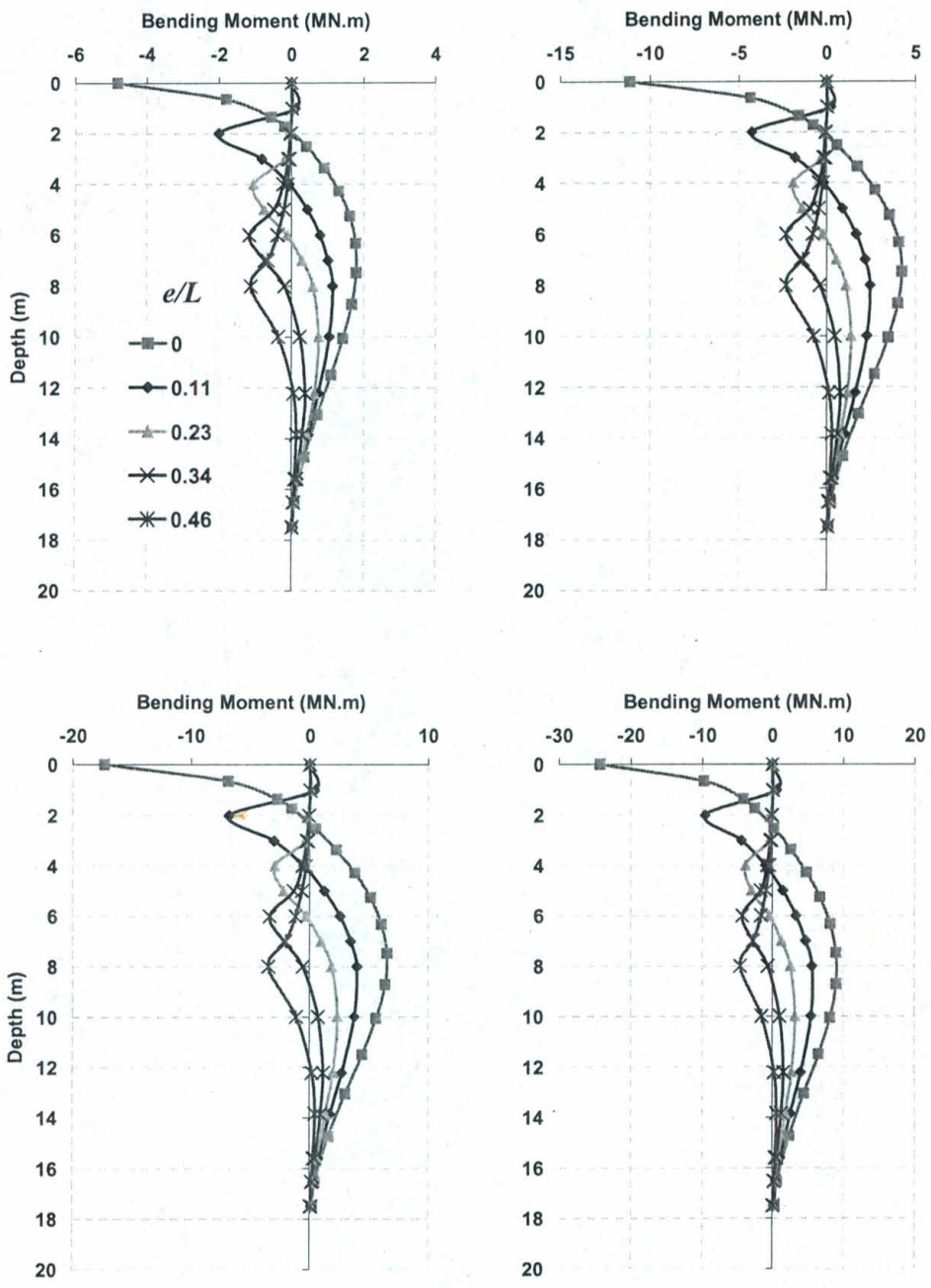

Fig. (7.48) Bending Moment Profile – Case # 10 – at Lateral Load Increments
(a) 1000 kN, (b) 2000 kN, (c) 3000 kN, (d) 4000 kN

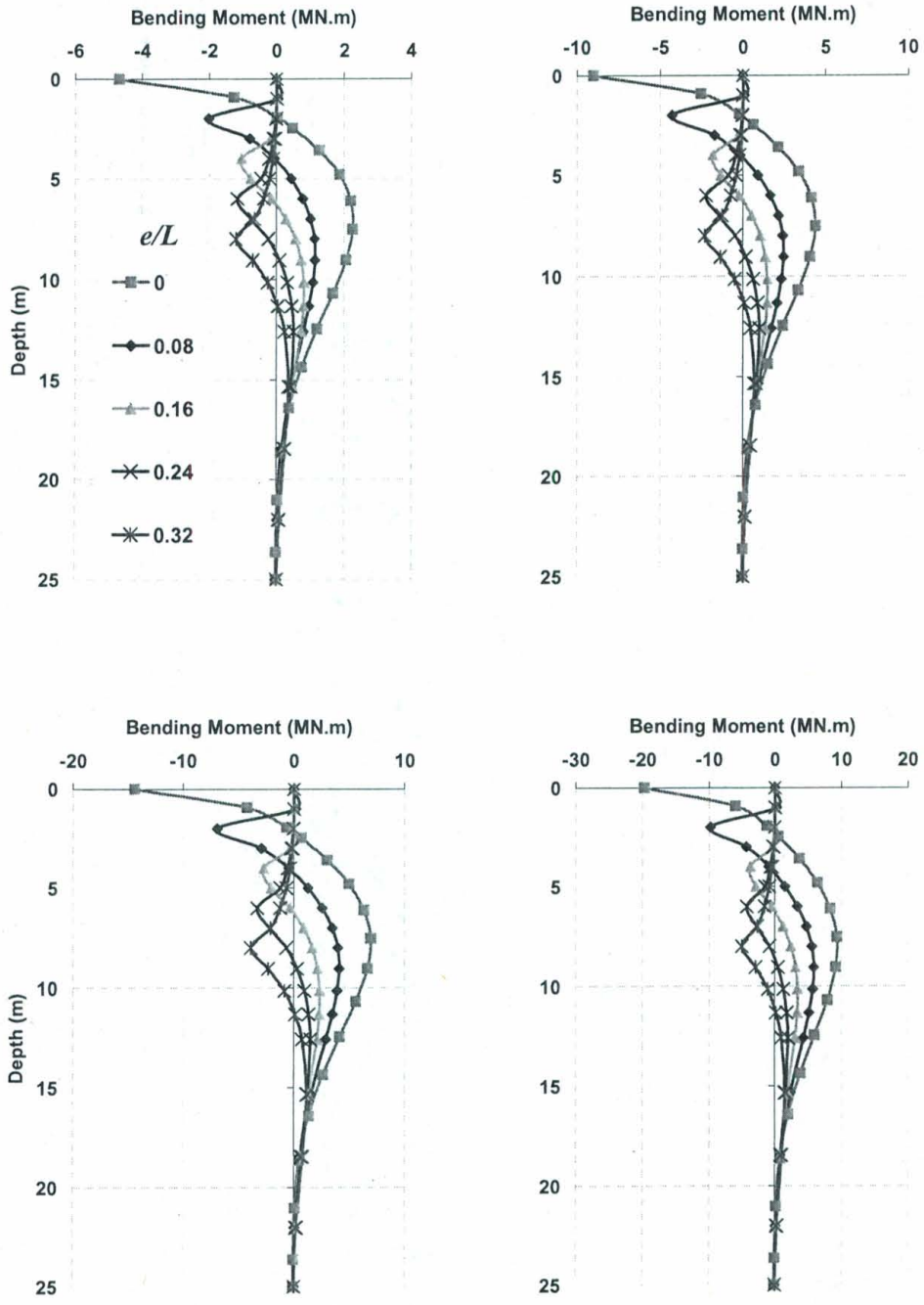

Fig. (7.49) Bending Moment Profile – Case # 11 – at Lateral Load Increments
(a) 1000 kN, (b) 2000 kN, (c) 3000 kN, (d) 4000 kN

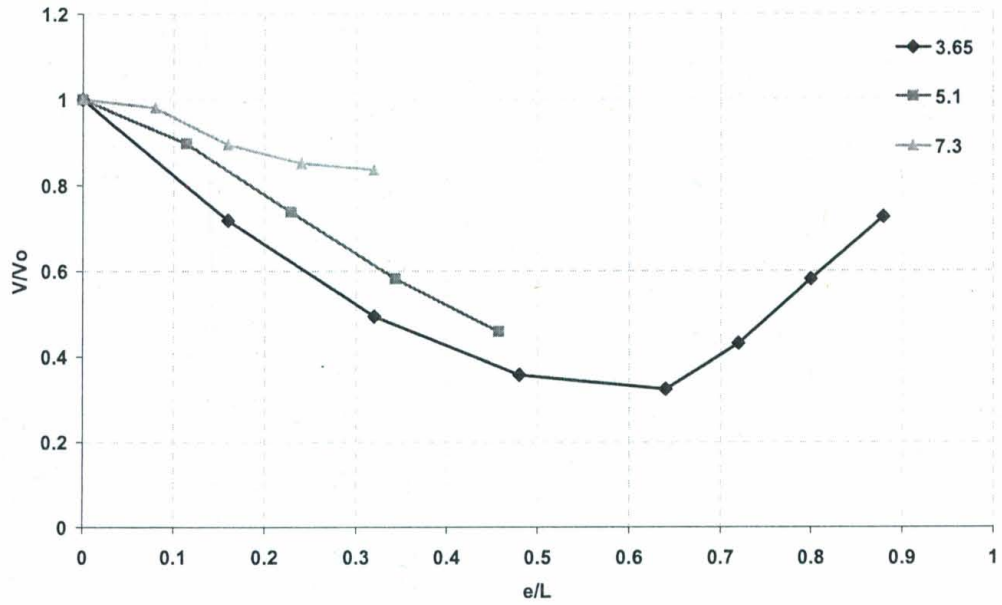

Fig. (7.50) Normalized Vertical Load versus Normalized Padeye Depth

7.4.4 Pile Ultimate Capacity Prediction:

For all cases of piles with different pile flexibility, the ultimate capacity of pile increases by increasing padeye depth. A trial was carried out to predict the increase of the ultimate capacity of pile at any depth of padeye and for different pile flexibilities. The ratio between the pile ultimate capacity for any depth of padeye (F') to the case of loading at the ground surface (F_o) is plotted in Fig. (7.51) versus the padeye depth ratio (x'). The padeye depth ratio (x') can be defined as:

$$x' = \left(\frac{e}{L}\right)^{T/L} \tag{7.7}$$

This ratio contains both the depth of the padeye and pile flexibility ratio (L/T). From the plot in Fig. (7.51), it can be seen that all data can follow one function regardless of pile flexibility as:

$$F'/F_o = 1 + \left(1.55 \times 10^{-5} \cdot e^{13x'}\right) \tag{7.8}$$

By determining the pile ultimate capacity for loading at the ground surface (F_o) using Eq. (7.1), the pile ultimate capacity for any depth of padeye can be obtained using Eq. (7.8). However, Eq. (7.8) is valid for e/L less than 0.7 which is the optimum depth of padeye.

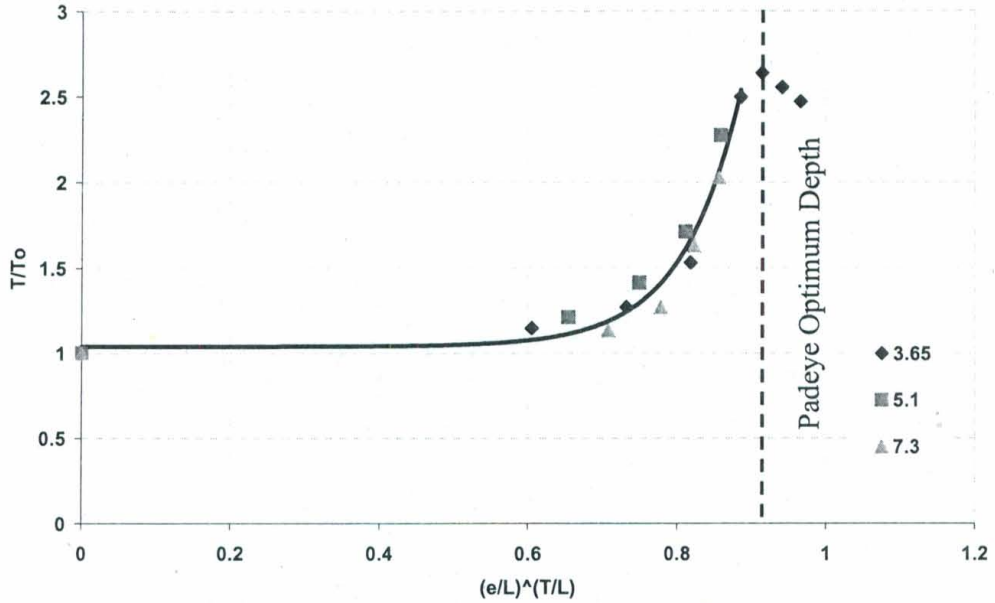

Fig. (7.51) Normalized Total Load versus Depth Ratio

7.5. Conclusion:

In this chapter, the calibrated FEM using the centrifuge tests results was used to perform a parametric study. The parametric study was carried out in two parts. In the first part, all cases were carried out by pulling out the pile at the ground surface. In the second part, the effect of padeye depth was studied.

For the cases where the piles are loaded at the ground surface, pile response becomes stiffer by increasing the loading angle from 0° (pure lateral loading) to 90° (pure tension loading). The pile ultimate capacity was taken as the total load corresponding

to failure in tension. The pile ultimate capacity and the corresponding pile head displacement increase by decreasing loading angle. There is a significant interaction between the lateral and tension loading. The tension load component causes pile elongation. This elongation increases pile bending stiffness and decreases soil pressure around the pile except at depths close to pile tip. As the soil pressure close to pile tip is high due to pile driving, soil pressure increases by increasing loading angle which means an increase in tension load component. In terms of soil shear stress, there is a small difference between small and large loading angles at the same tension load increment especially for piles of less flexibility. The reason for that is that the reduction in soil contact pressure on the back side of the pile in case of small loading angle (closer to pure lateral loading) is larger than that in case of large loading angle (closer to pure tension loading). This reduction in soil contact pressure will decrease soil shear stress and pile tension capacity. When the pile fails in tension, no more soil shear stress will be developed. The soil contribution to support the lateral forces decreases. When this soil contribution goes down, more load transfers to the pile. This will lead to a reduction in soil pressure at shallow depth and an increase at deeper depths as the resistance is going to deeper soil layers which can resist more. This is significant to what observed in bending moment profiles where maximum bending moment moved to deeper depths.

Two design methods were proposed. The first method is to predict the pile ultimate total capacity. The total capacity of the pile can be obtained by determining both the tension pile capacity and the corresponding lateral capacity of the pile at failure in tension. The tension capacity of the pile at any loading angles can be determined using Eq. (7.5). The corresponding pile lateral capacity to tension failure at different loading angles can be determined using Eq. (7.2) which is a function in pile flexibility (L/T) and the ultimate lateral capacity of rigid pile. The second method is to predict the maximum positive bending moment of a pile subjected to inclined pullout loading. The prediction depends upon the pile flexibility (L/T) and the maximum bending moment of the same pile at pure lateral loading.

In the second part of the current parametric study, the effect of padeye depth was examined. The parametric study was carried out for three different piles over a wide range of pile flexibility. The analysis supported the recommended optimum padeye depth of $e/L \approx 0.7$ by Supachawarote et. al (2004) for normally and lightly overconsolidated clay for suction caisson or rigid piles. It was found that pile response becomes stiffer by increasing padeye depth. A design method was proposed to predict pile ultimate capacity at any depth of padeye up to the optimum mentioned depth based on pile flexibility.

Chapter 8

Offshore Anchor Piles under Cyclic Loading

8.1. Introduction:

In this chapter, the centrifuge tests cyclic loading results will be discussed. The pile head load displacement relationship and the soil-pile interaction results are presented. The main objectives of these tests are to understand the interaction between the lateral and vertical pullout response of the piles under cyclic combined loads. The tests were conducted at 50g.

Three centrifuge tests were carried out at different loading angles 0°, 16°, and 90°. All tests were carried out displacement controlled at a rate of 0.1 mm/sec to ensure drained conditions as recommended by Dyson and Randolph (2001). In the following sections the analysis of the results will be discussed.

8.2. Test Results and Analysis:

From all tests, load-displacement curves were obtained. For the tension test, axial load along pile shaft was obtained. For piles that had been tested under lateral loading, bending moment profiles were obtained. The measured bending moment was fitted by quintic spline function and then differentiated twice to get the soil pressure (p) and integrated twice to get the pile deflection (y). At some load increments the load transfer curves or p-y curves can be derived at different depths. Degradation factors were calculated and a design recommendation is given. All results will be presented at prototype scale.

8.2.1 Tension Loading:

The pile was loaded monotonically first up to 0.15 m displacement and then sustained one way cyclic loading. 30 cycles were applied with displacement amplitude of 0.15 m at the actuator. The actual pile head displacement was measured using vertical LVDT. Figure (8.1) shows the load displacement relationship at pile head. After 30 cycles, the pile was pulled up to failure. It can be seen that pile capacity was fully mobilized after pulling the pile about 0.35 m. Figure (8.2) shows the tension load at different locations along the pile shaft versus vertical displacement at pile head. The cyclic loading caused a degradation of the tension load at the lower part of the pile up to about 0.25 L. However, during the cyclic loading the degradation factor is almost constant along the pile length of about 0.045. Only the degradation factor close to the pile tip is higher of about 0.13 as shown in Figs. (8.3) and (8.4). The degradation factor is calculated as:

$$\frac{V_{Nn}}{V_{N1}} = N^{-t} \tag{8.1}$$

where V_{Nn} is the axial load at n cycle, V_{N1} is the axial load at the first cycle, N is the cycle number, and t is the degradation factor. However, this high degradation close to the pile tip may not be happened in the presence of the residual stresses around the pile as discussed before especially at pile tip. Also, it can be seen in Fig. (8.3) that the axial load degradation along the pile shaft stabilized after 10 cycles.

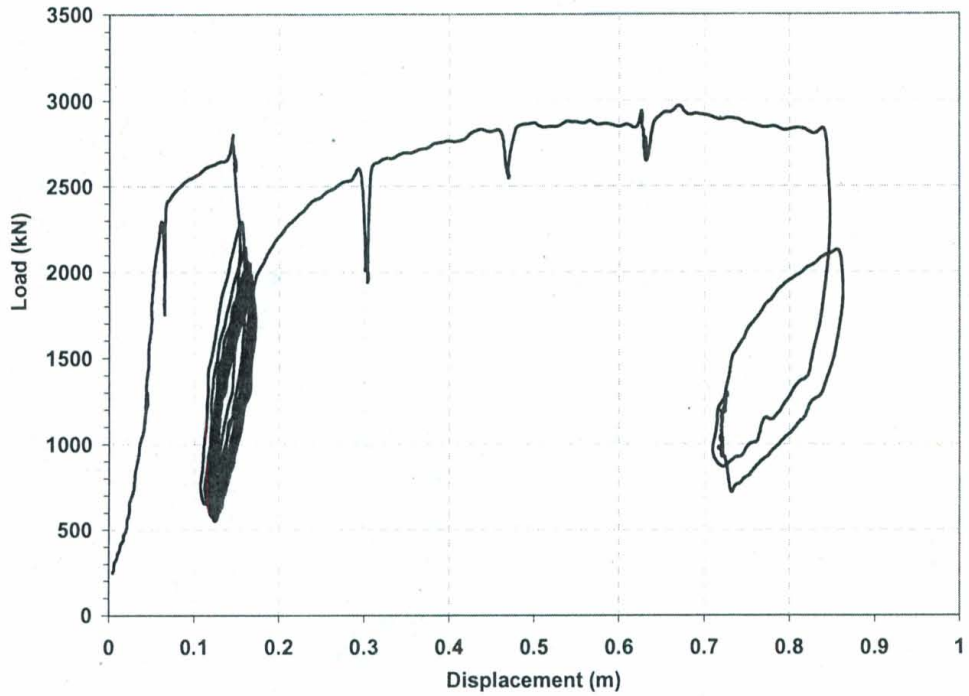

Figure (8.1) Vertical Load versus Vertical Displacement at pile head - 50g

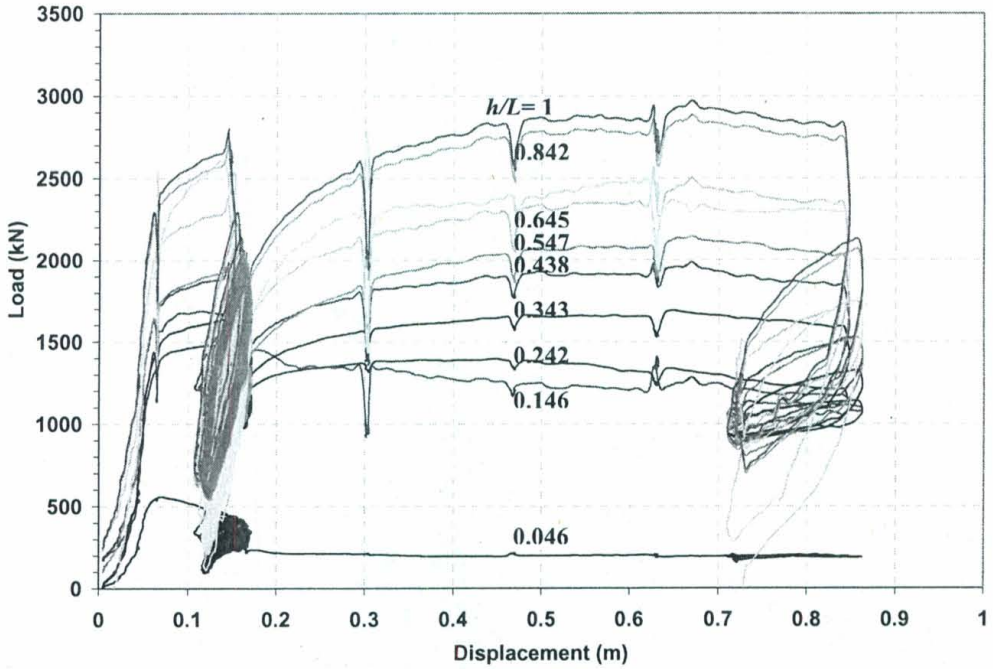

Figure (8.2) Vertical Load versus Vertical Displacement at different location along the pile - 50g

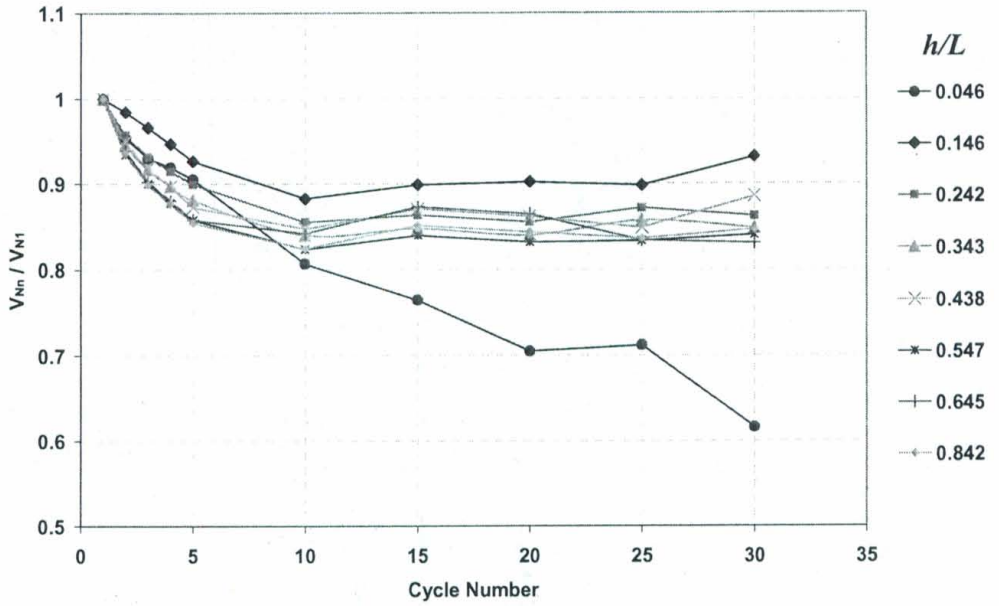

Figure (8.3) Normalized Vertical Load versus Cycles Number at different location along the pile - 50g

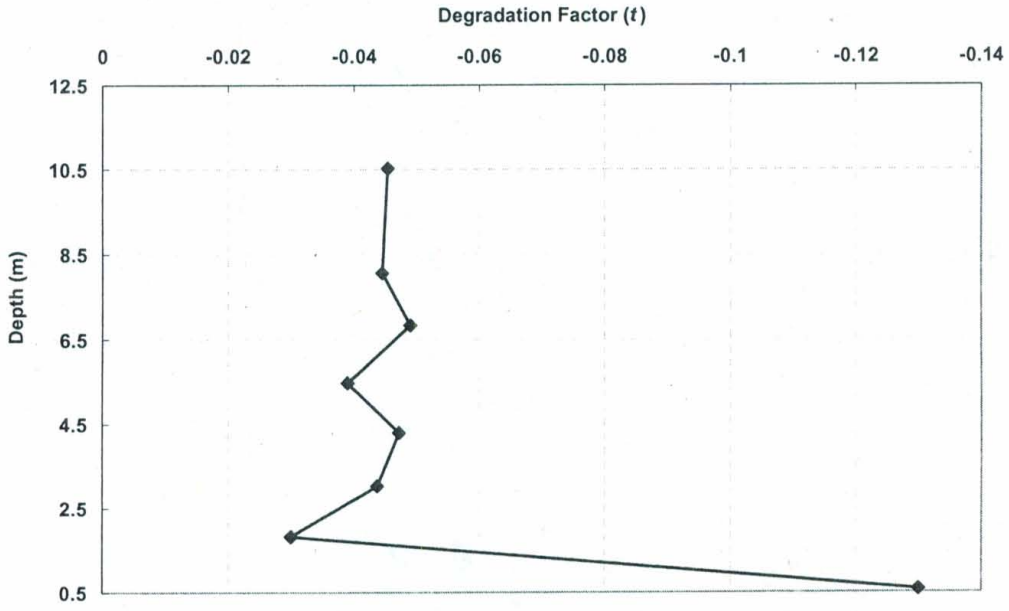

Figure (8.4) Degradation Factor versus Depth at different location along the pile - 50g

8.2.2 Lateral Loading:

The pile was loaded monotonically first up to a specified level of load. As the tests were carried out using displacement control, reaching the same level of load in both tests were not easy. The maximum load before applying the cyclic loading was 1450 kN and 1200 kN for loading angles tests 0° and 16°, respectively. The maximum load was selected to be within the service load 15% of the ultimate capacity of the pile under lateral load as suggested by Verdure et al. (2003). The ultimate capacity was 7400 kN calculated using the recommended method by Zhang et al. (2005). The number of cycles was 50 cycles. After completing the cyclic loading, the pile was pulled monotonically.

Figure (8.5) shows the total load-total displacement relationship. The global stiffness (K) (calculated as the ratio of load difference to displacement difference in each cycle) of the inclined pullout loading (loading angle 16°) is higher than that of pure lateral loading (loading angle 0°) of about 67%. During cycling loading, the global stiffness increases with a higher rate for the inclined pullout loading than the pure lateral loading. However, this global stiffness is affected by the displacement at pile head. Although the tests were carried out under displacement control at the actuator, the pile head displacement was slightly increasing during cyclic loading. This increase in displacement is about 10% of the initial displacement at the first cycle. However, it can be seen from Fig. (8.5) that pile stiffness did not change after cyclic loading. The load displacement curve follows the back bone curve after cycling.

To best understand the behavior of the pile under cyclic loading, the change in total load at pile head, maximum bending moment, and soil stiffness will be discussed.

8.2.2.1 *Effect of cyclic loading on total load:*

The total load degradation at pile head during cyclic loading for both tests at loading angles 0° and 16° is shown in Fig. (8.7). The degradation factor was calculated as:

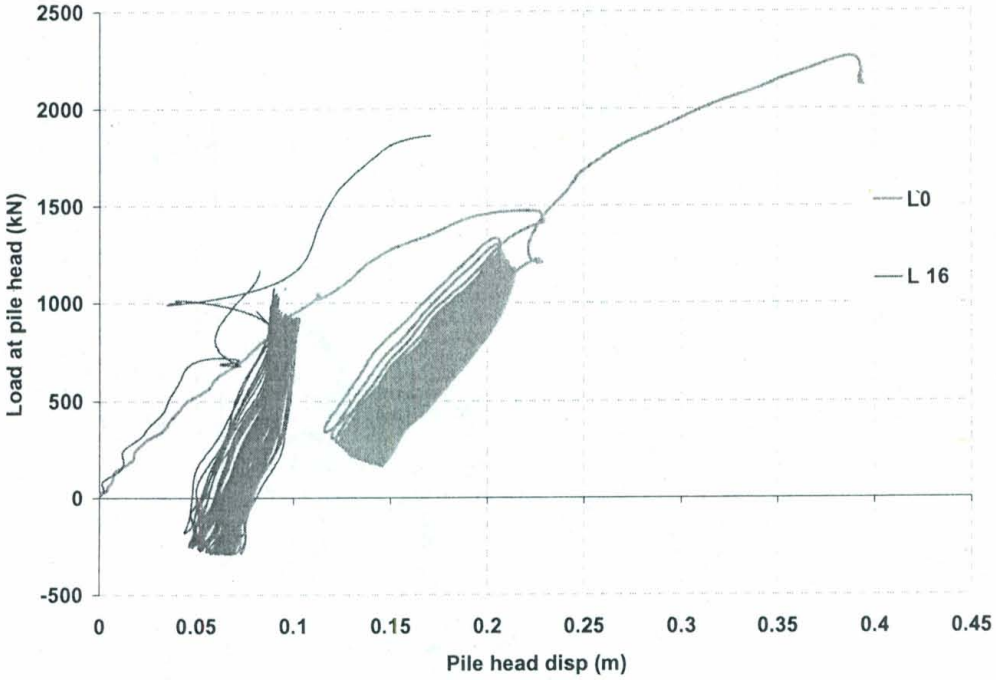

Figure (8.5) Total Load – Total Displacement Relationship for Tests at Loading Angles 0° and 16° - 50g

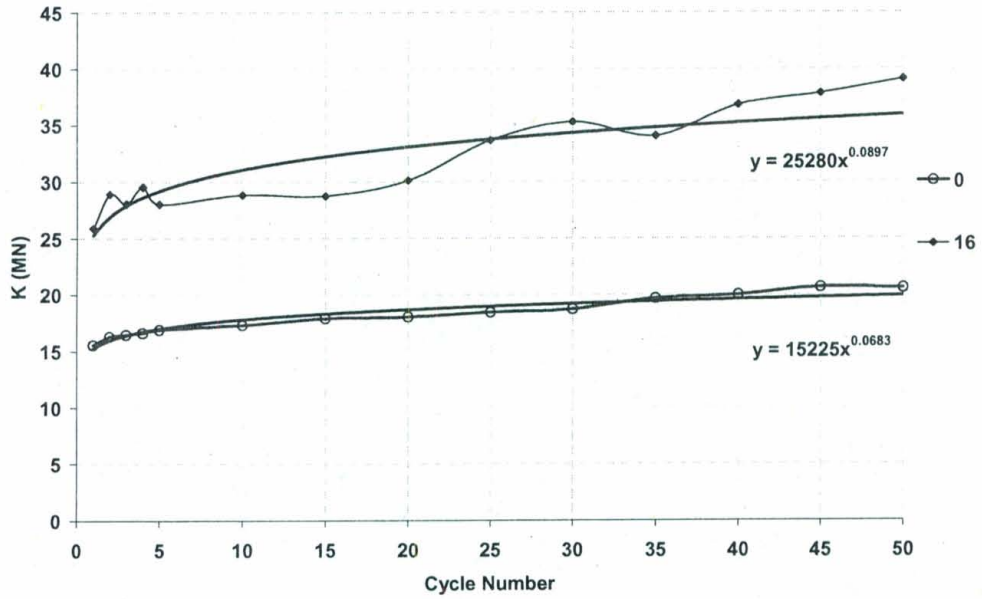

Figure (8.6) Global Stiffness Change during Cyclic Loading for Tests at Loading Angles 0° and 16° - 50g

$$\frac{H_{Nn}}{H_{N1}} = N^{-t} \tag{8.2}$$

where H_{Nn} is the lateral load at n cycle, and H_{N1} is the lateral load at the first cycle. The degradation factor (t) is 0.0378 and 0.0419 for tests at loading angles 0° and 16°, respectively. Although the difference between the degradation factors in both loading angles 0° and 16° is small, this difference shows that inclined pullout loading case could be affected more with cyclic loading due to the degradation in shear stresses along the pile shaft. The degradation factor for the loading angle 16° is almost same as that one for tension cyclic loading as discussed in the previous section.

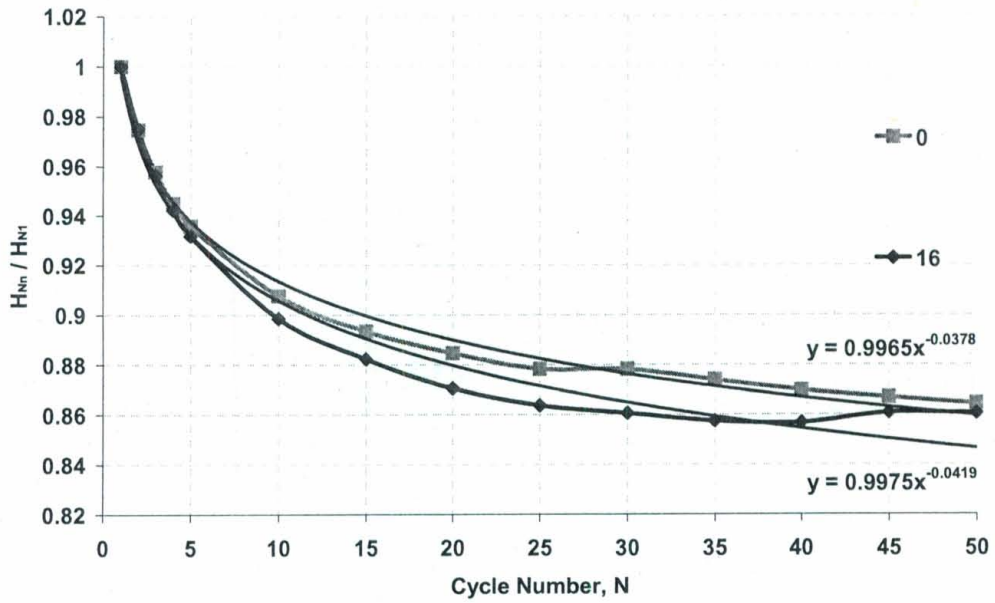

Figure (8.7) Total Load at Pile Head Change during Cyclic Loading for Tests at Loading Angles 0° and 16° - 50g

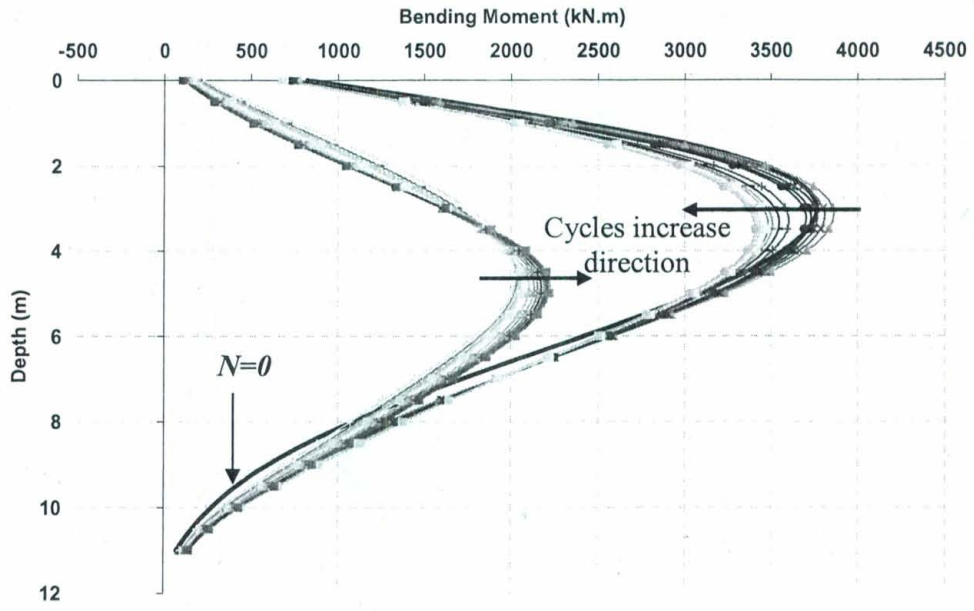

Figure (8.8) Bending Moment Profiles at Different Cycles Test at Loading Angle 0°- 50g

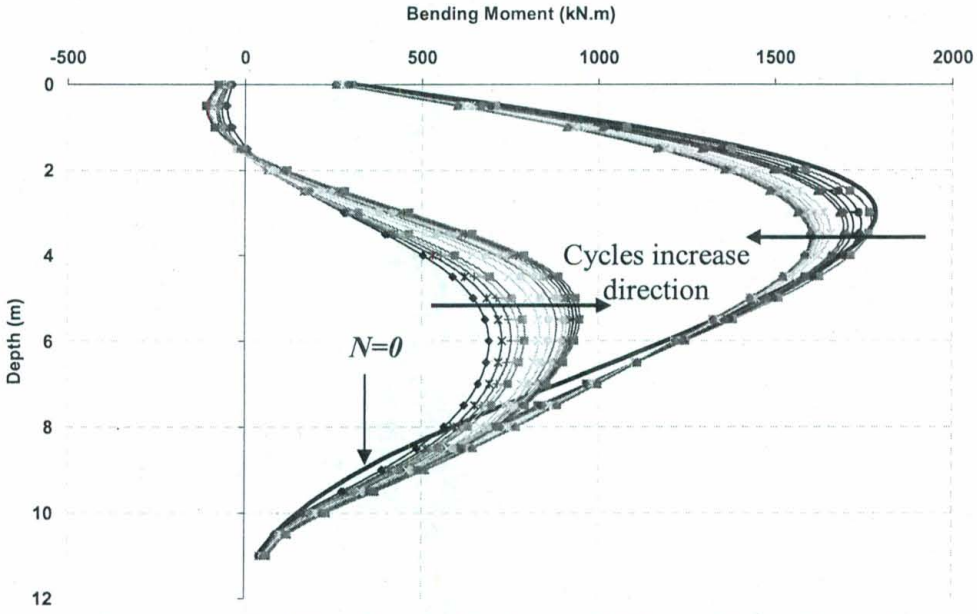

Figure (8.9) Bending Moment Profiles at Different Cycles Test at Loading Angle 16°- 50g

8.2.2.2 *Effect of cyclic loading on maximum bending moment:*

The measured bending moment from strain gages along the pile shaft was fitted using quintic spline function. The fitted curves are shown in Figs. (8.8) and (8.9) at maximum and minimum amplitudes during cyclic loading for tests at loading angles 0° and 16°, respectively. As discussed previously, the bending moment decreases as loading angle changes from pure lateral loading 0° to any angle larger than 0° regardless of the angle value due to the axial tension load in the pile. During cycling loading, the axial load along the pile shaft decreases by increasing the cycle number. This means that the axial load effect on the pile is decreasing and consequently its effect on the bending moment is decreasing. So the degradation factor for the pile tested at 16° is less than that for the pile tested at pure lateral loading 0°. Figure (8.10) shows the degradation of the maximum bending moment for both tests. The degradation factor is calculated as:

$$\frac{M_{\max Nn}}{M_{\max N1}} = N^{-t} \tag{8.3}$$

where $M_{max\ Nn}$ is the maximum bending moment at n cycle, and $M_{max\ N1}$ is the maximum bending moment at the first cycle. The degradation factor (t) is 0.0328 and 0.0264 for tests at loading angles 0° and 16°, respectively.

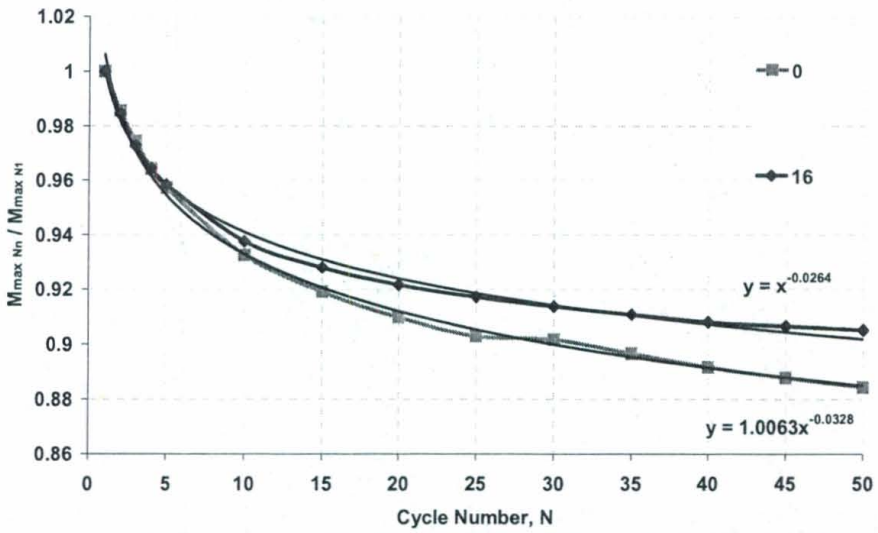

Figure (8.10) Maximum Bending Moment Change during Cyclic Loading for Tests at Loading Angles 0° and 16° - 50g

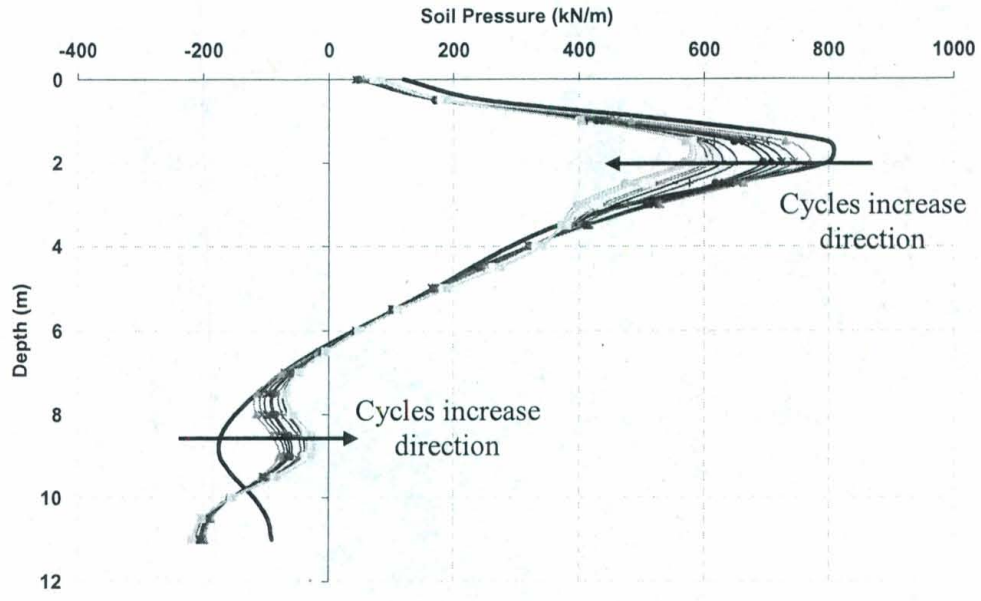

Figure (8.11) Soil Pressure Profiles at Different Cycles Test at Loading Angle 0°- 50g

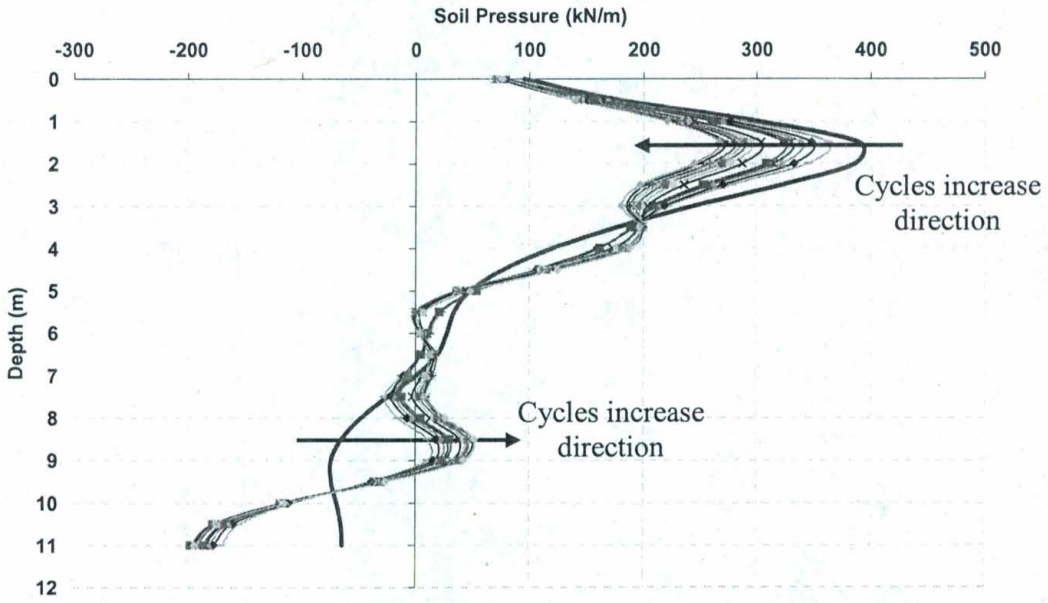

Figure (8.12) Soil Pressure Profiles at Different Cycles Test at Loading Angle 0°- 50g

8.2.2.3 *Effect of cyclic loading on soil stiffness:*

The fitted bending moment profiles were differentiated twice to get the soil pressure in (kN/m) at the maximum and minimum amplitudes during cyclic loading. Figures (8.11) and (8.12) show soil pressure profiles for tests at loading angles 0° and 16°, respectively. In both tests the degradation increases by increasing the depth. Maximum degradation can be found at depth to diameter ratio (Z/d) between 2 to 2.5. For $Z/d > 3$, the degradation decreases again. As the displacement was controlled at the actuator not at the pile head, pile deflection was increasing slightly during cyclic loading. To account for the change in both soil pressure and pile deflection, the ratio of soil pressure to pile deflection and pile diameter was used to calculate the degradation in soil stiffness (K_h) as follow:

$$K_h = \frac{p}{y \cdot d} \tag{8.4}$$

where p is soil pressure in (kN/m) at depth Z, y is pile deflection in (m) at the same depth Z, and d is pile diameter in (m).

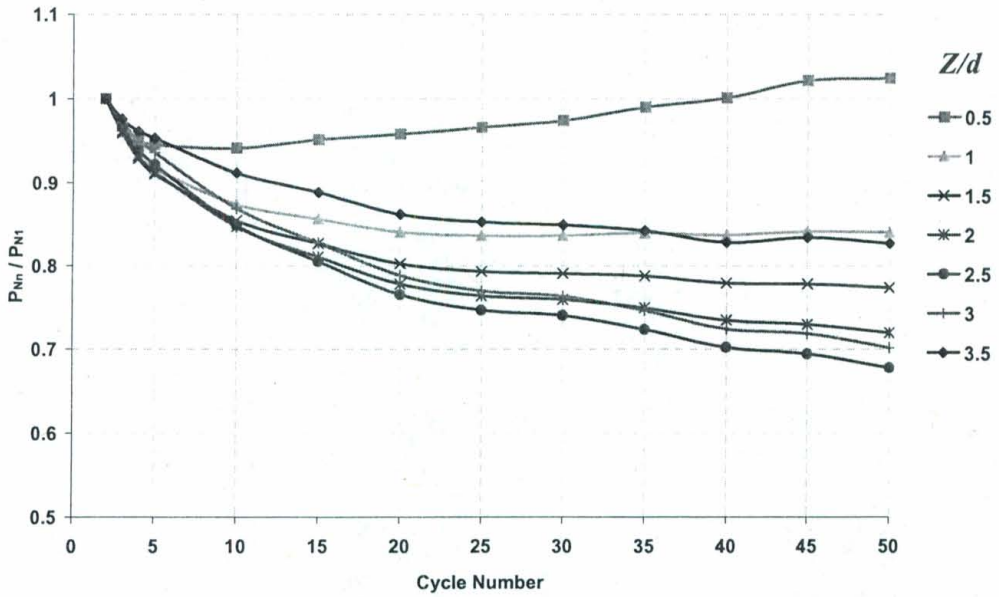

Figure (8.13) Soil Pressure Change at different depths during Cyclic Loading for Test at Loading Angle 0° - 50g

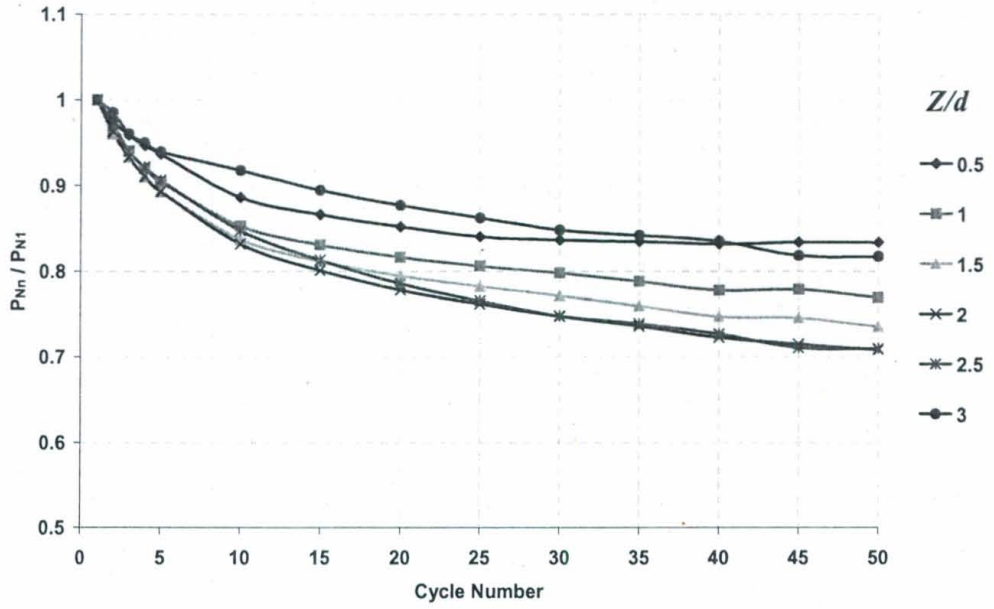

Figure (8.14) Soil Pressure Change at different depths during Cyclic Loading for Test at Loading Angle 16° - 50g

Figures (8.15) and (8.16) shows the degradation of soil stiffness during cyclic loading. The degradation factor can be calculated same as before:

$$\frac{K_{h\,Nn}}{K_{h\,N1}} = N^{-t} \tag{8.5}$$

where $K_{h\,Nn}$ is soil stiffness at n cycle, and $K_{h\,N1}$ is soil stiffness at the first cycle. The calculated degradation factors at different depths are plotted versus Z/d in Fig. (8.17). It can be seen that the degradation factor increases with depth up to about 2.5 d then decreases rapidly up to 4 d. The pile loaded under inclined pullout experienced higher degradation than that loaded under pure lateral. As discussed before, the axial tension load component causes a reduction in soil confining pressure around the pile. This reduction in soil pressure cause higher degradation in case of inclined pullout loading than in pure lateral loading case. The degradation increases by depth up to the depth of maximum soil pressure. Below this depth, the degradation values are not stable or

not following a function. The soil reactions at shallow depths govern the response of a flexible pile to lateral service loads. Although soil pressure profiles in Figs. (8.11) and (8.12) show an increase close to pile tip, the small values of bending moment at this location cause less accuracy in soil pressure calculation as recommended by Rosquoët et al. (2007).

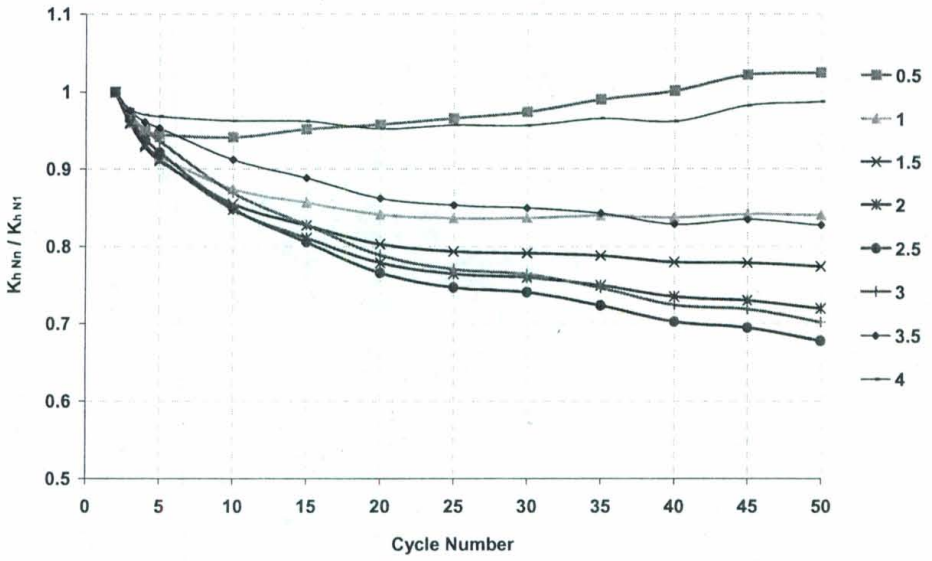

Figure (8.15) Soil Stiffness Change at different depths during Cyclic Loading for Test at Loading Angle 0° - 50g

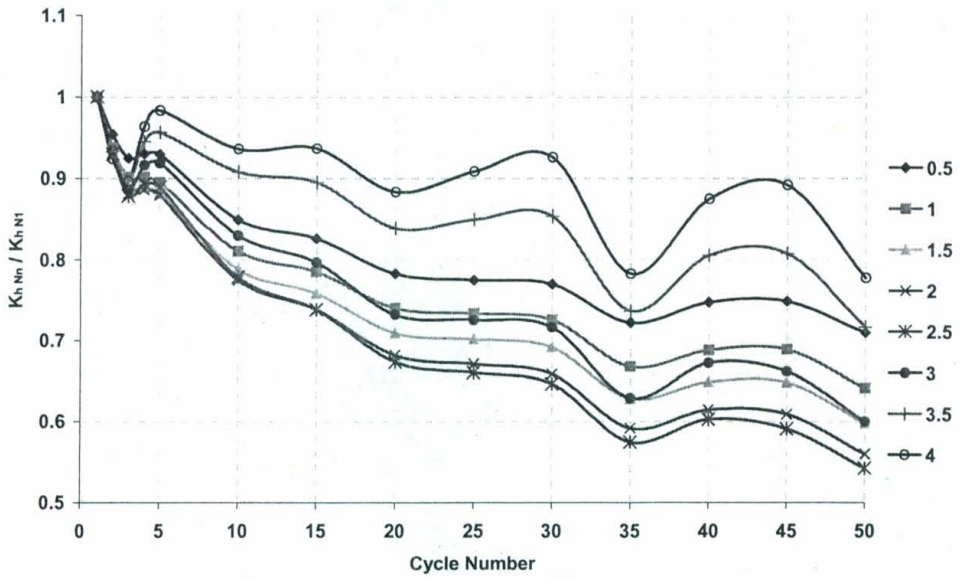

Figure (8.16) Soil Stiffness Change at different depths during Cyclic Loading for Test at Loading Angle 16° - 50g

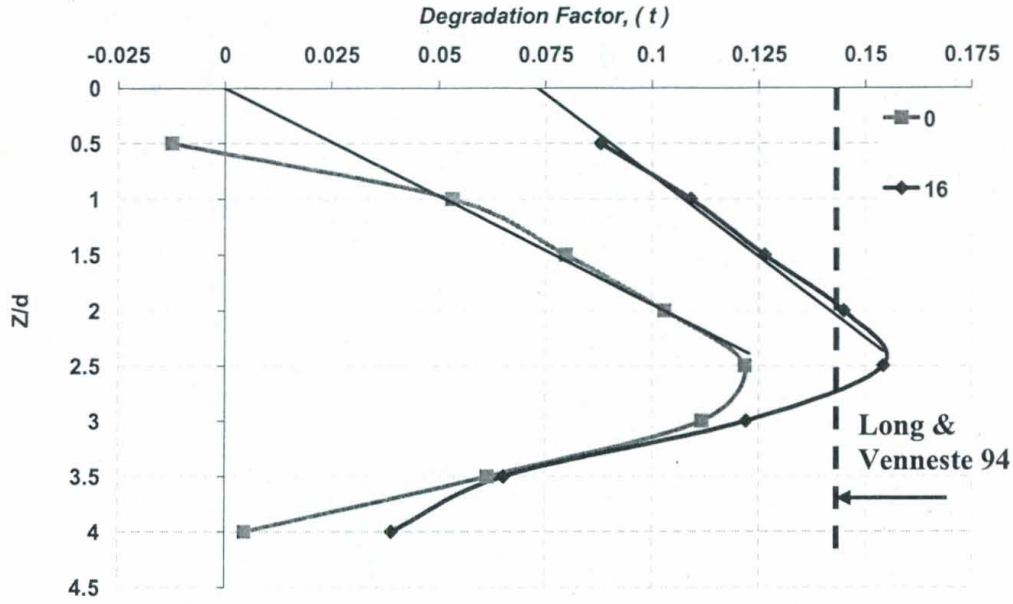

Figure (8.17) Soil Stiffness Degradation Factor versus depths for Tests at Loading Angles 0° and 16° - 50g

From the current results, the degradation factor of soil stiffness can be given as:

For pure lateral loading:

$$t = 0.0506 \cdot \frac{Z}{d} \qquad Z/d \leq 2.5 \qquad (8.6)$$

For inclined pullout loading:

$$t = 0.0337 \cdot \frac{Z}{d} + 0.074 \qquad Z/d \leq 2.5 \qquad (8.7)$$

This proposed method can be compared to the constant value suggested by Long and Venneste (1994) for the case of pure lateral loading as shown in Fig. (8.17). From the current study, it can be expected that using a constant value of degradation factor will under predict the load at pile head. The method recommended by Long and Venneste (1994) will also over predict the maximum bending moment degradation.

8.3. Finite Element Model (FEM):

The proposed method was implemented in the FEM (discussed before). In the FEM, soil Young's modulus was degraded as a function of cycle number. Equations (8.6) and (8.7) was used to calculate the degradation factor up to $Z/d = 2.5$. An average value of the degradation factor for $Z/d > 2.5$ was assumed as 0.14 (same as Long and Venneste, 1994) and 0.06 for pure lateral loading and inclined pullout loading, respectively. The reduction in the degradation factor in the case of the inclined pullout loading at $Z/d > 2.5$ was replaced by degradation in the lateral earth pressure coefficient (K). The lateral earth pressure coefficient (K) was degraded as a function of cycle number to account for the axial pullout load component degradation. The degradation factor was calculated from the case of pure tension loading (shown in Fig. 8.4) with an average value of 0.05 except a value of 0.13 at pile tip.

Figure (8.18) shows the relationship between load degradation and cycle number for pure lateral and inclined pullout loading cases using FEM. It can be seen that there a good agreement between the FEM and centrifuge tests results. Figure (8.19) shows the relationship between maximum bending moment and cycle number for pure lateral loading and inclined pullout loading. It can be seen that there is a very good agreement between FEM and the centrifuge tests results.

The current degradation model shows a good agreement with the centrifuge tests results. It was observed from the monotonic loading cases that for a loading angle larger than 0° the normalized maximum bending moment follows the same function with the normalized horizontal load at pile head regardless of the loading angle. This means that the current degradation model could be valid for other inclined loading angles. However, the current degradation model has some limitations. It should be checked at different loading levels. It also should be checked for cycle number larger than 50 cycles.

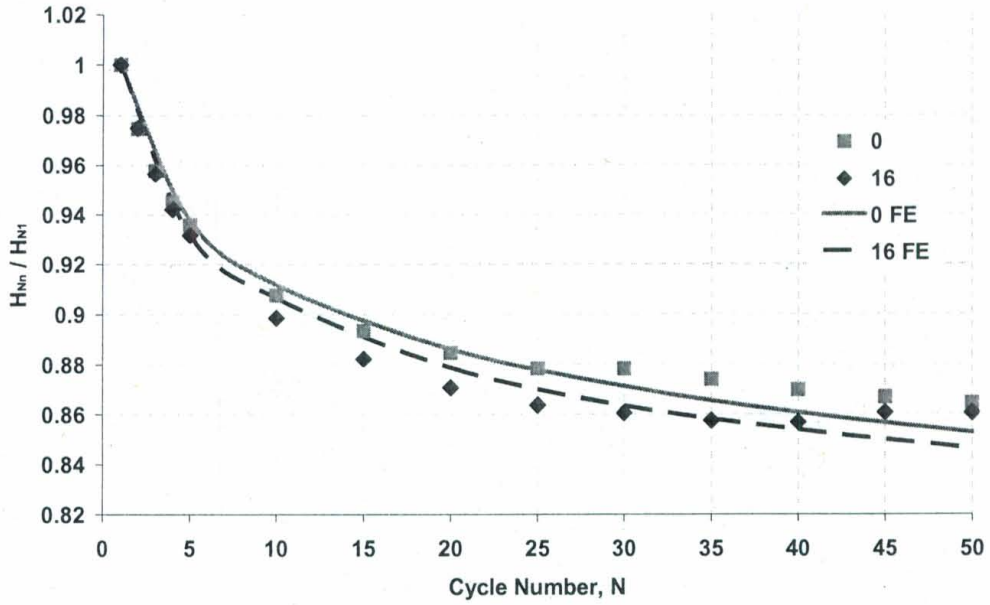

Figure (8.18) Lateral Load Degradation Comparison between FEM and Centrifuge Tests at Loading Angles 0° and 16°

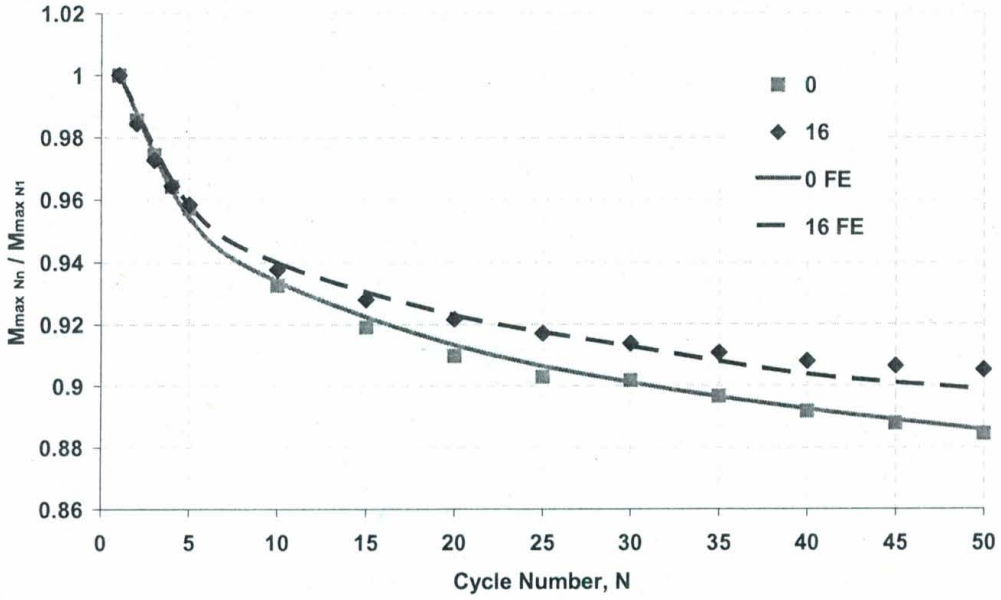

Figure (8.19) Maximum Bending Moment Degradation Comparison between FEM and Centrifuge Tests at Loading Angles 0° and 16°

8.4. Conclusion:

In this chapter, the behavior of anchor piles under cyclic loading was examined. Three centrifuge tests were carried out at different loading angles 0°, 16°, and 90° under drained conditions. For tension loading case (loading angle 90°), the tension load degrades with an average factor of 0.05 along the pile shaft except 0.13 at pile tip. The degradation stabilized after 10 cycles. For pure lateral and inclined pullout loading cases, the total lateral load at pile head slightly degrades more in the case of inclined pullout than that of pure lateral loading. This difference shows that inclined pullout loading case could be affected more with cyclic loading due to the degradation in shear stresses along the pile shaft. For the maximum bending moment, the degradation factor for the pile tested at 16° is less than that for the pile tested at pure lateral loading 0°. During cycling loading, the axial load along the pile shaft decreases by increasing the cycle number. This means that the axial load effect on the pile is decreasing and consequently its effect on the bending moment is decreasing. The pile loaded under inclined pullout experienced higher degradation in soil stiffness than that loaded under pure lateral due to the reduction in soil confining pressure around the pile in case of inclined pullout loading.

A degradation model is suggested based on the soil stiffness degradation. The model was implemented in the FEM. In the case of pure lateral loading, soil young's modulus was degraded with cycle number. For the inclined pullout loading, both soil young's modulus and lateral earth pressure coefficient were degraded to account for axial load degradation as well. The proposed model has some limitation before being used at higher load levels and cycles more than 50.

Chapter 9

Concluding Remarks

9.1 Summary:

In deep water, fixed offshore platforms are not economical due to the large amount of steel needed in constructing the supporting frame. Therefore, floating offshore structures became the economic alternative in deep waters. Floating Production Storage Offloading vessels (FPSOs) are widely used in offshore oil and gas industry in harsh environments reach at the Grand Banks. Vessels working at an offshore site must be held in position despite the effects of wind, waves, and current. Anchors used to hold offshore floating structures include piles, drag anchors, and suction caissons. The focus of this research is on piles which are widely used at offshore Newfoundland. The anchor pile resists pullout by a combination of bending plus passive resistance and skin friction shear.

There is relatively limited experimental information on anchor piles or piles subjected to oblique pull loads. Some of the existing theoretical models are semi-empirical based on 1g experimental tests. The current research summarized most of the previous research that is related to pure lateral loading, pure tension loading, and inclined pullout loading.

The presented work aims at identifying the behavior and capacity of anchor piles used for anchoring offshore floating structures in dense sand. As full-scale experimental verification is not always possible, this raises up the need to design a physical model which can simulate the behavior of the full-scale case. To simulate the important gravitational component, the physical model tests were conducted using the geotechnical centrifuge to investigate the anchor piles response to mooring forces in saturated dense sand. Two centrifuge tests setup were carried out. In each test setup four model pipe piles were jacked in flight in homogeneous saturated sand and subjected to monotonic and

cyclic pull-out forces with inclination angle 0° (pure lateral loading), 16°, 30°, and 90° (pure tension loading) with the horizontal. The soil pile interaction behavior was monitored through the strain gauges attached on the pile. While the undisturbed soil stiffness distribution with depth will be measured using a shear wave measurement system of bender elements which can provide soil shear modulus distribution with depth.

To study many factors that are affecting the model, a 3-D finite element model (FEM) will be calibrated from the experimental centrifuge results. The calibrated FEM will be used to do a parametric study to get design procedures and provide better understanding of the response of anchor piles to a variety of loading conditions. The parameters that will affect the pile behavior as suggested from the previous researchers and will be studied here are pile diameter, pile flexibility, load inclination angle, and padeye depth on the pile.

From the present study, it was found that there is a significant interaction between lateral and tension loading. A design method was proposed to predict the ultimate capacity of offshore anchor pile depending on pile flexibility, loading angle and padeye depth. Also, a design method was proposed to predict the maximum bending moment.

9.2. Conclusions:

According to the results obtained from the centrifuge modeling and numerical analysis of offshore anchor piles under mooring forces, the following conclusions can be drawn:

1. Shear wave velocity (V_S) was measured using piezoelectric transducers called bender elements. The measurements were carried out at three different depths in two tests. In both tests, V_S was measured during centrifuge spinning-up at increments of 10g up to 50g. It was observed that V_S values are higher in the second test (flight) than that in the first test (flight). It was concluded that as the soil consolidates, the horizontal effective stresses increase as a result of the plastic deformation of the soil. The lateral earth pressure coefficient was calculated from the CPT results. An equation was given to predict the maximum shear modulus with depth.

2. Shear wave velocity (V_S) was measured during pile installation at centrifuge acceleration of 50g. The measurements were taken at pile penetration increments of 50 mm (model scale). It was found that soil stiffness increases gradually as the pile tip reaches the measurement depth. However, as the pile tip advances beyond the measurement depth, soil stiffness decreases. This degradation in soil stiffness was recommended by other authors as a phenomenon called friction fatigue. A degradation factor was obtained from the current test to account for soil stiffness degradation along the pile shaft. Also, it was found that this degradation in soil stiffness decreases as we go far horizontally from the pile shaft.

3. The response of offshore anchor piles under mooring forces has been investigated using centrifuge modeling. Bending moment profile has been measured along the pile. For design purpose a fitting equation was given to predict the maximum bending moment for any loading angle larger than 0° as a function of the horizontal component of the load at the pile head. *P-y* curves were calculated from the bending moment profiles. It was found that at the same *Z/d* ratio the *p-y* curves have the same initial stiffness and are becoming softer at large displacements as the loading angle increases. However, the total load displacement curves become stiffer as the loading angle increases.

4. It was concluded from the centrifuge tests results that to analyze anchor piles under inclined pullout forces using load transfer curves at soil-pile interface, the use of *p-y* curves alone is not enough. The shear stresses at the soil-pile interface (called *t-z* curves) should be considered in the analysis. Neglecting these shear stresses will overestimate the design of these anchor piles in terms of maximum bending moment and the expected total carried load at the pile head.

5. A three dimensional (3-D) Finite Element Model (FEM) has been established to study the soil-pile interaction behavior under mooring forces. Mohr-Coulomb plastic model has been used to model the soil. The model has been calibrated based on the

centrifuge tests. The results of CPTs were used to calculate soil parameters needed for the FEM using some available correlations in the literature. The effect of pile installation was considered by increasing the lateral stress based on the recommendations of ICP' (2005). FEM predicts the tension capacity of the pile in a good agreement with ICP method. However, it slightly under-predicts the tension capacity in comparison to the centrifuge test due to the effect of soil dilation when using small scale model pile. FEM predicts well the behavior of pure laterally loaded pile in terms of load-displacement curve at pile head and maximum bending moment of the pile. For inclined pullout loading, FEM shows the same trend as the centrifuge tests. There is a little overprediction in the normalized maximum bending moment which could be due to the soil dilation effect as in the tension loading case. In general, FEM shows a good agreement with the centrifuge tests results.

6. The calibrated FEM using the centrifuge tests results was used to perform a parametric study. The parametric study was carried out in two parts. In the first part, all cases were carried out by pulling out the pile at the ground surface. In the second part, the effect of padeye depth was studied.

7. For the cases where the piles are loaded at the ground surface, pile response becomes stiffer by increasing the loading angle from 0° (pure lateral loading) to 90° (pure tension loading). The pile ultimate capacity was taken as the total load corresponding to failure in tension. The pile ultimate capacity and the corresponding pile head displacement increase by decreasing loading angle.

8. There is a significant interaction between the lateral and tension loading. The tension load component causes pile elongation. This elongation increases pile bending stiffness and decreases soil pressure around the pile except at depths close to pile tip. As the soil pressure close to pile tip is high due to pile driving, soil pressure increases by increasing loading angle which means an increase in tension load component. In terms of soil shear stress, there is a small difference between small and large loading angles at the same tension load increment especially for piles of less flexibility. The

reason for that is that the gapping in case of small loading angle (closer to pure lateral loading) is larger than that in case of large loading angle (closer to pure tension loading). This larger gapping will cause less contact area between soil and pile and consequently less soil shear stress and pile tension capacity.

9. Two design methods were proposed. The first method is to predict the pile ultimate total capacity. The total capacity of the pile can be obtained by determining both the tension pile capacity and the corresponding lateral capacity of the pile at failure in tension. The tension capacity of the pile at any loading angles can be determined using Eq. (7.5). The corresponding pile lateral capacity to tension failure at different loading angles can be determined using Eq. (7.2) which is a function in pile flexibility (L/T) and the ultimate lateral capacity of rigid pile. The second method is to predict the maximum positive bending moment of a pile subjected to inclined pullout loading. The prediction depends upon the pile flexibility (L/T) and the maximum bending moment of the same pile at pure lateral loading. **It should be noted that this proposed method is valid for very dense sand case.**

10. In the second part of the parametric study, the effect of padeye depth was examined. The parametric study was carried out for three different piles over a wide range of pile flexibility. The analysis supported the recommended optimum padeye depth of $e/L \approx 0.7$ by Supachawarote et. al (2004) for normally and lightly overconsolidated clay for suction caisson or rigid piles. It was found that pile response becomes stiffer by increasing padeye depth. A design method was proposed to predict pile ultimate capacity at any depth of padeye up to the optimum mentioned depth based on pile flexibility. **It should be noted that this proposed method is valid for very dense sand case.**

11. The behavior of anchor piles under cyclic loading was examined. Three centrifuge tests were carried out at different loading angles 0°, 16°, and 90° under drained conditions. For tension loading case (loading angle 90°), the tension load degrades with an average factor of 0.05 along the pile shaft except 0.13 at pile tip. The

degradation stabilized after 10 cycles. For pure lateral and inclined pullout loading cases, the total lateral load at pile head slightly degrades more in the case of inclined pullout than that of pure lateral loading. This difference shows that inclined pullout loading case could be affected more with cyclic loading due to the degradation in shear stresses along the pile shaft. For the maximum bending moment, the degradation factor for the pile tested at 16° is less than that for the pile tested at pure lateral loading 0°.

12. During cycling loading, the axial load along the pile shaft decreases by increasing the cycle number. This means that the axial load effect on the pile is decreasing and consequently its effect on the bending moment is decreasing. The pile loaded under inclined pullout experienced higher degradation in soil stiffness than that loaded under pure lateral due to the reduction in soil confining pressure around the pile in case of inclined pullout loading.

13. A degradation model was suggested based on the soil stiffness degradation. The model was implemented in the FEM. In the case of pure lateral loading, soil young's modulus was degraded with cycle number. For the inclined pullout loading, both soil young's modulus and lateral earth pressure coefficient were degraded to account for axial load degradation as well. The proposed model has some limitation before being used at higher load levels and cycles more than 50.

9.3. Future Research:

The current research can be extended to include many other aspects for further research. The future research that should be considered to improve the current research is:

1. The current research was limited to offshore anchor piles driven in dense sand. The future research should be extended to different sand relative density. The behavior of anchor piles in clay should be studied.

2. The condition of heterogeneous soil should be studied which is the case for most of seabed conditions.
3. The shear wave measurements can be extended to do a tomographic imaging. Soil pile interaction can be better understood by using a tomographic imaging system of bender elements. The imaging can be in horizontal sections at different depths or longitudinal section along the pile. By combining both imaging setup, three dimensional imaging can be obtained. Such imaging is very useful in observing the change in soil stress around the pile. It also helps in better calibration of the FEM.
4. The implemented method in the FEM to simulate the effect of pile installation should be improved. The increase in lateral stresses around the pile should be limited to a zone around the pile.
5. Centrifuge modeling of cyclic loading case should be improved. Cycle number should be increased to not less than 1000 cycles to simulate the offshore environment. The effect of cyclic load amplitude and load level should be studied.

References:

Abdel-Rahman, K., and Achmus, M. (2006), Numerical modeling of the combined axial and lateral loading of vertical piles, Proceedings of the sixth European Conference in Geotechnical Engineering, Graz, Austria.

Achmus, M., Abdel-Rahman, K., and Wörden, F. (2007), Geotechnical design of piles supporting foundation structures for offshore wind energy converters, Proceedings of the seventeenth International Offshore and Polar Engineering Conference, Lisbon, Portugal.

Altaee, A., and Fellenius, B. (1994), Physical modeling in sand. Canadian Geotechnical Journal 31: 420-431.

American Petroleum Institute (API), 2000, Recommended Practice for Planning, Designing and Constructing Fixed Offshore Platforms-Working Stress Design, RP2A-WSD 21st ed., American Petroleum Inst.

Arulnathan, R., Boulanger, R. W., Kutter, B. L. and Sluis, W. K. (2000), New tool for shear wave velocity measurements in model tests, Geotechnical Testing Journal, GTJODJ, 23, No.4, 444-453.

Awad, A. and Petrasovits, G. (1968), Consideration of the bearing capacity of vertical and batter piles subjected to forces acting in different directions, in: Proceedings of the 3rd Budapest Conferences on Soil Mechanics and Foundation Engineering, Budapest.

Baldi, G., Bellotti, R., Ghionna, V., Jamiolkowski, M., and Pasqualini, E., (1982), "Design Parameters for sands from CPT", Proceedings of the Second European Symposium on Penetration Testing, ESOPT II, Amsterdam, May 1982, Vol. 2, pp. 425-438.

Banerjee, P. K. and Davies, T. G. (1978), "The behavior of axially and laterally loaded single piles embedded in non-homogoneous soils." Geotechnique, 28(3), 309-326.

Bhattacharya, S., Carrington, T.M., and Aldridge, T.R. (2006), Design of FPSO piles against storm loading, Offshore Technology Conference, OTC 17861.

Bolton, M. D., 1986, "The strength and dilatancy of sands", Geotechnique, Vol. 36, No. 1, pp. 65-78.

Bolton, M. D. and Gui, M. W. (1993) "The Study of Relative Density and Boundary Effects for Cone Penetration Tests in Centrifuge", Technical Report (CUED/D-SOILS/TR256).

Bolton, M., Gui, M., Garnier, J., Corte, J., Bagge, G., Laue, J. and Renzi, R. (1999), Centrifuge cone penetration tests in sand, Geotechnique, 49, No. 4, 543-552.

Brandenberg, S. J., Kutter, B. L., and Wilson, D. W. (2008), Fast stacking and phase corrections of shear wave signals in a noisy environment, Journal of Geotechnical and Geoenvironmental Engineering, Vol. 134, No. 8.

Broms, B. B. (1964), Lateral resistance of piles in cohesionless soils. J. Soil Mechanics and Foundations Division, ASCE, 90(SM3), 123-156.

Broms (1965), Discussion of "Piles in cohesionless soil subject to oblique pull" by Y. Yoshimi. Journal of the Soil Mechanics and Foundations Division, ASCE 91: 199-205.

Brown, D. A., and Shie, C.-F., (1990), Three-dimensional finite element model of laterally loaded piles. Computers and Geotechnics, 10, 59-79.

Budhu, M., and Davies, T. G., (1987), Nonlinear analysis of laterally loaded piles in cohesionless soils, Canadian Geotechnical Journal, Vol. 24, No. 1, 289-296.

Canadian Geotechnical Society, (2007), Canadian Foundation Engineering Manual, 4th ed.

Chakrabortty, P., 2008, "Seismic Liquefaction of Heterogeneous Soil: Mechanism and Effects on Structural Response," Ph.D. thesis, Memorial University of Newfoundland, Newfoundland, Canada.

Chattopadhyay, B. C., and Pise, P. J. (1986), Ultimate resistance of vertical piles to oblique pulling load, Structural Engineering & Construction: Advances & Practice in East Asia & The Pacific, Proceedings of The First East Asian Conference on Structural Engineering & Construction, Bangkok, Thailand. 1: 1632-1641.

Corté, J. F., Garnier, J., Cottineau, L. M., and Rault, G., 1991, "Determination of model soil properties in the centrifuge", Centrifuge'91, Proceedings of the

International Conference Centrifuge 1991, Boulder, Colorado, Edited by Hon-Yim Ko, Francis G. Mclean.

Das, B. M. Seeley, G. R. & Raghu, D. (1976), Uplift capacity of model piles under oblique loads. Journal of the Geotechnical Engineering Division, ASCE. 102: 1009-1013.

De Nicola, A., and Randolph, M. F. (1993), Tensile and compressive shaft capacity of piles in sand. J. Geotech. Engng Div., ASCE 119, No. 12, 1952–1973.

De Nicola, A., and Randolph, M. F. (1999), Centrifuge modeling of pipe piles in sand under axial loads. Géotechnique, 49(3):295 – 318.

Dief, H.M., 2000, "Evaluating the Liquefaction Potential of Soils by the Energy Method in the Centrifuge," PhD thesis, Case Western Reserve University.

Dodds, A. (2005), A Numerical study of pile behavior in large pile groups under lateral loading, PhD thesis, University of Southern California, USA.

Dyson, G. J. and Randolph, M. F., 2001, "Monotonic Lateral Loading of Piles in Calcareous Sand," Journal of Geotechnical and Geoenvironmental Engineering, ASCE, 127(4), pp. 346-352.

Fan, C. (1996), The behavior of laterally loaded single piles and group piles in sand, PhD thesis, University of Illinois at Urbana-Champaign, USA.

Ferguson, K. A., and Ko, H. Y. (1985), "Application of centrifugal modeling to cone penetrometer technology", Centrifuge'85, 1985.

Fioravante, V. (2002). On the shaft friction modelling of nondisplacement piles in sand. Soils Found. 42, No. 2, 23–33.

Fu, L., (2004), Application of Piezoelectric Sensors in Soil Property Determination", PhD thesis, Case Western Reserve University, USA

Fu, L., X. Zeng, and Figueroa, L. (2004), Shear wave measurement in centrifuge using bender elements. International Journal of Physical Modelling in Geotechnics, 2: 1-11.

Gavin, K. and Lehane, B. (2003), The shaft capacity of pipe piles in sand, Canadian Geotechnical Journal, Vol. 40, No. 1, p 36-45

Gavin, K. and O'Kelly, B. (2007), Effect of Friction Fatigue on Pile Capacity in Dense Sand, Journal of Geotechnical and Geoenvironmental Engineering, Vol. 133, No. 1, January 1, 2007.

Gerwick, B. (2000), Construction of Marine and Offshore Structures, CRC press.

Gohl, W.B. and Finn, W.D.L. (1987): "Seismic response of pile foundation in a centrifuge," Prediction and Performance in Geotechnical Engineering, pp. 419-426.

Hibbitt Karlsson and Sorensen, Inc., (1998), ABAQUS/Standard User Manuals. (Pawtucket): Hibbitt. Karlsson & Sorensen, Inc, United States.

Hesar, M. (1991), Behaviour of Pile-anchors Subjected to Monotonic and Cyclic Loading, PhD Thesis, University of Sunderland, UK.

Ismael, Nabil F. (1989), Field tests on bored piles subject to axial and oblique pull. Journal of Geotechnical Engineering 115: 1588-1598.

Ismail, M. and Hourani, Y. (2003), An innovatve facility to measure shear wave velocity in centrifuge and 1g models, Centre for Offshore Foundations Systems (COFS), Report No. C1717

Jamnejad, G. H., and Hesar, M. H. (1995), Stability of pile anchors in the offshore environment. Trans IMarE 107: 119–134

Jamiolkowski, M., Ladd, C.C., Germaine, J. and Lancellotta, R., 1985, "New developments in field and lab testing of soils", Proceedings, 11th Intl. Conference on Soil Mechanics and Foundations Engineering, Vol. 1, San Francisco, 57-154.

Jardine, R. J. & Chow, F. C. (1996). New design methods for offshore piles, MTD Publication 96/103. London: Marine Technology Directorate.

Jardine RJ, Overy RF, and Chow FC. 1998 Axial capacity of offshore piles in dense north sea sands. J Geotechnical Geoenviron Eng, ASCE;124(2):171–8.

Kita, K., Shibata, T., Yashima, A. and Kobayashi, S. (1992), Measurement of shear wave velocities of sand in a centrifuge, Soils and Foundations, 32, No. 2, 134-140

Kraft LM, Ray RP, Kagawa T., (1981), Theoretical t–z curves, J Geotechnical Eng, ASCE;104(GT11):1543–60.

Kulhawy, F., and Mayne, P., (1991), Calibration chamber database and boundary effects correction for CPT data, Proc., 1st Int. Symp. on Calibration Chamber Testing (ISOCCT1), Potsdam, N.Y., A. B. Huang, ed., Elsevier, New York, 257-264.

Lancelot, L., Shahrour, I., and Al Mahmoud, M. (2006) "Failure and dilatancy properties of sand at relatively low stresses", Journal of Engineering Mechanics, ASCE, Vol. 132, No. 12, 1396-1399.

Lee, J.-S. and Santamarina. J.C. (2005), Bender elements: performance and signal interpretation. Journal of Geotechnical and Geoenvironmental Engineering, 2005. 131(9): 1063-1070.

Lehane, B. M. (1992), Experimental investigations of pile behavior using instrumented field piles. PhD thesis, Imperial College, UK.

Lehane, B.M., Jardine, R.J., Bond, A.J. and Frank, R. (1993), Mechanisms of shaft friction in sand from instrumented pile tests. J. Geot. Eng. Div., ASCE, 119(1), 19-35.

Leong, E. C., Yeo, S. H., and Rahardjo, H., 2005, "Measuring Shear Wave Velocity Using Bender Elements," Geotechnical Testing Journal, Vol. 28, No. 5, pp. 488–498.

Leshukov, M. R. (1975), Effect of oblique extracting forces on single piles, Soil Mechanics and Foundation Engineering Journal (English translation of Osnovaniya, Fundamenty i Mekhanika Gruntov). 12: 300-301.

Long, J.H., Vanneste, G., (1994), Effects of cyclic lateral loads on piles in sand, ASCE Journal of Geotechnical Engineering, Vol. 120, No. 1.

Mayne, P.W. (1995). CPT determination of OCR and Ko in clean quartz sands. Proceedings, CPT'95, Vol. 2, Swedish Geotech Society, Linkoping, 215-220.

Mayne, P.W., Mitchell, J.K., Auxt, J., and Yilmaz, R., 1995, "U.S. national report on the CPT", Proceedings, CPT'95, Vol. 1, Swedish Geotechnical Society, Linköping, 263-276.

Mayne, Paul W., 2001, "Stress-Strain-Strength-Flow Parameters from Enhanced In-Situ Tests," Proceedings, International Conference on In-Situ Measurement of Soil Properties & Case Histories [In-Situ 2001], Bali, Indonesia, pp. 27-48.

McClelland, B. and Focht, J. A., Jr. (1958), Soil modulus for laterally loaded piles, Trans., A.S.C.E., Paper No. 2954, 123, 1049-1063.

Merifield, R. S., White, D. J., and Randolph, M. F. _2008_. "Analysis of the undrained breakout resistance of partially embedded pipelines." Geotechnique, 58_6_, 461–470.

Meyerhof, G. G. (1973), The uplift capacity of foundations under oblique loads, Canadian Geotechnical Journal, 10, 64-70.

Meyerhof, G. G. 1995, Standard penetration tests and pile behaviour under lateral loads in cohesionless soils, Canadian Geotechnical Journal, Vol. 32, 913-916.

Mezazigh, S. and Levacher, D., 1998, "Laterally Loaded Piles in Sand: Slope Effect on P-Y Reaction Curves," Canadian Geotechnical Journal, 35, pp.433-441.

Nunez, 1. L., Hoadley, P. J., Randolph, M. F. and Huetett, J. M. (1988), Driving and Tension Loading of Piles in Sand on Centrifuge, Proc. of Centrifuge 85. Paris, France, pp. 352-362.

Ovesen N.K. (1979), The Scaling law relationship Proceedings of 7th European Conference on Mechanics and Foundation Engineering, Brighton, Vol. 4. pp. 319.323.

Paik, K. H., Salgado, R., Lee, J. & Kim, B. (2003), Behavior of open and closed-ended piles driven into sand. J. Geotech. Geoenviron. Engng Div., ASCE 129, No. 4, 296–306.

Phillips, R. (1995), Centrifuge Modelling: Practical Considerations in Geotechnical Centrifuge Technology, R. N. Taylor, Ed., Blackie Academic & Professional, London, pp. 34–60.

Poulos, H. G. (1971). "Behavior of laterally loaded piles: I - single piles." J Soil Mechanics and Foundations Division, ASCE, 97(SM5), 711-731.

Poulos and Davis. (1980), Pile foundation analysis and design. New York: John Wiley & Sons.

Puech, A. and Foray, P. (2002), "Refined Model for Interpreting Shallow Penetration CPTs in Sands" Offshore Technology Conference, OTC 14275

Salgado, R., and Prezzi, M. (2007), Computation of Cavity Expansion Pressure and Penetration Resistance in Sands", International Journal of Geomechanics, Vol. 7, No. 4, 251-265.

Schmertmann, J.H., (1978), "Guidelines for Cone Penetration Tests, Performance and Design". US Federal Highway Administration, Washington, DC, Report FHWA-TS-78-209, 145.

Schneider, J.A., and Lehane, B.M. (2005), "Correlations for shaft capacity of offshore piles in sand", International Symposium on Frontiers in Offshore Geotechnics, Perth, Australia, Taylor & Francis: 757-763.

Shirley, D.J., and Hampton, L.D. (1978): "Shear wave measurements in laboratory sediments," Journal of the Acoustical Society of American, 63 (2), pp. 607-613.

Stokoe, K. H. and Santamarina, J. C. (2000), Seismic wave based testing in geotechnical engineering, GeoEng 2000, An International Conference on Geotechnical and Geological Engineering, Vol.1, pp. 1490-1536

Sulaiman I. H, and Coyle H. M., (1976), Uplift resistance of piles in sand, J Geotechnical Eng, ASCE;102(GT5):559–62.

Supachawarote, C., Randolph, M., and Gourvenec, S., (2004), Inclined Pull-out Capacity of Suction Caissons, Proceedings of The Fourteenth, International Offshore and Polar Engineering Conference, Toulon, France, May 23-28, 2004.

Taylor, R.N., (1995). Centrifuge in modeling: principle and scale effects, Geotechnical centrifuge technology, R.N. Taylor, ed., pp. 19-33.

Terzaghi, K. (1955). Evaluation of coefficients of subgrade reaction, Geotechnique, 5, 297326.

Thompson, G. R. & Long, L. G. 1989. Hibernia geotechnical investigation and soil characterization. Canadian Geotechnical Journal. 26: 653-678.

Toolan, F. E., Lings, M. L. & Mirza, U. A. (1990). An appraisal of API RP2A recommendations for determining skin friction of piles in sand. Proc. 22nd Annual Offshore Technol. Conf., Houston, 33–42.

Trochanis, A. M., Bielak, J., and Christian, P. (1988). A Three-Dimensional Nonlinear Study of Piles Leading to the Development of a Simplified Model, Depaitment of Civil Engineering, Carnegie Institue of Technology, Carnegie Mellon University, Pittsburgh, PA 15213.

Trochanis, A. M., Bielak, J., and Christian°, P. (1991a). "Three-dimensional nonlinear study of piles." J. Geotech. Eng., ASCE, 117(3), 429-447.

Trochanis, A. M., Bielak, J., and Christian, P. (1991b). "Three-Dimensional Nonlinear Study of Piles and Simplified Models." In Geotechnical Engineering Congress 1991, Boulder, Colorado; June 10-12, 1991 (Geotechnical Special Publication No. 27), Vol. II, F. G. McLean, DeW. A. Campbell, & D. H. Harris (eds.), American Society of Civil Engineers, New York, New York 10017-2398, 356-366.

Turner, J. P. and Kulhawy, F. H. (1994) "Physical modeling of drilled shaft side resistance in sand" Geotechnical testing Journal, Vol. 17. No. 3, pp.282-290.

Rammah, K., Ismail, M., and Fahey, M. (2006), Development of a Centrifuge Seismic Tomography System at UWA, Proceedings of The Sixth International Conference on Physical Modelling in Geotechnics, Hong Kong.

Ramadan, M. I., Butt, S. D. and Popescu, R. (2009a), "Pipe piles under mooring forces", 17th International Conference of Soil Mechanics and Geotechnical Engineering, ICSMGE'09, Alexandria, Egypt, 5-9 October.

Ramadan, M. I., Butt, S. D. and Popescu, R. (2009b), "Finite element modeling of offshore anchor piles under mooring forces", 62nd Canadian Geotechnical Society Conference, GeoHalifax'09, Halifax, Canada.

Randolph, M., Worth, C., (1978), "Analysis of deformation of vertically loaded piles", J Geotechnical Eng, ASCE,104: 1465–88.

Randolph, M.F., Dolwin, J. and Beck, R.D. (1994), Design of driven piles in sand. Géotechnique, 44(3), 427-448.

Randolph, M.F. (2003), 43rd Rankine Lecture: Science and empiricism in pile foundation design. Géotechnique, 53(10), 847-875.

Randolph, M.F., Cassidy, M.J., Gourvenec, S. and Erbrich, C.J. (2005), Challenges of offshore geotechnical engineering, State of the Art paper. Proc. Int. Conf. on Soil Mech. and Found. Eng., Osaka.

Reese, L. C. (1958), Discussion: Soil Modulus for Laterally Loaded Piles. Trans., A.S.C.E., 123, 1071-1074.

Reese, L. C., Cox, W. R., and Koop, F. D. (1974), Analysis of laterally loaded piles in sand. In Proceedings, Sixth Annual Offshore Technology Conference, Paper No. 2080, OTC, Houston, Texas, 473-483.

Reese, L. C. and Van Impe, W. F. (2001), Single Piles and Pile Groups under Lateral Loading, A. A. Balkema, Brookfield, VT.

Remand, D. (1999), Pieux sons charges latérales : étude expérimentale de l'effet de groupe, These de doctorat, Université de Nantes.

Robertson, P.K. and Campanella, R.G. (1983). Interpretation of cone penetration tests: sands. Canadian Geotechnical Journal, Vol. 20 (4), 719-733.

Robertson, P. K., 2010, "Estimating in-situ state parameter and friction angle in sandy soils from CPT", CPT'10, 2nd International Symposium on Cone Penetration Testing, California, USA.

Rosquoët, F., Thorel, L., Garnier, J., Canepa, Y. (2007), Lateral Cyclic Loading of Sand-Installed Piles, Soils and Foundations, Vol. 47, No. 5, 821-832.

Rowe, P.W., (1962). The stress-dilatancy relation for static equilibrium of an assembly of particles in contact. Proc. of Royal. Society of London, 269(Series A), pp. 500-527.

Vaid, Y.P., Stedman, J.D., and Sivathayalan, S., 2001, "Confining stress and static shear effects in cyclic liquefaction", Canadian Geotechnical Journal, Vol. 38, No. 3, pp. 580-591.

Van der Poel, J. T. and Schenkeveld, F. M., 1998, "A preparation technique for very homogenous sand models and CPT research", Centrifuge'98, Proceedings of the International Conference Centrifuge 1998, Edited by: Kimura, Kusakabe and Takemura, pp. 149-154.

Vesic, A.S. 1970. Tests on instrumented piles, Ogeechee River site. J. of the Soil Mech. and Found. Div., ASCE, 96(SM2), 561-584.

Vidich, S., Kulhawy, F. ard Tfaurnrann, H., (1998). Laboratory Modeling of Inclined-loaded Shafts in Sand, Geotechnical testing Journal, Vol. 21. No. 3, pp.203-212

White, D. J. & Bolton, M. D. (2002). Observing friction fatigue on a jacked pile. In Centrifuge and constitutive modelling: two extremes (ed. S. M. Springman), pp. 347–354. Rotterdam: Swets & Zeitlinger.

White, D. J. and Bolton, M. D. (2005), "Comparing CPT and pile base resistance in sand", Proceedings of the Institute of Civil Engineers, Geotechnical. Engineering, Vol. 158, Issue GEI, pp. 3-14

Wijewickreme, D., Sriskandakumar, S., and Byrne, P. (2005), Cyclic loading response of loose air-pluviated Fraser River sand for validation of numerical models simulating centrifuge tests, Canadian Geotechnical Journal, Vol.42: 550-561

Yan, L., and Byrne, P. M., 1992, "Lateral Pile Response to Monotonic Head Loading," Canadian Geotechnical Journal, 29, pp. 955-970.

Yoshimi, Y. (1964), Piles in cohesionless soil subject to oblique pull. Journal of the Soil Mechanics and Foundations Division, ASCE 90: 11-24.

Zhao, Y., White, D. J., and Bolton, M. D. (2006), In situ seismic monitoring during centrifuge tests of jacked piles, Proceedings of the 6th International Conference on Physical Modelling in Geotechnics, V 2, p 907-912, 2006

Zhu, F., (1998), "Centrifuge Modelling and Numerical Analysis of Bearing Capacity of Ring Foundations on Sand", PhD thesis, Memorial University of Newfoundland, St. John's, Canada.

APPENDIX – A

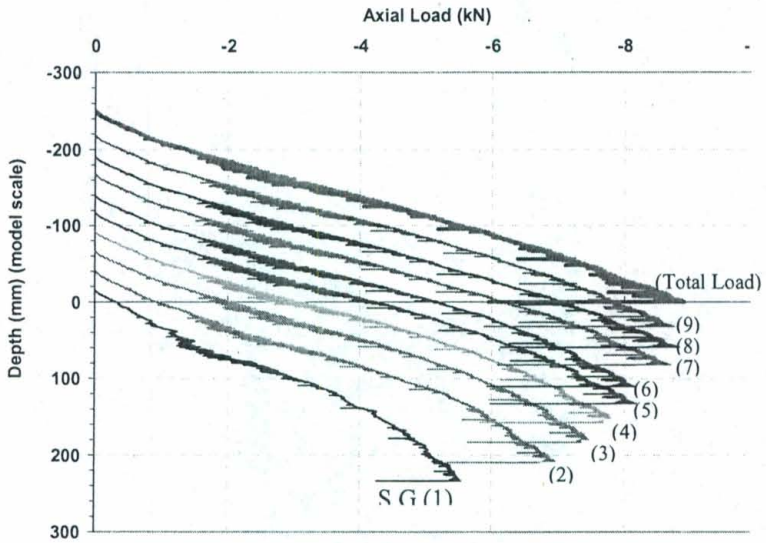

Figure (A-1): Axial Load measurements during Pile Installation – Pile# 1

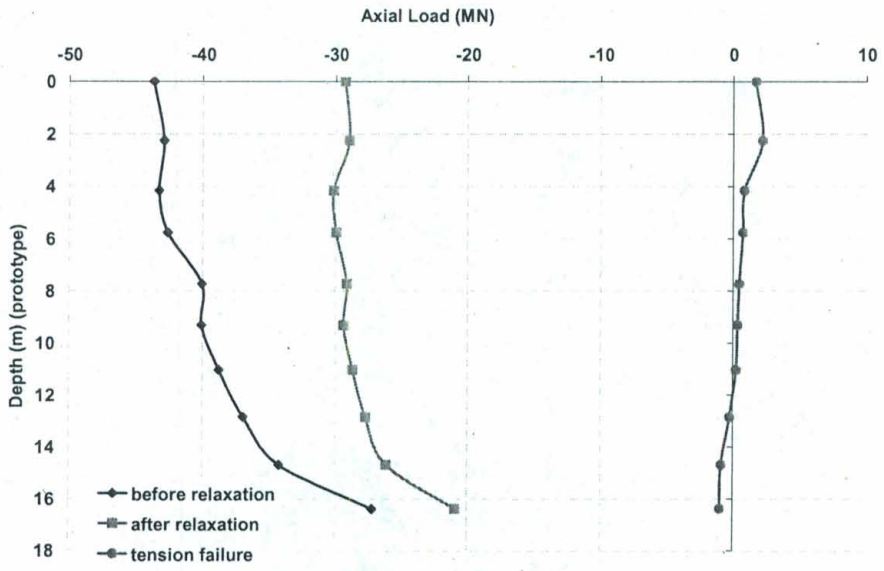

Figure (A-2): Axial Load Distribution along pile at different stages of the test – without centrifuge stopping pile driving and loading

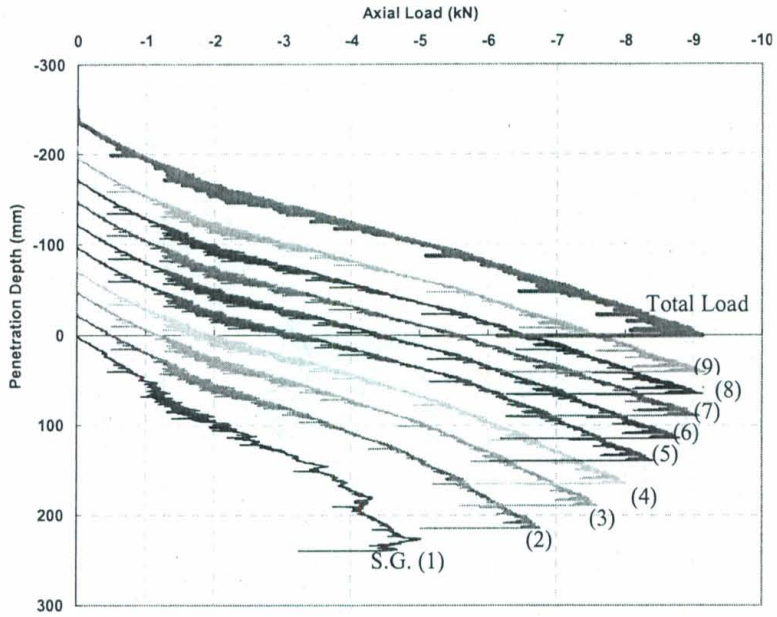

Figure (A-3): Axial Load measurements during Pile Installation – Pile#2

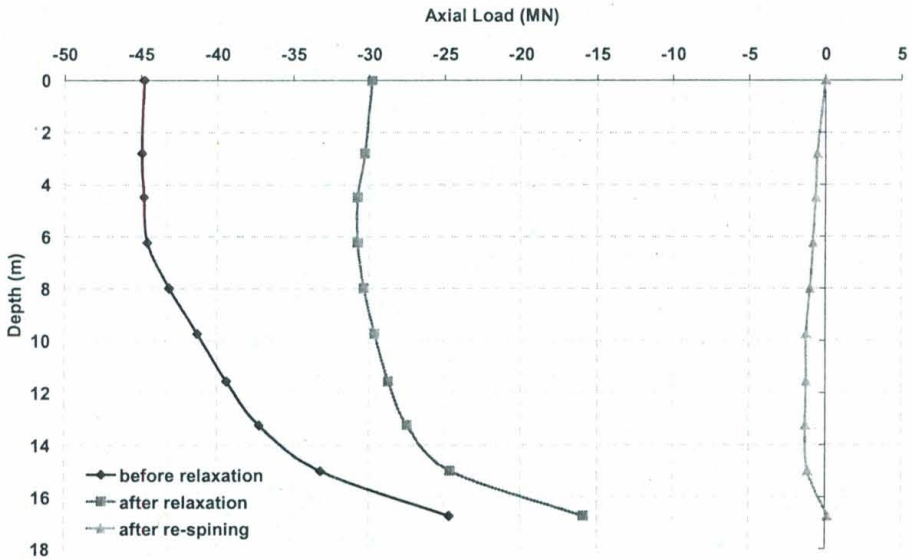

Figure (A-4): Axial Load Distribution along pile at different stages of the test – with centrifuge stopping pile driving and loading